

Institute of Experimental Pharmacology and Toxicology  
Center for Experimental Medicine  
University Medical Center Hamburg-Eppendorf

**Epigenetic mechanisms of transcriptional regulation in cardiac  
hypertrophy using engineered heart tissue**

---

**Dissertation**

Submitted to the Department of Chemistry  
Faculty of Mathematics, Informatics, and Natural Sciences  
University of Hamburg  
for the degree of  
**Doctor of Natural Sciences**  
**(Dr. rer. nat.)**

by

**Alexandra Löser**

Hamburg, 2018



1<sup>st</sup> Referee: Prof. Dr. Thomas Eschenhagen

2<sup>nd</sup> Referee: Prof. Dr. Elke Oetjen

Date of disputation: 14.12.2018

Practical supervision of this work was carried out by Dr. Dr. Justus Stenzig.



## Table of contents

1	Introduction .....	1
1.1	Cardiac hypertrophy and heart failure .....	1
1.2	Epigenetic mechanisms of gene regulation .....	3
1.2.1	Epigenetics in heart failure pathology .....	7
1.3	Human induced pluripotent stem cells (hiPSC).....	8
1.3.1	Differentiation of hiPSC into cardiomyocytes .....	11
1.4	Cardiac tissue engineering .....	14
1.5	CRISPR/Cas9-based genome editing .....	16
2	Aim.....	21
3	Materials and methods .....	22
3.1	Cell culture media .....	22
3.2	Stem cell culture.....	24
3.3	CRISPR/Cas9-mediated gene knockout.....	24
3.3.1	CRISPR design and cloning .....	24
3.3.2	Preliminary tests.....	28
3.3.3	Knock out of DNMT3A in ERC018 hiPSC.....	30
3.3.4	Subcloning and off-target analysis.....	31
3.3.5	Karyotyping .....	32
3.4	Cardiac differentiation .....	32
3.5	Engineered heart tissue (EHT) .....	36
3.5.1	EHT generation and culture.....	36
3.5.2	Video-optical contraction analysis .....	36
3.5.3	Baseline characterization of CRISPR cell lines in EHT format.....	37
3.5.4	Hypertrophic intervention .....	39
3.5.5	Termination of EHT experiments.....	40
3.6	Molecular analysis.....	40
3.6.1	Immunohistochemical staining .....	40
3.6.2	Gene expression analysis .....	40
3.6.3	Western blot.....	41
3.6.4	Reduced representation bisulfite sequencing (RRBS) .....	42
3.6.5	Sharp electrode measurements .....	42

3.6.6	Lipid staining with Oil red O .....	43
4	Results .....	44
4.1	Expression of DNMT isoforms in hiPSC and hiPSC-derived cardiomyocytes .....	44
4.2	CRISPR/Cas9-mediated knockout of DNMT3A .....	44
4.2.1	DNMT3A target sequence verification and sgRNA cloning .....	44
4.2.2	Comparison of Cas9 plasmids .....	45
4.2.3	Nucleofection optimization for ERC018 .....	47
4.2.4	Nucleofection and single clone expansion .....	48
4.2.5	Off-target analysis .....	52
4.2.6	Karyotype analysis .....	54
4.3	Cardiac differentiation .....	56
4.4	Effect of the DNMT3A mutations on mRNA and protein expression .....	57
4.5	Functional effects of DNMT3A knockout in EHT .....	60
4.5.1	Development and contractility .....	60
4.5.2	Baseline characterization of EHT function .....	64
4.5.3	Action potentials .....	70
4.5.4	Hypertrophic intervention .....	72
4.6	Molecular analysis .....	79
4.6.1	Histology .....	79
4.6.2	Gene expression analysis .....	85
4.6.3	DNA methylation analysis .....	89
5	Discussion .....	98
5.1	Generation of DNMT3A knockout hiPSC .....	98
5.2	DNA methylation in differentiation .....	100
5.3	Effect of DNMT3A knockout on EHT function .....	101
5.3.1	EHT contractility .....	101
5.3.2	Calcium handling and action potentials .....	104
5.3.3	Vacuolic accumulations in knockout EHTs .....	106
5.4	DNA methylation patterns and gene expression .....	108
5.5	DNMT3A and the effect of pro-hypertrophic treatment on EHT function .....	113
5.6	Conclusion and future perspectives .....	117
6	Summary .....	119

7	Zusammenfassung.....	120
8	References.....	121
9	Supplement.....	136
9.1	Supplementary figures and tables .....	136
9.2	List of abbreviations .....	143
9.3	Devices, materials and substances .....	148
9.3.1	Devices .....	148
9.3.2	Software.....	149
9.3.3	Materials and equipment.....	149
9.3.4	Cell culture medium and serum.....	150
9.3.5	Reagents.....	150
9.3.6	Kits and enzymes.....	152
9.3.7	Composition of reagents, buffers, and solutions .....	153
9.3.8	Antibodies .....	155
9.3.9	Primer lists and NanoString Expression CodeSets.....	156
9.4	Security information.....	158
9.4.1	EU-GHS Hazard (H) statements.....	160
9.4.2	EU-GHS Precaution (P) statements .....	161
9.5	Publications and congress participations.....	163
9.5.1	Publications.....	163
9.5.2	Participation at congresses and meetings .....	163
10	Acknowledgements.....	165
11	Declaration of academic honesty - Eidesstattliche Erklärung .....	166





# 1 Introduction

## 1.1 Cardiac hypertrophy and heart failure

Heart failure, the inability of the heart to sufficiently supply the body with oxygen and nutrients, is one of the leading causes of death worldwide and its incidence is steadily increasing (Ponikowski et al. 2014). The development of heart failure can be caused by a variety of conditions including myocardial infarction, valvular heart disease, hypertension, diabetes mellitus, and familial hypertrophic or dilated cardiomyopathy (Mosterd et al. 1999; Lips et al. 2003). In many of these pathologies the heart initially compensates for the mismatch between demand and supply of cardiac output and the elevated wall stress by increasing the size of cardiomyocytes, resulting in a state of compensated hypertrophy. However, if the pathological stimuli are maintained over a longer period the heart is no longer able to compensate, which leads to the manifestation of pathological hypertrophy and increases the risk for the development of heart failure (Berenji et al. 2005). In general, cardiac hypertrophy can be divided into physiological hypertrophy induced by pregnancy or exercise, and concentric or eccentric pathological hypertrophy caused by pressure or volume overload, respectively (Wakatsuki et al. 2004). In concentric hypertrophy, the heart responds to the pressure-induced elevation of wall stress with an increase in ventricular wall thickness. Eccentric hypertrophy in contrast leads to thinning of the walls and dilation of the ventricular chambers due to increased volume load (figure 1).

Development of cardiac hypertrophy is accompanied by several characteristic maladaptive changes both on the structural and the molecular level. One common hallmark of pathological hypertrophy is the reactivation of the fetal gene program leading for example to an increase in expression of the natriuretic peptides ANP and BNP (Takahashi et al. 1992; Arai et al. 1993). Moreover, the expression of both myosin heavy chain isoforms is altered during cardiac hypertrophy, resulting in an increased  $\beta$ -MHC/ $\alpha$ -MHC ratio, which affects the contractility of the heart due to the different contraction kinetics of the two isoforms (Locher et al. 2011). Metabolic processes are likewise affected by this fetal isoform switch. Under physiological conditions, adult cardiomyocytes mainly oxidize fatty acids for ATP generation. During cardiac hypertrophy, however, metabolic reprogramming takes place, lowering the rate of fatty acid metabolism and increasing instead the contribution of glycolysis to energy generation (Strøm et al. 2005). Moreover, the higher cardiac workload due to sustained pressure or volume overload leads to increased cardiac ATP consumption, which can only be insufficiently compensated. The development of interstitial and perivascular fibrosis in addition increases the stiffness of the cardiac walls, which impedes diastolic filling and further decreases cardiac contractility (Kong et

al. 2014). Additionally, changes in calcium handling can be observed in hypertrophic cardiomyocytes. One of the best studied examples is the decrease in expression of the sarco/endoplasmic reticulum calcium-ATPase SERCA2a in cardiac hypertrophy, resulting in impaired calcium clearance from the cytosol, further contributing to diastolic dysfunction (Hasenfuss et al. 1994). Moreover, several intracellular signaling cascades such as the  $\text{Ca}^{2+}$ /calmodulin-dependent protein kinase (CaMKII) and calcineurin/nuclear factor of activated T cells (NFAT) pathways are perturbed, further promoting cardiac remodeling and hypertrophic gene transcription (reviewed in (Heineke and Molkentin 2006).

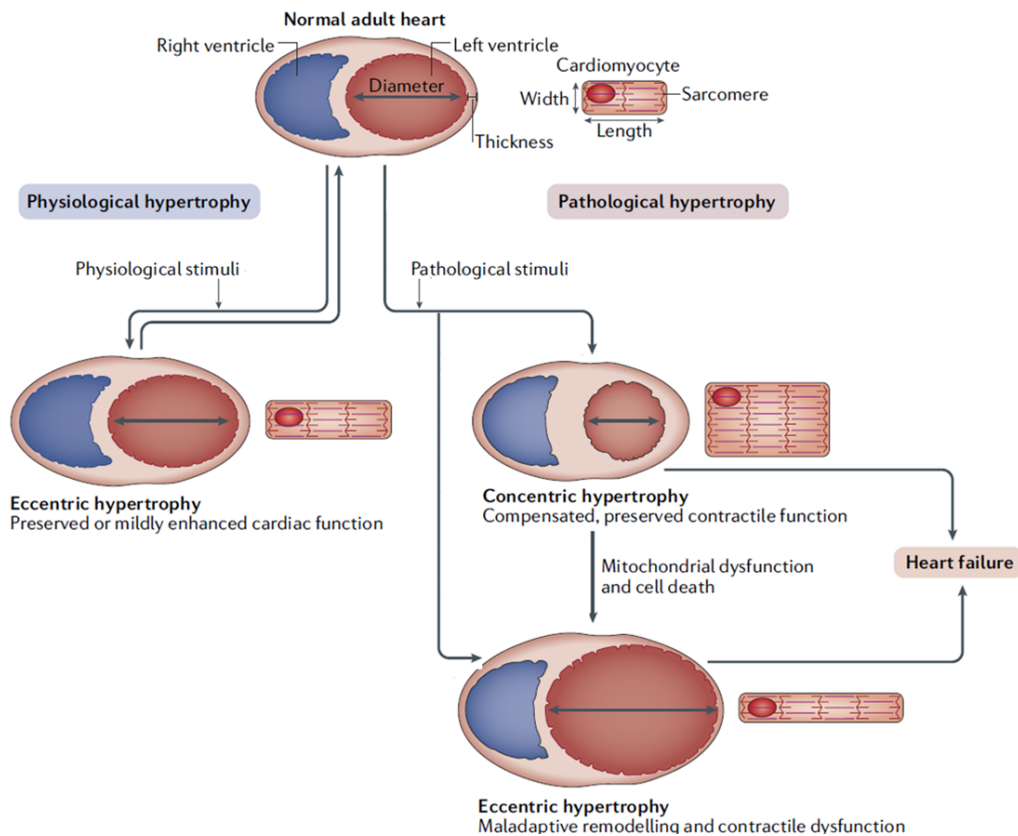


**Figure 1: Forms of cardiac hypertrophy.** The adult heart reacts to exercise or pregnancy stimuli by moderately increasing both its ventricular volume and ventricular wall thickness, preserving the cardiac function. This process of physiological hypertrophy is fully reversible. Pathological stimuli on the other hand induce either an irreversible thickening of the ventricular wall which reduces the left ventricular volume (pressure overload), or dilation of the ventricular chamber and thinning of the walls (volume overload) leading to contractile dysfunction and development of heart failure (adapted from Nakamura and Sadoshima 2018).

## 1.2 Epigenetic mechanisms of gene regulation

Epigenetic mechanisms, comprising all chromatin modifications which do not change the nucleotide sequence itself, have gained increasing attention over the last years as new players in the regulation of gene transcription in both cardiac development and disease. In general, epigenetic mechanisms can be broken down into four different classes: (i) posttranslational modifications of histone tails, (ii) DNA modifications such as methylation, (iii) chromatin-remodeling complexes, and (iv) regulatory non-coding RNAs.

Genetic information in cells is stored in the form of chromatin, which is a complex of DNA and proteins, most of which are histones around which the DNA is wrapped (forming the nucleosome). The N-terminal tails of the histones protrude from the DNA double strand, making them accessible for deposition of posttranslational modifications such as acetylation, methylation, phosphorylation, sumoylation, and ubiquitylation. Depending on the position and the type of modification it can result either in activation or repression of gene transcription (figure 2). The combination of the different histone modifications locally regulates chromatin structure, thereby changing the accessibility of different regions of the genome and contributing to gene regulation (reviewed in Jenuwein and Allis 2001).

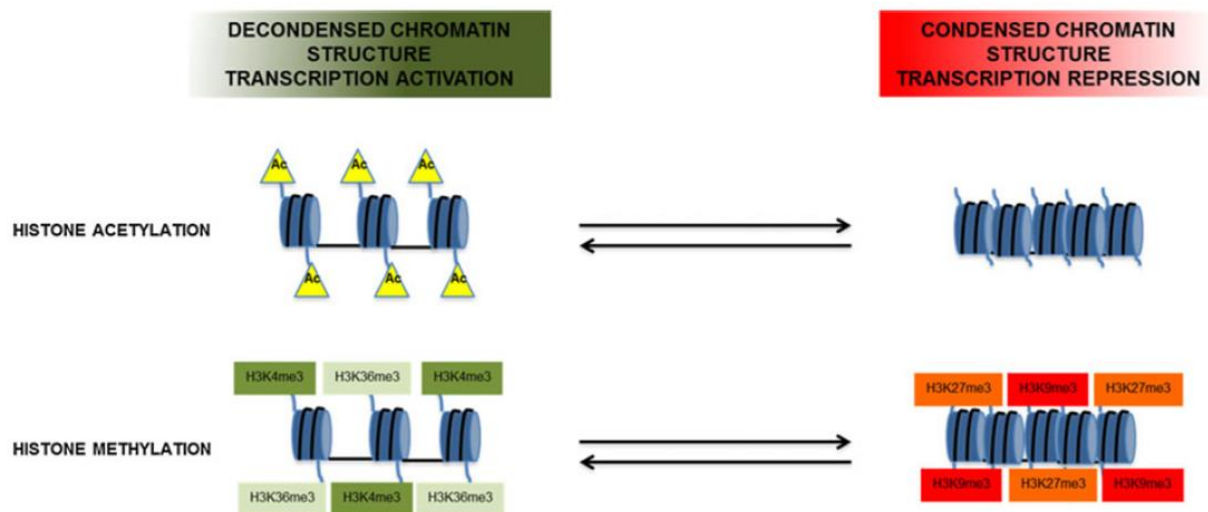


**Figure 2: Transcriptional regulation by histone modifications.** Acetylation of histone tails is generally associated with a decondensed chromatin structure allowing for gene transcription (top). Histone methylation on the other hand can facilitate both transcriptional activation and repression (bottom) depending on the position of the modified lysine in the histone tail (adapted from Papait et al. 2013).

Although thought to be a stable DNA modification in the beginning, DNA methylation has since been shown to be a dynamic, but nevertheless heritable process (Meissner et al. 2008). DNA methylation in mammalian somatic cells is mainly found in the context of CpG dinucleotides, in which a methyl group is added onto the 5' position of cytosine by DNA methyltransferases (DNMTs). Most CpG dinucleotides are located in high density in so-called "CpG islands" which are most often found in regulatory regions such as promoters at the 5' end of genes (McClelland and Ivarie 1982). Three active DNMT isoforms are encoded in the human genome (DNMT1, DNMT3A and DNMT3B), as well as the catalytically inactive co-factor DNMT3L. While DNMT1 in interaction with other proteins is mainly responsible for maintenance of already established DNA methylation patterns during DNA replication (Bashtrykov et al. 2014), DNMT3A and DNMT3B in cooperation with DNMT3L conduct *de novo* methylation of previously unmethylated regions (Okano et al. 1998; Wienholz et al. 2010). DNA methylation can modulate the expression of genes by different mechanisms. In this context methylation of promoter regions is usually associated with repression of the downstream gene (figure 3). The deposited methyl group can either directly interfere with transcription factor binding or recruit methyl-CpG-binding proteins (MBPs) which in turn attract co-repressor proteins leading to gene silencing. In addition, DNMTs have the ability to interact with histone methyltransferases (HMT) and deacetylases (HDACs) leading to deposition of repressive histone marks and chromatin remodeling which further supports repression of the gene (Klose and Bird 2006). In contrast to that, methylation of the gene body is thought to be associated with more active gene transcription (Ball et al. 2009).

The importance of DNA methylation during mammalian development was emphasized by *Dnmt* knockout studies in mice. Homozygous deletion of *Dnmt1* resulted in embryonic lethality (Li et al. 1992), which was also observed after global knockout of *Dnmt3b*, whereas homozygous *Dnmt3a* knockout mice developed to term but became runted at 3 weeks of age and died (Okano et al. 1999). In humans, mutations in DNMT3B are associated with the immunodeficiency, centromere instability and facial anomalies (ICF) syndrome (Xu et al. 1999), while DNMT3A mutations are often linked to the development of blood malignancies such as acute myeloid leukemia (AML, Yang et al. 2015).

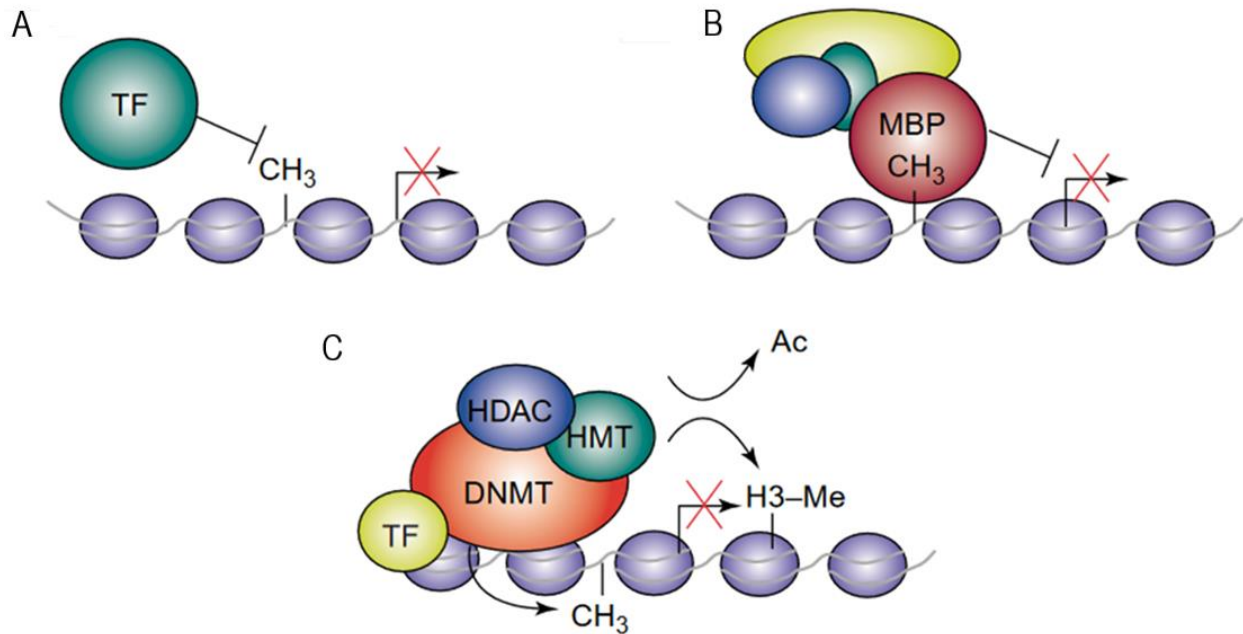


**Figure 3: Mechanisms of gene silencing by promoter methylation.** A) Methylation of a cytosine residue located in a transcription factor (TF) binding motif can disrupt binding of the respective TF and thereby prevent transcription. B) Methyl-CpG-binding proteins (MBP) recognize methylated cytosine residues and attract other co-factors to build up a transcription repressor complex. C) DNMTs can interact with HDACs and HMTs recruiting them to the promoter region. Additional deposition of repressive histone marks in the vicinity of the methylated promoter further supports gene silencing (adapted from Klose et al. 2006).

Additional epigenetic players in governing gene transcription are the ATP-dependent chromatin remodeling complexes (ADCRs), which alter the position of nucleosomes and thereby change the accessibility of transcription factor binding sites (reviewed in Lorch and Kornberg 2015). Four families of chromatin remodeling complexes have been identified so far, SWI/SNF, ISWI, CHD, and INO80, each of them conducting very specialized functions in development, cellular homeostasis, and disease (Hargreaves and Crabtree 2011).

In recent years it has also been shown that non-coding RNAs such as miRNAs of 19-25 nucleotides regulate gene expression not only by degradation of mRNAs through binding of their untranslated regions (UTR), but they are also able to directly target gene transcription in the nucleus (figure 4). Depending on the interaction with different chromatin modifying proteins, binding of miRNAs to promoter sequences can lead to deposition of histone marks, which in turn either activates or represses gene transcription (Huang and Li 2012).

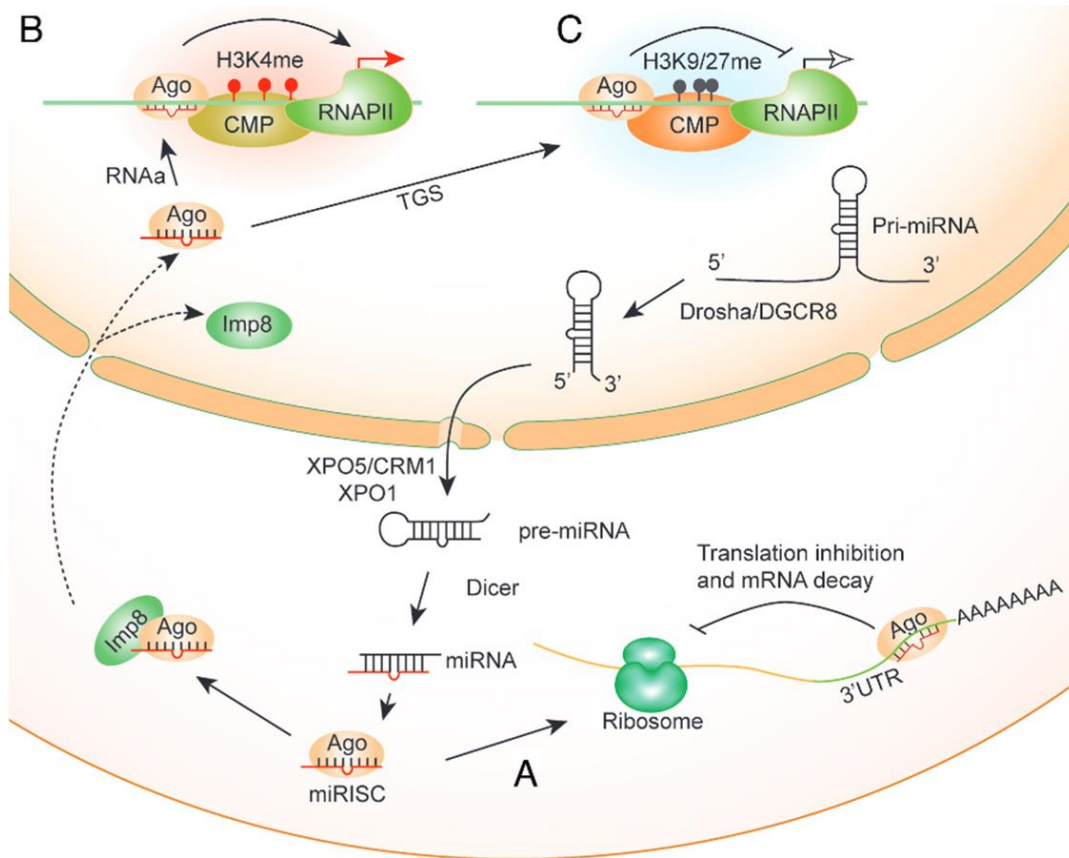


**Figure 4: Mechanisms of gene regulation by miRNAs.** After transcription, pre-miRNA is transported into the cytosol by XPO5/CRM1 and XPO1 and further processed into mature miRNA which interacts with the Argonaute (Ago) to build the miRNA-containing RNA induced silencing complex (miRISC). A) Binding of the miRISC to the 3'UTR of mRNA induces translational inhibition and degradation of the mRNA. Nuclear translocation of miRISC by binding to Importin8 (Imp8) allows for promoter binding where it can interact with chromatin modifying proteins (CMP). Binding of miRISC can result in either RNA activation (RNAa, B) or transcriptional gene silencing (TGS, C), depending on the type of interacting CMP and the induced chromatin modifications (Huang & Li 2012).

The interplay of these different epigenetic marks gives rise to a specific epigenetic landscape, which regulates both the global and regional chromatin architecture, defines regions of active and inactive chromatin and is thereby able to tightly control gene transcription in response to physiological and pathological stimuli. While research in the beginning mainly focused on the contribution of epigenetic changes to the pathology of cancer, the importance of epigenetics in other research fields like neurobiology and cardiology is now also beginning to emerge.

### 1.2.1 Epigenetics in heart failure pathology

To date, histone modifications represent the best studied epigenetic mechanisms in cardiac hypertrophy and heart failure and have been shown to be involved in many different pathways in the development of those pathologies. For example, while class II HDACs seem to mediate the repression of pro-hypertrophic genes (Zhang et al. 2002), HDACs of class I have been shown to negatively regulate expression of anti-hypertrophic genes (Trivedi et al. 2007). Consequently, overexpression of the histone acetyltransferase p300, as well as overexpression of the histone trimethyl demethylase JMJD2A led to increased cardiac hypertrophy in mice (Wei et al. 2008; Zhang et al. 2011).

The role of other epigenetic modifications in heart failure has only recently moved into focus. Regarding chromatin remodeling complexes, members of the SWI/SNF family have been most thoroughly investigated in the heart. In vertebrates the SWI/SNF ortholog is the BAF complex which harbors either Brm or Brg1 as the ATPase subunit and comprises a set of cell type-specific subunits (Wu 2012). Expression of Brg1 has been shown to be downregulated during heart development but is reactivated in response to hypertrophic stress stimuli. This is thought to be involved in the pathological switch from the adult myosin heavy chain isoform to the fetal isoform in cardiac hypertrophy and heart failure (Hang et al. 2010). In addition, the expression of several miRNAs has been shown to be altered both in animal models of cardiac hypertrophy and heart failure patients. Functional studies have suggested a direct role of those miRNAs in the pathology of heart failure (Latronico and Condorelli 2009).

Compared to the other epigenetic modifications, the role of DNA methylation in heart failure is poorly understood to date. First indications for an association of DNA methylation changes with cardiac disease were provided by two studies analyzing the cardiac DNA methylation in patients with end-stage heart failure (Movassagh et al. 2011) and dilated cardiomyopathy (Haas et al. 2013). In both studies a distinct DNA methylation signature was detected in diseased hearts, as compared to control hearts. These findings were further substantiated by a study performing whole-genome bisulfite sequencing after pressure overload-induced hypertrophy in mice (Gilsbach et al. 2014). The methylation profile of the failing cardiomyocytes differed significantly from controls and was found to be similar to the fetal state. However, in the following years conflicting findings were reported from cardiomyocyte-specific knockout models of murine Dnmts. In one study the deletion of Dnmt3b, according to the authors the main cardiac Dnmt isoform, resulted in a pronounced impairment of systolic function, exaggerated dilation, and fibrosis even in the absence of a hypertrophic stimulus (Vujic et al. 2015). In contrast, a study investigating the effect of a cardiomyocyte-specific Dnmt3a/Dnmt3b double knockout in mice found no significant

difference between the knockouts and wildtype mice both under control conditions and after transverse aortic constriction (TAC)-induced hypertrophy, arguing for a negligible role of de novo methylation in cardiomyocyte pathology (Nührenberg et al. 2015).

Meanwhile, prevention of DNA methylation by administration of non-specific DNMT inhibitors in models of cardiac hypertrophy had beneficial effects in several different studies. Two in vivo studies observed attenuation of hypertension or norepinephrine-induced hypertrophy and fibrosis in rats by treatment with the nucleosidic DNMT inhibitors 5-azacytidine and 5-aza-2'-deoxycytidine, respectively (Xiao et al. 2014; Watson et al. 2015). Similar protective effects of DNMT inhibition were observed in a study after treatment of TAC rats with the non-nucleosidic DNMT inhibitor RG108 (Stenzig et al. 2018), which had already been shown before to attenuate the detrimental effects of experimental in vitro hypertrophy in engineered heart tissue (Stenzig et al. 2016).

To gain deeper insight into the involvement of DNA methylation in the pathology of cardiac hypertrophy and heart failure, experiments on human models of cardiac hypertrophy in a stringently controlled environment are needed. The lately established possibility of reprogramming somatic cells into human induced pluripotent stem cells in combination with gene editing techniques and construction of three-dimensional cardiac tissue constructs from those cells therefore represents an attractive experimental approach.

### 1.3 Human induced pluripotent stem cells (hiPSC)

Reliable disease models can greatly contribute to a better understanding of the pathophysiology of a complex disease such as cardiac hypertrophy. Since the availability of human cardiac preparations is severely limited, cell culture systems and animal models are widely used in cardiac research. While several models of cardiac disease have successfully been established in mice and rat (e.g. Zaha et al. 2003), the considerable differences between the murine and human cardiac system aggravate direct translation of the results to human disease. A new human alternative to previous cell culture and animal models was introduced in 1998 with the first report of embryonic stem cells (hESC, Thomson et al. 2009). HESCs are derived from the inner cell mass of human embryos left over from fertility treatments. Since the donor embryos are destroyed during this process, the use of hESC in research raises several ethical concerns and is therefore legally restricted in many countries, including Germany. The introduction of human induced pluripotent stem cells (hiPSC) in 2006/2007 therefore represented a breakthrough in human disease research. The cells' capacity for constant self-renewal in conjunction with their



pluripotency, allowing for differentiation towards every cell type of all three germ layers, provides an endless supply of potentially all desired human cell types (figure 5).

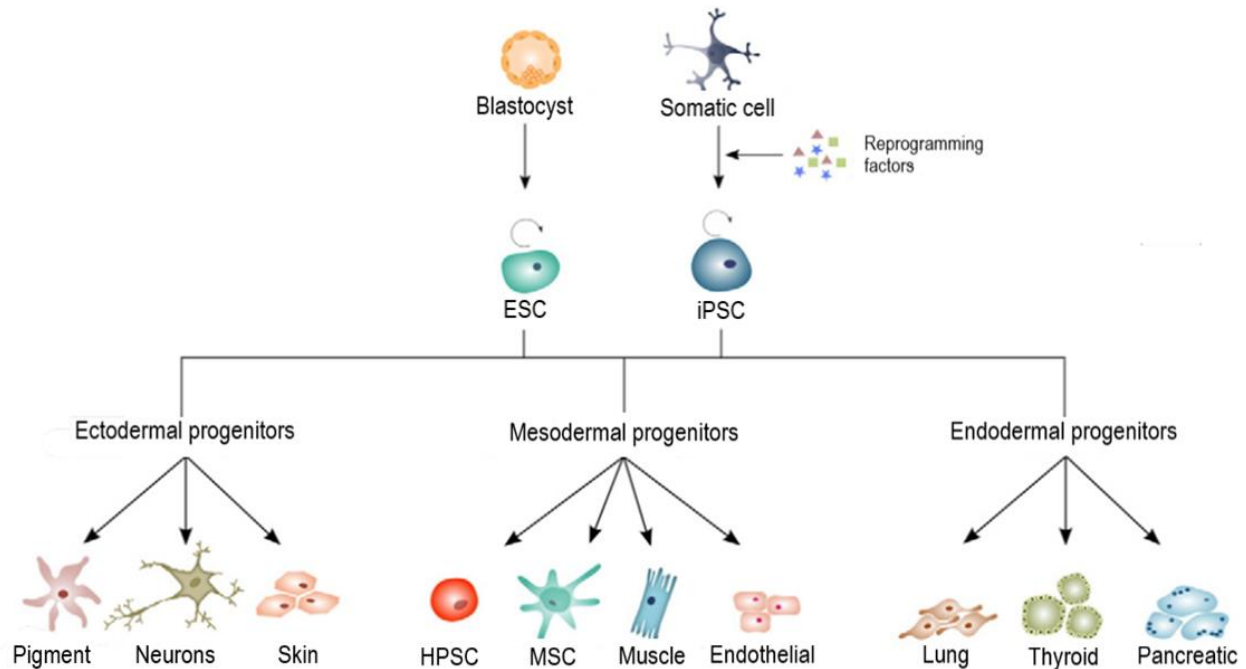


**Figure 5: Differentiation potential of ESC and iPSC.** ESCs can be derived from the inner cell mass of a blastocyst, while iPSCs are generated by treatment of somatic cells with reprogramming factors. Both cell types have the potential of constant self-renewal. The pluripotent ESCs and iPSCs can give rise to progenitors from all three germ layers (ectoderm, mesoderm, endoderm). These multipotent cells are in turn able to differentiate into the various cell types of the respective germ layer (adapted from Kaebisch et al. 2015).

In 2006 Yamanaka and colleagues discovered that both mouse embryonic and adult fibroblasts could be reprogrammed into pluripotent cells by inducing the expression of the four transcription factors Oct4, Sox2, c-Myc, and Klf4 by retroviral transduction (Takahashi and Yamanaka 2006). The resulting murine induced pluripotent stem cells (iPSC) displayed the same morphological and growth properties as ESCs and were able to differentiate into cell types from all three germ layers in a teratoma assay, reflecting their pluripotent potential. A year later, the same group also introduced the four factors into adult human fibroblasts, successfully creating the first human iPSCs and a new field of research (Takahashi et al. 2007). In the following years, the procedure was further improved and refined. It was shown that not only fibroblasts, but also other cell types

like different blood cells, keratinocytes, and hepatocytes could be reprogrammed into pluripotent stem cells (Aasen et al. 2008; Aoi et al. 2008; Loh et al. 2009). Moreover, iPSCs from other organisms were created, such as the Rhesus monkey and the Tibetan miniature pig (Liu et al. 2008; Esteban et al. 2009). However, the use of retroviruses for delivery of the four factors carries the risk of unwanted genomic alterations through random integration of the virus into the host genome. Moreover, constitutive expression of the reprogramming factors might to some extent interfere with subsequent differentiation steps (Martinez-Fernandez et al. 2014). These two considerations led to the establishment of integration-free delivery methods such as the non-integrating Sendai virus, yielding a transient expression of the reprogramming factors (Schlaeger et al. 2015).

Since their introduction, the use of hiPSC and hiPSC-derived cells has become a standard procedure in many fields of research, including cardiac disease modeling, drug testing, and efforts for patient-specific therapies (Musunuru et al. 2018). Complemented by the advent of efficient gene editing techniques, hiPSC gave rise to many new prospects in biomedical research, including identification of disease-specific treatment options and generation of genetically matched healthy cells for re-transplantation into the patient (figure 6). Moreover, disease modeling with cells carrying patient-specific mutations and genetically matched isogenic controls, in which the mutation in the patient's cells was corrected, opens up the unique possibility to directly correlate the mutation with a phenotype (Karakikes et al. 2015). Conversely, the same holds true for the introduction of a mutation into a cell line of a healthy control individual (Hinson et al. 2015).

Nevertheless, the use of hiPSC in research still faces some potential problems. As present in all biological systems, hiPSC display a certain degree of batch-to-batch, as well as clone-to-clone variations attributable to e.g. the passage number, which necessitates analysis of several different batches of the same cell line (Musunuru et al. 2018). Moreover, hiPSC have been shown to acquire somatic mutations in the process of reprogramming (Gore et al. 2011) and are prone to acquisition of karyotypic abnormalities during long-term culture (Taapken et al. 2011; Martin 2017). Since hiPSC display fast sub-clonal selection of clones harboring any sort of growth advantage (Brenière-Letuffe et al. 2018), such abnormalities can quickly spread in culture, even if only a few cells are affected at first. Additionally, although hiPSC are in theory able to give rise to all cell types of the three germ layers, establishing the right differentiation conditions for each cell type is laborious, and the resulting cell populations are generally very heterogeneous and display a rather immature state (Xi et al. 2010).

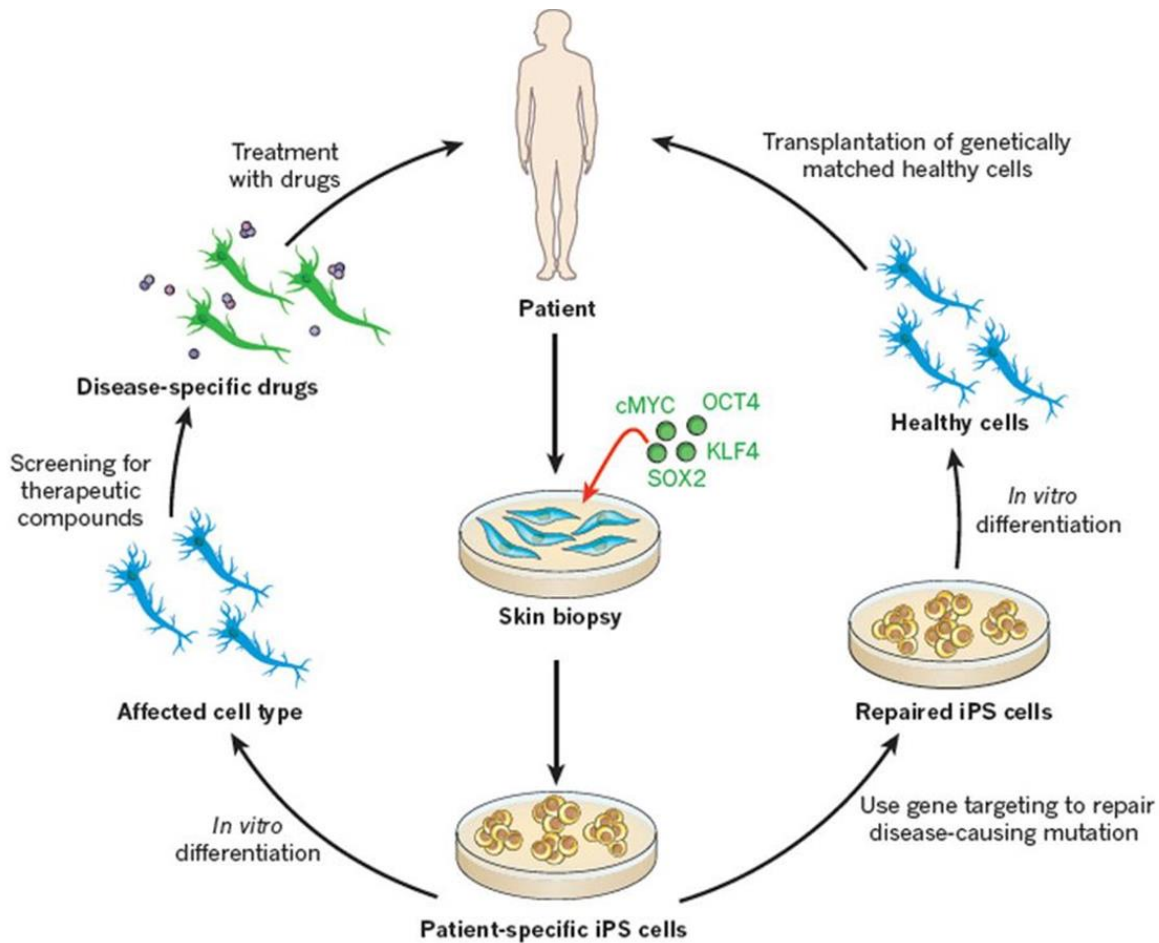


**Figure 6: Application of hiPSC in biomedical research.** Fibroblasts from a skin biopsy of a patient can be reprogrammed into patient-specific iPS cells by introduction of the four factors identified by Yamanaka and colleagues. Differentiation into the affected cell types (left part of the scheme) allows for screening for disease-specific therapeutic compounds which can be used to treat the patient. Alternatively, gene editing can be used to repair disease-causing mutations (right part) to generate healthy cells for subsequent transplantation of genetically matching cells into the patient (Robinton and Daley 2012).

### 1.3.1 Differentiation of hiPSC into cardiomyocytes

During the last two decades, many efforts have been made to establish conditions to differentiate cardiomyocytes from human pluripotent stem cells (hPSC), i.e. hESC and hiPSC by closely imitating the interplay of different signaling pathways during mammalian heart development (figure 7).

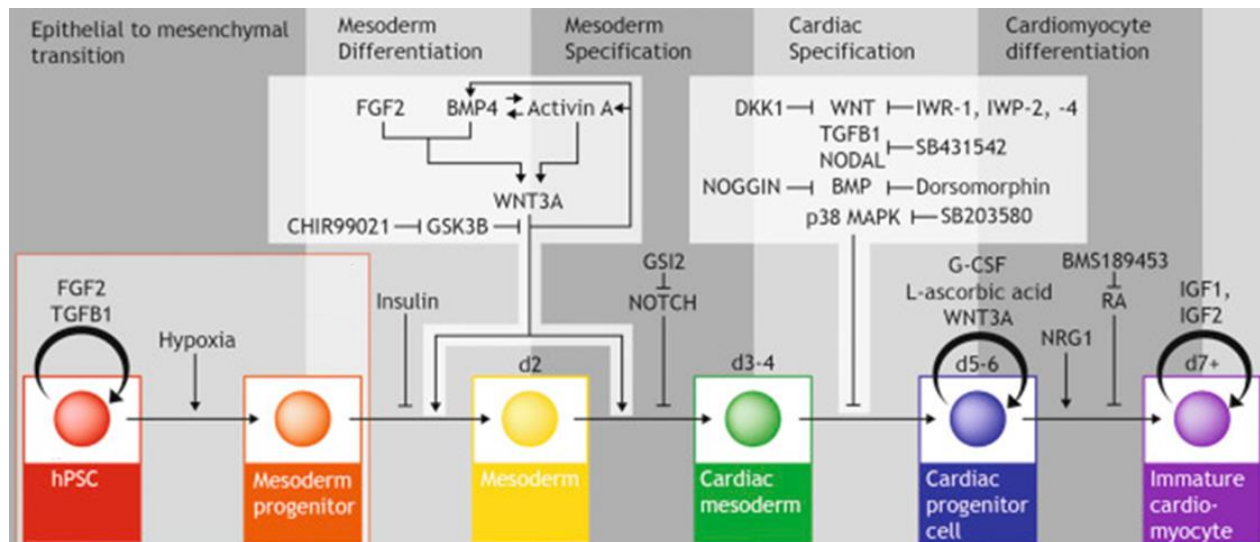


**Figure 7: Signaling pathways involved in cardiomyocyte differentiation from hPSC.** The most important signaling pathways involved in cardiac differentiation are depicted at each stage (adapted from Burrige et al. 2012).

Over time, a high number of different hiPSC protocols for differentiation into cardiomyocytes emerged, varying considerably in their experimental approach (figure 8). All these protocols can be divided into two subgroups: monolayer-based and suspension culture-based differentiation. The first subgroup comprises protocols utilizing simple monolayer cultures for differentiation (Laflamme et al. 2007), as well as co-cultures of hiPSC with other cell types for cardiac differentiation (Mummery et al. 2002; Passier et al. 2005), and “sandwich” monolayer differentiation (Zhang et al. 2012). The second subgroup utilizes the capacity of hiPSC to form small cell aggregates in suspension culture, so called embryoid bodies (EBs), supporting successful cardiac differentiation (Burrige et al. 2007; Breckwoldt et al. 2017). This culture format allows for easier scalability to meet the growing demand of differentiation of high cell numbers (Lecina et al. 2010).

However, even though the current differentiation protocols are continuously being further improved, to date all of them still face the problem of relative immaturity and heterogeneity of the resulting cell populations (Xi et al. 2010; Sirabella et al. 2015). This issue gave rise to several new methods aiming at further maturing the differentiated cardiomyocytes, such as electrical or mechanical stimulation or the use of tissue engineering to embed the cells in a 3D structure (Hansen et al. 2010; Zhu et al. 2014).

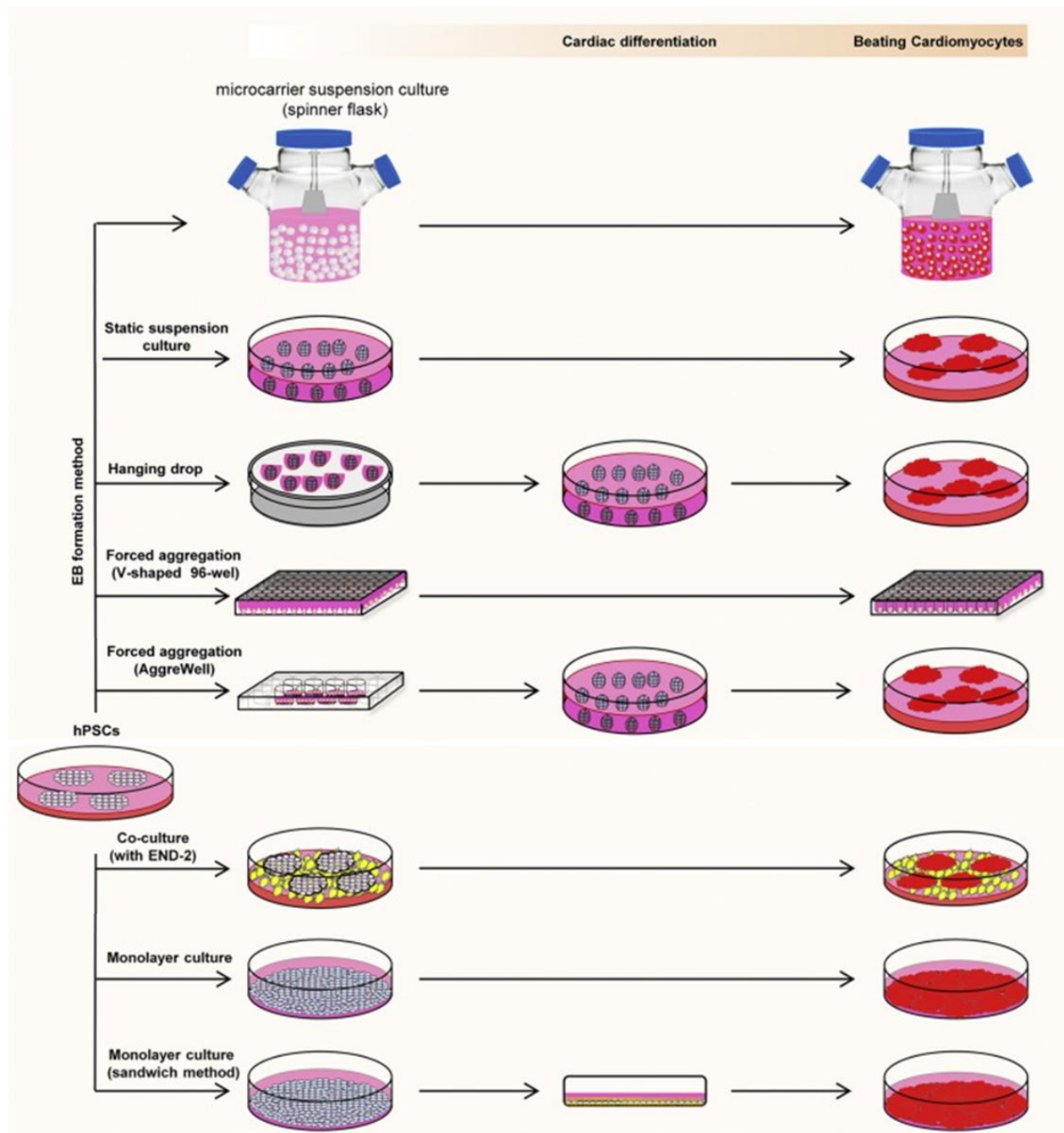


**Figure 8: Overview of cardiomyocyte differentiation methods from hPSCs.** Cardiac differentiation methods can be divided into 2D and 3D-based approaches. The 2D methods (bottom) comprise co-culture with other cells, monolayer culture, as well as “sandwich” differentiation of monolayer cells. The 3D differentiation protocols (top) instead utilize the ability of hPSCs to form cell aggregates (EBs) in suspension culture (e.g. forced aggregation, hanging drop, static or spinning suspension culture, adapted from Talkhabi et al. 2016).



## 1.4 Cardiac tissue engineering

Culturing cardiomyocytes in three-dimensional tissue constructs has many advantages over standard 2D-culture. The cardiomyocytes can be placed under constant stretch or mechanical load in this culture format, which has been shown to be crucial for development and maturation of cardiomyocytes (Fink et al. 2000). Additionally, directional contraction of muscle constructs creates force lines, along which the cells show improved alignment compared to 2D-culture (Vandenberg et al. 1991). Moreover, the controlled culture conditions which have been established for cardiac tissue constructs allow for easy genetic and pharmacological manipulation, as well as electrical stimulation which has been shown to lead to further maturation of cardiomyocytes (Hirt et al. 2014).

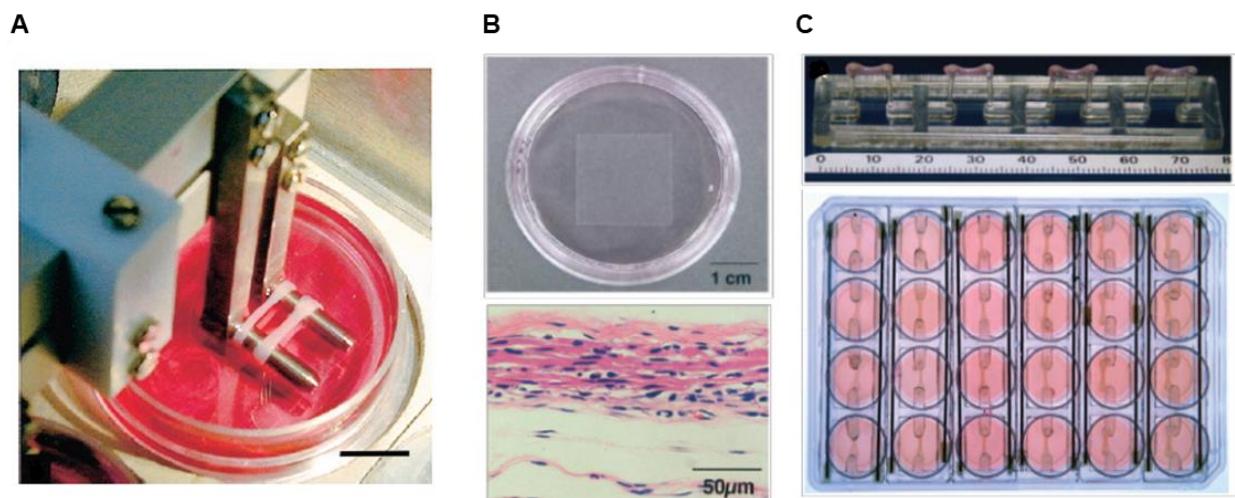


**Figure 9: Example of different cardiac tissue engineering constructs.** A) Circular EHT cultured under constant circular stretch (Zimmermann et al. 2002). B) EHT from stacked monolayer cardiomyocyte sheets (top: example of a single sheet in culture, bottom: Hematoxylin & eosin histology of cell sheet construct, Shimizu 2002) C) EHT cultured on flexible silicone posts (top) for 24-well culture format (bottom, Hansen et al. 2010).

Cardiac tissue engineering has been a focus of research for almost 25 years and has been steadily improved since its introduction. The first engineered heart tissue (EHT) construct was published in 1997 and consisted of embryonic cardiomyocytes from chicken which were embedded into a collagen matrix placed between two Velcro-coated glass tubes (Eschenhagen et al. 1997). Addition of Matrigel to the casting mix allowed for generation of tissue constructs also from neonatal rat cardiomyocytes (Zimmermann et al. 2000). Over time, several different approaches for EHT construction have been developed (figure 9), including circular EHT (Zimmermann et al.

2002), tissues build from stacked monolayers of cardiomyocytes (Shimizu 2002), and miniaturized fibrin matrix-based EHT in a 24-well format (Hansen et al. 2010). In addition to the initial cell sources, EHT have in the following years also been generated from mouse cardiomyocytes (Stöhr et al. 2013), as well as hESC and hiPSC-derived cardiomyocytes (Schaaf et al. 2011; Mannhardt et al. 2016).

In parallel with the progression of cardiac tissue engineering, systems for standardized EHT analysis have also been developed and improved over time. For example, a video-optical recording system including customized analysis software allows for automated measurement of up to 24 EHTs under controlled conditions (37 °C, fixed gas composition) in a glass roof incubator (figure 10; Stoehr et al. 2014). Over the last decade EHT has been successfully utilized for drug screening (Eder et al. 2014), studies of cardiac hypertrophy (Hirt et al. 2012), disease modeling of mutations in cardiac genes (Wijnker et al. 2016), as well as in transplantation experiments to study cardiac repair after myocardial infarction in different animal models (Lü et al. 2010; Weinberger et al. 2016).

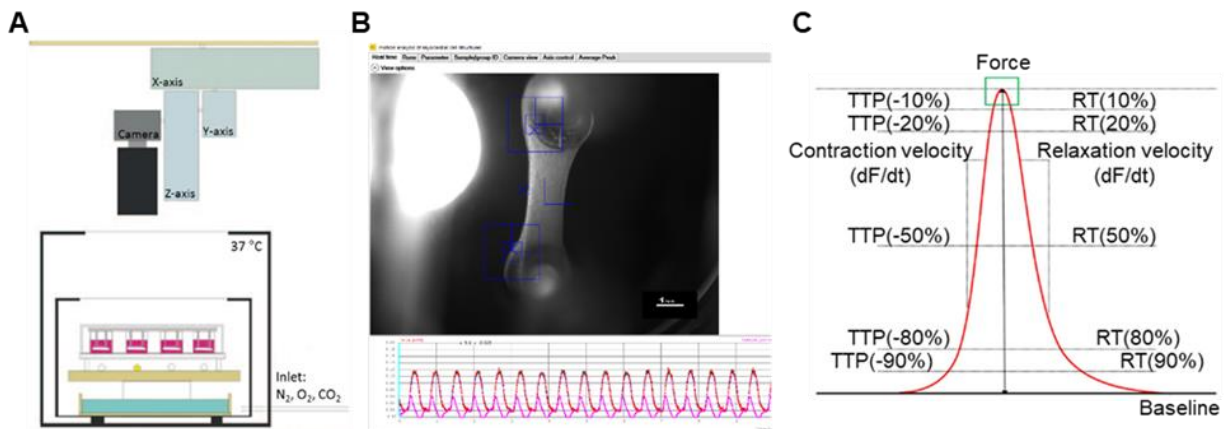


**Figure 10: Set-up for video-optical EHT contractility analysis.** A) A 24-well cell culture plate containing EHTs is placed into a glass roof-incubator at 37 °C with a defined gas composition. A camera moves along the three axes of the system to record the contraction of each individual EHT. B) A customized software generates force-over-time plots from the captured motion of the EHT and calculates the different contractility parameters, e.g. force, contraction and relaxation times (C, adapted from Hansen et al. 2010).

### 1.5 CRISPR/Cas9-based genome editing

The possibility to specifically alter the genomic sequence of cells or an entire organism has been an important tool in molecular biology research since the introduction of the first targeted genome editing relying on homologous recombination in the 1970s and 1980s (Scherer and Davis 1979; Thomas et al. 1986). However, these first approaches were laborious and yielded low efficiencies, requiring several rounds of genetic selections to obtain the desired genotype. The discovery of zinc-finger nucleases (ZFNs; Kim et al. 1996) and transcription activator–like effector nucleases (TALENs; Boch et al. 2009; Moscou and Bogdanove 2009) was finally able to overcome this limitation in the field. ZFNs and TALENs rely on the fusion of the catalytic domain of endonucleases to sequence-specific designed modular DNA-binding proteins and can hence be programmed to induce double-strand breaks (DSB) at the desired location and thereby facilitate induction of site-specific mutations, which greatly advanced the field.

The next breakthrough in genome editing was the discovery of the clustered regularly interspaced short palindromic repeats (CRISPR) adaptive immune system in bacteria and archaea. Until now, six different types of CRISPR systems have been identified (type I – VI), of which the type II system has until now been characterized in most detail (Jinek et al. 2012). The bacterial immune system relies on the integration of fragments of invading viral DNA into the bacterial genome, providing a memory of the infection for the future (figure 11). The invading DNA is processed into a 20 bp-long “protospacer” and is then integrated between two repeats into the type II CRISPR locus, which additionally contains a *tracrRNA* and a *Cas9* nuclease expression cassette. The protospacers are transcribed and processed into CRISPR RNAs (crRNAs), which then hybridize to the likewise transcribed *tracrRNAs* and form a complex with the *Cas9* nuclease. In case of a fresh infection with the same virus, the complex binds to the invading DNA via the homologous protospacer sequence, leading to degradation of the viral DNA by *Cas9*. To prevent self-targeting of the CRISPR locus by the complex, the *Cas9* is only able to induce DSBs if a protospacer-adjacent motif (PAM) sequence is present at the 3' end of the protospacer sequence in the targeted DNA. In case of the CRISPR system of *Streptococcus pyogenes*, which to date is the most widely used CRISPR system for genome editing, the DSB is introduced three base pairs upstream of a 5'-NGG-3' PAM sequence.



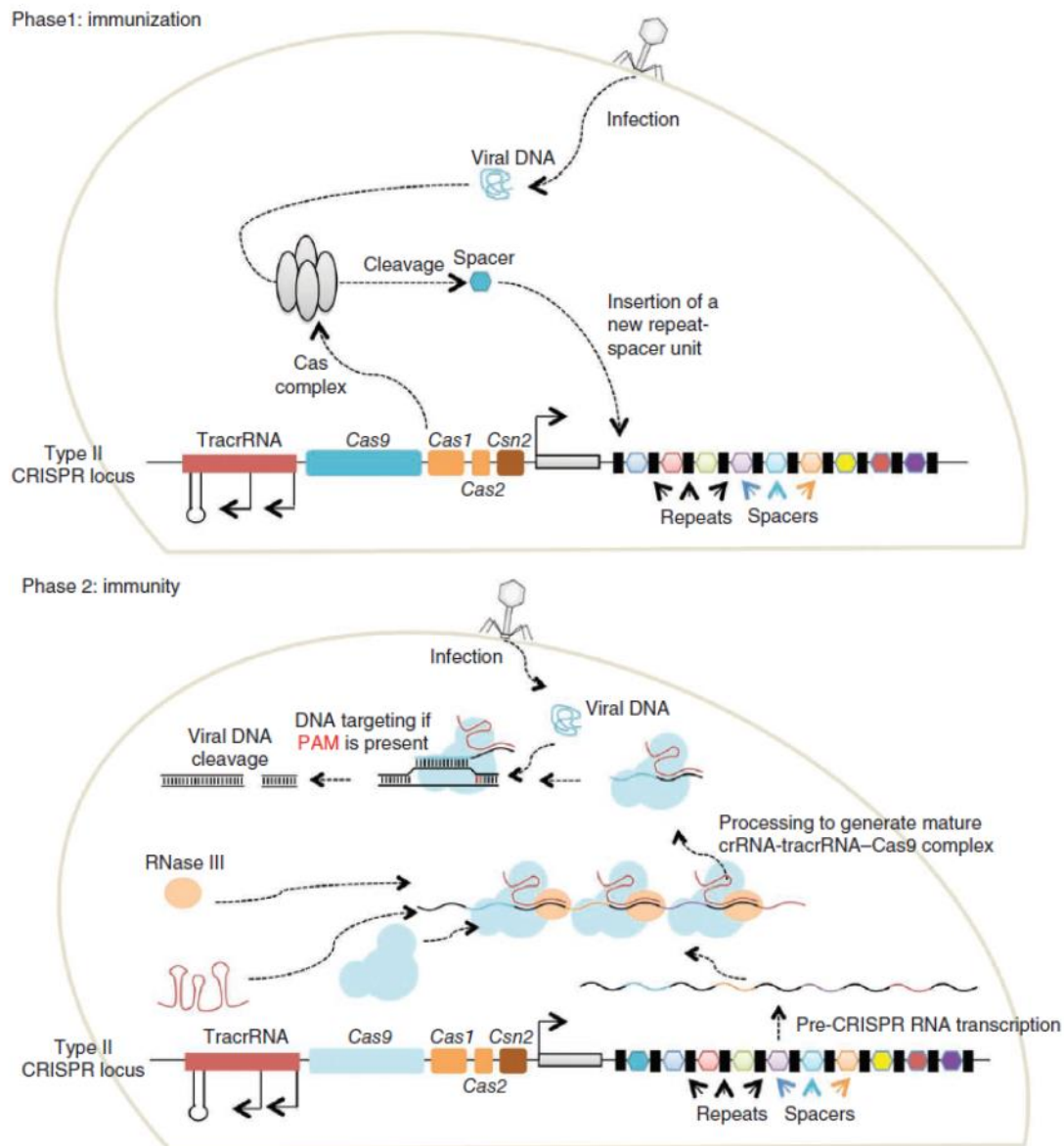


**Figure 11: Function of the bacterial clustered regularly interspaced short palindromic repeats (CRISPR) adaptive immune system.** Immunization phase (top): invading viral DNA is processed into a so-called spacer sequence, which is subsequently incorporated between two repeats into the CRISPR locus. Immunity phase (bottom): The CRISPR locus is transcribed giving rise to tracrRNA, Cas9 nuclease protein, and crRNA containing the spacer sequence. The three components form a complex, which is able to recognize a second infection of the same virus by binding to the complementary viral DNA. The invading viral DNA is subsequently destroyed by the Cas9 if a PAM sequence is present on the DNA strand (Mali et al. 2013).

The ability of the CRISPR/Cas9 system to induce DSBs at a specific target locus has made it a promising candidate for genome editing applications. To allow for efficient genome editing in human cells, the crRNA and tracrRNA were combined into a chimeric single-guide RNA (sgRNA) and encoded on a plasmid together with a human codon-optimized Cas9 and a selection marker, such as puromycin or GFP. For genome editing, this plasmid can be introduced into the target cells by transfection, nucleofection, or viral transfer (Ran et al. 2013b). After Cas9 has introduced a DSB in the genome of the target cell, the DNA repair machinery of the cell is utilized to induce random or specific mutations at the target site. When a cell detects DSB in its genome, it activates one of the two major pathways for DNA repair: non-homologous end joining (NHEJ) or homology-directed repair (HDR; figure 12).

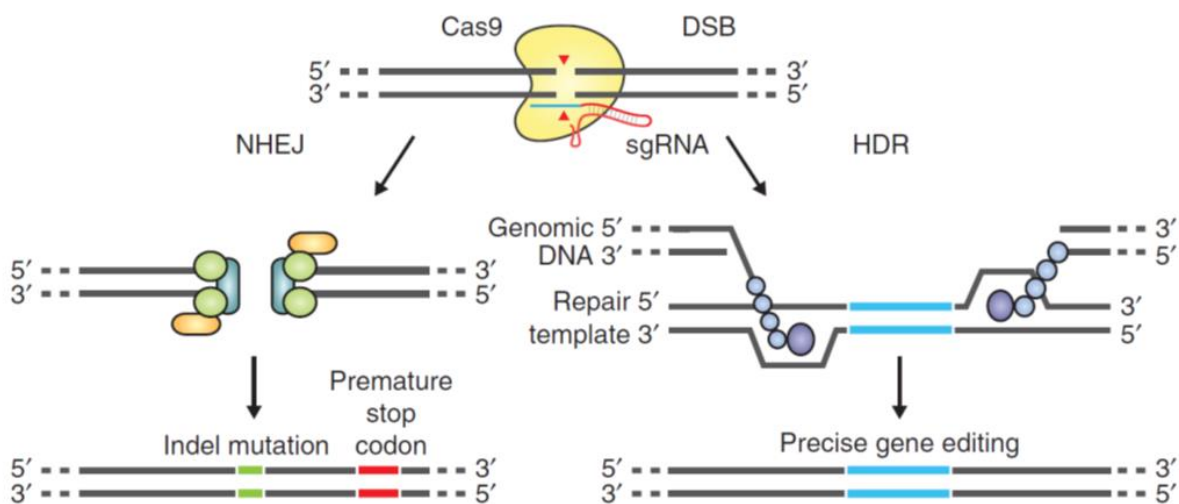


**Figure 12: DNA damage repair pathways for CRISPR-induced DSBs.** After Cas9 has cut both DNA strands and the cell has recognized the resulting DSB, one of the two major DNA repair mechanism is initiated. In the absence of a repair template, the two DNA strands are re-attached by NHEJ, resulting in indel mutations and frameshifts. In HDR a homologous repair template is used to repair the damage, resulting in precise gene editing (Ran et al. 2013).

The NHEJ pathway is active throughout the whole cell cycle and acts by joining the two ends of broken DNA together without the use of a template, which often results in indel mutations at the DSB site by addition or deletion of a few bases at random. As these mutations often lead to frameshifts and premature stop codons, NHEJ after CRISPR-mediated DSBs represents an easy option for the creation of gene knockouts. In contrast to that, HDR is mainly active during G2 and late S-phase and requires the presence of a repair template. Since HDR leads to precise gene

editing, it can be utilized to induce specific mutations by introduction of a repair template carrying the desired mutations flanked by homology arms into the cell (Ran et al. 2013b).

CRISPR/Cas9 has quickly replaced ZFNs and TALENs as the genome editing technique of choice, due to its comparatively easy customization properties. While redirection of the TALEN system to a new genomic target would require construction of two completely new TALEN genes, it is sufficient for the CRISPR/Cas9 system to replace the target sequence of the sgRNA on the plasmid with the desired sequence, if a PAM sequence is present at the desired locus (Jinek et al. 2012). Nevertheless, CRISPR also has a few limitations for its application in genome editing. In addition to the already mentioned requirement of the NGG-PAM at the locus of interest, the occurrence of DSBs and thereby the introduction of indel mutations at off-target sites with high sequence-similarity to the sgRNA can be problematic. In order to minimize the probability of off-target effects, several online prediction tools for CRISPR (e.g. <http://crispr.mit.edu/>, Zhang laboratory, MIT, 2013) have been developed. All available sgRNAs in the region of interest are scored by the software according to their similarity to other genomic regions in the target species and their number of potential off-target sites, providing the user with a ranking of the most suitable sgRNA, as well as a list of the most likely off-target sites (figure 13).

all guides			guide #1    quality score: 74		
scored by inverse likelihood of offtarget binding			guide sequence: CTGTTTGTGCAGGGCTCCGA    GGG		
mouse over for details    ... show legend			on-target locus: chr1:+38605786		
			number of offtarget sites: 228 (25 are in genes)		
	score	sequence	top 20 genome-wide off-target sites		
Guide #1	74	CTGTTTGTGCAGGGCTCCGA    GGG			
Guide #2	67	ACTGTTTGTGCAGGGCTCCG    AGG			
Guide #3	55	TGTCCTGGGACTGTTTGTGC    AGG			
Guide #4	55	GGGCTCCGAGGGGACCCATG    TGG			
Guide #5	54	GTCCTGGGACTGTTTGTGCA    GGG			
Guide #6	53	CGAGGGGACCCATGTGGCTC    AGG			
Guide #7	51	AGCCCTGCACAAACAGTCCC    AGG			
Guide #8	50	CTGCAGGGACCTCCATGTCC    TGG			
Guide #9	50	GCAATGCTGCCCCACCCGC    TGG			
Guide #10	50	GAGGGGACCCATGTGGCTCA    GGG			
Guide #11	46	TGTTTGTGCAGGGCTCCGAG    GGG			
Guide #12	45	TGTGGCTCAGGGTGGCTAAG    GGG			
Guide #13	42	TGCAGGGACCTCCATGTCCT    GGG			
Guide #14	42	ATGTGGCTCAGGGTGGCTAA    GGG			
			sequence	score	mismatches
			CTGGATGGGCAGGGCTCCGAGAG	2.4	3MMs [4:5:8]
			CTGAATGTGCAGGGCTCCAAGGG	1.0	3MMs [4:5:19]
			CGGAATTTGCAGGGCTCCGATGG	0.9	4MMs [2:4:5:7]
			CGGTTTGAAAAGGGCTCCGAGAG	0.8	4MMs [2:8:9:10]
			CTTGTTGAGCTGGGCTCCGAGAG	0.8	4MMs [3:4:8:11]
			CTGTGTGAGGTGGGCTCCGAGGG	0.7	4MMs [5:8:10:11]
			CCCTGTGTGCAGGGCTCCGCAGG	0.7	4MMs [2:3:5:20]
			CAGTTTGGGCAGGGCTCAGATGG	0.7	3MMs [2:8:18]
			CAGTTTAGACAGGGCTCCGAAGG	0.6	4MMs [2:7:8:9]
			CGGTTTGAGAAGGGCTTCGAGAG	0.6	4MMs [2:8:10:17]
			CTGTGTGTGTAGGGCTCAGAGAG	0.6	3MMs [5:10:18]
			CTGTGTGTGCTGGGCTCCCAAAG	0.6	3MMs [5:11:19]

**Figure 13: Output example of an sgRNA designing tool.** For each guide (sgRNA) a score is calculated (left) and a list of possible off-target sites in the target genome, including a probability-score for each off-target site (right), is generated (<http://crispr.mit.edu/>, Zhang laboratory, MIT, 2013).

Additional efforts to reduce off-target activity were made by the creation of different Cas9 derivatives. For example, the introduction of a point mutation in one of the two conserved Cas9 nuclease regions (RuvC or HNH) resulted in a Cas9 nickase which upon binding would only introduce a single-stranded nick rather than a DSB. Combination of the Cas9 nickase with two neighboring sgRNAs on different DNA strands in the region of interest would still induce a DSB and enable genome editing, albeit at a lower frequency than the wildtype Cas9, but with greater specificity. At the same time, the off-target probability is greatly reduced, since simultaneous binding of both sgRNAs at the off-target site would be needed to induce DSBs and indel mutations (Ran et al. 2013a). Another approach pursued by Kleinstiver and colleagues (Kleinstiver et al. 2016) was the generation of a high-fidelity Cas9 (Cas9-HF) by mutating the residues responsible for non-specific Cas9-DNA interactions, while at the same time retaining the residues needed for on-target activity. Comparison of their Cas9-HF with the wildtype resulted in >85% of on-target activity, while no off-target effects were detectable.

Since its introduction as a genome-editing tool, CRISPR/Cas9 has been widely implemented into many research fields, including agriculture, disease modeling, and therapeutics (Kim et al. 2017a). In cardiac research, CRISPR/Cas9 has also been successfully used to further facilitate the understanding of cardiac disease by insertion of disease causing DNA mutations into a wildtype background or correcting them in a diseased genome both in mice models and in hiPSCs (reviewed in Motta et al. 2017).

## 2 Aim

While DNA methylation already represents a well-established therapeutic target in other diseases such as cancer, its role in cardiac pathologies, such as cardiac hypertrophy, still remains unclear and controversial. In order to better understand the mechanisms of DNA methylation and uncover a possible involvement in the pathophysiology of cardiac disease, reliable models are needed. This study therefore aimed to analyze the role of de novo DNA methylation in a human engineered heart tissue (EHT) model under both basal and stress conditions.

The first objective of the study was the establishment of the CRISPR/Cas9 genome editing technique for hiPSC in order to generate human knockout cell lines for the DNA methylation transferase (DNMT) DNMT3A, which was discovered to be the main cardiac isoform in cardiomyocytes. The second objective was to unravel the effect of a cardiomyocyte-specific DNMT3A knockout on basic cardiac function. To this end, the generated knockout cell lines were differentiated into beating cardiomyocytes and used for the generation of human EHT. The controlled environment of EHT allowed for thorough characterization of the effect of the knockout on basic cardiac function in absence of any confounders. Additionally, the impact of the knockout on pharmacologically induced cardiac hypertrophy was analyzed. Upon completion of the experiments, the EHTs were characterized on the molecular level.

### 3 Materials and methods

All reagents, devices, and materials used in this project can be found in detail in the supplement.

#### 3.1 Cell culture media

The composition of all cell culture media can be found in table 1.

**Table 1: Composition of cell culture media**

Medium	Composition
Conditioned medium (CM)	DMEM/F12 without glutamine 1% (v/v) Non-essential amino acids 1% (v/v) L-glutamine 0.5% (v/v) Penicillin/streptomycin 3.5 $\mu$ L/500 mL 2-Mercaptoethanol 20% (v/v) Knockout serum replacement 10 ng/mL Basic fibroblast growth factor (bFGF)  After incubation on mitotically inactivated mouse embryonic fibroblasts (strain CF-1) for 24 hours, the medium was collected and sterile filtered (0.1 $\mu$ m filter). Fresh bFGF (30 ng/mL) was supplemented directly before use.
FTDA	DMEM/F-12 without glutamine 2 mM L-glutamine Lipid mix (Sigma, 1:1000) 5 mg/L Transferrin 5 $\mu$ g/L Selenium 0.1% (v/v) Human serum albumin 5 $\mu$ g/mL Insulin 2.5 ng/mL Activin-A 30 ng/mL bFGF 50 nM Dorsomorphin 0.5 ng/mL TGF $\beta$ 1
EB formation medium	FTDA 4 mg/mL Polyvinyl alcohol 10 $\mu$ M Y-27632
Basic cell culture medium	DMEM 1% (v/v) Penicillin/streptomycin 10% (v/v) Fetal calf serum (heat inactivated)

Mesoderm induction medium	RPMI 1640 4 mg/mL Polyvinyl alcohol 10 mM HEPES 0.05% (v/v) Human serum albumin 250 $\mu$ M Phosphoascorbate 5 mg/L Transferrin 5 $\mu$ g/L Selenium Lipid mix (1:1000) 10 $\mu$ M Y-27632 3 ng/mL Activin-A 10 ng/mL BMP-4 5 ng/mL bFGF
Cardiac differentiation medium I	RPMI 1640 10 mM HEPES 0.5% (v/v) Penicillin/streptomycin 0.05% (v/v) Human serum albumin 250 $\mu$ M Phosphoascorbate 5 mg/L Transferrin 5 $\mu$ g/L Selenium Lipid mix (1:1000) 1 $\mu$ M Y-27632 1 $\mu$ M XAV-939
Cardiac differentiation medium II	RPMI 1640 2% (v/v) B27 plus insulin 10 mM HEPES 0.5% (v/v) Penicillin/streptomycin 500 $\mu$ M 1-Thioglycerol 1 $\mu$ M Y-27632 1 $\mu$ M XAV-939
Cardiac differentiation medium III	RPMI 1640, 2% (v/v) B27 plus insulin 10 mM HEPES 0.5% (v/v) Penicillin/streptomycin 500 $\mu$ M 1-Thioglycerol 1 $\mu$ M Y-27632
EHT casting medium	DMEM 1% (v/v) Penicillin/streptomycin 2 mM L-glutamine 10% (v/v) Fetal calf serum (heat inactivated)
EHT culture medium	DMEM 1% (v/v) Penicillin/streptomycin 10% (v/v) Horse serum 10 $\mu$ g/mL Insulin 33 $\mu$ g/mL Aprotinin

Serum-free EHT culture medium	DMEM
	1% (v/v) Penicillin/streptomycin
	10 µg/mL Insulin
	33 µg/mL Aprotinin
	50 ng/mL Hydrocortisone
	0.5 ng/mL T <sub>3</sub>

### 3.2 Stem cell culture

All basic cell culture work was performed as described in Breckwoldt et al. (2017). The experiments were based on the in-house control hiPSC line ERC018, which was established by the UKE Stem cell core facility by reprogramming fibroblasts from the skin biopsy of a healthy individual with the Sendai virus-based CytoTune kit (Life Technologies). Cell culture and cell expansion for differentiation was done in FTDA under hypoxic conditions in Geltrex-coated cell culture plates and flasks. Standard passaging was done with Accutase (Sigma-Aldrich). The cells were tested for mycoplasma contamination by PCR on a regular basis by June Uebeler (IEPT, UKE, Hamburg, Germany). Stem cell culture and expansion was performed by Birgit Klampe and Thomas Schulze (IEPT, UKE, Hamburg, Germany).

### 3.3 CRISPR/Cas9-mediated gene knockout

#### 3.3.1 CRISPR design and cloning

The knockout strategy for DNMT3A was adapted from Liao et al. (2015; figure 14). For validation of the genomic target sequence, DNA was purified from ERC018 hiPSC with the DNeasy kit (QIAGEN). The region of interest was amplified by PCR with the HOT FIREPolDNA Polymerase (see table 2 + 3; Solis BioDyne) and sent for sequencing at MWG/Eurofins.



Table 2: PCR reaction mix for HOT FIREPol DNA Polymerase

Component	Per reaction
10x BD buffer	2 µL
10x MgCl <sub>2</sub>	2 µL
2.5 mM dNTPs	1 µL
10 µM primer mix	1 µL
DNA template	50-100 ng
HOT FIREPol DNA Polymerase	1 µL
Aqua dest.	Ad 20 µL

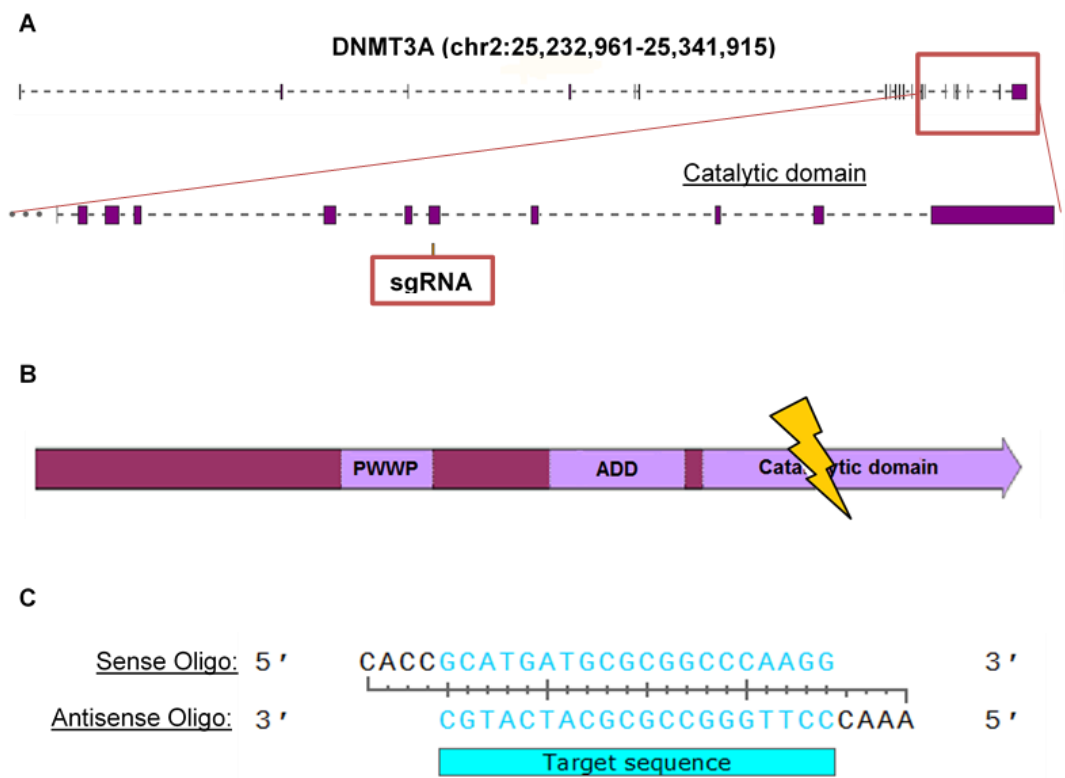


**Figure 14: CRISPR strategy for catalytic knockout of DNMT3A.** (A) Exon/intron structure of human DNMT3A and the sgRNA binding site. (B) The double strand break induced by Cas9 is situated in the catalytic domain at the C-terminal end of the protein, downstream of the nucleosome-binding PWWP domain and the ADD domain which mediates binding of DNMT3A to histone tails. (C) Sequence of the sense and antisense sgRNA oligos including 5' overhangs for cloning.

**Table 3: Touch-down PCR program for HOT FIREPol DNA Polymerase**

Temperature	Time	Cycles
95 °C	7 minutes	1
95 °C	30 seconds	10x
$T_m - 0.4$ °C per cycle	30 seconds	
72 °C	1 minute / kb product	
95 °C	30 seconds	30x
$T_m - 4$ °C	30 seconds	
72 °C	1 minute / kb product	
72 °C	7 minutes	1
4 °C	hold	

Two different Cas9-containing plasmids were tested in preliminary experiments to compare their efficiency. The first plasmid, pSpCas9(BB)-2A-GFP (PX458), was a gift from Feng Zhang (Addgene plasmid #48138). The second plasmid was based on the VP12 plasmid which contains a high-fidelity version of Cas9 (Addgene #72247, deposited by Keith Joung) with lower off-target activity. The T2A-EGFP tag and a gRNA cassette (amplified from Addgene #48140 and #52961, respectively) were inserted into the VP12 vector by Dr. Ingke Braren from the UKE Virus Core Facility by In-Fusion-cloning. Refer to supplementary figure S1 for a plasmid map of both vectors. The sgRNA published by Liao and colleagues was ordered as unmodified oligonucleotide in sense and antisense orientation from MWG/Eurofins including 5' overhangs needed for cloning (figure 14). Oligo annealing was performed by incubation of 20  $\mu$ M of each oligo in annealing buffer on a thermomixer at 95 °C for 5 minutes and subsequent cool-down to room temperature. Insertion of the annealed sgRNA into pSpCas9(BB)-2A-GFP and the modified VP12 vector was done by restriction cloning with BbsI and BsmBI, respectively (figure 15). After gel extraction (QIAquick gel extraction kit, QIAGEN), the sgRNA was ligated into both vectors with T4 Ligase (NEB) and amplified in Top10 cells (Thermo Fischer Scientific). The correct insertion was verified by sequencing with the U6-fw primer.

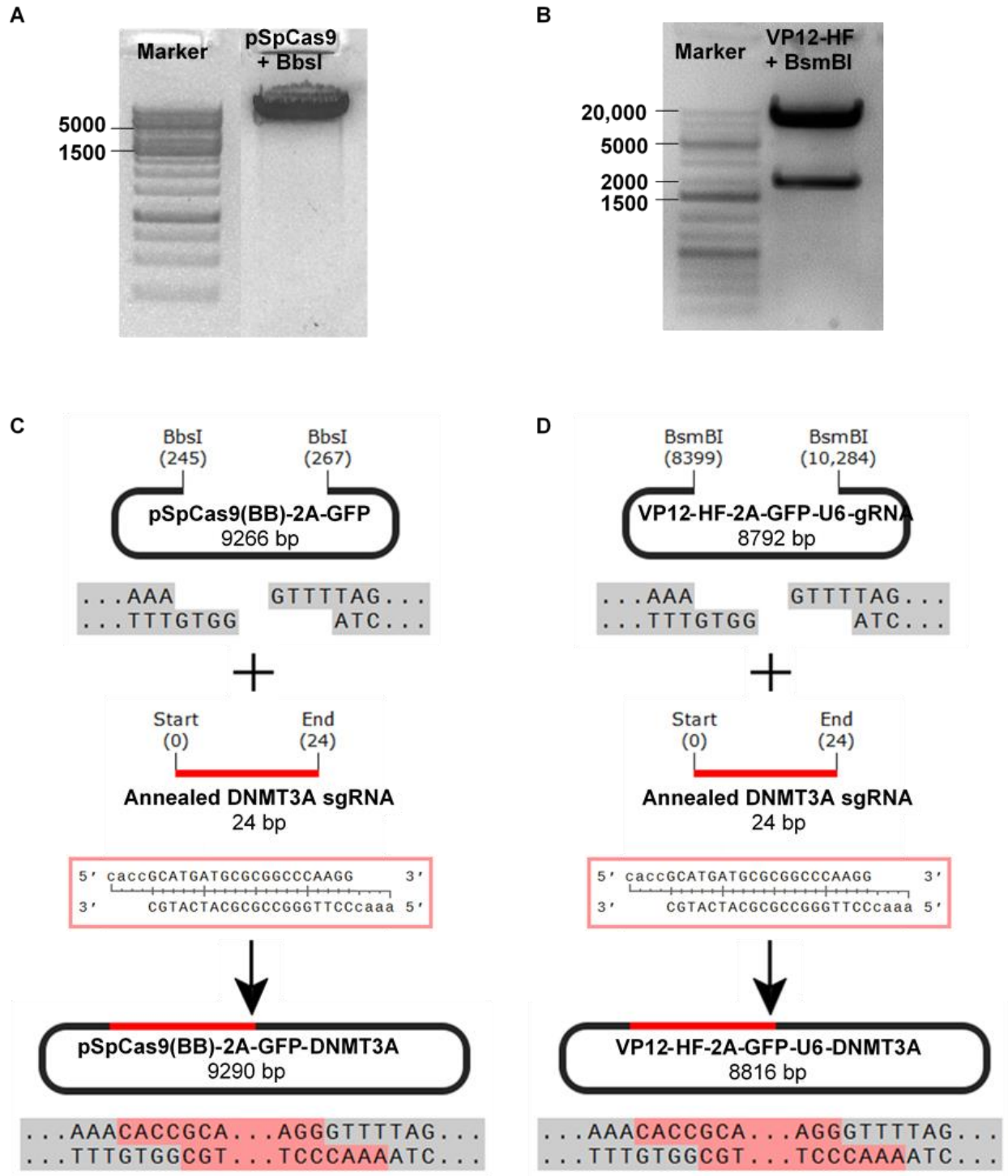


**Figure 15: Work flow of sgRNA cloning into the Cas9-containing vectors.** (A) + (B) Agarose gel of pSpCas9(BB)-2A-GFP and VP12-HF-2A-GFP-U6-gRNA after digestion with BbsI and BsmBI, respectively. (C) + (D) Ligation of the annealed sgRNA into the two vectors.

### 3.3.2 Preliminary tests

The two CRISPR constructs were first tested in HEK 293T cells. To this end 200,000 cells per well were plated in basic cell culture medium in a 6-well plate. On the following day the cells were transfected with TurboFect Transfection Reagent (Thermo Fisher Scientific) with either 4 µg of one of the two plasmids or a vehicle control. GFP expression was analyzed after 30 hours by fluorescent microscopy and the cells were harvested after 54 hours for subsequent gene expression analysis. The RNeasy kit (QIAGEN) was used to purify RNA from the cell pellet and the High-Capacity cDNA Reverse Transcription Kit (Thermo Fisher Scientific) was used to generate cDNA (reaction set up see table 4 + 5).

**Table 4: Reaction mix High-Capacity cDNA Reverse Transcription Kit**

Component	Per reaction
10x RT buffer	2.5 µL
10x RT random primer	2.5 µL
25x dNTPs [100 mM]	1 µL
MultiScribe RT [50 U/µL]	1 µL
RNA	Up to 2000 ng
Aqua dest.	Ad 25 µL

**Table 5: Reverse transcription cyclor program**

Temperature	Time
25 °C	10 minutes
37 °C	120 minutes
85 °C	5 minutes
4 °C	hold

Gene expression analysis to test the knockout efficiency was done by SYBR green dye based quantitative real time PCR (qPCR) on the ABI PRISM 7900HT Sequence Detection System (Applied Biosystems) with the HOT FIREPol EvaGreen qPCR Mix Plus Rox (Solis BioDyne; see table 6 + 7). Transcript levels were normalized to glucuronidase beta (GUSB). The plasmid that displayed a higher transfection rate and a more efficient gene knockdown was chosen for the subsequent experiments.

**Table 6: Reaction mix qPCR**

Component	Per Reaction
EvaGreen Master mix	2 $\mu$ L
10 $\mu$ M Primer mix	0.5 $\mu$ L
cDNA	2 $\mu$ L
Aqua dest.	5.5 $\mu$ L

**Table 7: qPCR cyclers program**

Temperature	Time	Cycles
50 °C	2 minutes	1
95 °C	10 minutes	
95 °C	15 seconds	40
60 °C	60 seconds	
95 °C	15 seconds	1%
60 °C	15 seconds	ramping
95 °C	15 seconds	rate

In the next step of the establishment of CRISPR, an optimization protocol was run with the Amaxa P3 and P4 Primary Cell 4D-Nucleofector X Kits on the 4D-Nucleofector X Unit (Lonza) to assess which combination of nucleofection buffer and nucleofection program was best suited for the ERC018 cell line. Cells at passage number p35 were treated for 1 hour with the apoptosis inhibitor Y-27632 and subsequently dissociated into single cells by incubation in Accutase (Sigma) solution for 5 minutes at 37 °C. The cells were divided into 16 fractions of 1.7 Mio cells each and resolved in 170  $\mu$ L of either the P3 or P4 nucleofection buffer. In each tube, 0.5  $\mu$ g of the pMax GFP control plasmid (Lonza) were added before pipetting 20  $\mu$ L from each tube onto the 16-well nucleovette strip. For each of the buffers, 7 different programs as well as the negative control program were run (table 8). After nucleofection, the cells were plated in a 24-well plate in CM supplemented with bFGF and Y-27632 for 24 hours. The morphology and GFP expression of all conditions were microscopically analyzed and compared on the following day and the cells were subsequently dissociated into single cells for flow cytometric measurement in order to analyze cell survival as well as transfection rate by determination of the GFP-positive cell fraction. The measurement was performed at the UKE FACS Core Facility on a FACSCantoII flow cytometer (BD).

**Table 8: Layout 16-well nucleovette strip**

	<b>A</b>	<b>B</b>
<b>1</b>	P3 + CA-137	P4 + CA-137
<b>2</b>	P3 + CB-150	P4 + CB-150
<b>3</b>	P3 + CD-118	P4 + CD-118
<b>4</b>	P3 + CE-118	P4 + CE-118
<b>5</b>	P3 + CM-113	P4 + CM-113
<b>6</b>	P3 + DC-100	P4 + DC-100
<b>7</b>	P3 + DN100	P4 + DN100
<b>8</b>	P3 w/o nucleofection	P4 w/o nucleofection

### 3.3.3 Knock out of DNMT3A in ERC018 hiPSC

ERC018 cells at passage number p37 were cultured in 6-well plates in FTDA medium and supplemented with Y-27632 1 hour before the start of the experiment. The cells were washed once with PBS and dissociated into single cells with Accutase for 5 minutes at 37 °C. Next, the cells were resuspended in conditioned medium and 400,000 cells were plated directly as a negative control. 800,000 cells per nucleofection run were centrifuged at 200 g for 5 minutes and resuspended in 82  $\mu$ L P3 buffer and 18  $\mu$ L volume supplement. The cells were transferred to a nucleofector cuvette and co-nucleofected with 2000 ng of the CRISPR plasmid and 0.5  $\mu$ g of the pMax GFP control plasmid using the CB-150 program of the 4D-Nucleofector X Unit. The cuvette was incubated at 37 °C for 5 minutes before the cells were transferred into a Matrigel-coated 24-well plate containing FTDA, supplemented with bFGF and Y-27632. After 24 hours, GFP fluorescence was analyzed by fluorescent microscopy and fresh medium was added to the cells. 48 hours after nucleofection, the Y-27632 treated cells were washed with PBS and dissociated into single cells for cell sorting at the UKE FACS Core Facility with the FACSAriaIIIu cell sorter (BD). The resulting cells were pelleted by centrifugation and resuspended in 200  $\mu$ L PBS. GFP-positive cells were sorted into 1.5 mL reaction tubes containing conditioned medium. The cell suspension was transferred into a Matrigel-coated 6-well plate containing CM supplemented with bFGF and Y-27632 and colonies were allowed to form and grow under daily medium change. 13 days after FACS, 16 single colonies were picked from the 6-well plate into coated 48-well plates. To this end, a sterile 100  $\mu$ L pipette tip was used to carefully scrape off a single colony from the 6-well plate. The detached cells were aspirated with the pipette and transferred into the coated 48-well plate. Colonies which grew close to others were not used for picking. The cells were allowed to grow with daily medium change until almost confluent, before transferring them by EDTA detachment into a 24-well plate. In this format, the cells were again allowed to grow, before

passaging them in a 1:2 ratio. Half of the cells were replated in a 24-well plate, while the other half was used for DNA isolation with the DNeasy kit (QIAGEN) and subsequent sequencing of the DNMT3A target region (see 3.3.1). Unmodified clones were discarded after sequencing. The remaining clones were passaged two more times in a 1:2 ratio and cells were cryopreserved at passage number p41 and p42. Additionally, all cell lines were transferred to FTDA medium and expanded for cryo stock production. The CRISPR experiments were performed with the kind help of Dr. Sandra Laufer of the UKE Stem Cell Core Facility.

### 3.3.4 Subcloning and off-target analysis

Successfully mutated CRISPR clones were subjected to subcloning to analyze the sequence of each of the two alleles individually. To this end the target sequence was amplified with the PrimeSTAR Polymerase (Takara) to yield blunt ended PCR products (see table 9 + 10) which were directly ligated into the pJet1.2 blunt cloning vector from the ThermoFischer CloneJet PCR cloning kit. The plasmid was amplified in Top10 cells and for each clone 6-9 single bacteria colonies were picked for plasmid DNA preparation with the NucleoSpin Plasmid Mini kit (Machery+Nagel) and subsequent sequencing using the Liao-Seq-fw primer.

**Table 9: PCR reaction mix for PrimeSTAR DNA Polymerase**

Component	Per reaction
5x PS buffer	10 µL
2.5 mM dNTPs	4 µL
10 µM primer mix	1 µL
DMSO	1 µL
PrimeSTAR Polymerase	0.5 µL
DNA template	50 ng
Aqua dest.	Ad 50 µL

**Table 10: Touch-down PCR program for PrimeSTAR DNA Polymerase**

Temperature	Time	Cycles
98 °C	10 seconds	10
$T_m - 0.4$ °C per cycle	5 seconds	
72 °C	1 minute / kb product	
98 °C	10 seconds	30
( $T_m - 4$ °C)	5 seconds	
72 °C	1 minute / kb product	
72 °C	7 minutes	1
4 °C	hold	

As a next step the clones were analyzed for possible off-target activity of the Cas9 nuclease. The CRISPR web-tool of the Zhang laboratory (MIT, 2015; <http://crispr.mit.edu>) was used to identify the 10 most likely off-targets of the chosen sgRNA in the human genome. Primers specific for a 400-600 bp region around each of the ten off-targets were designed with the NCBI primer blast tool (<https://www.ncbi.nlm.nih.gov/tools/primer-blast/>; supplementary table S5). The amplified PCR products were sent for sequencing and compared to the entries from the NCBI database.

### 3.3.5 Karyotyping

All three CRISPR cell lines were subjected to karyotype analysis test for culture or CRISPR-induced genomic abnormalities. To this end, cryo tubes between passage number p45 and p50 were thawed and taken into standard FTDA culture. The cells were expanded for two passages before plating them on Geltrex-coated 6-well plates. When the cells reached approximately 70-80% confluency, they were transferred to the Institute of Human Genetics at the UKE for cytogenetic analysis by G banding.

### 3.4 Cardiac differentiation

The three DNMT3A CRISPR cell lines as well as the original ERC018 hiPSC were differentiated into cardiomyocytes with the growth factor and embryoid body (EB)-based differentiation protocol which had previously been established in our laboratory and was published by Breckwoldt et al. in 2017. A schematic overview of the procedure can be found in figure 16.



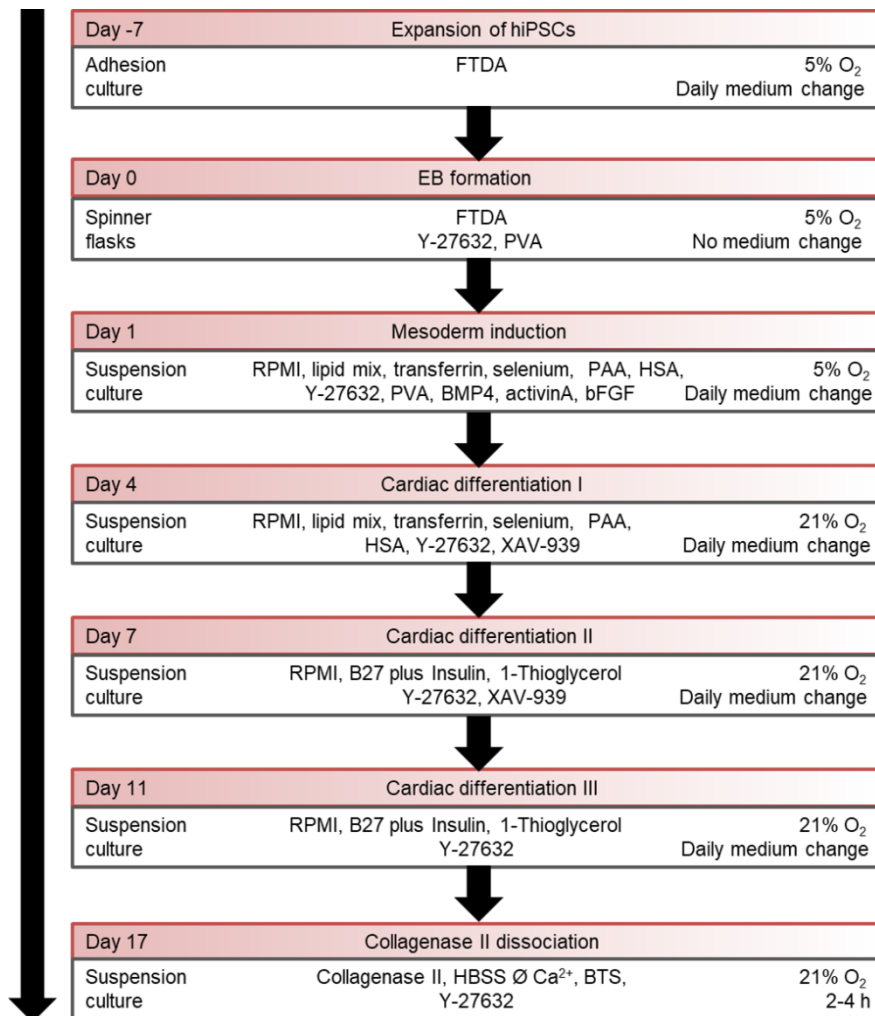


**Figure 16: Overview cardiac differentiation.** Displayed is each stage of the differentiation protocol including time point, culture format, medium composition, and culture conditions (adapted from Breckwoldt et al. 2017).

In short, hiPSC cultured in a monolayer in Geltrex- (Gibco) coated T80 cell culture flasks were detached with EDTA and transferred into 500 mL spinner flasks containing embryoid body (EB) formation medium at a density of 30 Mio cells per 100 mL. The cells were incubated under constant stirring on a magnetic plate overnight to allow for EB formation. The EBs were washed on the next day before the overall EB volume was estimated. 200-250 µL EBs were transferred in mesoderm induction medium into T175 suspension flasks and cultured under hypoxic conditions for three days. The EBs were washed again, the volume was estimated and 200-250 µL of EBs were transferred to cardiac induction medium 1 and cultured for three days with daily exchange of half of the medium volume. At the next medium change, the medium was exchanged completely for

cardiac induction medium 2, which contains insulin and the WNT-signaling inhibitor XAV-939. After 4 days of culture in this medium with half medium-changes, the WNT-inhibitor was no longer added to the medium and the cells were cultured for 5 more days. EBs usually displayed visible beating activity between day 9 and day 11 of the procedure. At day 17, the EBs were dissociated into single cardiomyocytes by collagen II treatment and transferred into cryo tubes in freezing solution (FCS containing 10% DMSO). The cryopreservation system Asymptote EF600M (Grant Instruments) was used to cool the cells down to -80 °C at a controlled ramping rate within 60 minutes, after which they could be transferred to -150 °C for long-term storage. The differentiation efficiency and cell viability were analyzed by flow cytometry after staining with the Fixable Viability Dye eFluor 450 (eBioscience) and a fluorescently-labeled cTnT antibody (Miltenyi Biotech). An example for this analysis can be found in figure 17.

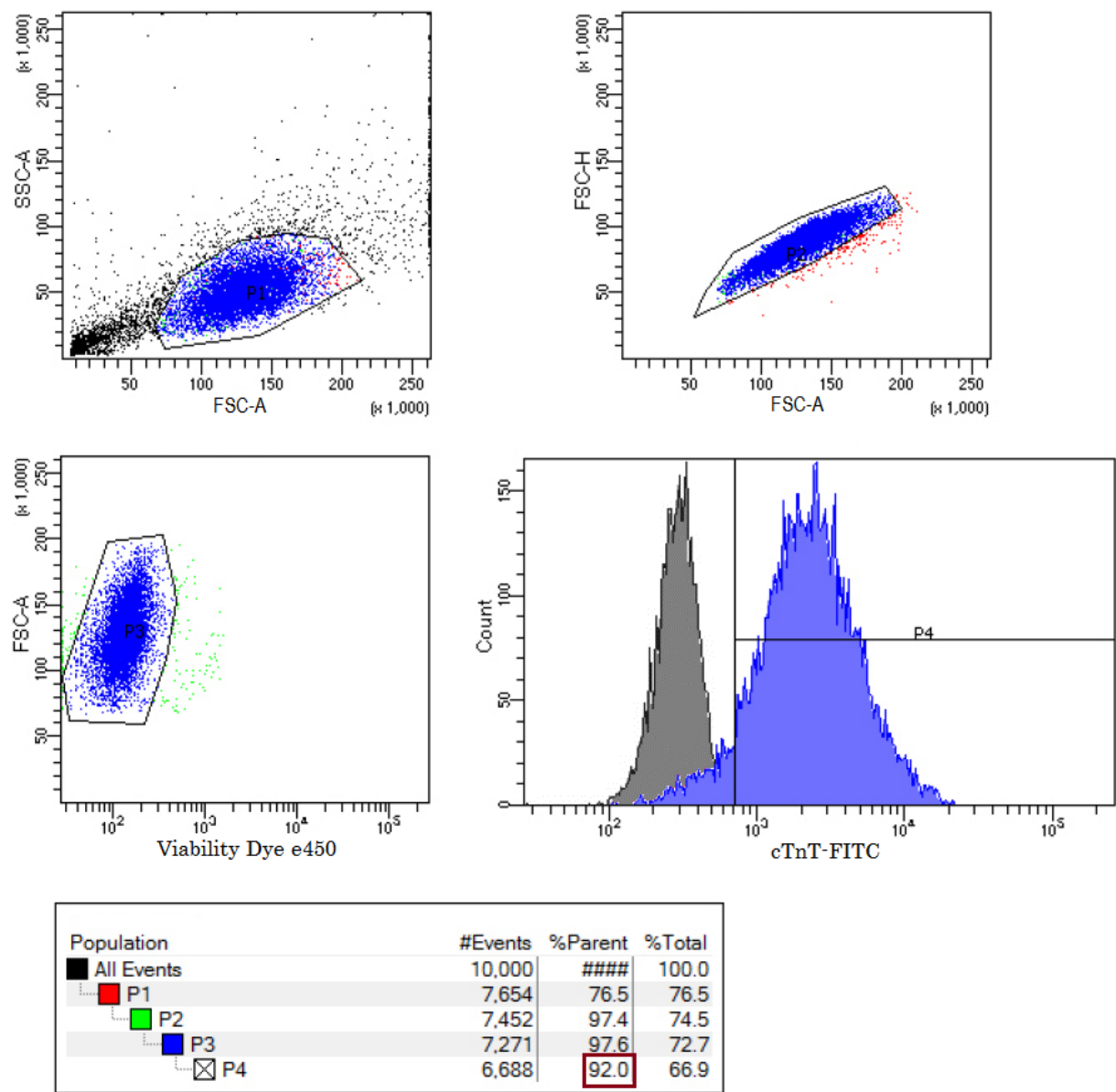


**Figure 17: Flow cytometric analysis of hiPSC-derived cardiomyocytes.** As a first step, cells were gated in to exclude debris (P1). Subsequently, doublets were gated out to only include single cells in the analysis (P2, top right). Only viable cells negative for the eFluor dye (P3, lower left) were used for determination of the proportion of cTnT-positive cells (P4, lower right, histogram plot). The FITC-isotype control is shown in grey, the cTnT-FITC staining in blue.

### 3.5 Engineered heart tissue (EHT)

#### 3.5.1 EHT generation and culture

Generation of EHT from hiPSC-derived cardiomyocytes of all cell lines was performed according to the procedure published by Hansen et al. (2010). In short, the cells were thawed in a water bath and RPMI 1640 medium supplemented with 1% penicillin/streptomycin was added drop-wise to minimize the osmotic stress on the cells. Agarose casting molds for EHT generation were created by placing polytetrafluorethylene (PTFE) spacers (EHT Technologies) in 24-well plates into a 2% agarose/PBS solution at room temperature until the solution had solidified. Silicone EHT racks (EHT Technologies) were then placed into the molds and 100  $\mu\text{L}$  of the EHT master mix containing the thawed cells in EHT casting medium, 2x DMEM, Matrigel, Y-27632, and fibrinogen (table 11) were mixed with 3  $\mu\text{L}$  of thrombin (3 U) and quickly pipetted into the casting mold between the flexible silicon posts. The EHTs were allowed to polymerize at 37 °C for 1.5 hours before pre-warmed medium was added on top of the EHTs for 15 to 30 minutes to help detach the EHTs from the agarose and enable their subsequent transfer into a new plate with fresh EHT medium. EHTs were cultured for 30 days at 37 °C, 7% CO<sub>2</sub>, 40% O<sub>2</sub>, and 98% humidity with medium changes three times per week.

**Table 11: EHT master mix per single EHT (including 10% excess for pipetting errors)**

Component	Volume
hiPSC-derived cardiomyocytes	1.1 x 10 <sup>6</sup>
EHT casting medium	86.9 $\mu\text{L}$
2x DMEM	6.2 $\mu\text{L}$
10% Matrigel	11 $\mu\text{L}$
0.1% Y-27632	0.11 $\mu\text{L}$
Fibrinogen	2.8 $\mu\text{L}$

#### 3.5.2 Video-optical contraction analysis

Parameters of EHT contraction, e.g. force and contraction kinetics, were analyzed over time after each medium change with a video-optical analysis set-up, which was designed specifically for this purpose in our institute. The system is described in detail in Hansen et al. (2010) and on the company website of EHT Technologies, through which the set-up has been made commercially available. The EHTs were placed into a glass-roof incubator at 37 °C, 7% CO<sub>2</sub>, 72% N<sub>2</sub>, and 21% O<sub>2</sub>. A video camera can be moved above the glass roof along the X, Y, and Z-axis and is used to

record a video file of each EHT. A schematic of the set-up and a screen-shot of the software is displayed in figure 18. The files are analyzed with a custom-designed software (Consulting Team Machine Vision; CTMV), which uses figure-recognition to track the movement of a defined part of the EHT over time and calculates the beating frequency, as well as contraction parameters (force, contraction/relaxation times and velocities) and regularity of beating (interdecile range of average beat-to-beat variation; RR scatter) based on this movement.

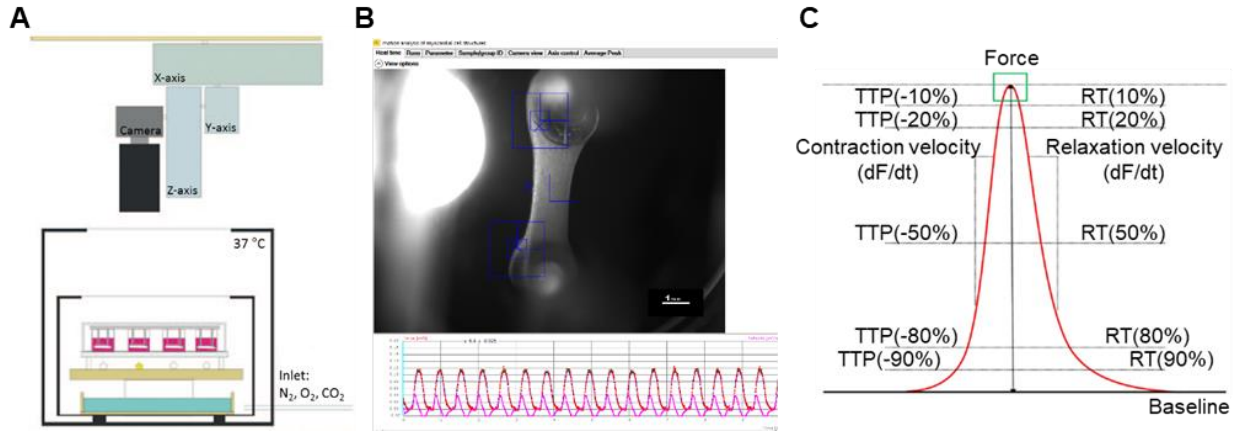


**Figure 18: Video-optical analysis of EHT (adapted from Hansen et al. 2010).** (A) Schematic of the video-optical recording system showing an EHT culture plate in the glass-roof incubator at 37 °C under defined gas influx. A video camera moves along the glass roof to capture each individual EHT. (B) Screenshot of the CTMV EHT analysis software. A live video of each EHT is recorded (top) from which the software generates force over time curves (bottom) by tracking the deflection of the EHT posts due to EHT contraction. (C) EHT contractility parameters calculated by the software from the EHT recordings.

### 3.5.3 Baseline characterization of CRISPR cell lines in EHT format

All cell lines used for EHT generation were characterized at baseline with regard to their beating behavior under electrical stimulation, their calcium EC<sub>50</sub>, force-frequency relationship, and reaction to long-term exposure to elevated calcium concentrations. All measurements were performed in Tyrode's solution (table 12). The desired calcium concentration was set by addition of calcium chloride to the Tyrode's solution. 24-well cell culture plates with Tyrode's solution were regularly prepared the evening before the experiment and pre-incubated overnight at 37 °C, 7% CO<sub>2</sub>, and 40% O<sub>2</sub>.

**Table 12: Calcium free Tyrode's solution**

Component	Concentration
NaCl	120 mM
KCl	5.4 mM
MgCl <sub>2</sub> x 6·H <sub>2</sub> O	1 mM
NaH <sub>2</sub> PO <sub>4</sub>	0.4 mM
NaHCO <sub>3</sub>	22.6 mM
Glucose	5 mM
Na <sub>2</sub> EDTA	0.05 mM
HEPES (pH 7.4, in PBS)	25 mM
Aqua ad injectabilia	

a) Electrical stimulation and average contraction peaks

Electrical stimulation of EHTs with carbon pacing units was done according to the procedure published by Hirt et al. (2014) with the Grass S88X Dual Output Square stimulator (Natus Neurology Incorporated) at 2.5 V with biphasic pulses of 4 ms. The EHTs were first measured without electrical stimulation and the stimulation frequency for subsequent measurements was chosen as 1.5-times the spontaneous beating frequency. Only EHTs which were able to follow the pacing pulses during the whole course of the experiment were taken into account for contractility analysis. Average contraction peaks of each stimulated EHT in 1.8 mM calcium Tyrode's solution were calculated by the CTMV software by taking the average of 15 - 20 individually recorded peaks.

b) Calcium concentration-response curve

The EC<sub>50</sub> of calcium was calculated from a calcium concentration-response curve for each EHT line. For baseline measurements, EHTs were incubated in 1.8 mM calcium containing Tyrode's solution for 30 minutes before measuring them with and without electrical stimulation. All following measurements were done under electrical stimulation. The EHTs were transferred to a 24-well cell culture plate with low calcium concentration Tyrode's solution (0.3 mM calcium) to wash out remaining calcium. Progress of the wash out was closely monitored by video-optical recording and was stopped as soon as the EHTs reached the minimal force threshold of 0.02 mN. The EHTs were subsequently transferred to a new similar plate and measured. For measurement of the other concentration steps, for each step, the EHTs were transferred to a new plate with Tyrode's solution of the desired calcium concentration and incubated for 15 minutes before measurement. With this procedure contractility was measured consecutively at calcium concentrations of 0.3 mM, 0.4 mM,

0.5 mM, 0.6 mM, 0.7 mM, 0.8 mM, 1.0 mM, 1.2 mM, 1.4 mM, 1.8 mM, 2.4 mM, 3.3 mM, 5.5 mM, and 10 mM. Calculation of the  $EC_{50}$  was done with GraphPad Prism 5 with the non-linear regression function 'log(agonist) vs. normalized response – variable slope'.

c) Force-frequency relationship

EHTs were incubated in 1.8 mM calcium for 30 minutes and baseline recordings were made with and without pacing. Wash-out of excessive calcium was done as in b) before the EHTs were transferred into submaximal calcium Tyrode's solution (0.8 mM calcium). After incubation for 30 minutes, baseline measurements were again recorded with and without stimulation. For analysis of the force-frequency relationship, the EHTs were measured repetitively under electrical stimulation at frequencies ranging from 0.7 Hz – 6.9 Hz with 0.2 Hz increments after each measurement. The force-frequency relationship, as well as the pacing capture and contraction/relaxation time was analyzed with GraphPad Prism 5.

d) Long-term exposure to elevated calcium concentrations

Baseline activity in 1.8 mM calcium was measured as in b) and c). The EHTs were subsequently transferred into new plates containing either 1.8 mM or 3 mM calcium ( $\geq 4$  EHT per concentration) for overnight incubation in the video-optical recording system. The continuous mode of the software was used to measure the EHTs repetitively once each hour over a period of 10 hours for 50 seconds per EHT. The effect of long-term elevated calcium on the beating regularity of each EHT line was evaluated by analysis of the RR scatter over time.

#### 3.5.4 Hypertrophic intervention

The EHTs were switched from standard EHT culture medium to serum-free EHT medium additionally containing 0.5 ng/mL triiodothyronine (T3) and 50 ng/mL hydrocortisone prior to the start of the hypertrophic intervention to prevent anti-hypertrophic effects of serum components which would interfere with the experiment (Hirt et al. 2012). Phenylephrine (PE) and endothelin-1 (ET-1) were added to the medium in final concentrations of 20  $\mu$ M and 50 nM, respectively, for the duration of 7 days. The medium was changed and supplemented with fresh PE and ET-1 on a daily basis and video-optical analysis was done each day  $\geq 1$  hour after media change.

### 3.5.5 Termination of EHT experiments

EHT experiments were terminated at the end of the hypertrophic intervention on day 30/31 of culture. After the final measurement, the EHTs were removed from the culture medium and washed in PBS. For histological analysis, 3-4 EHTs of each group, still attached to the silicone posts, were transferred into a new 24-well plate containing Roti-Histofix fixation solution (Roth) and fixed overnight at 4 °C. After 24 hours, the fixed EHTs were detached from the silicone posts and transferred to TBS supplemented with sodium azide. The EHTs were further histologically processed by the Mouse Pathology Core Facility of the UKE (Kristin Hartmann). For calcium sensitivity measurements with the Aurora system (aurora scientific), 2-3 control EHTs from each cell line were detached from the posts and transferred to a relaxing solution containing 50% glycerol and 1% triton X-100 and subsequently stored at -20 °C. All remaining EHTs were detached from the posts and transferred to 2 mL reaction tubes and snap frozen in liquid nitrogen before storing them at -80 °C for subsequent RNA and DNA extraction.

## 3.6 Molecular analysis

### 3.6.1 Immunohistochemical staining

Histological processing (embedding, sectioning, staining) was kindly performed by Kristin Hartmann of the Mouse Pathology Core Facility of the UKE. For all stainings, EHTs were embedded in paraffin and sliced into longitudinal sections of 4 µm thickness. Hematoxylin and eosin (H&E) staining was performed according to standard procedure in an automated manner. The BenchMark XT system (Ventana) was used for all immunohistochemical stainings. Antigens were retrieved by incubation for 30 minutes in citrate buffer. EHT sections were stained with antibodies directed against MLC2V (Synaptic Systems, 1:3000), collagen1 (Abcam, Ab138492, 1:1500), connexin43 (BD Biosciences, 610061, 1:100), Ki-67 (abcam, Ab15580, 1:100), atrial natriuretic peptide (ANP; Millipore, MAB348, 1:6000), caspase3 (R&D Systems, AF835, 1:300). Antibody staining was visualized with the UltraView Universal DAB Detection Kit (Roche). Microscopic imaging was done with the BZ-X710 microscope (Keyence).

### 3.6.2 Gene expression analysis

RNA isolation was kindly supported by Grit Höppner (IEPT, UKE, Hamburg, Germany). RNA for gene expression analysis by qPCR and the nCounter SPRINT Profiler (NanoString) was isolated with the RNeasy Plus Mini Kit (QIAGEN). For this procedure, 350 µL of RLT Plus buffer with 2-



mercaptoethanol were added to the snap frozen EHT in a 2 mL reaction tube. A steel bead was added into the tube and the tissue was disrupted and homogenized with a TissueLyser disruptor device (QIAGEN) for 2 minutes at 30 Hz. The lysate was transferred to the gDNA eliminator column and further processed according to the manufacturer's manual. The isolated RNA was reverse transcribed to cDNA (High-Capacity cDNA Reverse Transcription Kit, Applied Biosystems) for subsequent qPCR analysis with the ABI PRISM 7900HT Sequence Detection System (Applied Biosystems; see section 3.3.2). For expression analysis with the NanoString technology, 50 ng of total RNA were hybridized with customized Gene Expression CodeSets (NanoString) before loading into the nCounter SPRINT Profiler for analysis (Prondzynski et al. 2017). Transcript levels were normalized to a set of 6 housekeeping genes. The CodeSets used are shown in supplementary table S7.

RNA for qPCR and NanoString experiments from the respective same batch of EHT, was isolated with TRIzol (Life Technologies). For this, 1000  $\mu$ L of the reagent and a steel bead were added to the frozen tissue on ice, which was then disrupted and homogenized with the TissueLyser disruptor device (QIAGEN) for 2 x 1 minute at 30 Hz. The steel bead was taken out and 200  $\mu$ L chloroform were added. The mixture was shaken by hand for 15 seconds before incubation for 3 minutes at room temperature. After centrifugation for 15 minutes at 16,000 g and 4 °C, the aqueous phase containing RNA was transferred to a new reaction tube. The RNA was precipitated with isopropanol, washed in 70% ethanol and reconstituted in 20  $\mu$ L of RNase-free water.

### 3.6.3 Western blot

DNMT3A protein levels in hiPSC were kindly determined by Western blot analysis by Grit Höppner (IEPT, UKE, Hamburg, Germany). To this end, the cells were pelleted and resuspended in 1x Laemmli buffer. The samples were heated at 95 °C for 5 minutes before 40  $\mu$ L per sample were loaded on an SDS-PAGE gel. The proteins were blotted wet for 2 hours at 350 mA onto a PVDF membrane. The membrane was blocked for 45 minutes with 5% (w/v) BSA in TBS-Tween and subsequently stained for DNMT3A (CST #2160, 1:500) and GAPDH (HyTest #5G4, 1:2000) at 4 °C overnight. The anti-rabbit and anti-mouse IgG peroxidase-conjugated secondary antibodies (Sigma, 1:10,000) were incubated under shaking for 1 hour at room temperature before proteins were visualized with SuperSignal West Dura ECL (Thermo Fisher) on the Bio-Rad ChemiDoc Touch Imaging System (Bio-Rad Laboratories). Quantification of DNMT3A protein bands relative to the housekeeping protein GAPDH was performed with ImageLab (Bio-Rad Laboratories).

### 3.6.4 Reduced representation bisulfite sequencing (RRBS)

Analysis of DNA methylation by reduced representation bisulfite sequencing (RRBS) was done as described before (Stenzig et al. 2018). In short, individual EHTs were disrupted and homogenized in PBS using the TissueLyser disruptor as described in 3.6.2 for RNA isolation. DNA was subsequently isolated with the DNeasy blood and tissue kit (QIAGEN) according to the manufacturer's instructions. The DNA was sent to the Genome Institute of Singapore (GIS) for further processing and sequencing. DNA was fragmented by MspI (Thermo Fisher), followed by further processing with the NEBNext Ultra DNA Library Prep Kit for Illumina and adaptor ligation with NEBNext Multiplex Oligos for Illumina. The products were then purified (Agencourt AMPure XP - PCR Purification kit, Beckman Coulter) and treated with sodium bisulfite (EpiTect Bisulfite, QIAGEN) before they were amplified with the PfuTurbo CX Hotstart Polymerase (Agilent) and NEBNext Multiplex Oligos for Illumina in a PCR cycler for 14 cycles. PCR products of 150 – 500 bp including adaptors were purified with size selection (Agencourt AMPure XP - PCR Purification kit) and subsequently sequenced on an Illumina HiSeq2500 sequencer. The RRBS procedure was kindly performed by Dr. Dr. Justus Stenzig (IEPT, UKE, Hamburg, Germany), and sequencing was carried out by Dr. Wendy Soon of the Genome Institute of Singapore sequencing core. Raw data was processed using R-script by Wilson Tan. Data mapping was done for all differentially methylated cytosines with an adjusted p-value <0.05 and a beta value >15% with the Ingenuity Pathway Analysis software (IPA, QIAGEN) with kind support of Christian Müller (Molecular Cardiology, UKE, Hamburg, Germany).

### 3.6.5 Sharp electrode measurements

Action potential measurements by sharp microelectrode were kindly performed by Julia Krause (Molecular Cardiology, UKE, Hamburg, Germany) and Tobias Krause (IEPT, UKE, Hamburg, Germany) as described before (Wettwer et al. 2013). 17-20 days old EHTs were transferred into a bath solution containing 127 mM NaCl, 4.5 mM KCl, 1.5 mM MgCl<sub>2</sub>, 1.8 mM CaCl<sub>2</sub>, 10 mM Glucose, 22 mM NaHCO<sub>3</sub>, and 0.42 mM NaHPO<sub>4</sub>. The EHTs were superfused with Tyrode's solution at 36.5±0.5 °C and field-stimulated at 1 Hz. Action potentials were measured by impalement of the tissue with a standard sharp microelectrode. The Lab-Chart software (ADInstruments, Spechbach, Germany) was used for analysis.

### 3.6.6 Lipid staining with Oil red O

Staining for lipid accumulations in EHT was performed as described before for Zebrafish embryos (Schlegel and Stainier 2006; Fraher et al. 2015). A 5% Oil red O (Sigma) stock solution was prepared in 100% 2-propanol and kept at 4 °C for up to 6 months. The working solution was prepared by diluting the stock solution with distilled water to a final concentration of 0.3% Oil red O in 60% 2-propanol. Roti-Histofix fixation solution was added to shock-frozen EHTs and incubated overnight. The fixed EHTs were washed once with 60% 2-propanol and 1 mL of the Oil red O working solution was added for 2 hours. The EHTs were subsequently washed two times in 60% 2-propanol for 10 minutes before staining was documented under a microscope.

## 4 Results

### 4.1 Expression of DNMT isoforms in hiPSC and hiPSC-derived cardiomyocytes

DNMT3A is the most expressed DNMT isoform in cardiomyocytes. However, as this finding was still controversially discussed when this work was conceived, the transcript levels of the three DNMT isoforms were first analyzed to determine which isoform was most abundant in both hiPS cells and hiPS-derived cardiomyocytes (figure 19). In hiPSC, DNMT3B transcript was most abundant, while DNMT1 and DNMT3A only reached 2.8% and 12% of DNMT3B level, respectively. After differentiation of hiPSCs into cardiomyocytes, DNMT3B transcripts were virtually absent, leaving DNMT3A as the dominant DNMT isoform. Both DNMT1 and DNMT3A levels did not change significantly during differentiation. Based on these results, DNMT3A was chosen for CRIPSR/Cas9-mediated DNMT knockout in a control hiPSC line.

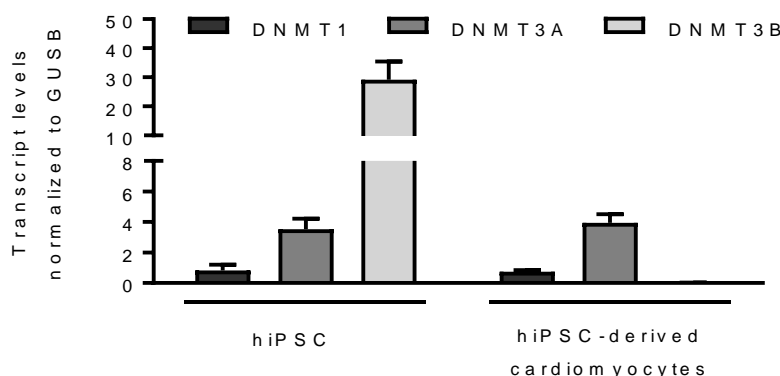


**Figure 19: Effect of differentiation into cardiomyocytes on DNMT isoform expression.** The transcript levels of the three DNMT isoforms were analyzed in hiPSC and hiPSC-derived cardiomyocytes by qPCR. Transcript levels were normalized to GUSB, n=4 for hiPSC, n=10 for hiPSC-derived cardiomyocytes.

### 4.2 CRISPR/Cas9-mediated knockout of DNMT3A

#### 4.2.1 DNMT3A target sequence verification and sgRNA cloning

In 2015, Liao and colleagues published an approach for CRISPR/Cas9-mediated knockout of the different DNMT isoforms in hESC (see figure 14 in Materials and methods). Before this knockout strategy for DNMT3A could be adapted to the control hiPSC line ERC018, the target region of this cell line had to be sequenced in order to verify absence of polymorphisms which could have interfered with sgRNA binding. Results of the sequencing are shown in figure 20. Since no

polymorphisms or mutations were detected in the DNMT3A target sequence, the published sgRNA from Liao et al. could be used without modifications.

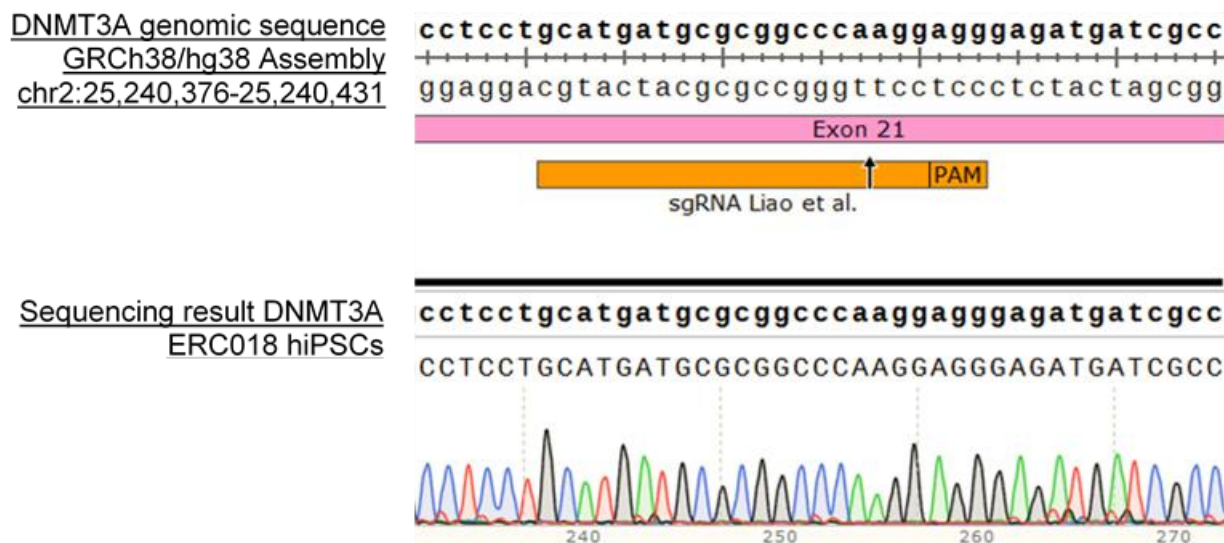


**Figure 20: Verification of the sgRNA target sequence in the genome of ERC018.** The upper panel shows the database sequence for the target region in the human genome assembly GRCh38/hg 38, while the lower panel displays the sequencing results of the target region in ERC018. The sequence alignment was done with SnapGene. PAM = Protospacer Adjacent Motif.

#### 4.2.2 Comparison of Cas9 plasmids

Since the introduction of CRISPR for gene editing, several different Cas9-containing plasmids have been constructed. Two different plasmids were chosen for evaluation of their efficiency for the knockout of DNMT3A. The sgRNA was cloned into both the pSpCas9(BB)-2A-GFP, containing the human codon-optimized pSpCas9, and the VP12-HF-2A-GFP plasmids, which contains a high-fidelity version of Cas9 with supposedly lower off-target activity. Sequencing of the plasmids after cloning verified the correct insertion of the sgRNA into the gRNA cassette. The two constructs were first tested in HEK293T cells to compare their transfection efficiency as well as their ability to knock out the target gene. Cell morphology after transfection did not differ between control cells and the two transfection conditions (figure 21) ruling out cytotoxic effects of the different constructs. The Cas9 carried a GFP tag in both constructs, allowing for estimation of the transfection efficiency. The high-fidelity plasmid displayed very low transfection efficiency (figure 21 C) compared to the SpCas9 plasmid, for which GFP was detectable in almost every cell (figure 21 B).

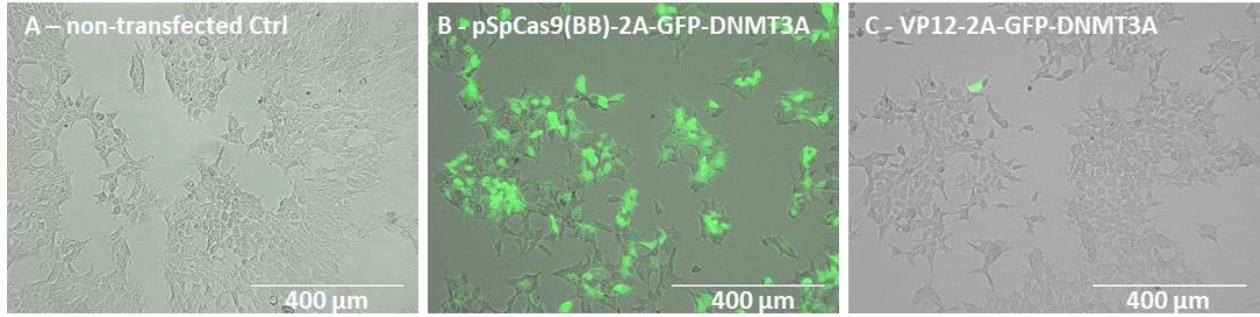


**Figure 21: Transfection efficiency of Cas9-containing plasmids.** Fluorescence microscopic images of GFP expression in HEK293T non-transfected Ctrl cells (A), as well as cells transfected with the pSpCas9(BB)-2A-GFP-DNMT3A (B) and VP12-2A-GFP-DNMT3A plasmids (C).

To verify the functionality of the combination of the encoded Cas9 and sgRNA, DNMT3A transcript levels were measured in the HEK293T cells after harvesting (figure 22). In line with the low transfection efficiency, no reduction in DNMT3A transcript abundance could be detected in the cells transfected with VP12-HF-2A-GFP-DNMT3A. In contrast, transfection with pSpCas9(BB)-2a-GFP-DNMT3A yielded significant reduction of the transcript level by ~50%. Due to the better transfection and knock-out efficiency, the pSpCas9(BB)-2a-GFP-DNMT3A plasmid was used for the following CRISPR experiments.

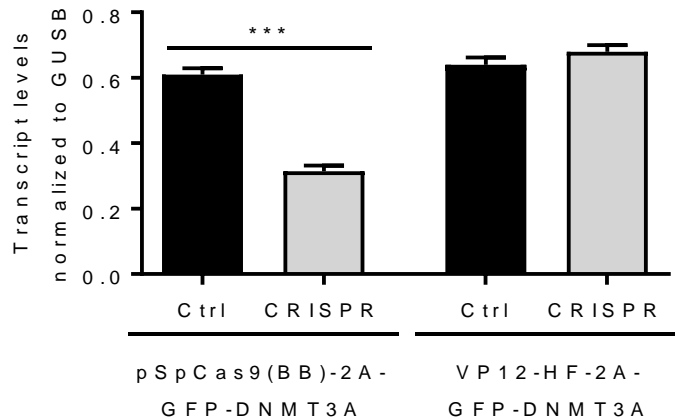


**Figure 22: DNMT3A transcript levels in HEK293T after CRISPR.** RNA was isolated from non-transfected control cells, as well as from cells transfected with one of the two DNMT3A CRISPR plasmids and used for DNMT3A RT-qPCR. n=3 for each plasmid and condition, 1-way ANOVA plus Tukey's post-test for multiple comparisons, \*\*\*p<0.001.

#### 4.2.3 Nucleofection optimization for ERC018

HiPSC are known to be difficult to transfect, with nucleofection yielding the best results. However, individual hiPSC cell lines differ significantly with respect to their susceptibility to nucleofection conditions. The best suitable combination of nucleofection buffer and program was therefore tested for ERC018 with an optimization run with a control GFP plasmid. The flow cytometry results of the 14 different combinations of the two available buffers and the seven programs are shown in table 13. Overall, buffer P3 yielded better results than buffer P4 with regards to both cell survival and nucleofection efficiency. The best combination of cell survival and transfection efficiency was observed with buffer P3 and program CB-150, which was consequently used for the subsequent experiments.

**Table 13: Flow cytometry results of the nucleofection optimization.** For each condition the number of surviving cells 48 h after nucleofection, as well as the number and percentage of GFP-positive cells were measured. The best combination of buffer and program is highlighted in yellow.

Buffer	Program	Cell number	GFP <sup>+</sup> cells	Nucleofection efficiency
P3	CA-137	2450	1186	48.4%
	CB-150	4285	1885	44%
	CD-118	3923	1278	32.6%
	CE-118	3421	1171	34.2%
	CM-113	3637	1326	36.5%
	DC-100	2426	900	37.1%
	DN-100	1086	439	40.4%
P4	CA-137	1533	647	42.2%
	CB-150	2419	899	37.2%
	CD-118	3329	1138	34.2%
	CE-118	3197	1076	33.7%
	CM-113	4536	1607	35.4%
	DC-100	2309	622	26.9%
	DN-100	1426	518	36.3%

#### 4.2.4 Nucleofection and single clone expansion

ERC018 hiPSC of passage p37 were used for DNMT3A knockout by CRISPR/Cas9. In order to yield a higher GFP fluorescence for positive cell selection, pSpCas9(BB)-2A-GFP-DNMT3A was co-nucleofected with a pMaxGFP control plasmid. The cells were cultivated for 24 hours post nucleofection, before GFP expression was analyzed microscopically. A GFP signal could be detected in the nucleus of a small percentage of nucleofected cells together with many dead cells (figure 23).

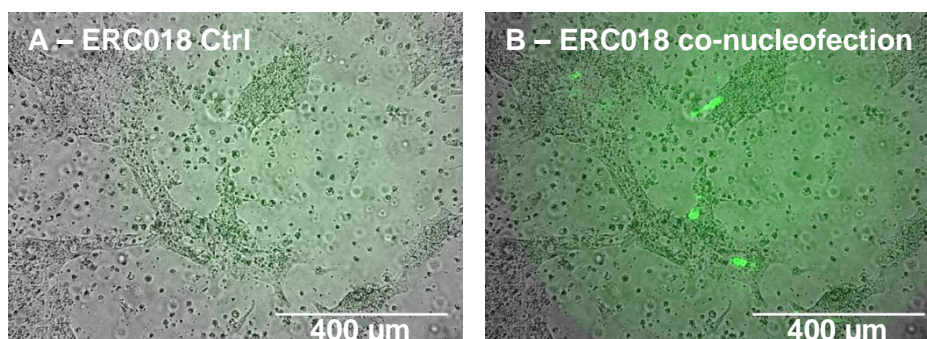


**Figure 23: GFP expression in ERC018 24 hours after nucleofection.** (A) non-nucleofected control cells and (B) ERC018 cells co-nucleofected with the CRISPR vector and the pMax GFP control plasmid.

To decrease the workload during subculture of single cell clones, only cells that were successfully nucleofected, i.e. cells which were GFP-positive, were used for further culture. The separation of positive and negative cells was achieved by fluorescence activated cell sorting (FACS). The sorting layout is depicted in figure 24. Only single cells with a GFP signal were sorted into a reaction tube, while negative cells were discarded. Doublet cells were also not included into the sorting to reduce contamination by non-fluorescent cells which might stick to a positive cell. FACS revealed a nucleofection efficiency of 0.8% and yielded 793 GFP-positive cells, which were seeded for colony formation in a 6-well plate. After 13 days of culture, 16 single colonies had formed and were transferred to 48-well plates for single clone expansion.

The clones #14 and #15 started to differentiate spontaneously during culture and were discarded. The remaining 14 clones were analyzed by PCR amplification and subsequent sequencing of the target sequence (figure 25). Sequencing revealed a non-modified wildtype sequence for 10 of the 14 clones (#1+2, #4-8, #10-12), one clone (#16) could not be sequenced since it did not yield a



product after amplification by PCR, suggesting a larger deletion of the genomic region. The negative clones were discarded after sequencing results were received.

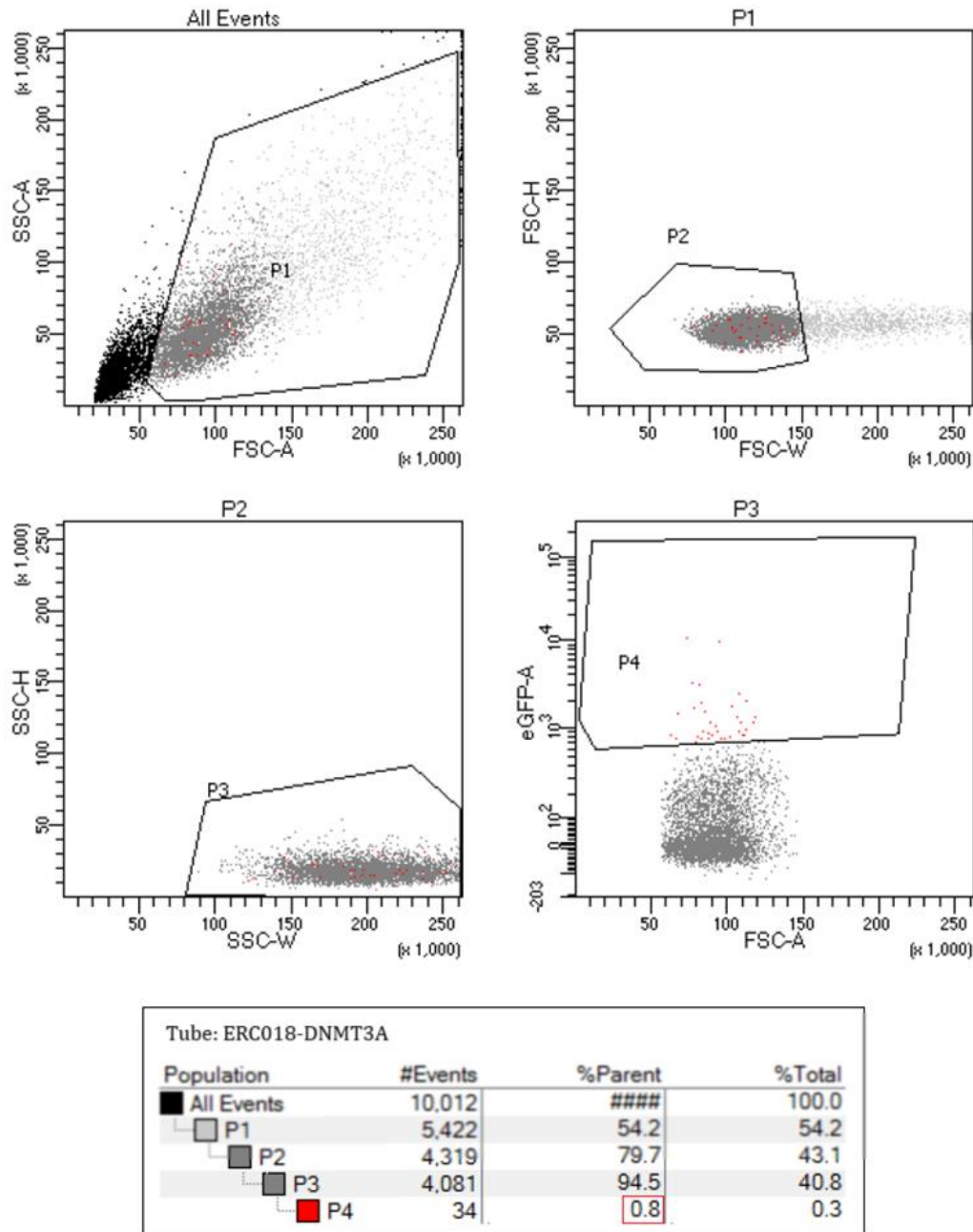


**Figure 24: Sorting layout DNMT3A CRISPR of ERC018.** First, the cells were gated according to their size (FSC) and granularity (SSC) in order to gate out small debris (P1). P2 and P3 excluded all cell aggregates from the sorting to yield single cells only. Single, GFP-positive cells were found in P4 and sorted into a collection tube. Bottom: population statistics of the nucleofected cells. The nucleofection efficiency is marked in red.

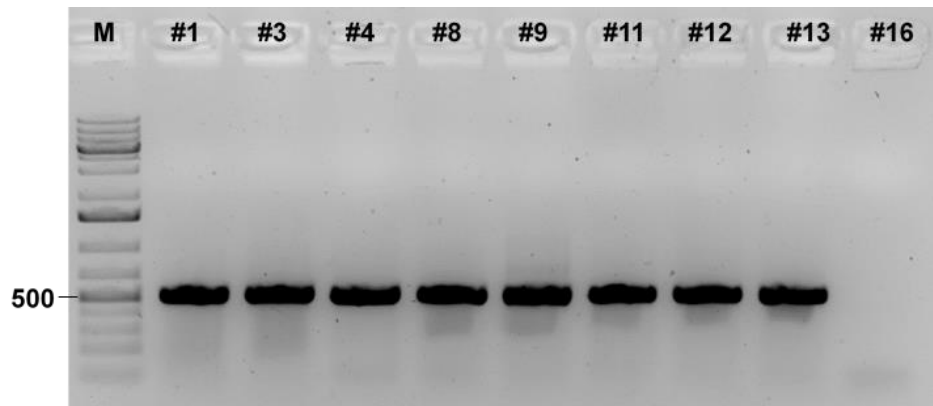


**Figure 25: Agarose gel of DNMT3A target sequence PCR for several CRISPR clones.** Clones #1-13 showed a band of the expected size and were further processed for sequencing, while clone #16 showed no band and was discarded. M = 1 kb plus DNA ladder.

Sequencing of clone #13 revealed insertion of a single adenine base at the DSB site on both alleles (i.e. a homozygous mutation), while clones #3 and #9 displayed double peaks in the electropherogram beginning at the designated Cas9 cutting site (figure 26 A). To differentiate whether these two clones were heterozygous or compound heterozygous, subcloning of the individual alleles was done. Independent sequencing of the alleles of clone #3 revealed a heterozygous genotype with one unaltered wildtype allele and one mutated allele with an additional adenine inserted at the DSB site (figure 26 B). Clone #9 was shown to be compound heterozygous, where on one allele an additional adenine was inserted, while the other allele had a 20 bp deletion starting at the cutting site (figure 26 C). An overview of the CRISPR results is displayed in table 14.

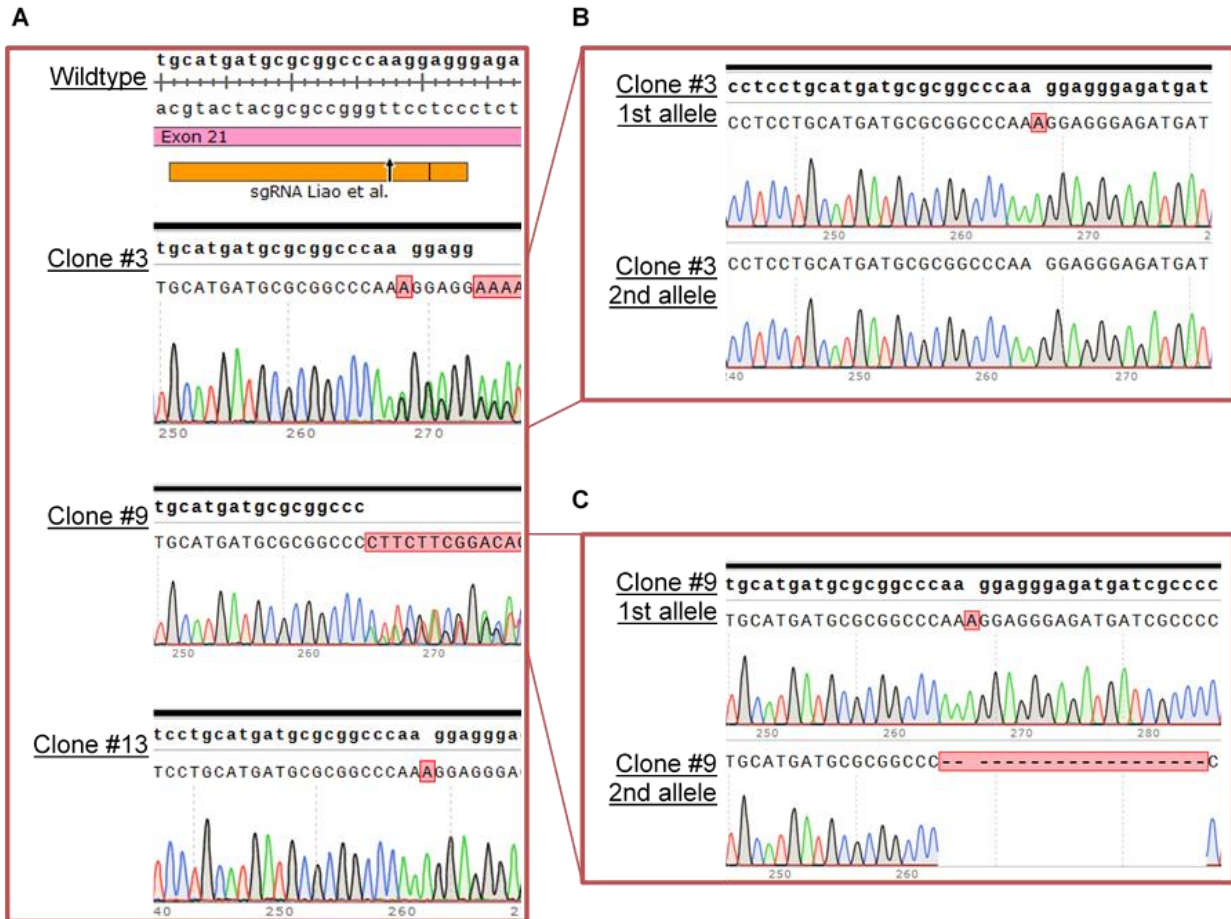


**Figure 26: Sequencing results of successfully mutated ERC018 clones.** (A) First sequencing results of the three positive clones. Clone #13 revealed a homozygous insertion, clone #3 and #9 yielded no clear sequencing results, indicating diverging sequences on the two alleles. (B) + (C) Allele-specific sequencing of clone #3 revealed a heterozygous insertion, while clone #9 showed an insertion on one allele and a 20 bp deletion on the other allele. Upper row in bold: database sequence; lower row: sequencing result, mismatches with the database sequence are indicated in red.

**Table 14: Overview CRISPR-mediated knockout of DNMT3A.**

FACS GFP <sup>+</sup>	Seeded cells	Clones analyzed / picked	Sequencing results
0.8%	793	14 / 16	10 clones not modified 1 clone heterozygous (#3) 1 clone compound heterozygous (#9) 1 clone homozygous (#13) 1 clone without PCR product (#16, deletion?)

#### 4.2.5 Off-target analysis

The relatively short length of the sgRNA of 20 nucleotides and according low binding specificity raises the possibility of binding of the sgRNA to sequences in the genome with close sequence similarity, which would lead to induction of DSBs and mutations at unwanted sites in the genome. The CRISPR online tool of the MIT (<http://crispr.mit.edu/>) was used to calculate the likelihood of off-target activity based on parameters such as the number of mismatches between sgRNA and genomic sequence and generates a table of the most likely off-target sequences including a likelihood score. The top ten most likely off-target sequences (table 15) were chosen for off-target analysis in the three CRISPR clones. For each of the 10 off-target sequences, primers specific for that genomic region were designed and the region was amplified from the DNA extracted from these three clones by PCR. The correct size of each product was verified on an agarose gel (figure 27) before purification for sequencing. All three clones showed no mutations and thereby no off-target activity for any of the ten genomic loci. Figure 28 shows the sequencing results for off-target #1 and #2 from all three clones as an example.

**Table 15: Top ten off-target sequences for the used sgRNA.** For each potential off-target sequence the score representing the likelihood of sgRNA binding to the respective sequence and the size of the PCR product for sequencing is shown. If the off-target sequence is located inside a gene the respective accession number is additionally indicated.

	Score	Gene	Product size
Target	100	NM_153759	
OT#1	1.18	None	469 bp
OT#2	0.87	NM_020945.1	450 bp
OT#3	0.86	NM_001256399.1	614 bp
OT#4	0.80	NM_006885.3	490 bp
OT#5	0.68	NM_001170738	573 bp
OT#6	0.67	NM_015253.1	464 bp
OT#7	0.64	NM_001316309.1	461 bp
OT#8	0.51	NM_015209.2	580 bp
OT#9	0.47	NM_001111018.1	453 bp
OT#10	0.46	None	487 bp

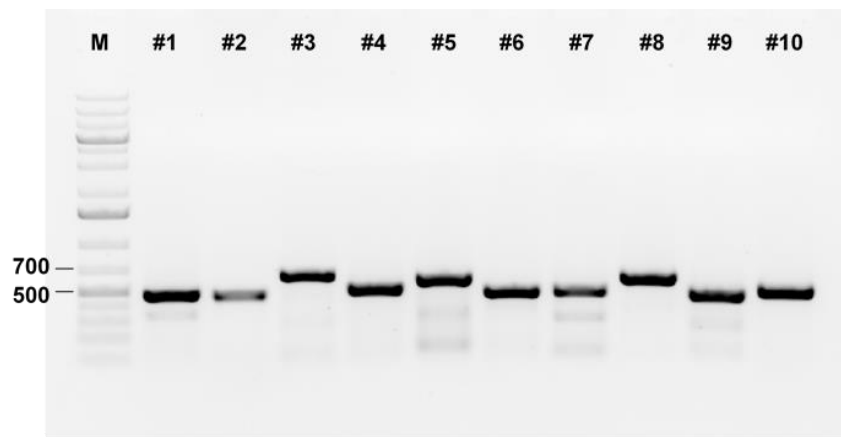


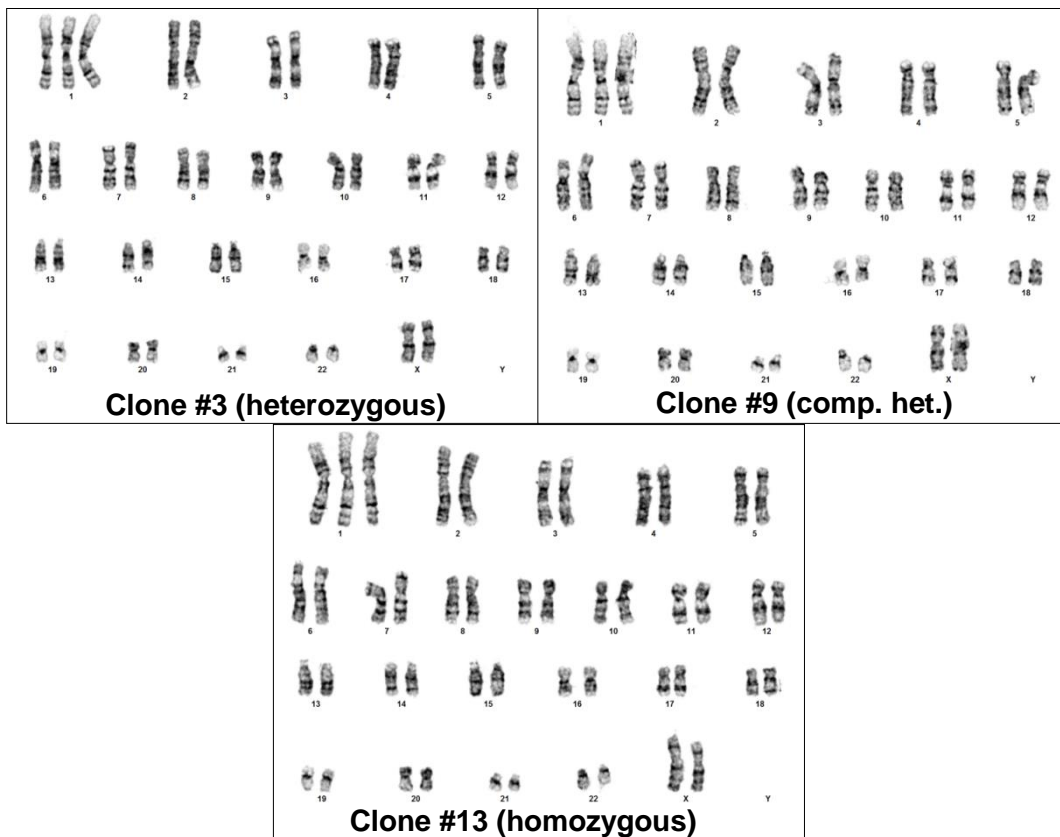
**Figure 27: Agarose gel of the ten off-target sequence PCRs from clone #13.** All off-target sequences (#1 - #10) showed the expected bands between 400 and 700 bp. M = 1 kb plus DNA standard marker.



**Figure 28: Sequencing results of off-target sequence #1 and #2.** The database sequences of both off-target sequences were aligned to the sequencing results of all three clones revealing no mutations.

#### 4.2.6 Karyotype analysis

Since long-term culture of hiPSC is prone to produce karyotypic abnormalities, the karyotype of all three CRISPR clones was analyzed at the end of the procedure to verify the absence of culture or CRISPR-induced abnormalities. Unfortunately, the analysis performed by the Human Genetics Department (UKE) revealed a 47, XX karyotype with a trisomy of chromosome 1 (figure 29). In order to discriminate between CRISPR mutation-induced and trisomy-induced phenotypic differences, an ERC018 clone harboring the same trisomy was later used as an additional control for the following EHT experiments. An overview of all cell lines used in this study can be found in table 16.



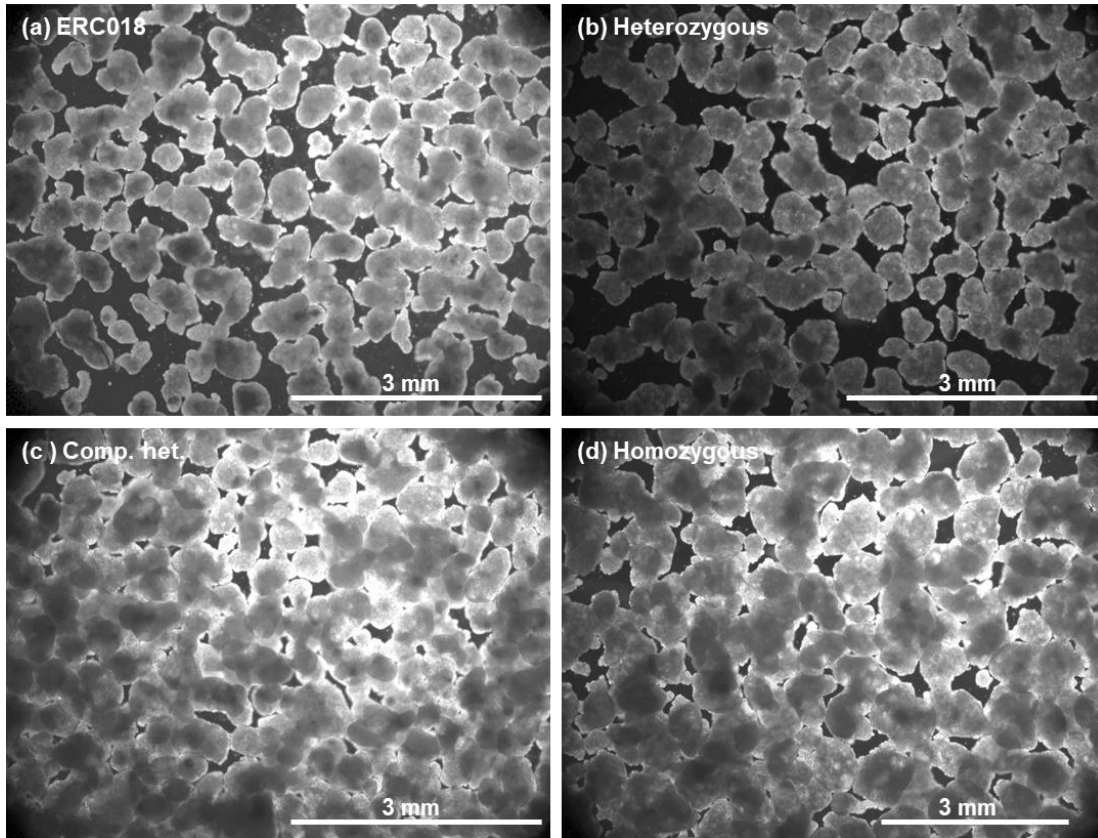
**Figure 29: Karyotype of the CRISPR cell lines.** The karyotype of all three cell lines was analyzed by G banding in the Department for Human Genetics at the UKE. All clones showed an abnormal karyotype with a trisomy of chromosome 1.

Table 16: Overview of the cell lines used in this study.

Cell line	DNMT3A	Karyotype	Experiments
ERC018	Wildtype	46, XX	EHT contractility measurements EHT baseline characterization EHT pro-hypertrophic treatment Histology NanoString & qPCR expression analysis DNA methylation analysis Action potential measurements
Trisomy control	Wildtype	47, XX + 1	EHT contractility measurements EHT baseline characterization EHT pro-hypertrophic treatment Histology NanoString & qPCR expression analysis
Heterozygous	Heterozygous insertion of A	47, XX + 1	EHT contractility measurements EHT baseline characterization EHT pro-hypertrophic treatment Histology qPCR expression analysis
Compound heterozygous	Insertion of A + 20 bp deletion	47, XX + 1	EHT contractility measurements EHT baseline characterization EHT pro-hypertrophic treatment Histology qPCR expression analysis Action potential measurements
Homozygous	Homozygous insertion of A	47, XX + 1	EHT contractility measurements EHT baseline characterization EHT pro-hypertrophic treatment Histology NanoString & qPCR expression analysis DNA methylation analysis

### 4.3 Cardiac differentiation

During differentiation of hiPSC into different cell types, DNA methylation changes dynamically (Boland et al. 2014). Since it was not yet known which of the DNMT isoforms is involved in establishment of new DNA methylation signatures during cardiac differentiation, it was possible that knockout of DNMT3A could interfere with differentiation into cardiomyocytes. To test the ability of the three CRISPR lines to differentiate into beating cardiomyocytes, all three lines as well as the ERC018 control and ERC018 trisomy lines were subjected to the in-house differentiation protocol. Embryoid body (EB) formation, which represents the first step of the process, was not impaired by (heterozygous or homozygous) mutations of DNMT3A. All cell lines formed stable EBs, which did not differ in size or morphology (figure 30).



**Figure 30: EBs on day 16 of cardiac differentiation.** All cell lines formed morphologically similar, stable EBs which started to beat between day 8 and 11 of the procedure.

The EBs derived from all five cell lines started to beat coherently between day 8 and day 11 of the differentiation protocol, which is in the usual range for this protocol. After dissociation on day 17,



the cardiomyocyte fraction of all output cells was determined by flow cytometric analysis of the cardiomyocyte marker cardiac troponin T (cTnT). In addition, the differentiation efficiency was calculated by dividing the number of cells which were yielded after dissociation of the EBs by the number of input cells that was used in the first stage. The knockout cell lines were compared to the results of the ERC018 control line with regard to these two parameters to identify possible effects of DNMT3A mutations on the differentiation procedure. As seen in figure 31 A, there was no statistically significant difference between the four cell lines with regard to cardiomyocyte fraction, as all four cell lines yielded cTnT values between 60% and 99%. The differentiation efficiency of all four cell lines varied between 0.3 and 1.4 in the different differentiation runs, again revealing no significant difference between the cell lines (figure 31 B). Both the percentage of cTnT-positive cells and the differentiation efficiencies yielded with the knockout lines are in the expected range for the differentiation protocol. Differentiation of the ERC018 trisomy cell line could not be systematically compared to the others, since only one differentiation run was performed.

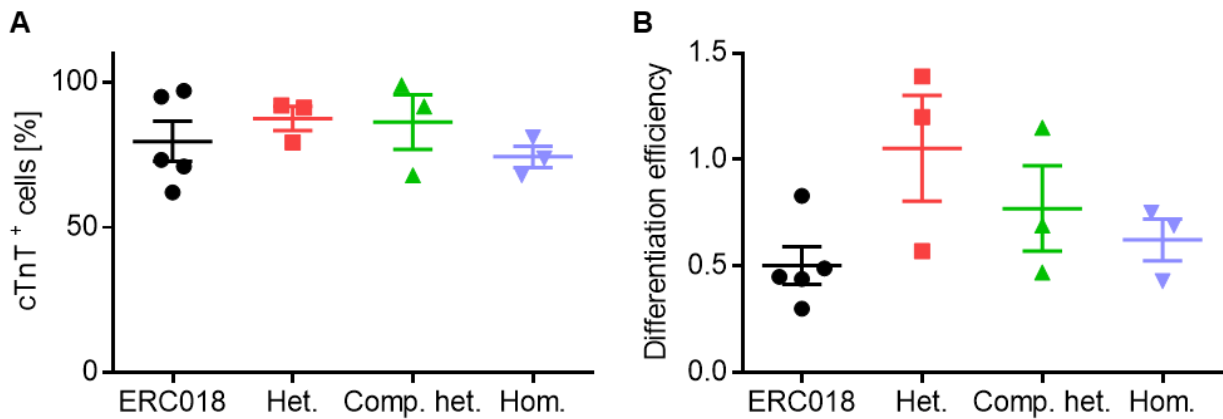


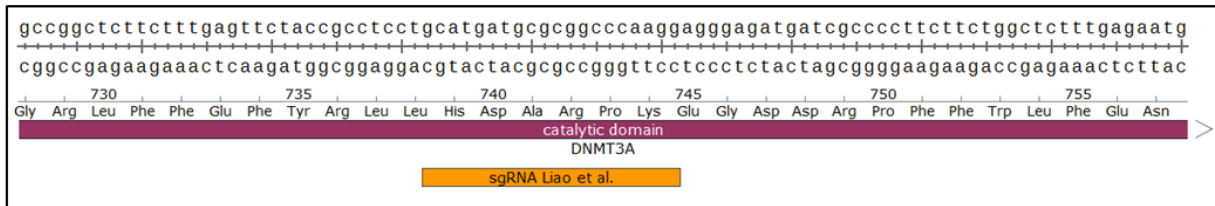
**Figure 31: Quality parameters of differentiation.** (A) The cardiomyocyte content after differentiation was analyzed by flow cytometry after staining of the cardiomyocyte marker cTnT. (B) The differentiation efficiency was determined by dividing the number of output cells by the number of input cells.

#### 4.4 Effect of the DNMT3A mutations on mRNA and protein expression

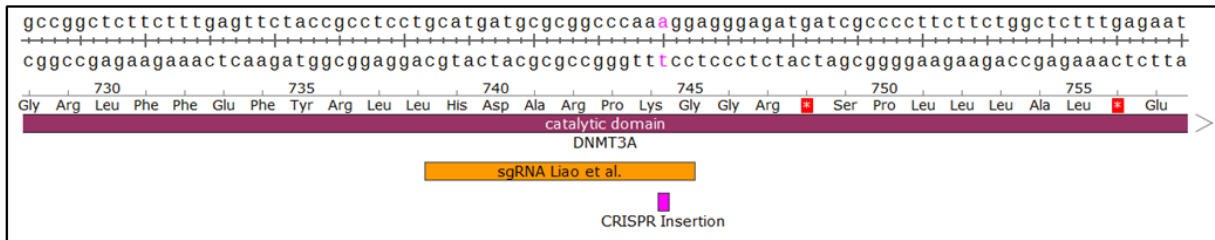
Mutations in the genomic sequence of a protein encompass different forms. Point mutations can either lead to no change (silent) or the exchange of a single amino acid for another, which also can lead to the formation of a stop codon and a premature stop of translation. Insertion or deletion mutations often lead to a frame shift with a change of all following amino acids and, frequently,

premature stop codons. In the CRISPR cell lines both the insertion of a single adenine, as well as the deletion of 20 base pairs is expected to result in a frame shift of the mRNA. The expected new reading frames were simulated with the SnapGene software. Figure 32 A shows the codon sequence and the amino acids of the DNMT3A mRNA, which in total has 912 amino acids in its longest isoform. Insertion of a single adenine at the DSB site (figure 32 B) leads to a frame shift starting at p.Glu745Gly and a premature stop codon at position p.748. Similarly, deletion of 20 base pairs at the DSB site results in a frame shift starting at p.Lys744Leu and a premature stop codon at amino acid 749 (figure 32 C).

### A Wildtype mRNA



### B Insertion [A] mRNA



### C 20 bp deletion mRNA

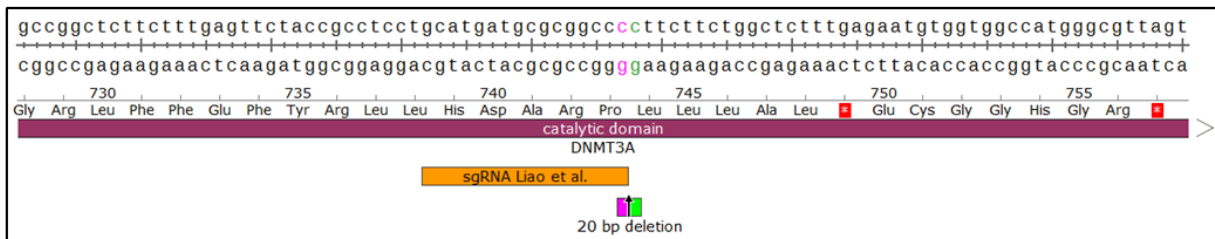


**Figure 32: Effect of the CRISPR mutations on the mRNA sequence of DNMT3A.** (A) Wildtype mRNA sequence of DNMT3A in the region of sgRNA binding. The longest isoform of DNMT3A codes for 912 amino acids. (B) Insertion of a single adenine (purple), as seen in all three CRISPR clones, leads to a frame shift and a premature stop codon at position p.748 (red asterisk). (C) Deletion of 20 bp (purple/green), as present on one allele of the compound heterozygous clone, also leads to a frame shift, with a premature stop codon at p.749.

Since truncated proteins can have toxic effects, cells have developed a mechanism to prevent translation of affected proteins. Components of the nonsense-mediated mRNA decay pathway recognize the premature stop codon already on the mRNA level and mark it for degradation, ensuring that no truncated protein will be produced (Lykke-Andersen and Jensen 2015). The transcript levels of DNMT3A were measured in the three CRISPR lines and compared to ERC018 in both hiPSC and hiPSC-derived cardiomyocytes by qPCR with primers binding upstream of the DSB site, to analyze whether stable transcripts of the truncated sequence are produced. The other two DNMT isoforms, DNMT1 and DNMT3B, were also analyzed to exclude compensatory changes in their expression. In hiPSC the main isoforms in all four cell lines was DNMT3B, with no significant differences between the cell lines (figure 33 A). DNMT1 also showed the same low transcript levels in all four cell lines. The DNMT3A transcript levels were significantly reduced in the heterozygous knockout and virtually absent in the homozygous and compound heterozygous knockout cell lines. After differentiation into cardiomyocytes, DNMT3B transcripts were absent from all four cell lines and DNMT1 expression remained similarly low as in the hiPSC (figure 33 B). In contrast, the DNMT3A transcript level was higher in differentiated cardiomyocytes than in the corresponding hiPSC in the three CRISPR lines, while it remained roughly the same as in hiPSC in the ERC018 line. In effect, the heterozygous knockout displayed almost the same level as ERC018, while the two complete knockouts displayed 15 – 20% of the ERC018 DNMT3A transcript level.

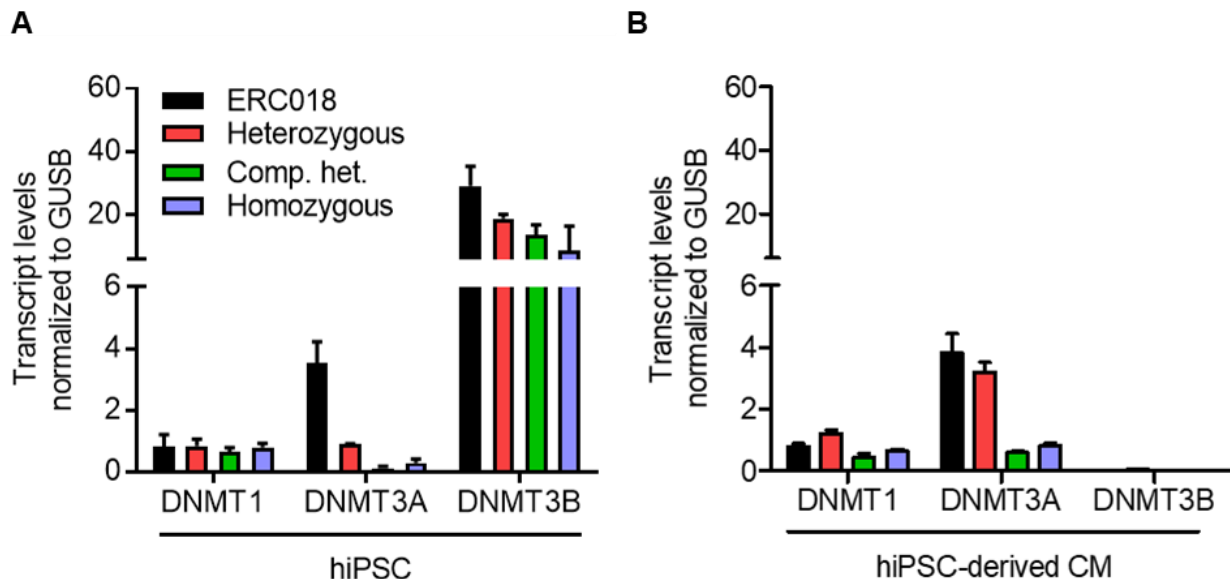


**Figure 33: DNMT transcript levels in hiPSC and hiPSC-derived cardiomyocytes.** (A) DNMT isoform transcript analysis in wildtype ERC018 and the DNMT3A knockout lines. (B) Transcript levels of the three DNMT isoforms after differentiation into cardiomyocytes in ERC018 and the three CRISPR clones.

In addition to analysis of transcript levels, DNMT3A protein expression was analyzed by Western blot in the three CRISPR hiPSC lines, as well as in the ERC018 cell line. A representative image of this analysis is shown in figure 34 A. The heterozygous clone, as well as ERC018 showed a distinct band at the expected size of approximately 130 kDa. This band could be detected neither in the compound heterozygous nor the homozygous knockout line. The protein level of DNMT3A was quantified relative to the band size of the housekeeping protein GAPDH (glyceraldehyde 3-phosphate dehydrogenase; figure 34 B). In the heterozygous clone approximately half of the ERC018 protein level could be detected. In the other two cell lines quantification was impossible due to the absence of a band.

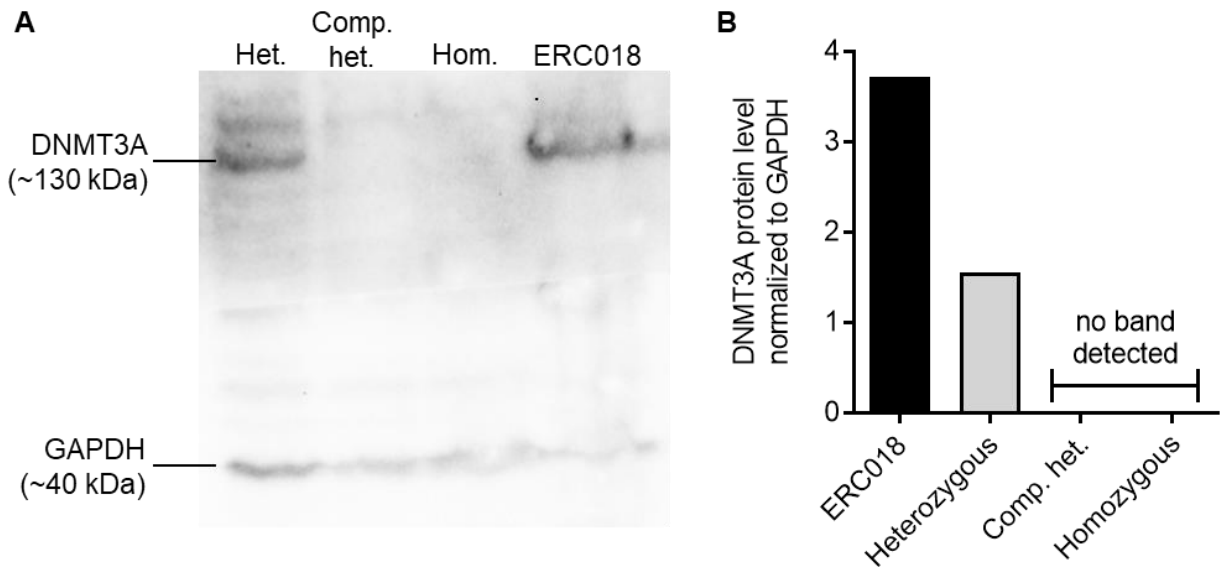


**Figure 34: DNMT3A protein level quantification by Western blot.** (A) Western blot analysis of DNMT3A yielded bands of the expected size only in the heterozygous clone and ERC018. (B) Quantification of the DNMT3A bands in comparison to the housekeeping protein GAPDH.

## 4.5 Functional effects of DNMT3A knockout in EHT

### 4.5.1 Development and contractility

In order to analyze whether the knockout of DNMT3A had any consequences for cardiomyocyte function, EHTs were generated from all five cell lines. Three different batches of EHTs were prepared for each of the three CRISPR cell lines and ERC018, each batch prepared from a separate differentiation run, while due to time constraints only one batch of ERC018 with the

trisomy 1 karyotype was generated. All cell lines remodeled similarly quick after casting and first twitching of cells was detectable already after 3-5 days. Measurable deflection of the silicone posts was observed between day 6 and day 8 in all cell lines and batches. All cell lines displayed steadily increasing force generation over time until they reached a plateau phase between day 15 and 17 (figure 35). ERC018 EHTs developed quicker in the beginning, reaching higher force than the other cell lines between day 6 and day 11. Starting on day 23-24 the EHTs were transferred from regular EHT medium to serum-free EHT medium. ERC018 EHTs, as well as the trisomy control EHTs reacted to the altered medium condition with the onset of another steady increase in force generation (+50% at day 30), leaving their previous plateau steady state. This effect of serum free medium conditions was not observed in any of the CRISPR lines. On the contrary, heterozygous knockout EHTs showed a decline in force starting at day 30 (-25%), while the DNMT3A deficient cell lines (homozygous and compound heterozygous mutation) already displayed a decreasing force generation from day 26/27 onwards leading to markedly reduced contraction force at the end of culture (-45% and -70%, respectively).

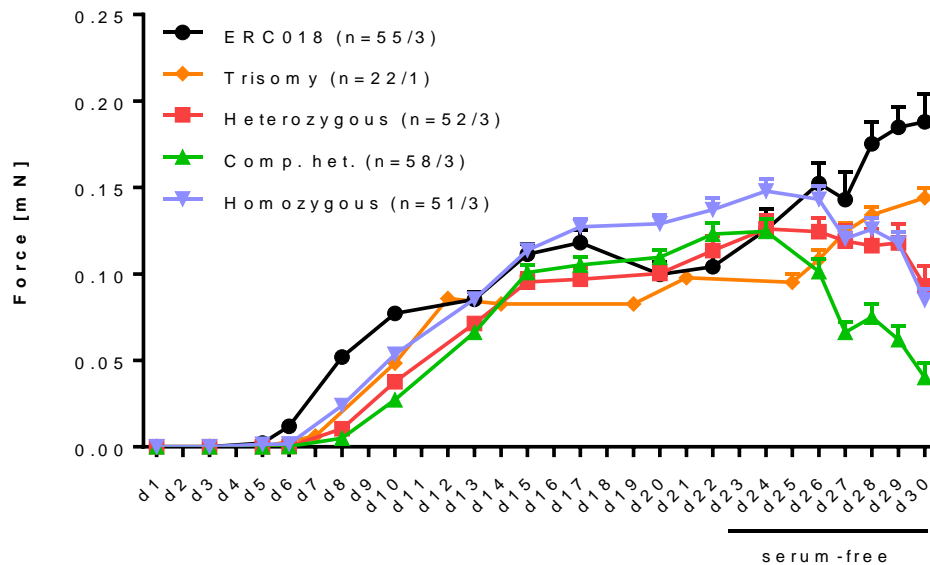


**Figure 35: EHT force generation over time.** EHT contractility of each cell line was measured one hour after each medium change. EHTs were cultured in serum-free medium from day 23/24 onwards with daily medium changes. n = number of EHTs / number of EHT batches.

In parallel to the observed decline in force, the knockout EHT lines started to beat in a less regular manner over time. An example of the irregularities is depicted in figure 36. The RR scatter (figure 37 A), which is a surrogate parameter for occurrence of irregularities in the beating patterns of EHTs, significantly increased for the knockout lines from day 26 onwards. The severity of those irregularities was in accordance with the degree of force reduction. The heterozygous and homozygous EHTs yielded similar values, while the compound heterozygous EHTs performed significantly worse with respect to both parameters. Both control EHT lines showed no increase in RR scatter over time.

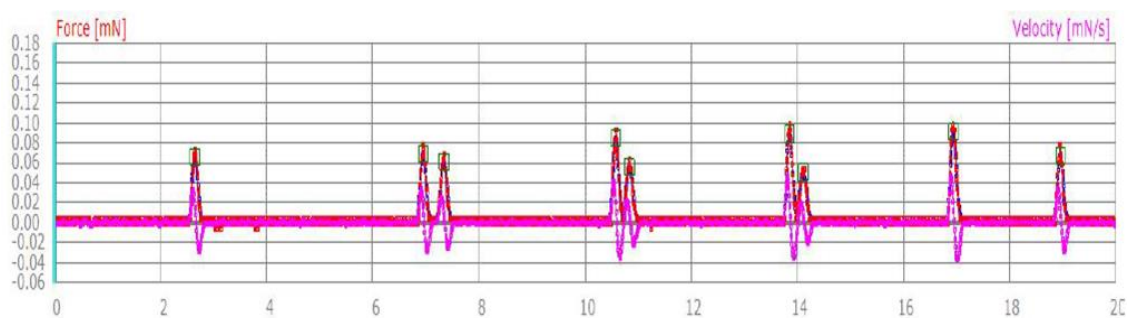


**Figure 36: Beating irregularities in DNMT3A knockout EHTs.** Force-over-time trace from video-optical recording of a knockout EHT. The EHTs often displayed a reduced beating frequency paired with irregular distribution of the contractions over time.

In addition to force generation, the beating pattern of all cell lines was analyzed by video-optical recordings. Figure 37 B shows the spontaneous beating frequencies of all five cell lines during the plateau phase and at the end of the culture period. All genetically modified cell lines and the control cell line ERC018 showed spontaneous frequencies between 70 and 80 bpm at the beginning of the plateau phase and did not differ significantly from each other. In contrast, the trisomy control EHTs beat at a significantly higher rate than the other four cell lines with a spontaneous frequency of approximately 135 bpm. During the course of culture, all EHTs showed a decline in frequency. However, this decline was more pronounced in the knockout lines, resulting in significantly lower beating frequencies of all three knockout lines compared to ERC018 at the end of culture. Although the beating frequency of the trisomy control EHTs did also steadily decrease over time, it was still significantly higher than the other four cell lines at the end of the experiments.

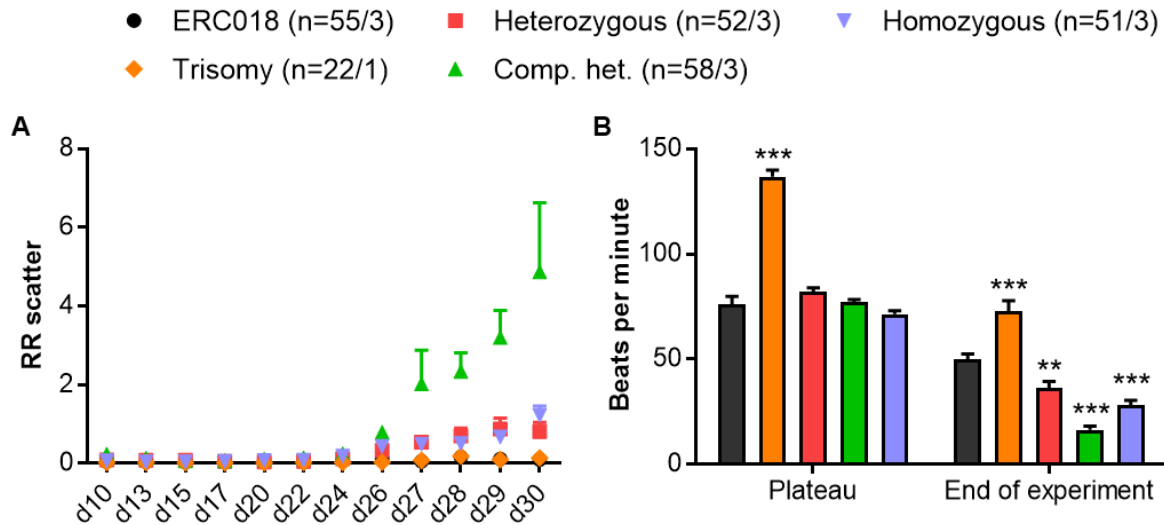


**Figure 37: Contractility analysis of spontaneous EHT activity.** (A) RR scatter over time. The RR scatter is calculated as the interdecile range of average beat-to-beat variation and therefore represents an estimate of beating irregularities. While both the ERC018 and the trisomy control EHTs displayed stable RR scatter values over time, all three CRISPR lines developed beating irregularities over time, represented by an increase in RR scatter. (B) Displayed are the spontaneous beating frequencies of all five cell lines during the plateau phase and at the end of the experiments. 2way ANOVA plus Bonferroni's post-test for multiple comparisons. \*\* $p < 0.01$ , \*\*\* $p < 0.001$  vs. ERC018.

Since contraction and relaxation kinetics are closely linked to the beating frequency, these parameters are difficult to compare under spontaneous contraction conditions. In order to provide more comparable values, EHTs from all groups were measured under electrical stimulation at a frequency of 2 Hz. Normalized average contraction peaks of all five cell lines, matched at the peak, clearly differed in the downstroke of the contraction peaks (figure 38 A). Force of the complete knockout cell lines returned to baseline fastest, followed by the heterozygous EHTs and the trisomy control line. ERC018 displayed the slowest downstroke velocity. When looking at the relaxation time (RT (80%)), which is the time needed for relaxation from peak to 20% above baseline, there were significant differences between ERC018 and the three knockouts, but also between ERC018 and the trisomy control line (figure 38 B). Importantly, the trisomy control line was also significantly slower than the complete knockouts but was similar to the heterozygous clone.

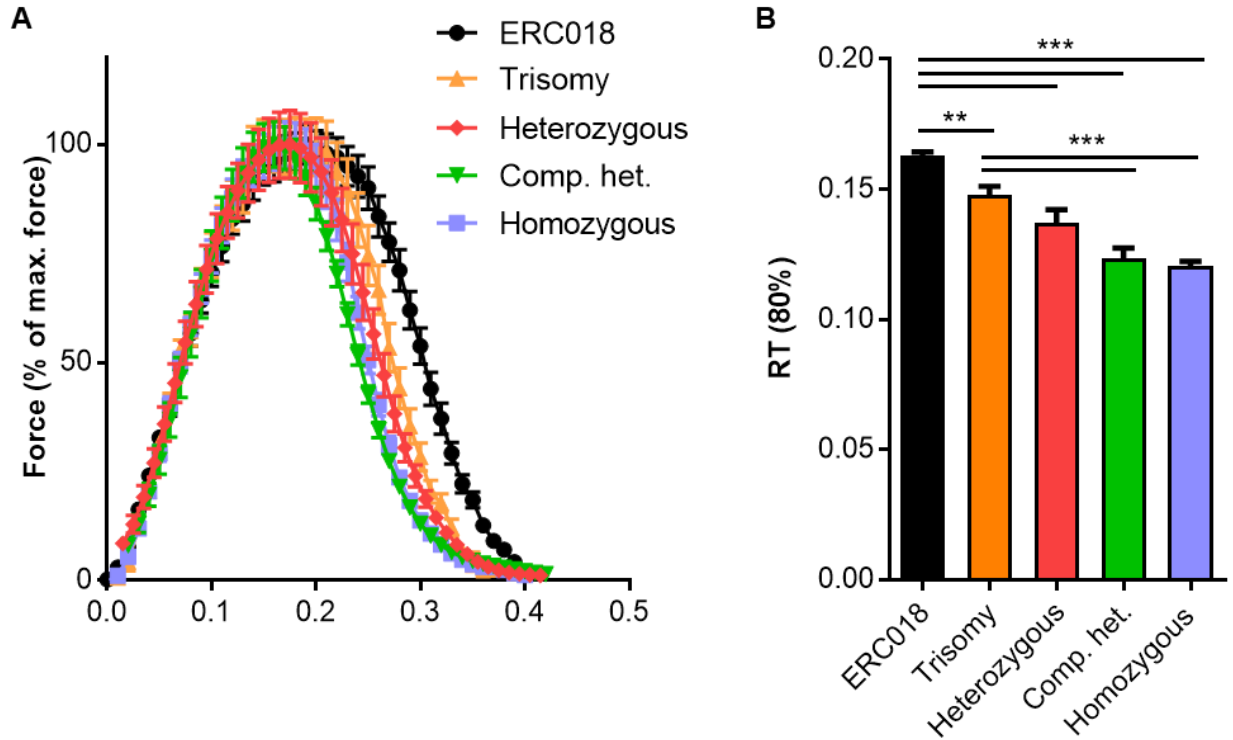


**Figure 38: Contraction kinetics of EHT under electrical stimulation at 2 Hz.** (A) Normalized average EHT contraction peaks of all five cell lines in 1.8 mM calcium Tyrode's solution. (B) Relaxation time of all five cell lines from peak to 20% above baseline at 2 Hz.  $n=7-12$  EHTs per group, 1way ANOVA plus Bonferroni's post-test for multiple comparisons. \*\* $p<0.01$ , \*\*\* $p<0.001$ .

#### 4.5.2 Baseline characterization of EHT function

The cell lines were further characterized in EHT with regard to their calcium handling and force-frequency properties. As a first step, the  $EC_{50}$  values for calcium were compared in a calcium concentration-response curve. In the first experiment, the three CRISPR lines were compared to ERC018, but no significant difference was observed regarding the  $EC_{50}$ . All cell lines reached half-maximal force at approximately 0.85 - 0.89 mM calcium (figure 39 A). In the second experiment, ERC018 control EHTs and trisomy control EHTs were compared. In this batch, both cell lines reacted unusually strong to calcium wash-out with loss of contractility. The EHTs recovered after they were placed in higher calcium concentrations, but the results of the calcium concentration-response curve were influenced considerably. The problems during the procedure led to a higher  $EC_{50}$  compared to the first experiment (1.19-1.37 mM calcium), but nonetheless no significant differences between ERC018 and the trisomy control could be detected (figure 39 B).



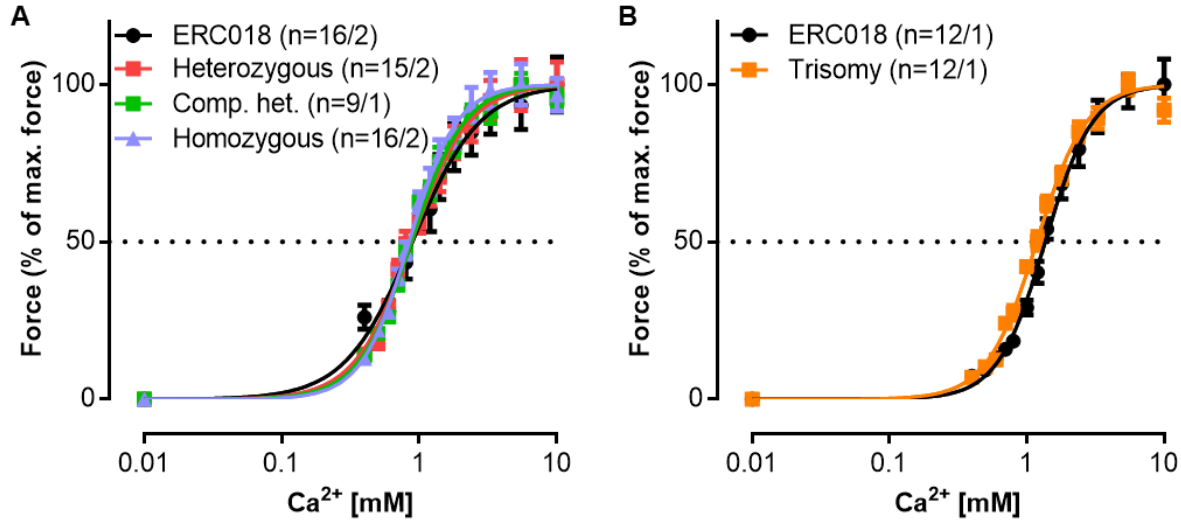


**Figure 39: Calcium concentration-response curves.** (A) Calcium concentration-response curve of ERC018 and the three knockout cell lines. Calculation of the  $EC_{50}$  yielded no significant differences between the four cell lines: ERC018 0.89 mM, heterozygous 0.88 mM, compound heterozygous 0.88 mM, homozygous 0.85 mM. (B) Concentration-response curve of ERC018 and the trisomy control cell line. Calculation of the  $EC_{50}$  for calcium yielded 1.37 mM for ERC018 and 1.19 for the trisomy control. 2way ANOVA plus Tukey's post-test for multiple comparisons, no significant differences.

After no significant difference in the sensitivity to acute changes in medium calcium concentration could be detected, the EHTs were compared with respect to their ability to handle high calcium concentrations over longer periods of time. In overnight measurements, EHTs were subjected to calcium concentrations of 3 mM and contractility was measured once every hour over a period of 10 hours, in order to analyze whether the calcium overload induced beating irregularities. EHTs in 1.8 mM calcium were measured in parallel as a control. All cell lines displayed a small degree of beating irregularities at both 1.8 mM and 3 mM calcium, with no significant differences between the two concentrations among each EHT line (figure 40). Knockout of DNMT3A did not result in higher RR scatter at both concentrations compared to both control groups.

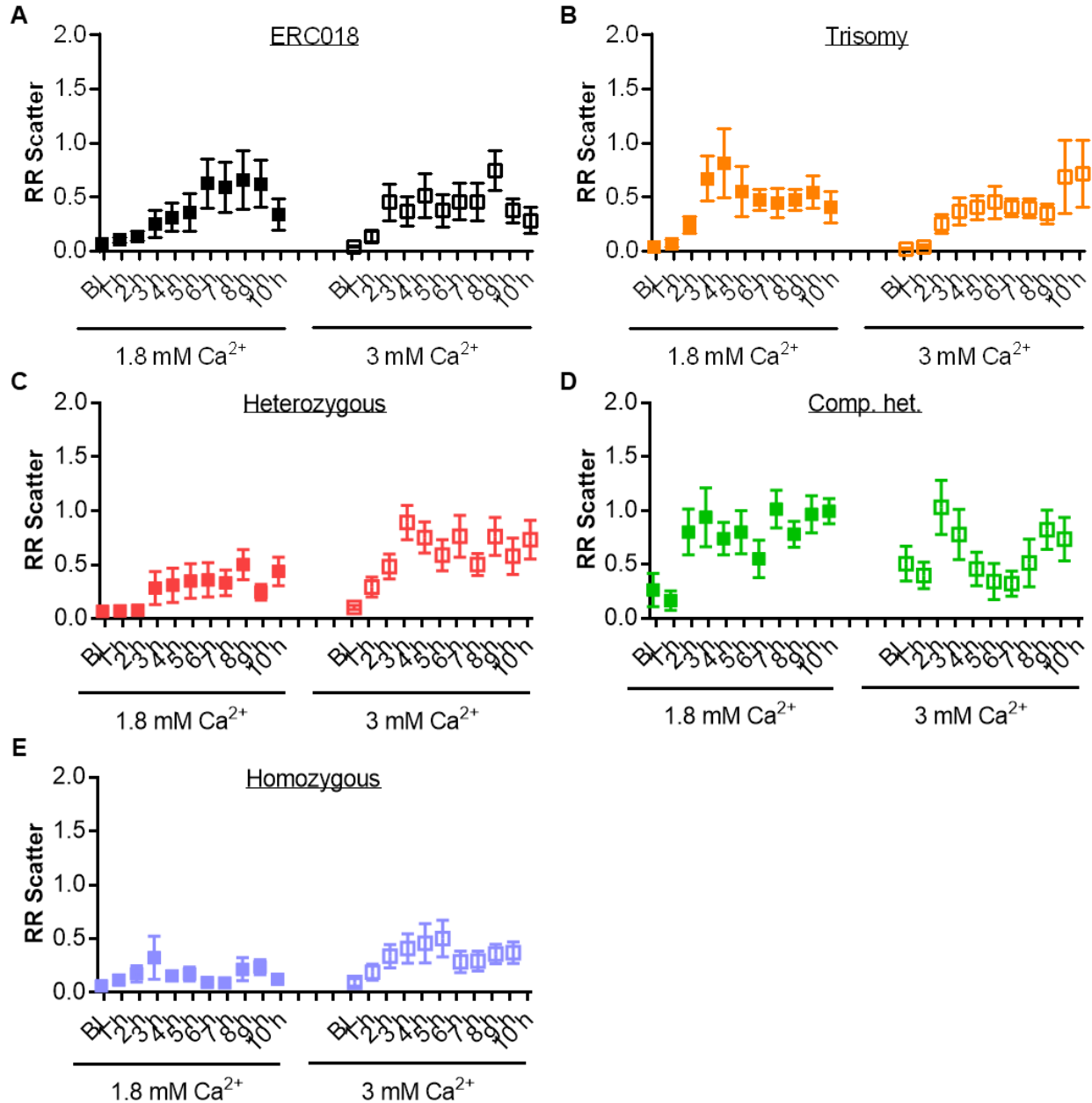


**Figure 40: Long-term exposure to high calcium.** RR scatter of EHTs from ERC018 (A), the trisomy control (B), as well as the heterozygous (C), compound heterozygous (D), and homozygous CRISPR clone (E) over time in the presence of 1.8 and 3 mM calcium.  $n=7-10$  EHTs from 2 batches per group, 2way ANOVA plus Bonferroni's post-test for multiple comparisons. No significant differences between the two concentrations or different cell lines were observed.

The ability to react to electrical stimulation is another important and variable feature of EHT. Different cell lines can differ regarding both the threshold frequency up to which the EHT can still follow the stimulation, as well as the relationship between force and frequency. In order to analyze the effect of DNMT3A knockout on pacing capture, EHTs were paced at a submaximal calcium concentration of 0.8 mM with increasing frequencies from 0.7 to 7 Hz and their ability to follow the stimulation signal was evaluated. Figure 41 shows the measured EHT beating frequency plotted against the stimulation frequency. ERC018 EHTs started to lose capture of the pacing pulses above 3 Hz and starting from around 5 Hz more than half of the EHTs were no longer following the stimulation (figure 41 A). The DNMT3A knockout EHTs were able to follow the pacing pulses up to higher frequencies and first loss of capture was only detected at frequencies higher than 6 Hz (figure 41 B - D).

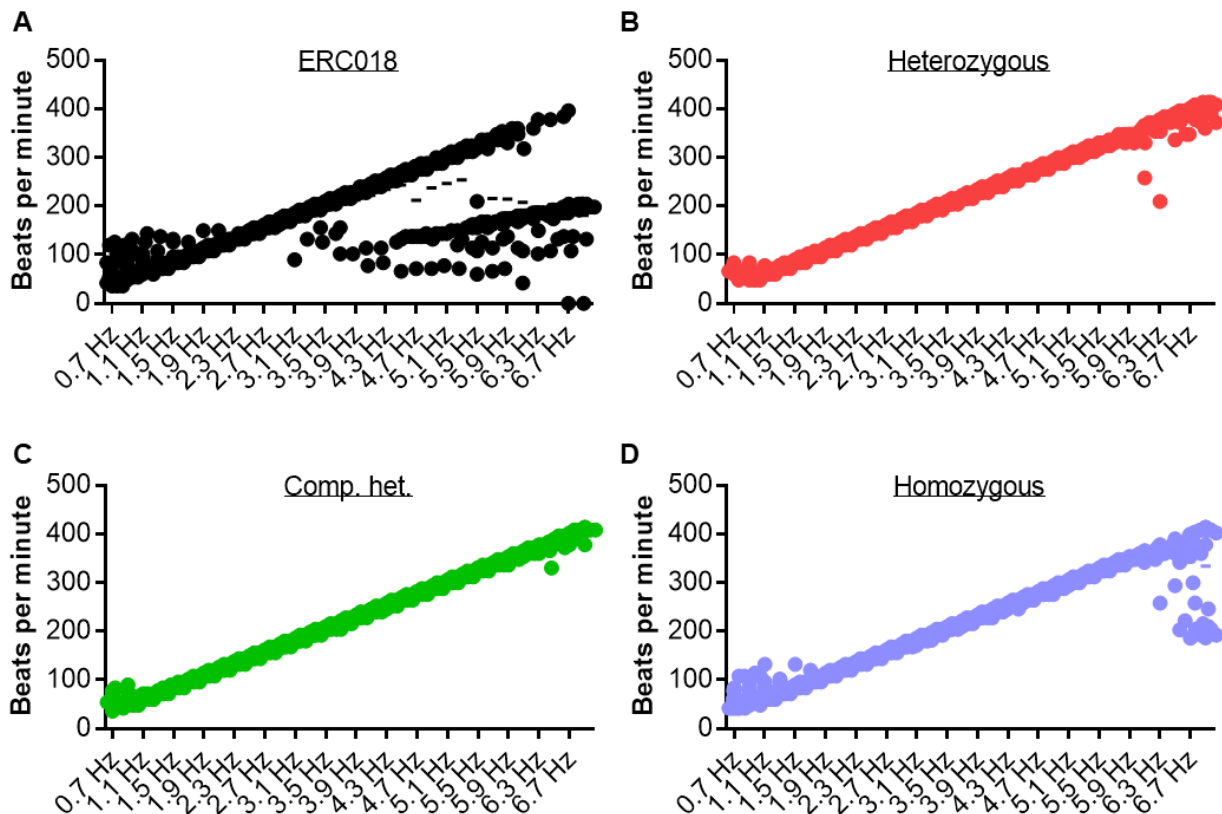


**Figure 41: Pacing capture in 0.8 mM calcium.** The pacing capture of EHTs from ERC018 (A), the heterozygous knockout (B), the compound heterozygous knockout (C), as well as the homozygous knockout (D) was analyzed from 0.7 to 7 Hz with 0.2 Hz increments between measurements. Each dot represents a single EHT, n=15-20 EHTs per group.

In a second experiment, ERC018 and the homozygous knockout EHTs were compared to the trisomy control EHTs (figure 42). Since the ERC018 and trisomy control EHTs again reacted unusually strong to calcium wash-out with loss of contractility, pacing capture for ERC018, the trisomy control, and the homozygous knockout could not be analyzed in 0.8 mM calcium and was instead measured in 1.8 mM calcium. The ERC018 and trisomy control lines started to lose capture at 4.3 and 5.1 Hz, respectively and were no longer able to follow pacing altogether at frequencies higher than 5.5 Hz. In contrast to that all homozygous knockout EHTs were still able to follow the pacing pulses at 6 Hz.

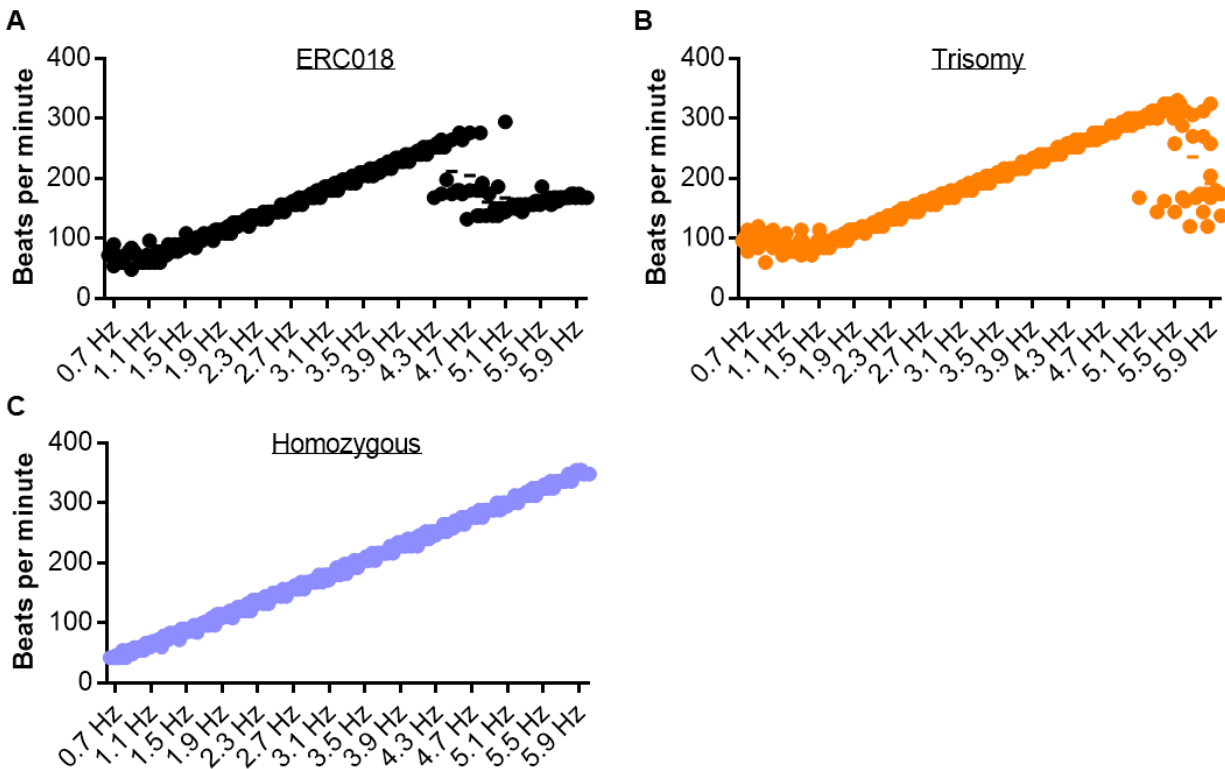


**Figure 42: Pacing capture in 1.8 mM calcium.** The pacing capture of ERC018 (A), the trisomy control (B), and the homozygous knockout (C) was analyzed from 0.7 to 6 Hz with 0.2 Hz increments between measurements. Each dot represents a single EHT, n=8-10 EHTs per group.

For analysis of the force-frequency relationship (FFR), only EHTs that had been able to follow the pacing pulses at the according frequency in 0.8 mM calcium were taken into account. Measurements in 1.8 mM calcium were not analyzed, since the higher calcium doesn't leave enough room for force increments to detect a positive FFR, due to the already high initial force. The four analyzed cell lines showed an initially positive FFR, followed by a short plateau phase

and a conversion to a negative FFR (figure 43). ERC018 displayed a significantly steeper decline in force after the plateau phase than the compound heterozygous and homozygous knockout.

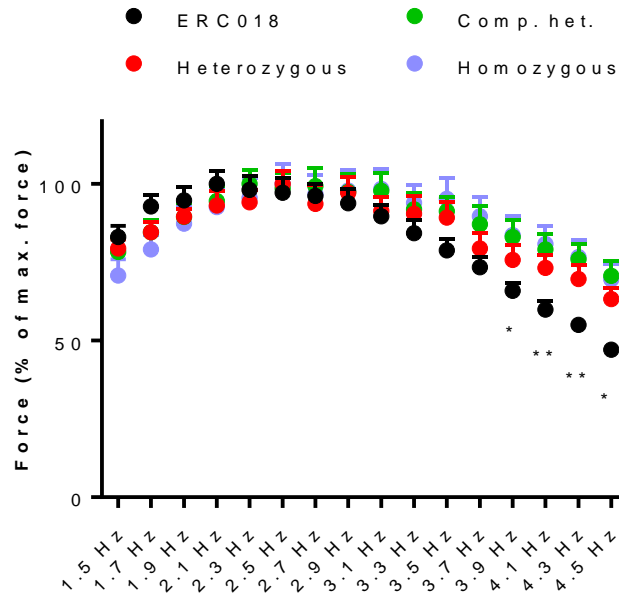


**Figure 43: Force-frequency relationship.** Normalized force generation over stimulation frequency of ERC018, the heterozygous, compound heterozygous, and homozygous knockout. Reduction in force at higher frequencies (3.9 – 4.5 Hz) was significantly more pronounced in ERC018 than in the compound heterozygous and homozygous knockouts.  $n=15-20$  EHTs per group, 2way ANOVA plus Tukey's post-test for multiple comparisons,  $*p<0.05$ ,  $**p<0.01$ .

Not only force generation, but also contraction and relaxation kinetics are highly dependent on beating frequency. All five cell lines showed the expected frequency-dependent acceleration of contraction and relaxation. The contraction time TTP (-80%) - the time from a force of 20% above baseline to peak force - of all CRISPR lines was significantly lower than in ERC018 EHT (heterozygous  $p<0.05$ , compound heterozygous and homozygous  $p<0.001$ ) at the beginning (1.7 Hz). The trisomy control did only display significant differences to the compound heterozygous and homozygous cell lines ( $p<0.05$ ) but not to ERC018 or heterozygous EHTs (figure 44 A). Frequency-dependent shortening of the contraction time led to equalization of the values of all five cell lines at around 4.5 Hz. Differences between the cell lines were even more pronounced with regard to relaxation time (figure 44 B). ERC018 displayed significantly slower relaxation than all

other cell lines ( $p < 0.001$ ) at 1.7 Hz, while the trisomy control was similar to the heterozygous knockout. Here again, the frequency-dependent acceleration of relaxation led to an equalization of the relaxation times of all five cell lines at frequencies above 4 Hz.

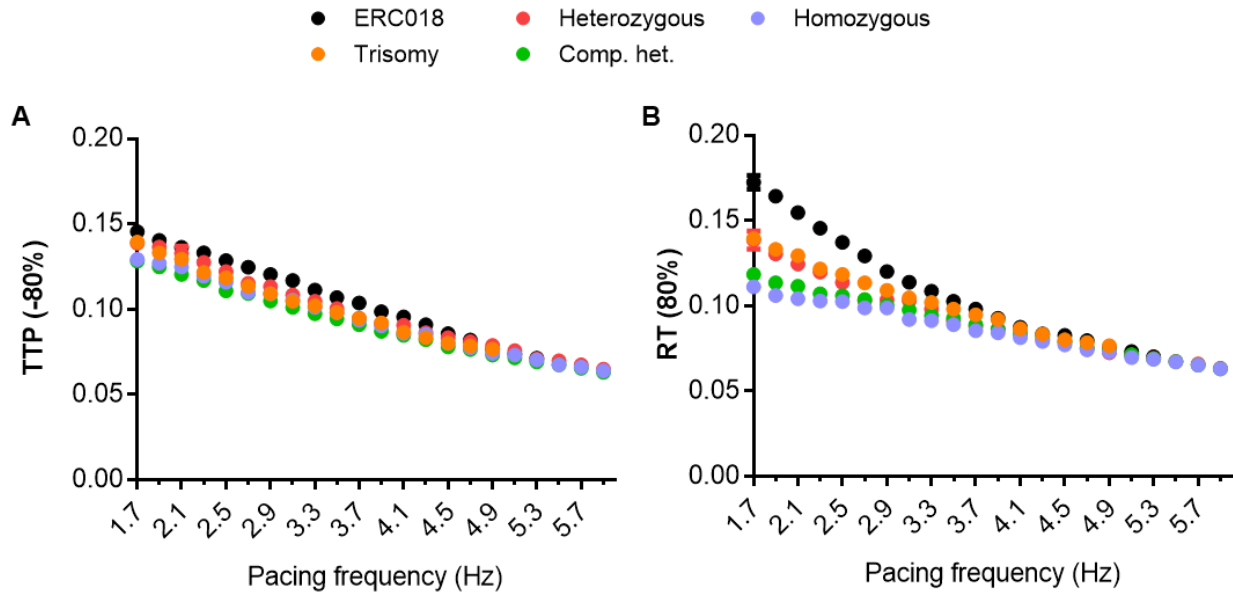


**Figure 44: Frequency-dependency of contraction and relaxation times.** Displayed are (A) the contraction time TTP (-80%) and (B) the relaxation times RT (80%) of the five cell lines at increasing stimulation frequencies.  $n=15-20$  EHTs per group, 2way ANOVA plus Bonferroni's post-test for multiple comparisons.

#### 4.5.3 Action potentials

The shorter contraction kinetics in the knockouts prompted the idea that the action potential might also be affected by knockout of DNMT3A. Accordingly, action potentials were recorded from ERC018 and compound heterozygous knockout EHTs by sharp electrode measurements by Julia Krause (University Heart Center, UKE, Hamburg, Germany). The shape of the action potential differed significantly between the two groups (figure 45 A + B). The knockouts reached a significantly lower action potential amplitude but had a significantly higher maximal upstroke velocity (figure 45 C + D). Moreover, after the upstroke, compound heterozygous EHTs displayed a depolarizing notch in their action potential after which they returned significantly faster to their resting membrane potential compared to control (figure 45 B). In accordance with this, the action potential duration to 90% repolarization was significantly shorter in knockout EHTs than ERC018 (APD 90, figure 45 E).

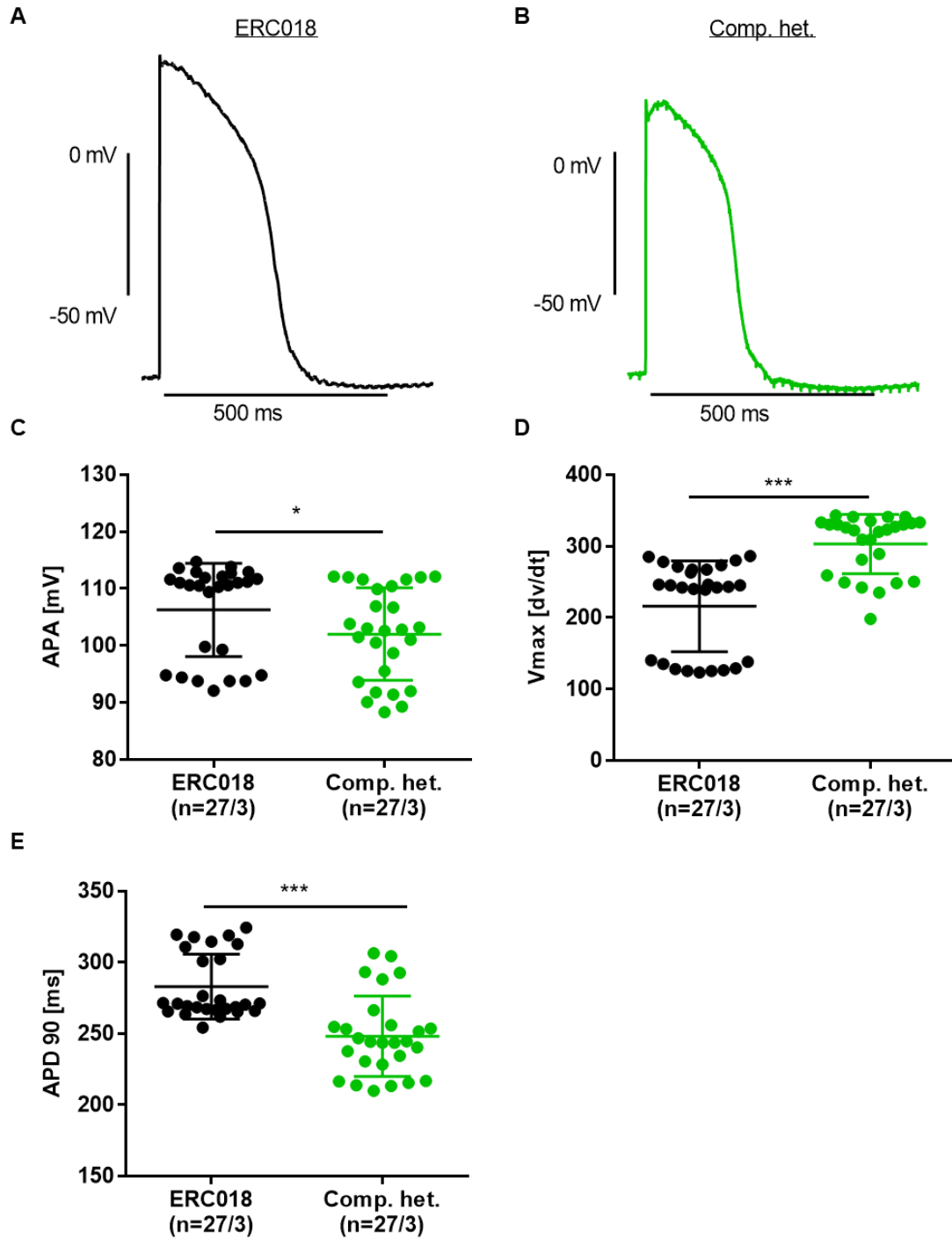


**Figure 45: Sharp electrode measurement of action potentials.** Representative examples of single action potential plots for (A) ERC018 and (B) compound heterozygous knockout. The values for (C) action potential amplitude, (D) maximal upstroke velocity, and (E) action potential duration to 90% repolarization (APD 90) were calculated for both EHT lines. n=27 impalements from 3 EHTs, Mann-Whitney test, \*p<0.05, \*\*\*p<0.001.

#### 4.5.4 Hypertrophic intervention

Previous experiments with DNMT inhibitors in models of cardiac hypertrophy have suggested an involvement of DNA methylation in this pathology. However, since DNMT isoform-specific inhibitors are lacking, it is currently not clear which isoform is involved in the process. To evaluate whether DNMT3A is important for the development of *in vitro* hypertrophy, the DNMT3A knockout lines, as well as the two control lines were treated with the pro-hypertrophic compounds phenylephrine (PE) and endothelin-1 (ET-1) under serum-free conditions and regularly analyzed by video-optical recording for a week. The treatment showed a positive chronotropic effect on all cell lines, increasing the EHTs' beating frequency significantly at all time points (figure 46 A – E).

One important hallmark of pathological cardiac hypertrophy is the resulting reduction of contractility of the heart. In line with this, the treatment of ERC018 and the trisomy control line with PE and ET-1 led to significantly lower force generation (figure 47 A + E). In contrast to this, treated knockout EHTs did not show a decrease in force, but rather steadily increased force generation over time (figure 47 B – D), similar to what was observed in untreated control ERC018. The heterozygous EHTs reached significantly higher forces under treatment than their untreated counterparts starting on day 6. For the two full knockout lines, the difference in force was already significant at day 3 of treatment and became steadily more pronounced during the course of the experiment.



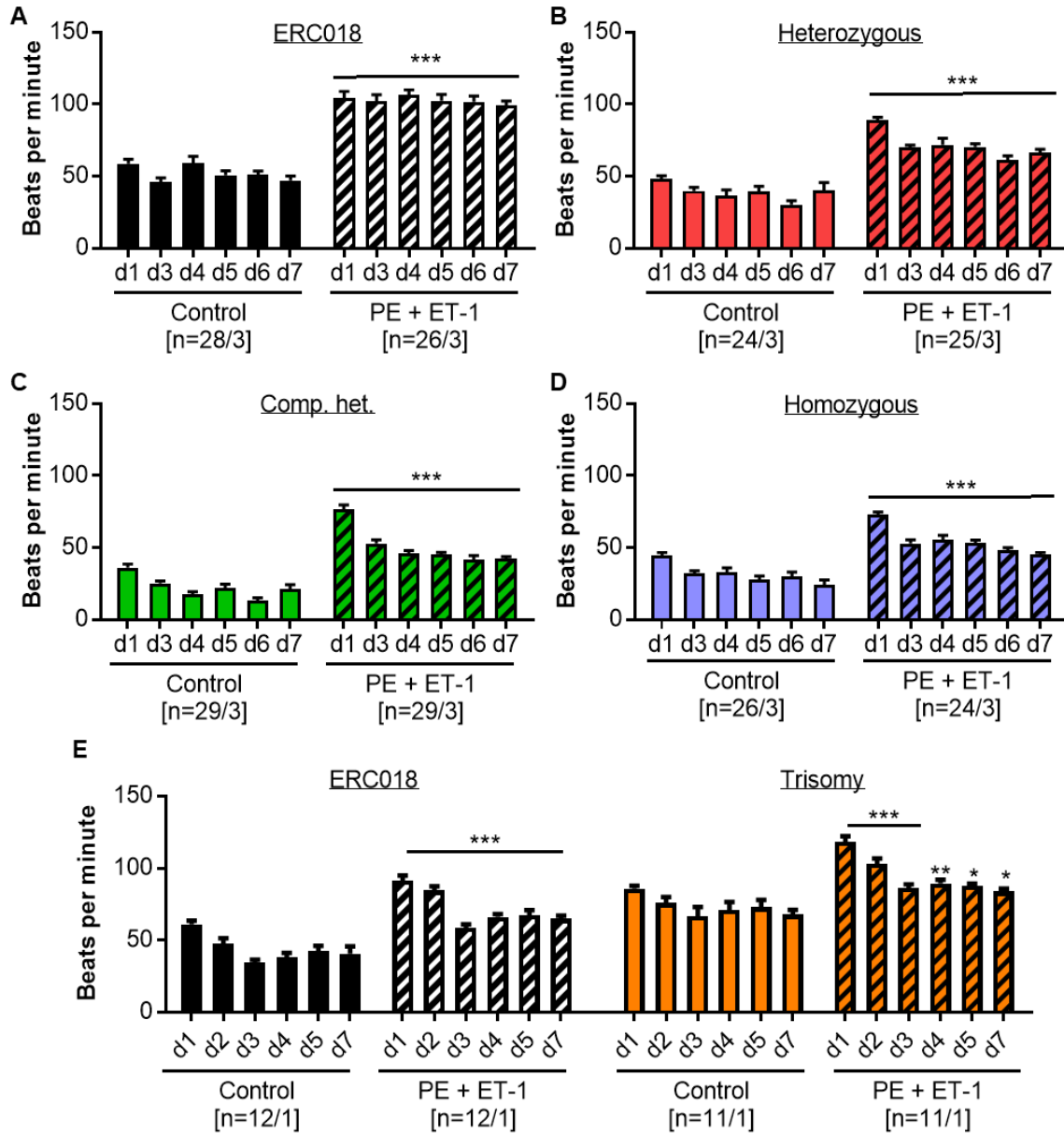


**Figure 46: Effect of PE and ET-1 on spontaneous beating frequency.** Treatment with PE and ET-1 significantly increased the beating frequency of ERC018 (A), heterozygous (B), compound heterozygous (C), homozygous (D), and trisomy control EHTs (E) at all time points compared to the respective control. (E) Comparison of ERC018 and trisomy control cell line measured in parallel. D1-d7 indicates the number of days since switch to serum-free medium and treatment begin. 2way ANOVA plus Bonferroni's post-test for multiple comparisons vs. control. \* $p < 0.05$ , \*\* $p < 0.01$ , \*\*\* $p < 0.001$ .

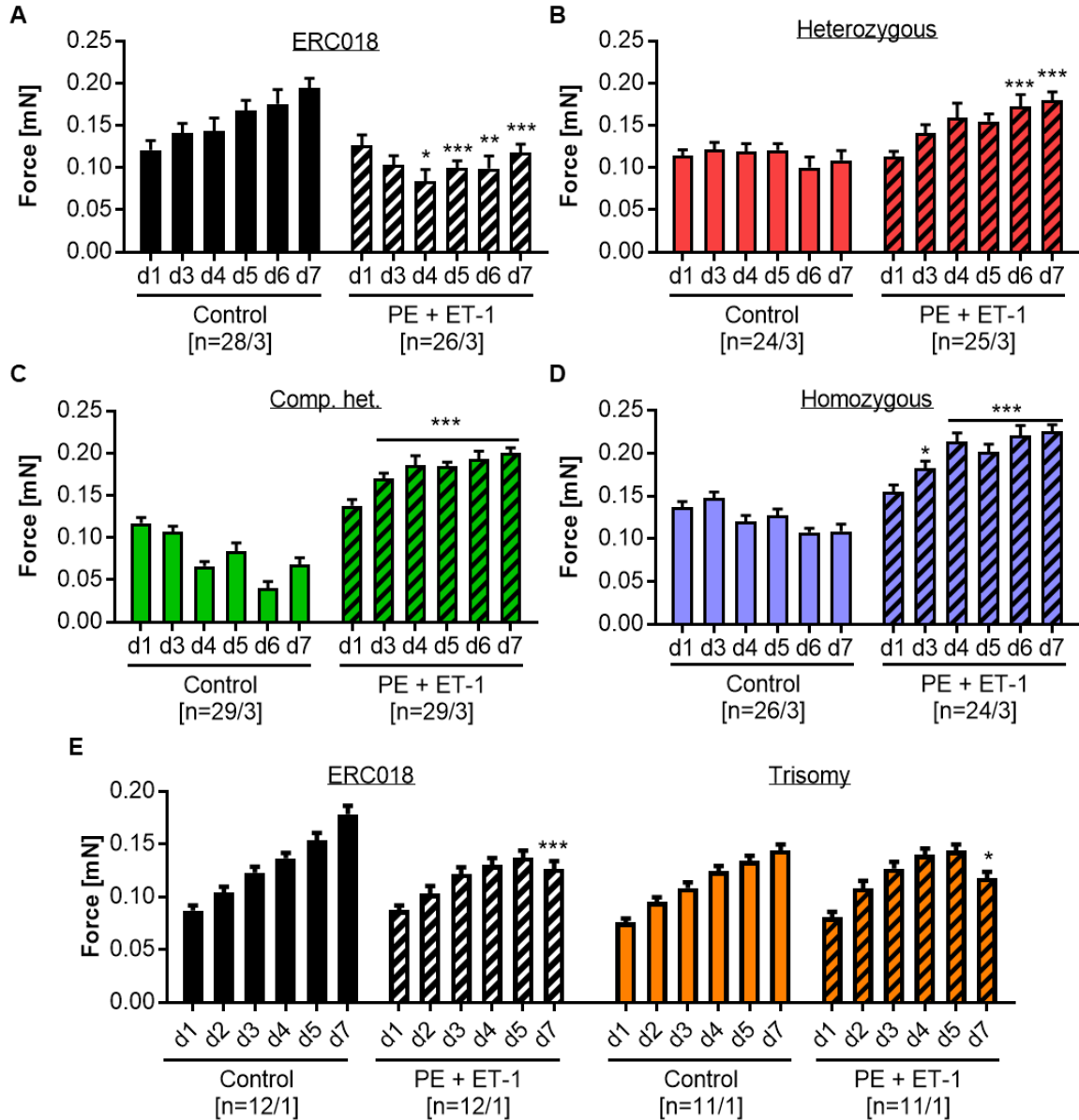


**Figure 47: Effect of PE and ET-1 on EHT force generation.** Treatment of ERC018 (A) and the trisomy control line (E) led to a significant reduction in force compared to controls, whereas knockout EHTs (B – D) generated higher forces under treatment than untreated controls. (E) Comparison of ERC018 and trisomy control cell line measured in parallel. D1-d7 indicates the number of days since switch to serum-free medium and treatment begin. 2way ANOVA plus Bonferroni's post-test for multiple comparisons vs. control. \* $p < 0.05$ , \*\* $p < 0.01$ , \*\*\* $p < 0.001$ .

Treatment with the pro-hypertrophic substances also had an effect on the contraction and relaxation kinetics of EHTs. All EHT lines showed an initial increase in contraction velocity under treatment (figure 48). However, at the end of treatment, contraction velocity of the trisomy control line was no longer significantly different from treated EHTs and untreated controls and the contraction velocity of treated ERC018 EHTs was even significantly lower than in control EHTs (figure 48 A + E). In contrast to that, the contraction velocity of all three CRISPR lines steadily increased over time under treatment and was still significantly higher at the end of the experiment (figure 48 B – D). A similar effect was observed on relaxation kinetics. While prolonged treatment with PE and ET-1 led to significantly lower or unchanged relaxation kinetics in ERC018 and the trisomy control, respectively (figure 49 A + E), the relaxation velocity of all knockout lines was significantly increased under treatment compared to controls (figure 49 B – D). Moreover, the relaxation velocity of both control lines steadily increased under control conditions, while it remained unchanged in heterozygous EHTs and even decreased in the other knockouts.

Pro-hypertrophic treatment did not influence the beating regularity of ERC018 and trisomy control EHTs. Both cell lines displayed a consistently low RR scatter under control and treatment conditions at all time points, indicating the absence of beating irregularities (figure 50 A + E). In contrast to that, treatment of knockout EHTs with PE and ET-1 significantly reduced the occurrence of the described beating irregularities over time (figure 50 B – D). Under treatment the RR scatter of the knockout lines was no longer significantly different from the two control lines.

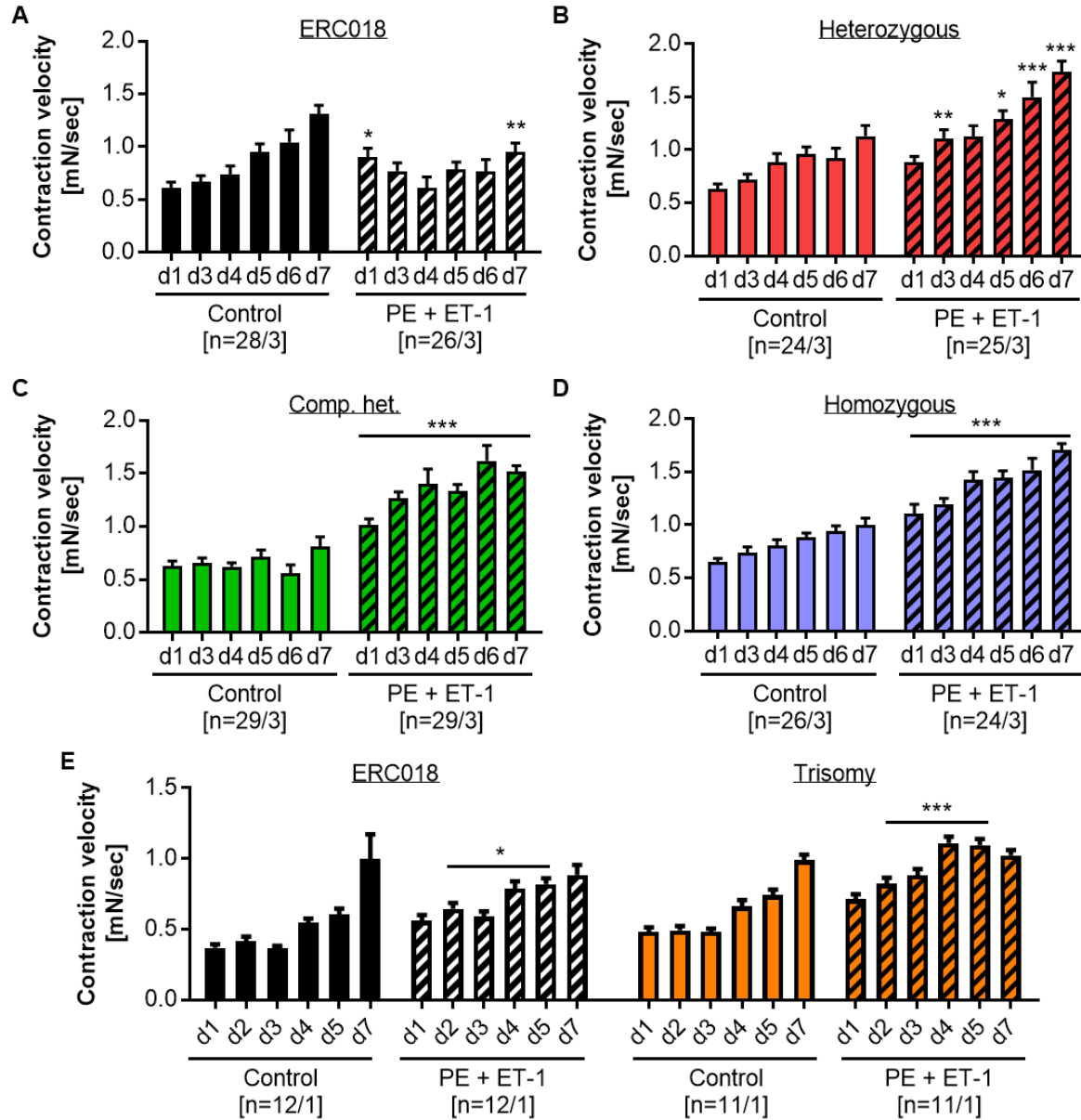


**Figure 48: Effect of PE and ET-1 on contraction kinetics.** Displayed is the contraction velocity of ERC018 (A), heterozygous (B), compound heterozygous (C), homozygous (D), and trisomy control EHTs (E) under both control and treatment conditions. (E) Comparison of ERC018 and trisomy control cell line measured in parallel. D1-d7 indicates the number of days since switch to serum-free medium and treatment begin. 2way ANOVA plus Bonferroni's post-test for multiple comparisons vs. control. \* $p < 0.05$ , \*\* $p < 0.01$ , \*\*\* $p < 0.001$ .

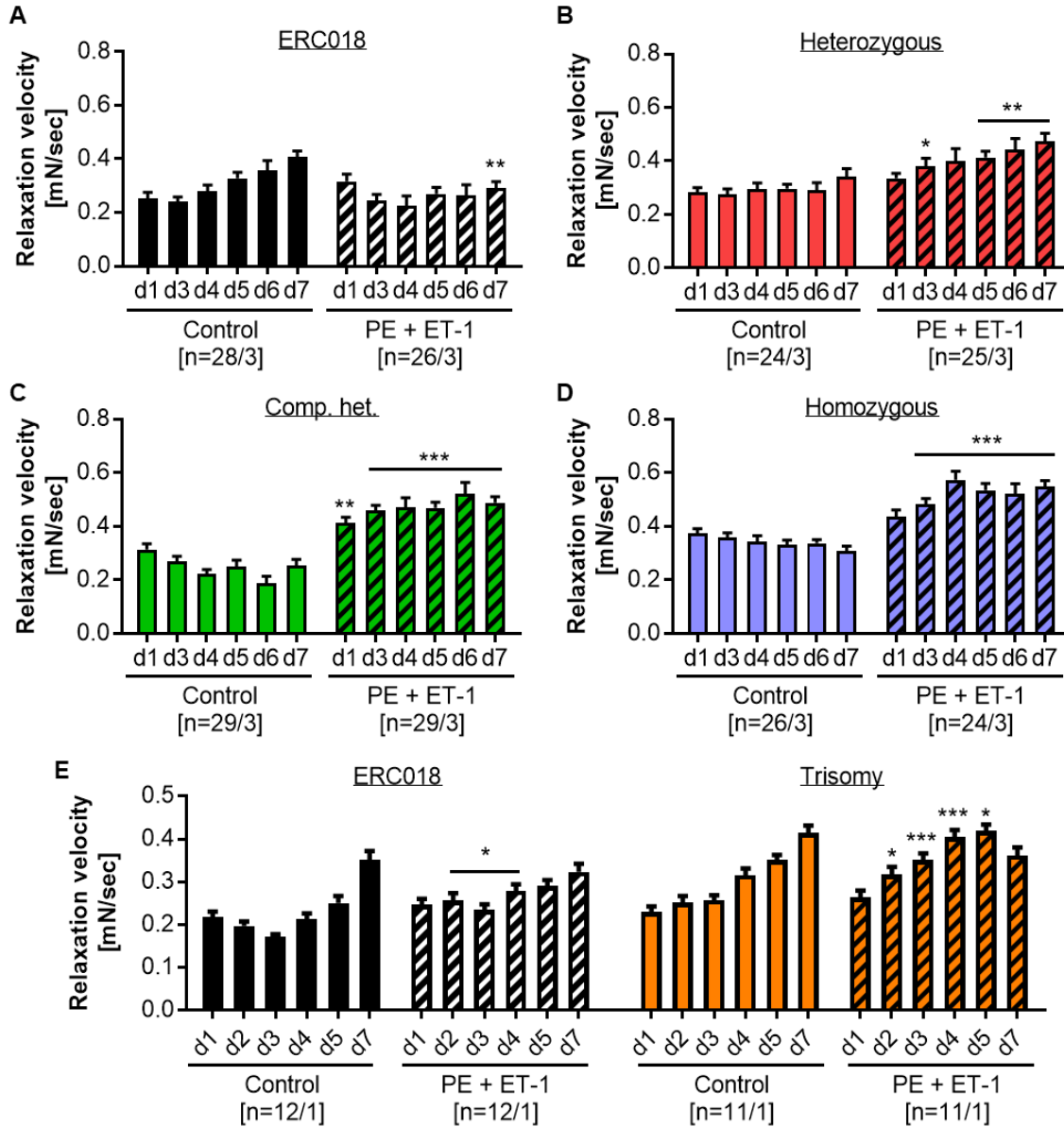


**Figure 49: Effect of PE and ET-1 on relaxation kinetics.** Displayed is the relaxation velocity of ERC018 (A), heterozygous (B), compound heterozygous (C), homozygous (D), and trisomy control EHTs (E) under both control and treatment conditions. (E) Comparison of ERC018 and trisomy control cell line measured in parallel. D1-d7 indicates the number of days since switch to serum-free medium and treatment begin. 2way ANOVA plus Bonferroni's post- test for multiple comparisons vs. control. \* $p < 0.05$ , \*\* $p < 0.01$ , \*\*\* $p < 0.001$ .

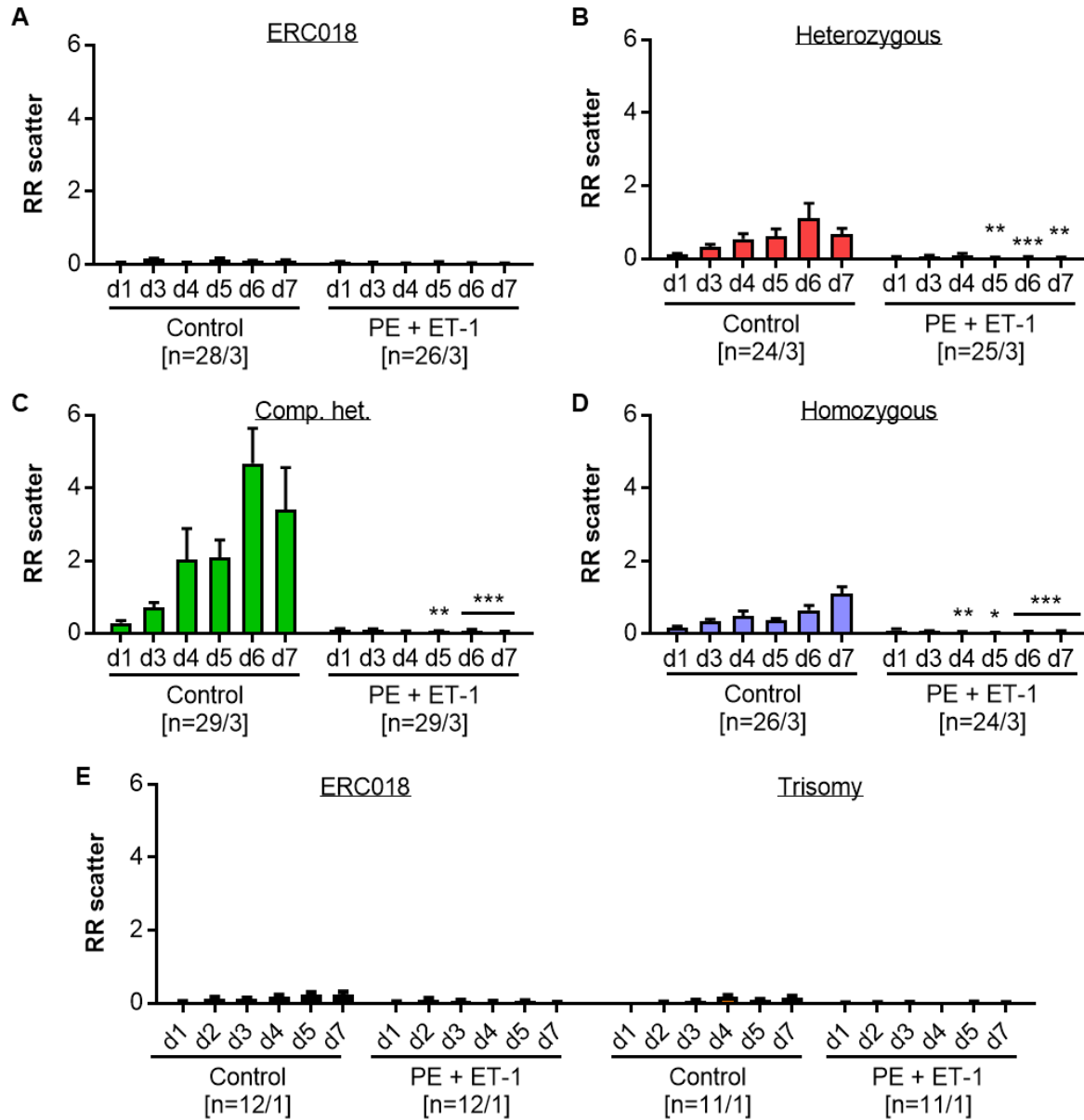


**Figure 50: Effect of PE and ET-1 on beating regularity.** The RR scatter as a surrogate parameter for the occurrence of beating irregularities is displayed ERC018 (A), heterozygous (B), compound heterozygous (C), homozygous (D), and trisomy control EHTs (E) under both control and treatment conditions. (E) Comparison of ERC018 and trisomy control cell line measured in parallel. D1-d7 indicates the number of days since switch to serum-free medium and treatment begin. 2way ANOVA plus Bonferroni's post-test for multiple comparisons vs. control. \*p<0.05, \*\*p<0.01, \*\*\*p<0.001.

Taken together, there were only minor effects of DNMT3A knockout on the development of EHT. The most important differences to the control lines were a decline in force and beating activity at the end of culture accompanied by irregular beating patterns. Moreover, significantly faster relaxation kinetics were observed in the knockouts than in both controls, which were more pronounced in full knockouts compared to the heterozygous knockout. Additionally, knockouts displayed better pacing capture at high frequencies than controls, whereas no differences in calcium handling were observed. Treatment with PE and ET-1 yielded opposing results in the different groups with decreased contractility in the two control cell lines and increased contractility after knockout.

## 4.6 Molecular analysis

### 4.6.1 Histology

In order to investigate the mechanisms underlying the phenotypical differences of the DNMT3A knockout lines, EHTs were first analyzed histologically. The basic EHT morphology was visualized by H&E staining (figure 51). Both control cell lines revealed a longitudinally aligned layer of cells close to the EHT surface with no obvious differences between control and treatment conditions. In contrast to this, all three knockouts showed a substantially disrupted cell layer with distinct vacuolic structures under control conditions. Interestingly, these vacuoles were almost absent after PE and ET-1 treatment, which apparently partially restored the aligned cell layer. The cardiomyocyte structure was analyzed in more detail by additional staining for the muscle filament protein MLC2v (figure 52). As expected, the two control lines, both with and without treatment, revealed a continuous layer of MLC2v-positive cells with muscle filaments longitudinally aligned along the force lines of the EHT. However, in the knockouts the staining was located along the edges of the vacuolic structures leading to disruption of the continuous filament alignment. Treatment with the pro-hypertrophic reagents reduced the vacuolic location of MLC2v reestablishing longitudinal filament alignment to some extent. Similar results were obtained from immunohistochemical staining of the gap junction protein connexin 43 (figure 53). The dotted staining pattern visible in ERC018 EHTs around all cells was reduced in the knockouts under control conditions and localized around the vacuoles. In contrast, treatment with PE and ET-1 increased the signal abundance which was then localized around the cells in a denser cell layer. Additional stainings for the apoptosis marker caspase 3, the proliferation marker Ki-67, and type I collagen did not show significant differences between both the different genotypes and the treatment conditions (supplementary figures S2 – S4).



Moreover, the EHT sections were stained for the hypertrophy marker ANP to analyze whether treatment with PE and ET-1 had the predicted effect on the tissue, i.e. increasing ANP abundance (figure 54). Under control conditions, only single cells were stained positive for ANP with no obvious differences between the genotypes. Hypertrophic treatment however, significantly increased the number of positive cells in all genotypes.

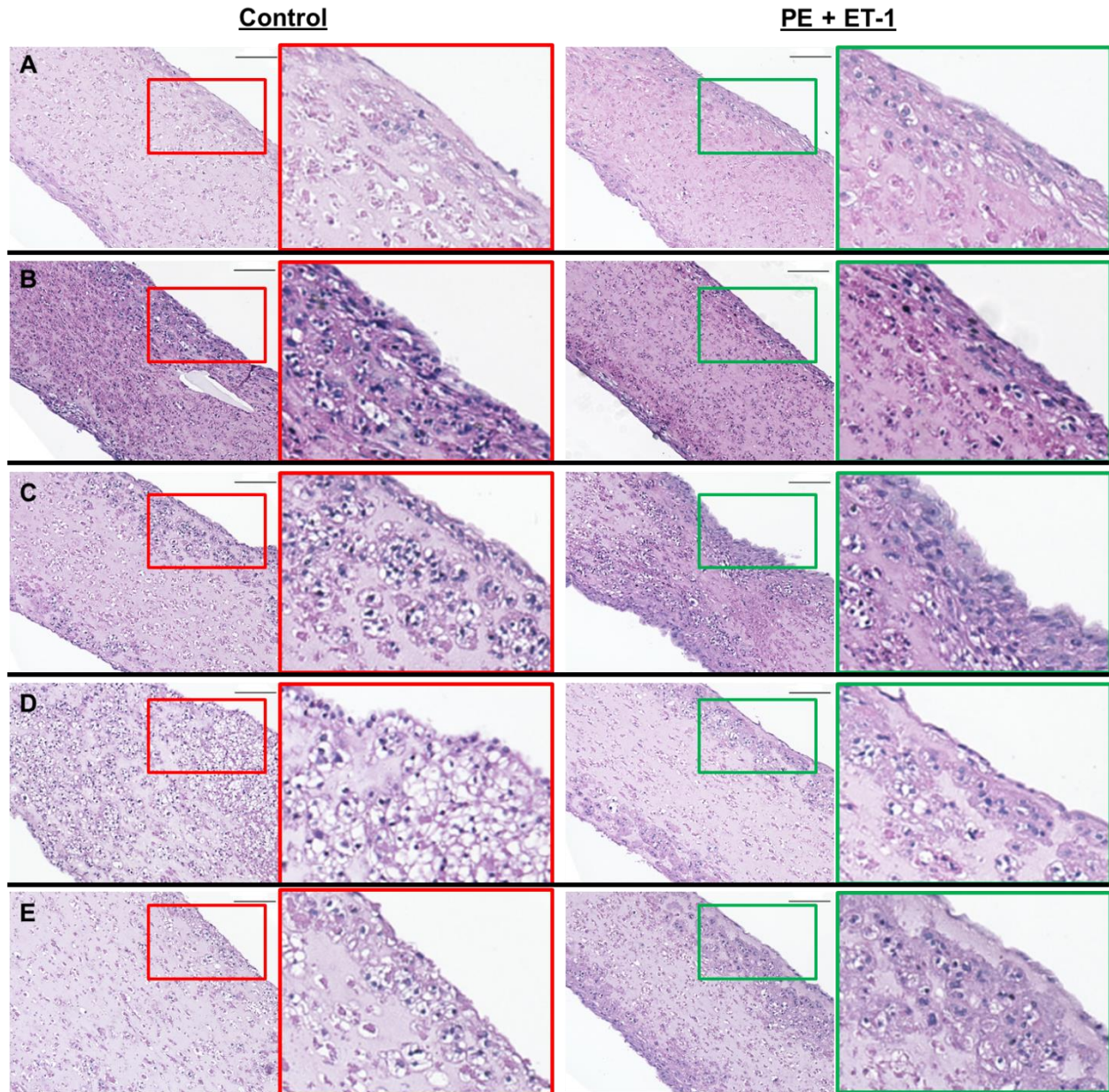


**Figure 51: H&E staining.** EHT paraffin sections of control EHTs (left columns) and PE + ET-1-treated EHTs (right columns) after H&E staining. (A) ERC018, (B) Trisomy control, (C) heterozygous, (D) compound heterozygous, (E) homozygous. The red and green boxes show a zoom-in of the indicated areas. Scale bar = 100  $\mu$ m.



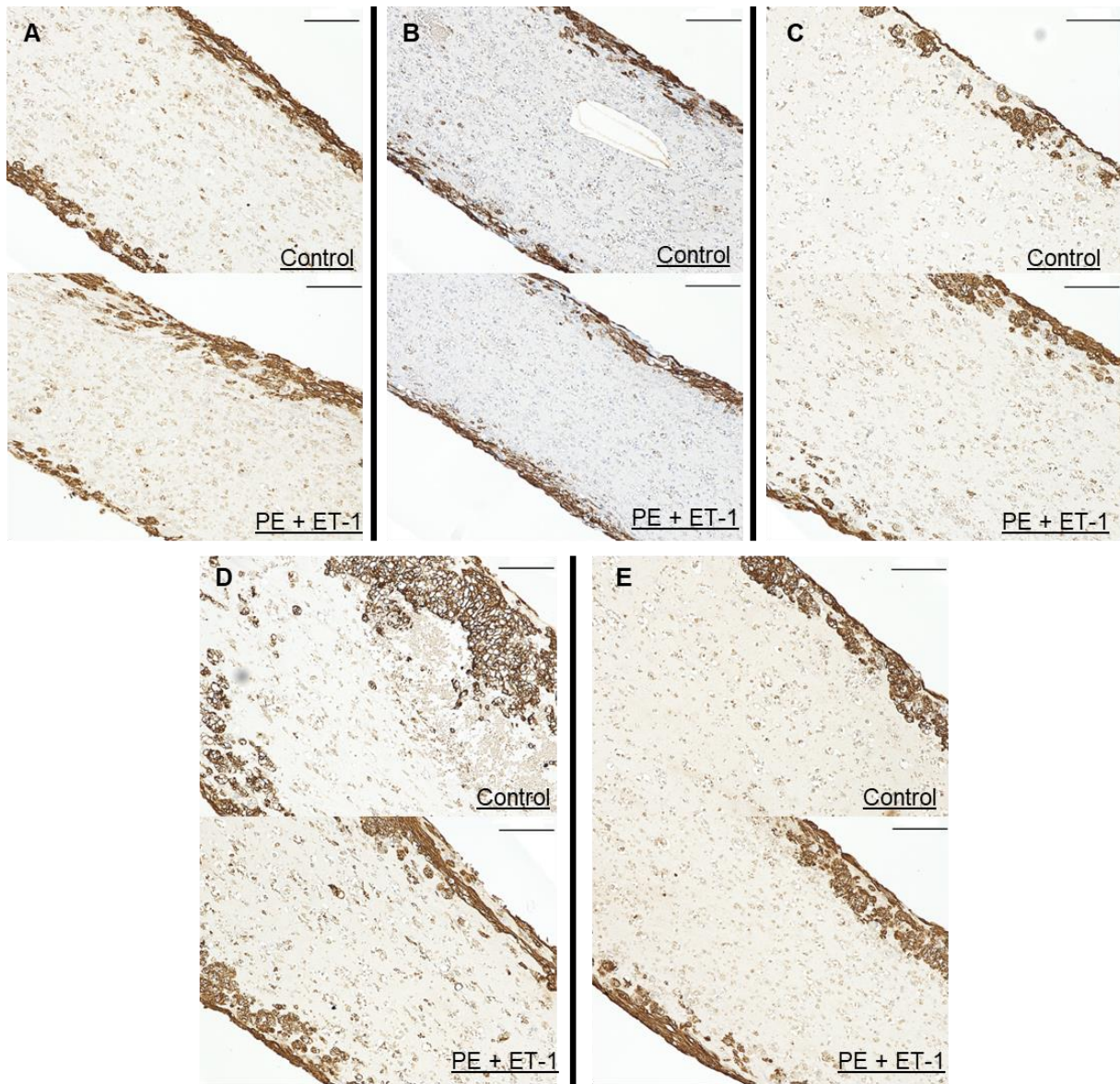


**Figure 52: MLC2v staining.** EHT paraffin sections of control and PE + ET-1-treated EHTs after MLC2v staining. (A) ERC018, (B) Trisomy control, (C) heterozygous, (D) compound heterozygous, (E) homozygous. Scale bar = 100 μm.

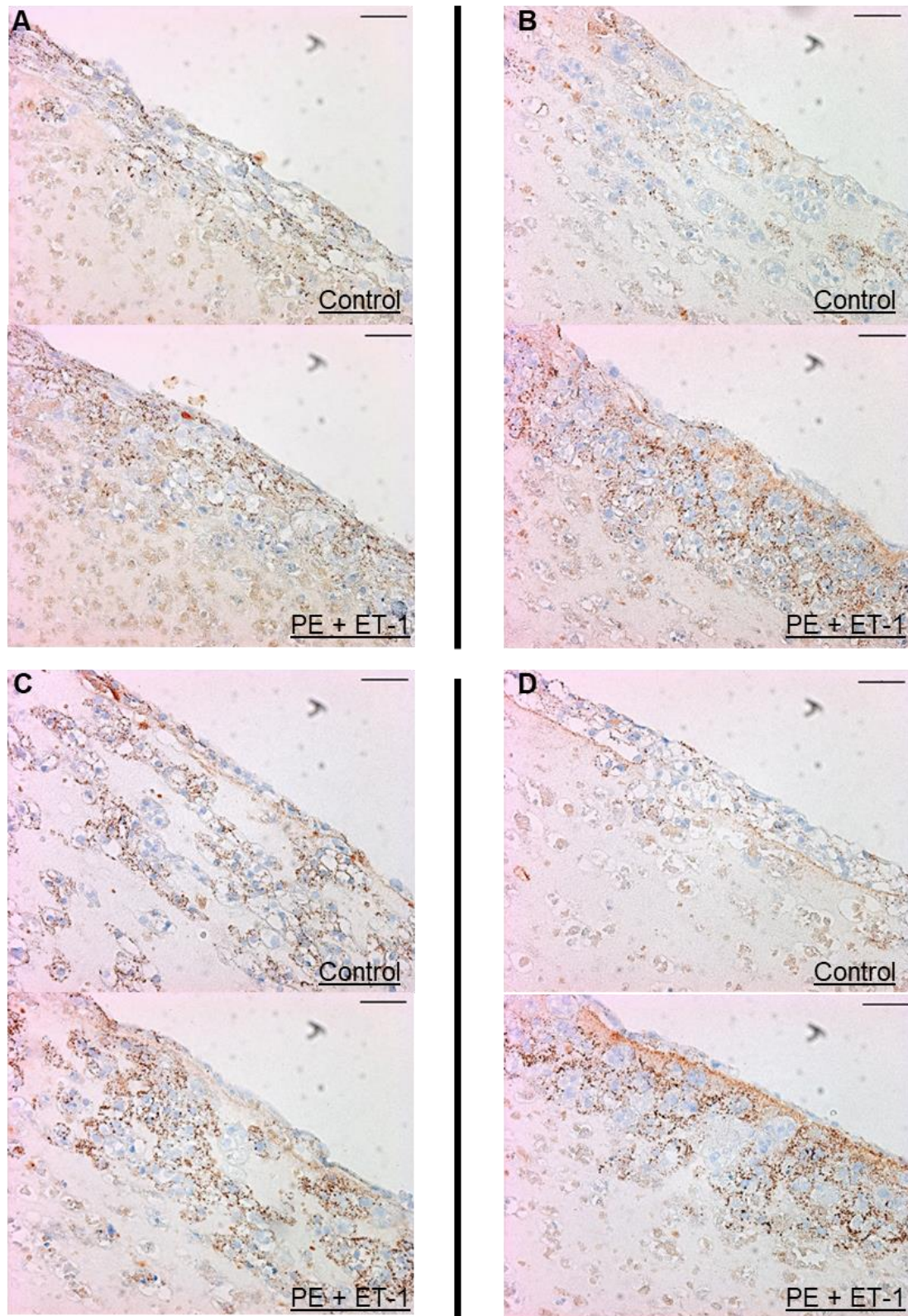


**Figure 53: Connexin 43 staining.** EHT paraffin sections of control EHTs and PE + ET-1-treated EHTs after staining for connexin-43. (A) ERC018, (B) heterozygous, (C) compound heterozygous, (D) homozygous. Scale bar = 50  $\mu$ m.



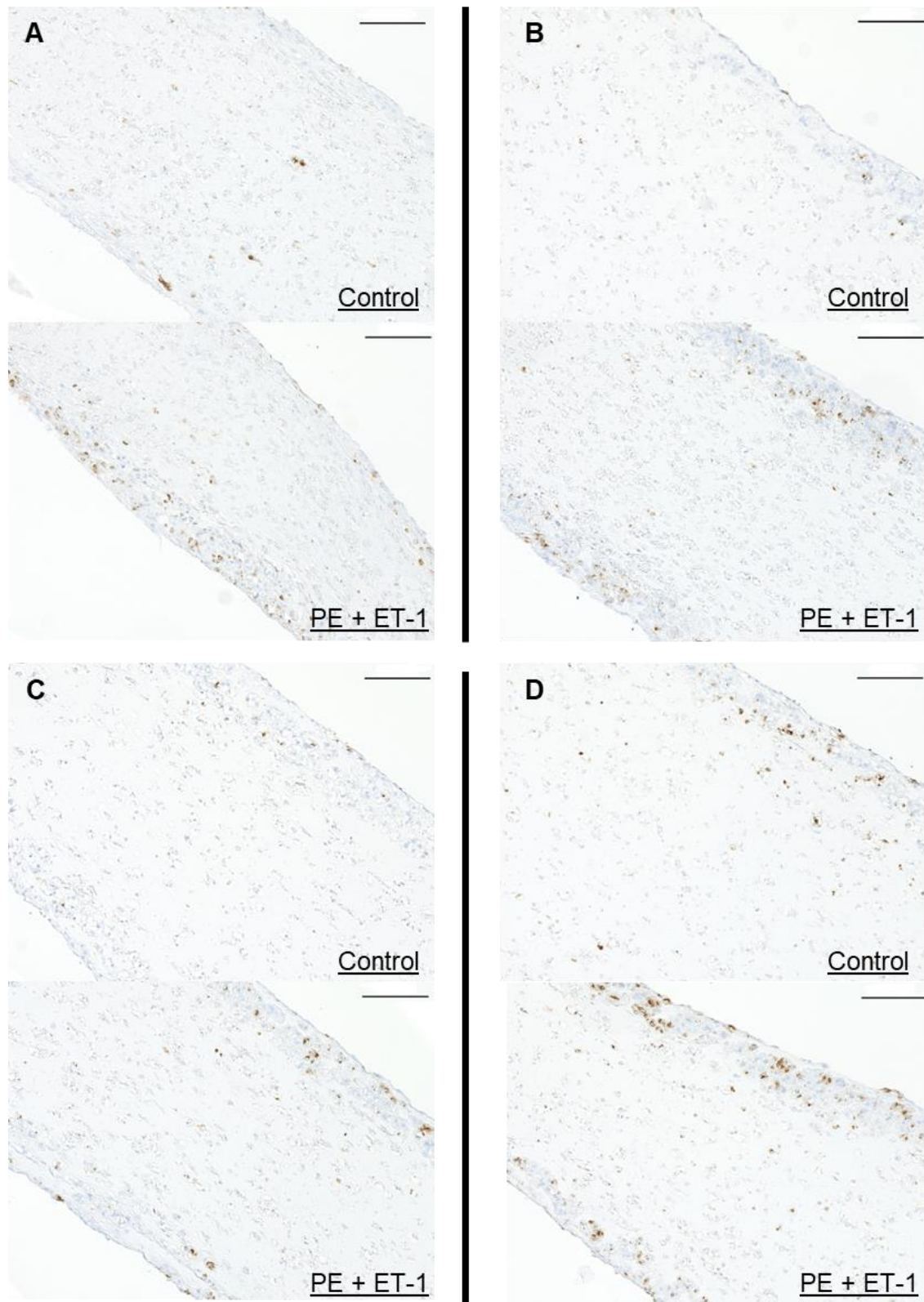


**Figure 54: ANP staining.** EHT paraffin sections of control EHTs and PE + ET-1-treated EHTs after staining for ANP. (A) ERC018, (B) heterozygous, (C) compound heterozygous, (D) homozygous. Scale bar = 100  $\mu$ m.

In order to analyze the identity of the vacuolic structures in the knockout EHTs, a lipid staining with Oil red O was performed in the two control lines and the compound heterozygous knockout as the morphology was suggestive of lipid accumulation. ERC018 and trisomy EHTs displayed only very sparse staining of single dots after Oil red O treatment both under control and PE + ET-1 conditions (figure 55 A + B). In contrast, untreated compound heterozygous knockout EHTs displayed a distinct staining with numerous red dots inside the EHT which were not present in PE and ET-1 treated EHTs (figure 55 C).

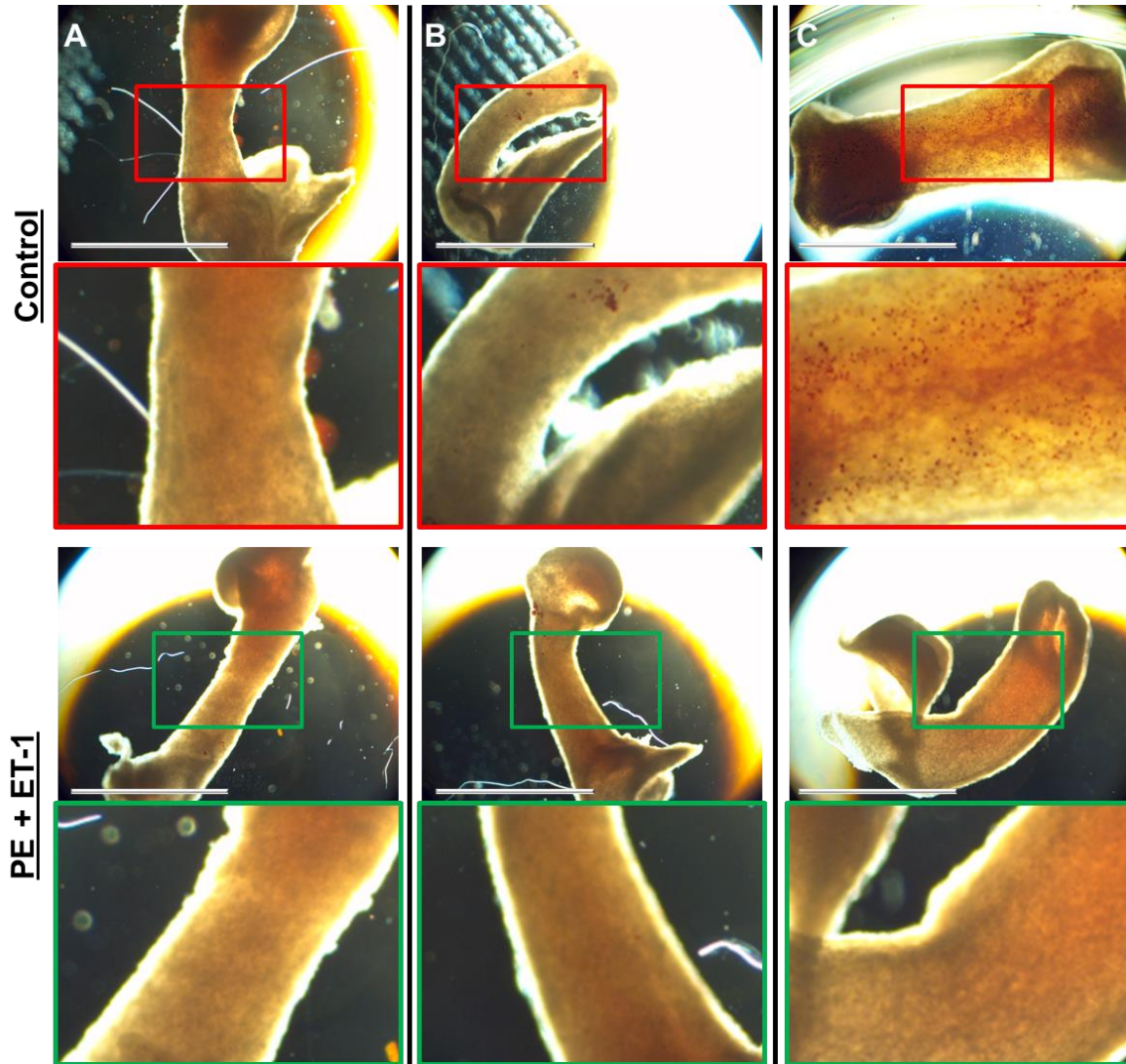


**Figure 55: Lipid staining with Oil red O.** Staining of whole-mount (A) ERC018, (B) trisomy, and (C) compound heterozygous EHTs under control (upper panels) and hypertrophic conditions (lower panels). The red and green boxes show a zoom-in of the indicated areas. Scale bar = 3 mm.

#### 4.6.2 Gene expression analysis

As a next step, ERC018 and homozygous knockout EHTs were analyzed for gene expression changes induced by either the knockout of DNMT3A or the pro-hypertrophic treatment. NanoString analysis of 54 important cardiac target genes revealed gene a specific pattern of expression changes in knockout EHTs compared to ERC018 dividing the analyzed genes into three groups. The first group consisted of genes which were detected only at background levels in both ERC018 and DNMT3A knockout. The second group contained genes which showed low transcript abundance in ERC018 and trisomy control lines and significantly higher levels in DNMT3A knockout (figure 56 A, B and supplementary figure S5). The genes in the third group had high transcript levels in ERC018 which were either unchanged or significantly lower in the knockout (figure 56 C).

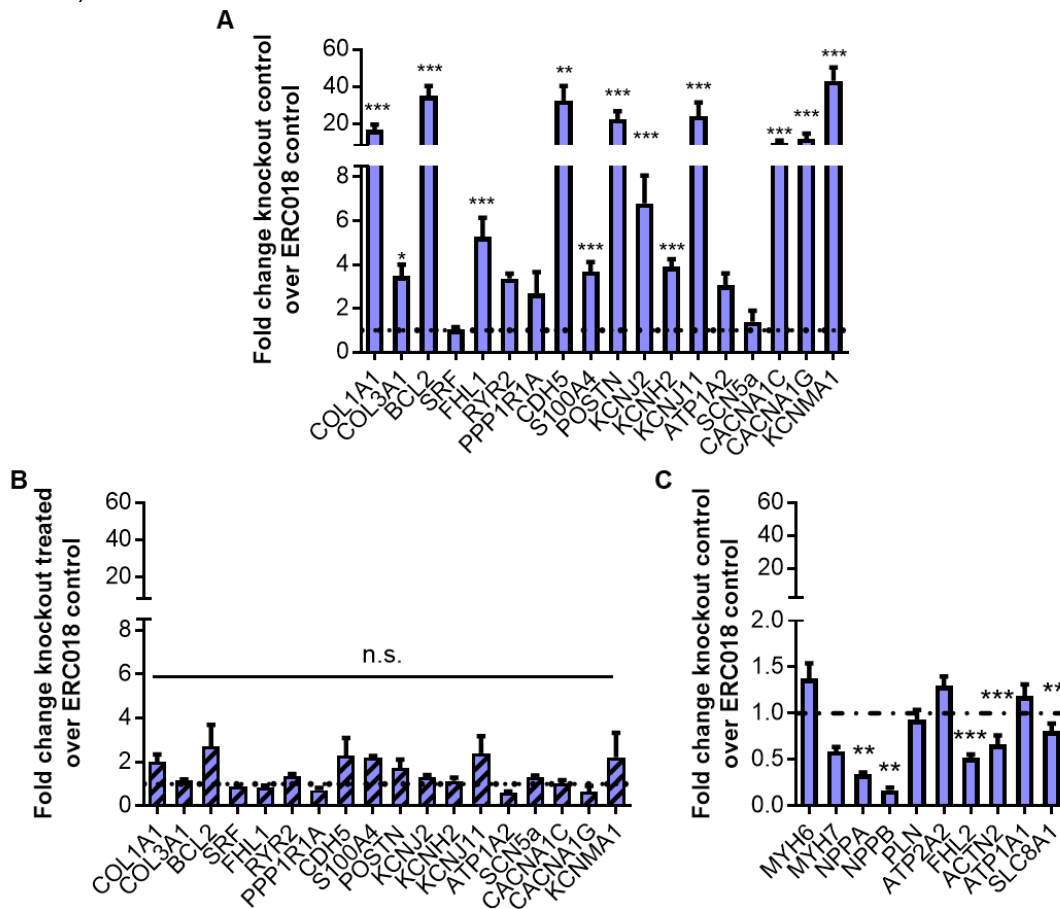


**Figure 56: Overview of NanoString gene expression analysis.** (A) Fold change of low abundance genes in knockout control EHTs compared to ERC018 control (dotted line). (B) Fold change of low abundance genes in PE and ET-1-treated knockout EHTs compared to ERC018 control (dotted line). (C) Fold change of high abundance genes in knockout control EHTs compared to ERC018 control (dotted line). n=3 EHT per group, 2way ANOVA plus Bonferroni's post-test for multiple comparisons vs. control, \*\*p<0.01, \*\*\*p<0.001.

Importantly, treatment of the knockout EHTs with PE and ET-1 normalized expression of these genes to the level of ERC018 control EHTs (compare figure 56 B to 56 A). Looking at the gene expression changes in more detail, knockout of DNMT3A changed transcript abundance of the two myosin heavy chain isoforms MYH6 and MYH7 with slightly higher MYH6 and lower MYH7 expression (figure 57 A). Although these differences themselves were not significant, the ratio of MYH7/MYH6 was significantly lower in knockout EHTs than in ERC018 under control conditions (figure 57 B). Treatment with PE and ET-1 decreased MYH6 expression in both genotypes. MYH7 however, slightly decreased with treatment in ERC018 EHTs only, while treatment of knockouts led to higher transcript abundance, which led to a significantly higher MYH7/MYH6 ratio in knockouts under hypertrophic treatment. The MYH7/MYH6 ratio in the trisomy control was also slightly lower than ERC018, but still significantly higher than in the knockout (figure 57 C).

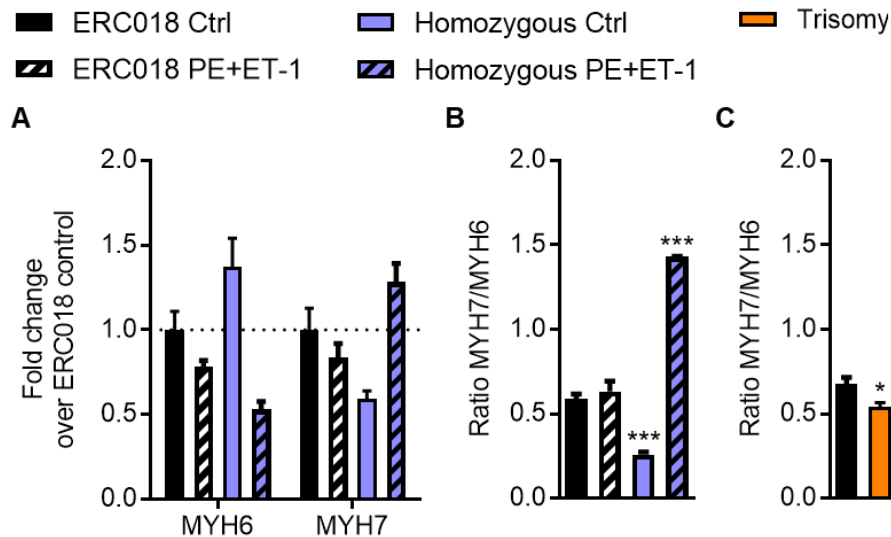


**Figure 57: Hypertrophic gene program in ERC018 and homozygous knockout EHT.** (A) Fold change of MYH6 and MYH7 in ERC018 and knockout EHTs under control and treatment conditions. (B) MYH7/MYH6 ratio in ERC018 and knockout EHTs under control and hypertrophic conditions. (C) MYH7/MYH6 ratio in ERC018, trisomy control and knockout EHTs.  $n=3$  EHT per group, 2way ANOVA plus Bonferroni's post-test for multiple comparisons vs. control, \* $p<0.05$ , \*\* $p<0.01$ , \*\*\* $p<0.001$ .

With regards to natriuretic peptides, NPPA and NPPB were significantly lower expressed in knockout EHTs than in ERC018 controls (figure 58). Pro-hypertrophic treatment however, induced expression of the two hypertrophic markers significantly in both genotypes. Transcript abundance



of ATP2A2 was not affected by knockout of DNMT3A, however, transcript levels were significantly lower under PE and ET-1 treatment compared to controls in both genotypes.

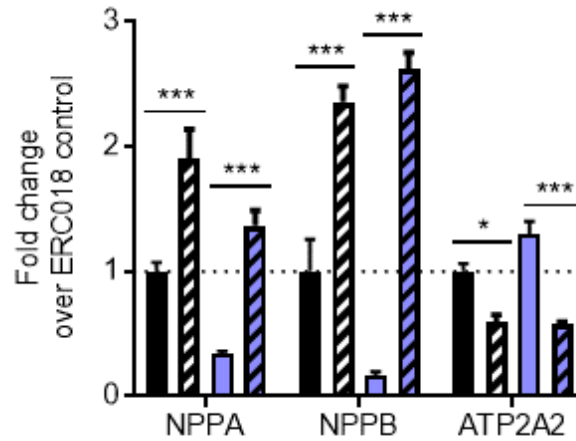


**Figure 58: NanoString expression levels of hypertrophic marker genes.** Fold change of NPPA, NPPB, and ATP2A2 in ERC018 and knockout EHTs under control and treatment conditions.  $n=3$  EHT per group, 2way ANOVA plus Bonferroni's post-test for multiple comparisons vs. control, \* $p<0.05$ , \*\*\* $p<0.001$ .

Furthermore, the NanoString panel used for gene expression analysis also contained genes encoding several ion channels. Interestingly, the potassium channel genes KCNJ2, KCNH2, and KCNJ11 which encode for subunits of the channels responsible for the  $I_{K1}$ ,  $I_{Kr}$ , and  $I_{KATP}$  currents, respectively, were significantly higher expressed in DNMT3A knockout (figure 59 A). The data fit well to shorter APD of the DNMT3A knockout EHTs (figure 45). KCND3, KCNA4, and KCNIP2 encoding for components of the  $I_{to}$  current were also expressed at significantly higher levels in the knockouts but displayed overall low transcript abundance just above background signals. Similarly, transcripts of the genes encoding for the calcium L-type and T-type channels, as well as the calcium-activated potassium channel BK (CACNA1C, CACNA1G, and KCNMA1, respectively; figure 59 B) were significantly more abundant in the knockout EHTs than ERC018. Importantly, expression levels of all ion channels were equalized to ERC018 levels by treatment with PE and ET-1.

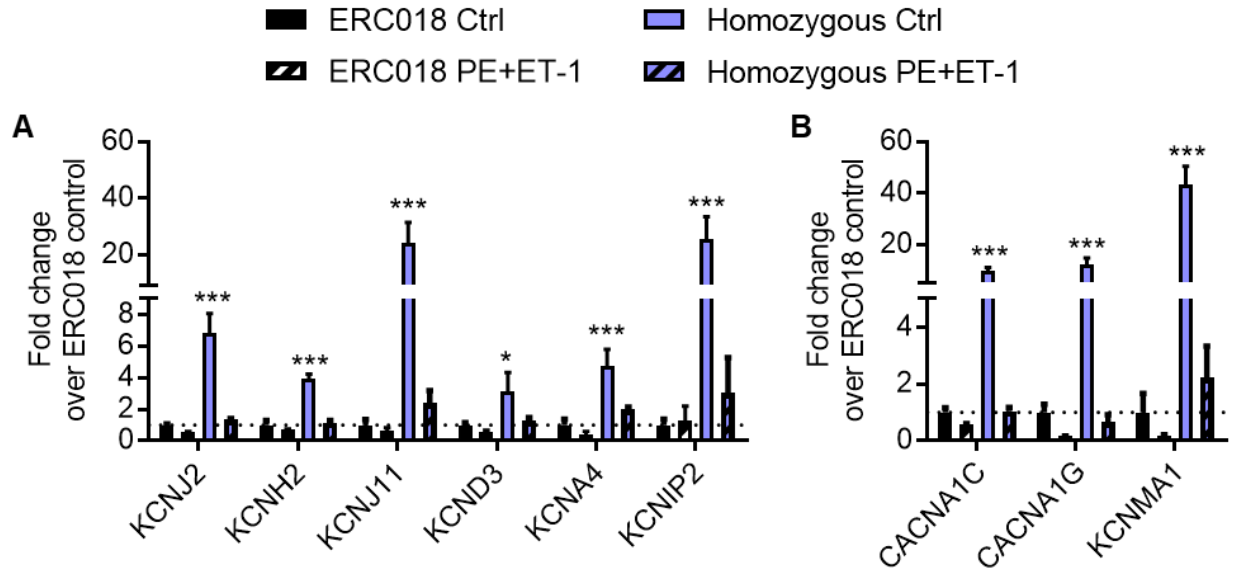


**Figure 59: Ion channel expression.** (A) Fold change of KCNJ2 ( $IK_1$ ), KCNH2 ( $IK_r$ ), KCNJ11 ( $IK_{ATP}$ ), KCND3, KCNA4, and KCNIP2 ( $I_{to}$ ) in ERC018 and knockout EHTs under control and treatment conditions. (B) Fold change of CACNA1C (L-type calcium channel), CACNA1G (T-type calcium channel), and KCNMA1 (calcium-activated potassium channel BK) in ERC018 and knockout EHTs under control and treatment conditions.  $n=3$  EHT per group, 2way ANOVA plus Bonferroni's post-test for multiple comparisons vs. control, \* $p<0.05$ , \*\*\* $p<0.001$ .

Since the histological analysis revealed lipid deposits in the knockout EHTs, two genes involved in lipid metabolism (peroxisome proliferator-activated receptor gamma;  $PPAR\gamma$ ) and adipocyte signaling (adipsin) were additionally analyzed by qPCR.  $PPAR\gamma$  was significantly higher expressed in heterozygous and homozygous DNMT3A knockout EHTs compared to both ERC018 and the trisomy control EHTs (figure 60 A). Although overall adipsin transcript abundance was comparatively low in all EHTs, DNMT3A-deficient EHTs showed significantly higher levels than both controls (figure 60 B). Under treatment with PE and ET-1 both genes displayed transcript levels similar to the two control EHT lines.



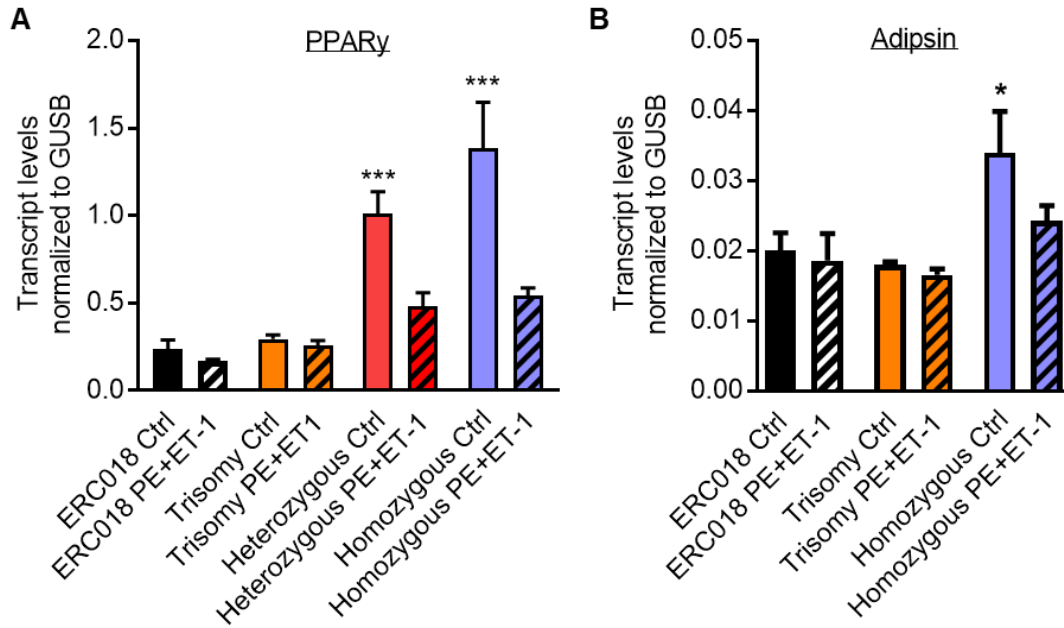


**Figure 60: Lipid metabolism and adipocyte gene expression.** (A) Relative transcript levels of PPAR $\gamma$  in ERC018, trisomy control, heterozygous, and homozygous knockout EHTs under control and hypertrophic treatment conditions. (B) Relative transcript levels of adipsin in ERC018, trisomy control, and homozygous knockout EHTs under control and hypertrophic treatment conditions. N=3-4 EHTs per group, transcript levels normalized to GUSB, 2way ANOVA plus Bonferroni's post-test for multiple comparisons vs. control, \* $p < 0.05$ , \*\*\* $p < 0.001$ .

#### 4.6.3 DNA methylation analysis

The effect of DNMT3A knockout on DNA methylation was analyzed by reduced representation bisulfite sequencing (RRBS) of ERC018 and DNMT3A homozygous knockout EHTs under control and pro-hypertrophic conditions. The RRBS quality data revealed no significant differences between the four groups with regards to library size, mapping efficiency, number of mapped reads, or number of cytosines covered (figure 61), arguing for a minimal influence of technical bias on the results.

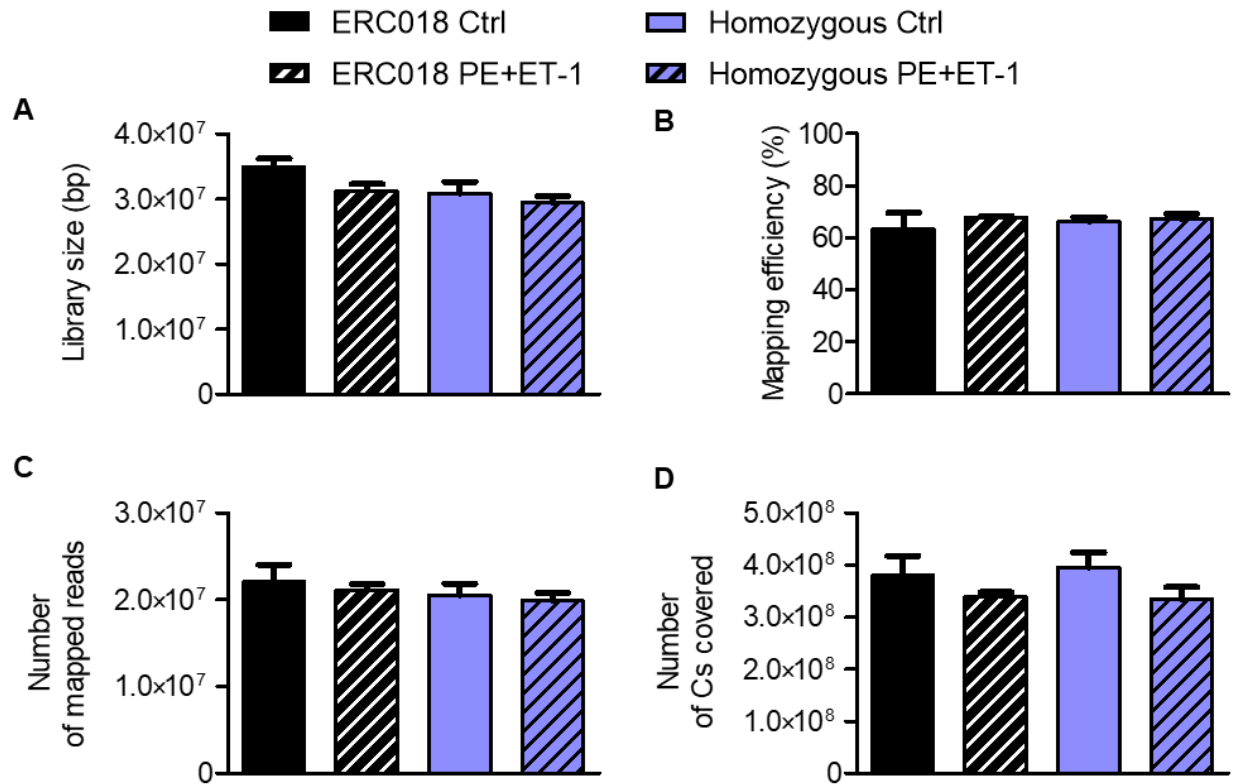


**Figure 61: RRBS quality data.** (A) Library size, (B) mapping efficiency, (C) number of mapped reads, and (D) number of Cs covered in the RRBS analysis.  $n=3-4$  EHTs per group, 1way ANOVA plus Bonferroni's post-test for multiple comparisons, no significant differences.

When looking at genome-wide methylation levels, the knockout showed significantly lower methylation levels compared to ERC018, well compatible with the loss of a de-novo DNA methylation enzyme. Treatment with PE and ET-1 did not alter the global DNA methylation level in the two genotypes further (figure 62). On the single base level, differentially methylated cytosines (DMCs) between both the genotypes and the treatment conditions could be observed, but the number of DMCs differed greatly between the different comparisons (figure 63). The highest number of DMCs was obtained when comparing the DNMT3A KO EHTs to ERC018 EHTs. In total, 2985 analyzed cytosines were differentially methylated in the knockout, out of which 933 were higher methylated and 2052 lower methylated than ERC018. Comparing the two genotypes under pro-hypertrophic treatment resulted in 1020 DMCs (211 hypermethylated and 809 hypomethylated). Treatment with PE and ET-1 had a minor effect on the methylation of both

genotypes. Under treatment ERC018 showed 74 hypermethylated and 36 hypomethylated regions (110 total) compared to untreated conditions, while in the knockout treatment resulted in 69 hypermethylated and 181 hypomethylated DMCs (250 total).

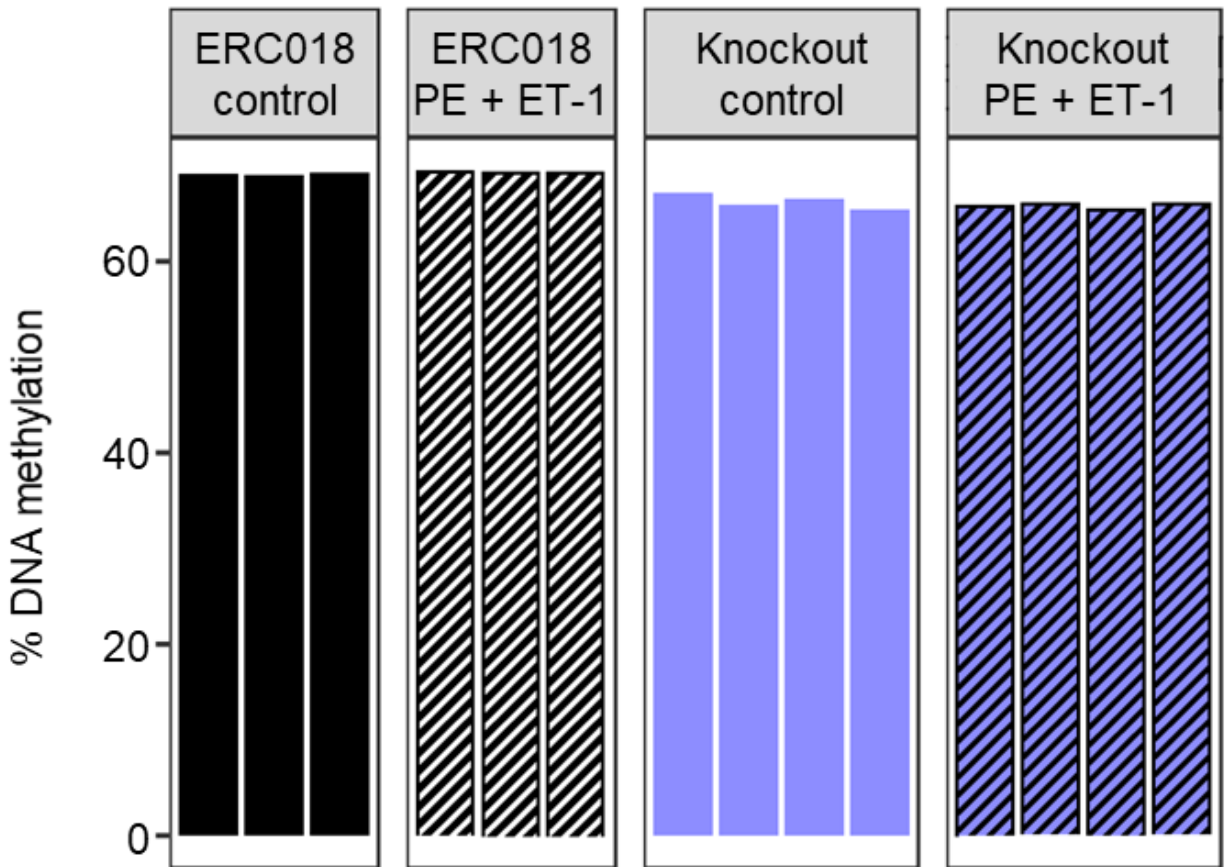


**Figure 62: Global DNA methylation levels measured by RRBS.** Each column represents the overall DNA methylation degree of a single sample from the respective group. n=3 for ERC018 control and PE + ET-1, n=4 for knockout control and PE + ET-1.

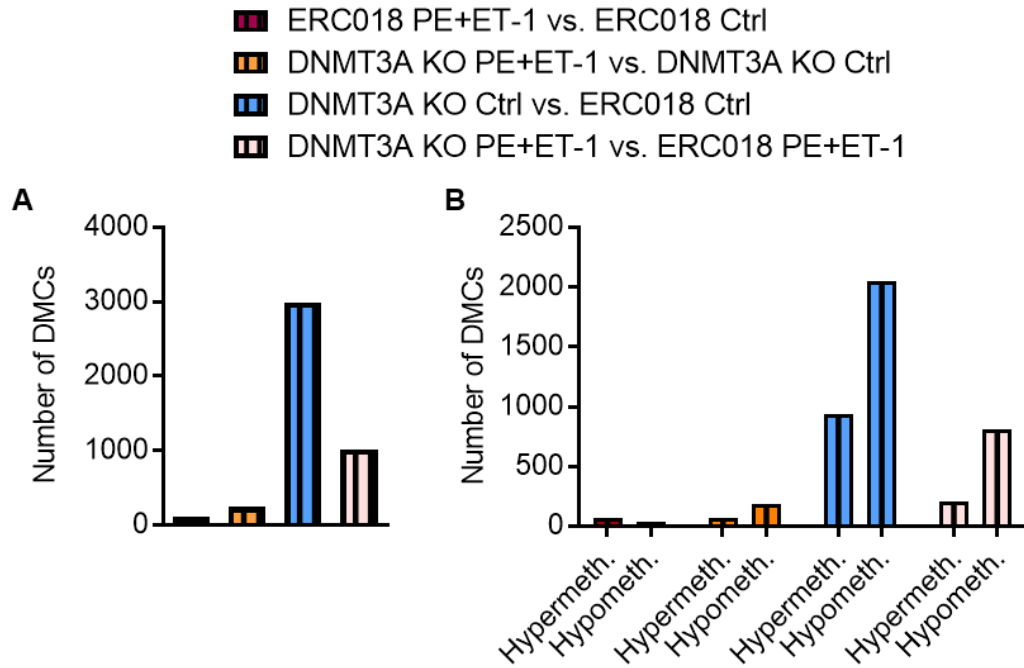


**Figure 63: Differentially methylated regions (DMCs).** (A) Overall number of DMCs between the different genotypes and treatment conditions. (B) Subdivision of the DMCs into hyper and hypomethylated regions.

The distribution of the DMCs on the different genomic functional regions (intergenic, promoter, exon, intron, and transcription end site) was similar in all comparisons (figure 64). Most DMCs were located in the promoter region of genes (34% - 50%; defined as the region within 1000 bp of the transcription start site) or in intergenic regions (26% - 39%). Approximately one fifth of the DMCs were located in intronic regions of annotated genes and less than 10% were found in exons or at the transcription end site (TES).

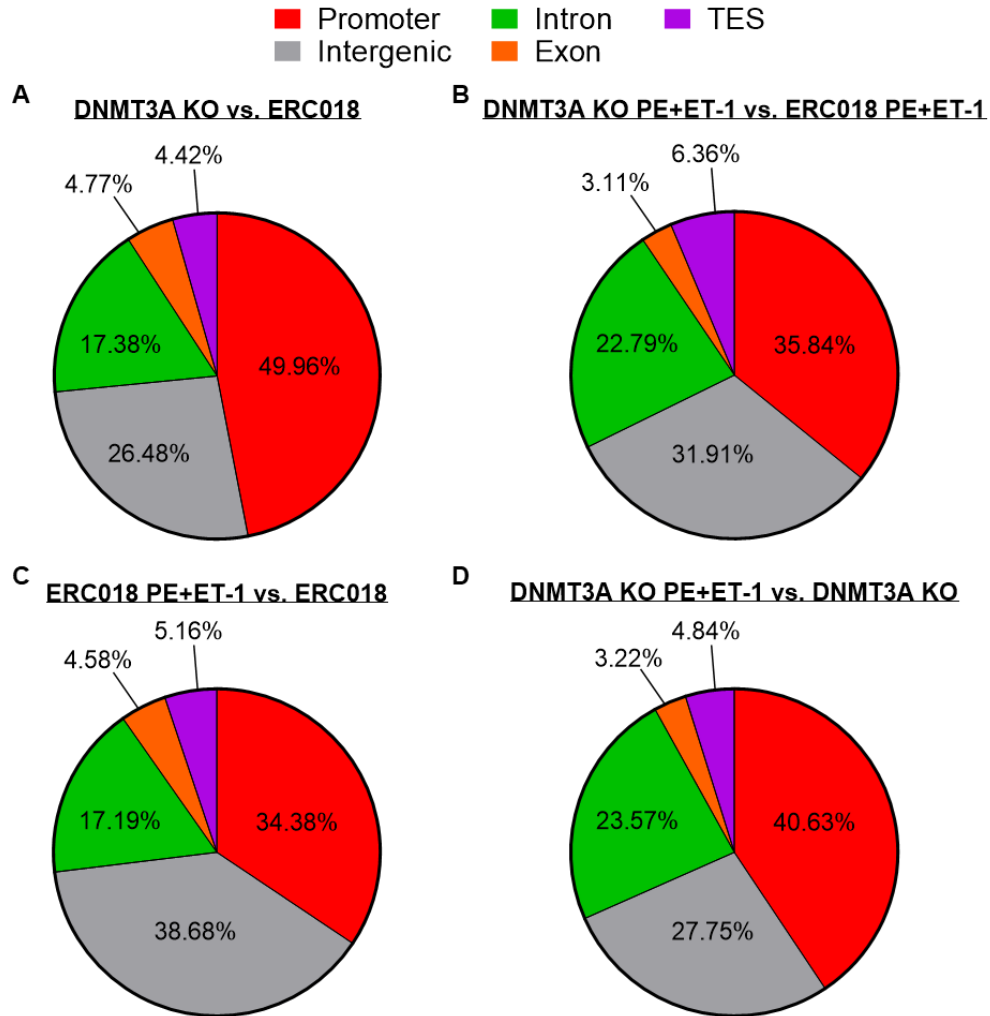


**Figure 64: DMC distribution among functional regions.** Percentage of DMCs in promoters, intergenic, intronic, exonic, and TES regions in (A) knockout control vs. ERC018 control, (B) knockout treated vs. ERC018 treated, (C) ERC018 treated vs. ERC018 control, and (D) knockout treated vs. knockout control. TES: transcription end site.

The RRBS samples were furthermore analyzed with regards to sample clustering according to their DNA methylation signature. In the group comparisons between the two genotypes as well as the comparison of ERC018 control vs. treatment, the samples clustered closer together with their respective replicates from the same genotype and treatment than with samples from the other groups (figure 65 A - C). For the knockout under control vs. treatment conditions, this distinct clustering of the different treatment conditions was not as clear-cut (figure 65 D).

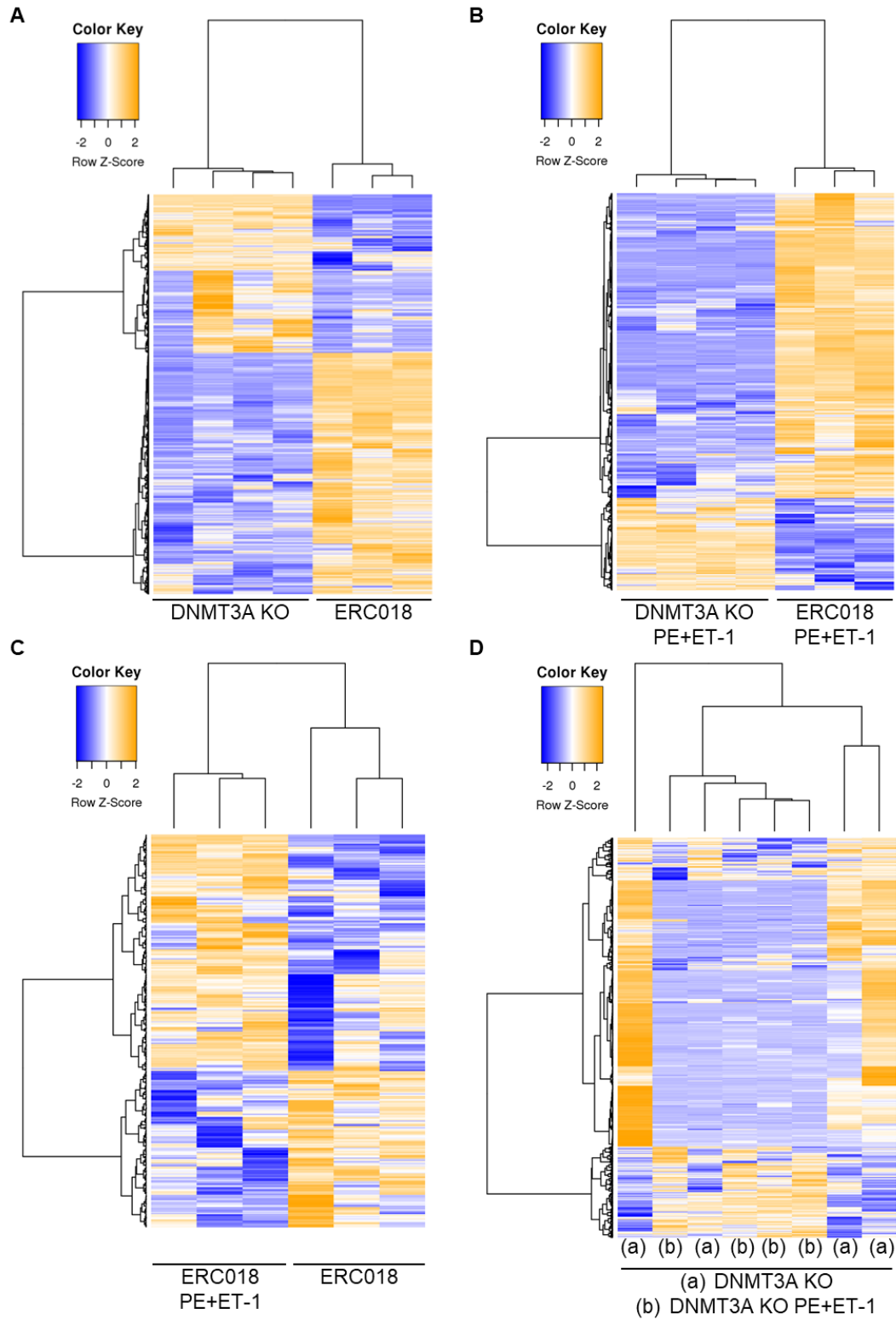


**Figure 65: Clustering of RRBS samples.** (A) Knockout control vs. ERC018 control, (B) knockout treated vs. ERC018 treated, (C) ERC018 treated vs. ERC018 control, and (D) knockout treated vs. knockout control according to their methylation signature. Blue: low methylation, orange: higher methylation.

The genes associated with DMCs were subjected to pathway mapping analysis. Using Ingenuity Pathway Analysis Software (IPA), a “tox list analysis” was performed in order to find pathologies associated with differential methylation in the group comparisons (figure 66). In ERC018 control EHTs, PE and ET-1 had no significant effect, i.e. no specific pathway showed a significant change in methylation. In DNMT3A knockout EHTs, PE + ET-1 significantly affected the “TGF $\beta$ -signaling”, “cardiac hypertrophy” and “NF $\kappa$ B” pathways (orange in figure 66). The most clear-cut differences were seen in the comparison between ERC018 and DNMT3A knockout (blue and green in figure 66). Pathways that associate with “renal necrosis/cell death”, “RAR activation”, NRF2-mediated oxidative stress response”, “increases liver damage”, and “p53 signaling” were all significantly affected in knockout vs. ERC018, without apparent differences between control and PE + ET-1 conditions. Two pathway abnormalities differed between the latter. Association of knockout vs. ERC018 with “PPAR $\alpha$ /RXR $\alpha$  activation” was significant only for comparison under PE + ET-1, while “Increases (in) cardiac proliferation” associated with the comparison of knockout vs. ERC018 only under control conditions. Importantly, all of the observed differences were no longer significant when the p-value was adjusted for multiple testing with the Benjamini-Hochberg procedure. This can be explained by the fact that in this procedure the adjusted p-value is calculated by division of the unadjusted p-value by the number of analyzed pathways, which was comparatively high in the present analysis.

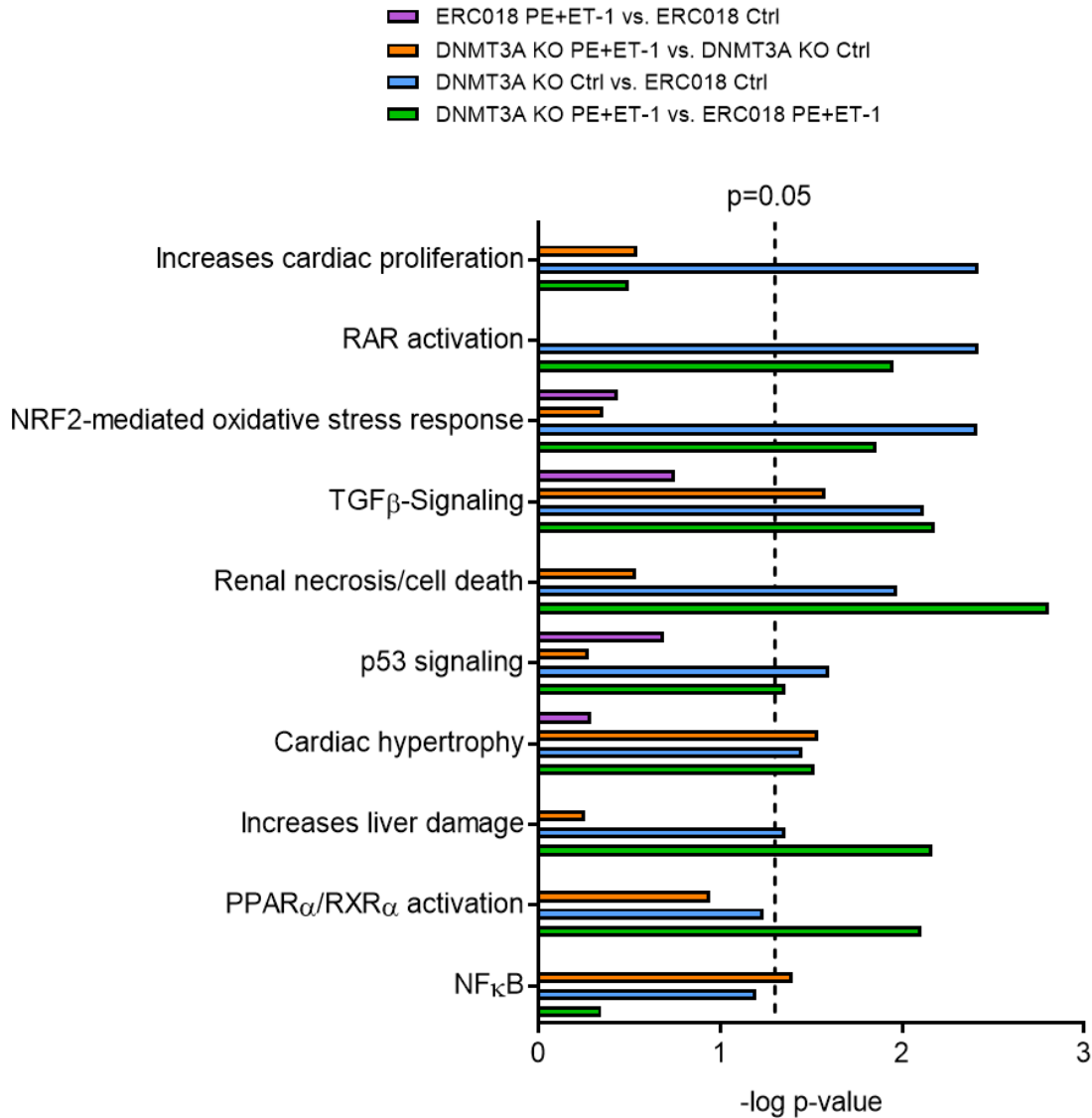


**Figure 66: IPA tox lists from DNA methylation analysis.** Pathologies significantly associated with DMCs are plotted against the negative logarithm of their p-value. The dotted line marks the p-value threshold of  $p=0.05$ .

In addition, upstream analysis was performed in the IPA software to identify upstream regulators which are significantly associated with the observed DNA methylation patterns. From the analysis results, only regulators with a z-value assigned by the IPA software were taken into account, as only regulators with high probability and highest degree of verification are assigned a z-value by the software. In this analysis, treatment with PE + ET-1 was not associated with a z-value in any genotype. In contrast, 34 regulators were found to associate with DNMT3A knockout vs. ERC018 control, and this difference diminished to 13 under treatment with PE + ET-1 (table 17). A list of



the regulators can be found in the supplement (supplementary table S1). The single regulators of both comparisons were grouped into functional categories according to their downstream signaling (table 17). Under control conditions the majority of regulators were associated with pluripotency, differentiation, cell proliferation, and apoptosis (e.g. Wnt, POU5F1, SOX2, GATA6), while under treatment most regulators were grouped to apoptosis, cell cycle, and DNA damage functions (e.g. MAPK9, TP53). Moreover, the number of regulators involved in cell migration, fat metabolism, adipocyte signaling, and cell proliferation was greatly reduced under treatment.

**Table 17: Upstream regulators DMCs.** All obtained regulators were grouped into functional categories according to their downstream signaling. Note that each regulator can have multiple functions.

Function	Knockout Ctrl vs. ERC018 Ctrl	Knockout PE+ET-1 vs. ERC018 PE+ET-1
Apoptosis / senescence	9 regulators	6 regulators
Cell migration	8 regulators	0 regulators
Pluripotency, development & differentiation	15 regulators	3 regulators
Fat metabolism and adipocyte signaling	5 regulators	1 regulator
Cell proliferation	9 regulators	1 regulator
General gene regulation	8 regulators	4 regulators
Cell cycle / DNA damage	2 regulators	6 regulators

## 5 Discussion

The present study aimed to investigate the contribution of DNA methylation to cardiac physiology and disease by generation of a DNMT knockout hiPSC cell line, differentiation into knockout cardiomyocytes, and evaluation of functional consequences of the knockout in EHT under both baseline conditions and pro-hypertrophic treatment.

### 5.1 Generation of DNMT3A knockout hiPSC

In order to analyze the DNMT knockout with the highest physiological relevance for cardiomyocytes, transcript levels of the three DNMT isoforms were compared in hiPSC and hiPSC-derived cardiomyocytes. qPCR revealed DNMT3A to be the main isoform in cardiomyocytes, which was in line with previous expression analyses conducted in rat heart (Stenzig et al. 2018). DNMT1 was found to be expressed at approximately one fifth of DNMT3A levels, while DNMT3B was virtually absent. These findings were conflicting with the results published by Vujic et al. (2015) where DNMT3B was determined to be the main isoform in both mice and human hearts. However, this observation has been challenged: since the protein lysates used for DNMT isoform detection in the latter study were derived from whole LV samples, contamination with cell types other than cardiomyocytes has possibly influenced the results. In our study, expression levels of the different DNMT isoforms in hiPSC and differentiated cardiomyocytes were rather in line with the findings published by Liao et al. (2015) in hESC. DNMT3B on the other hand, representing the main DNMT isoform in both hESC and hiPSC, as well as in early mouse development (Okano et al. 1999), seems to have an important function in pluripotent cells and during development. In comparison with the pluripotent state, Liao and colleagues did not only observe reduced expression of DNMT3B after differentiation induction, as was observed in our study during differentiation towards hiPSC-derived cardiomyocytes, but also a switch from the active DNMT3B1 isoform to the inactive isoform DNMT3B3. Lastly, the expression level of DNMT1 and DNMT3A of hiPSC remained largely unchanged after differentiation into cardiomyocytes in our results, again reflecting the published results obtained in hESC.

To study the importance of DNA methylation in cardiomyocytes, knockout of DNMT3A was performed by CRISPR/Cas9. The knockout approach published by Liao et al. was adapted since it had yielded good knockout efficiencies in hESC and viable and differentiable cell clones. Adaptation of the DNMT3A knockout strategy to ERC018 hiPSC resulted in three successfully

mutated clones (~23% overall editing efficiency), out of which one clone was homozygously mutated (~8% efficiency). While the latter is well in line with the frequency obtained in hESC by Liao et al. (~8% vs. ~6%), the overall proportion of mutated clones was considerably higher in hESC (~67%). One explanation could be the known difficulties to transfect hiPSC with foreign DNA. The transfection efficiencies reached in the current experiments were below 1% of cells, while nucleofection efficiencies for hESC have been reported to reach up to 95% (Wang et al. 2015). Nucleofection conditions will have to be further optimized in the future to account for differences between single hiPSC lines. Moreover, a considerably smaller number of cell clones for analysis was obtained in the hiPSC experiment than what had been reported for hESC (13 vs. 48 cell clones, respectively). This smaller sample size could also have an impact on the number of successfully mutated clones. Nevertheless, the results show that knockout of DNMT3A was technically feasible in the ERC018 hiPSC line with the presented approach.

The successfully established gene edited clones did not show signs for Cas9 off-target activity in the analysis of the ten most likely loci, which is in line with the low off-target activity of Cas9 in hiPSC described by others (Smith et al. 2014; Veres et al. 2014; Tan et al. 2015). However, in order to fully exclude off-target mutations in the clones, whole-genome sequencing would have to be performed since single nucleotide polymorphisms could lead to higher sequence similarity with the sgRNA than predicted in the *in silico* sgRNA design, leading to off-target activity in previously unanticipated regions (Kosicki et al. 2018).

Karyotypic analysis of the CRISPR clones revealed a trisomy of chromosome 1 in all three cell lines. The occurrence of the same abnormality in three cell lines argues against the CRISPR procedure as the cause of the trisomy, since introduction of the same abnormality in three separate cell lines by chance would be highly unlikely (Närvä et al. 2010). Moreover, several cell lines from a different CRISPR project using the same ERC018 cell line as starting material, as well as the ERC018 cells that were used for the CRISPR procedure themselves at a later passage (p63) were eventually tested positive for the same trisomy. It can therefore be assumed that the ERC018 line had already had an abnormal karyotype at the beginning of the CRISPR procedure at passage p37. A study by Taapken and colleagues (Taapken et al. 2011) described a strong propensity of both hESC and hiPSC for acquisition of karyotypic abnormalities, which were independent of reprogramming procedure and culture conditions. Even though it has been shown that these abnormalities can already be present at low passage numbers (Mayshar et al. 2010), they accumulate increasingly over prolonged culture time due to their growth advantage (Närvä et al. 2010). This strongly emphasizes the importance of rigorous quality standards when working with hiPSC. Cells should be kept in culture for only a few passages and should regularly be

analyzed for genomic integrity (Brenière-Letuffe et al. 2018). The establishment of a cell bank with verified karyotype for each cell line at a low passage number can help circumvent problems of genomic instability when working with hiPSC. Chromosomal aberrations of chromosome 1 are frequently observed in malignant diseases, especially at the terminal stage of disease, suggesting the presence of oncogenes or tumor suppressors involved in disease progression in these regions (Olah et al. 1989; Caramazza et al. 2010). However, the impact of trisomy 1 on cardiac function in humans remains elusive, since only two cases of non-mosaic trisomy 1 pregnancies have been reported to date, both resulting in prenatal death of the embryo (Hanna et al. 1997; Dunn et al. 2001). In general, an effect of the trisomy on hiPSC or the derived cardiomyocytes cannot be excluded as chromosome 1 represents the largest human chromosome and harbors approximately 2,000 genes. Since the CRISPR procedure in this study could not be repeated with karyotypically normal control cells due to time constrictions, all functional experiments were repeated once with ERC018 cardiomyocytes carrying the same chromosomal abnormality in order to discriminate between trisomy and CRISPR mutation-induced effects. The results are discussed below (chapter 5.3).

## 5.2 DNA methylation in differentiation

Naïve stem cells display lower levels of DNA methylation than differentiated somatic cells and a different pattern of distribution. During differentiation, as well as during embryonic development, a wave of de novo methylation can be observed, generating cell type-specific methylation patterns in differentiated cells (Ehrlich 2003). While the wave of de novo methylation certainly plays a role in selectively inactivating gene expression of embryonic genes, the exact role of DNA methylation in the differentiation of different cell types is not yet fully resolved. Its role during cardiac differentiation and in cardiomyocytes remains particularly poorly understood. Treatment of neonatal rat hearts with the nucleosidic DNMT inhibitor 5-azacytidine led to a delay in development and cardiomyocyte differentiation, suggesting the necessity of DNA methylation in this process (Kou et al. 2010). While it has been shown that severe hypomethylation in mouse ESCs blocks their differentiation ability completely (Jackson et al. 2004), it is not clear which DNMT isoform is involved in the different stages of differentiation. Hypomethylation induced by knockout of Dnmt1 in mouse ESCs did not only block differentiation in this study, but also induced apoptosis of the ESCs, whereas double-knockout of Dnmt3a and Dnmt3b yielded ESCs which had lost their differentiation potential but were viable. Moreover, another study reported an impaired mesodermal differentiation ability of mouse iPSC after deletion of both Dnmt3a and Dnmt3b (Pawlak and Jaenisch 2011). Additional evidence points to an alternative short Dnmt1 isoform,

normally only expressed in testis and mediating de novo DNA methylation during gametogenesis, which has been suggested to be transiently expressed during differentiation of skeletal muscle in mice (Aguirre-Arteta et al. 2000). Differentiation of multipotent hematopoietic stem cells on the other hand, was suggested to be dependent on the activity of Dnmt3a since loss of the methyltransferase resulted in upregulation of multipotency genes inhibiting efficient differentiation (Challen et al. 2011). In the present study, deletion of DNMT3A in hiPSC did neither affect the self-renewal potential, nor their pluripotency and ability to give rise to cardiomyocytes following mesodermal induction, suggesting expendability of DNMT3A for these processes in hiPSC. Both the differentiation efficiency ( $0.7 \pm 0.3$  cardiomyocytes per iPSC) and the cardiomyocyte proportion after differentiation ( $82 \pm 12\%$ ) were similar in knockout and control cells. This observation is in line with data from hESC where ablation of both DNMT3A and DNMT3B did not compromise pluripotency and differentiation induction, whereas homozygous deletion of DNMT1 resulted in death of the hESC (Liao et al. 2015).

While these data show that mesodermal, endodermal, and ectodermal induction in hESC does not rely on DNMT3A or DNMT3B, it is conceivable that later stages of differentiation require de novo methylation. The high expression levels of DNMT3B in undifferentiated cells and its virtual absence after differentiation could indicate an involvement of DNMT3B in DNA methylation during early differentiation steps with only minor contribution of DNMT3A. This theory is also compatible with the proposed temporal differences of Dnmt3a and Dnmt3b activity during development, with a higher importance of Dnmt3b during early stages. Dnmt3b knockout mice die prenatally, displaying several birth defects starting from day E9.5, while Dnmt3a knockout mice develop to term and only start showing defects at 3-4 weeks of age and eventually die (Okano et al. 1999). Taken together, results from different studies suggest a role of DNMT1 for the maintenance and survival of pluripotent cells, while de novo methylation mediated especially by DNMT3B is important for differentiation into other cell types. DNMT3A seems to be largely dispensable or compensable by DNMT3B during differentiation of pluripotent cells, but probably plays an important role at later stages, such as the terminal differentiation of multipotent cells.

### 5.3 Effect of DNMT3A knockout on EHT function

#### 5.3.1 EHT contractility

Upon deletion of DNMT3A, no compensatory upregulation of the other two DNMT isoforms was observed in hiPSC or differentiated cardiomyocytes. Accordingly, even though target redundancy of DNMT3A and DNMT3B has been estimated to be above 95% (Liao et al. 2015), the virtual

absence of DNMT3B after differentiation of hiPSC into cardiomyocytes clearly eliminated the possibility of compensation of DNMT3A loss by DNMT3B. In consequence, the DNMT3A knockout resulted in de novo methylation-deficient cardiomyocytes. However, EHT generation and early EHT development were not visibly affected by the absence of de novo methylation activity. All EHTs showed regular extracellular matrix remodeling after a few days in culture and started to generate measurable force between day 6 and 8. The plateau phase of force development was reached in a comparable time frame and the maximally generated force during plateau was similar. During later EHT development however, functional degeneration of EHTs marked by low beating activity, irregular beating patterns, and reduced force generation was observed in knockouts. Since trisomy control EHTs behaved like ERC018 in this respect and showed no signs of degradation, the absence of DNMT3A and thereby most likely of de novo methylation can be assumed to be causal. Moreover, both the starting point and the severity of functional degeneration was detectable in a gene dose-dependent manner with compound heterozygous and homozygous DNMT3A knockout EHT performing significantly worse than heterozygous. Importantly, an even more severe phenotype was observed in compound heterozygous knockout EHTs than in the homozygous knockout. One possible explanation could be the toxicity of the two differently truncated mRNAs, aggravating the effect of the knockout. Moreover, possible CRISPR-induced off-target mutations which have not been detected in the targeted off-target analysis could act in synergy with the knockout of DNMT3A, leading to an exaggerated phenotype.

The above-mentioned phenotypic observations are concordant with results from a study on siRNA-mediated knockdown of *Dnmt3a* in primary mouse cardiomyocytes (Fang et al. 2016). Beating activity of the cardiomyocytes 24 hours after siRNA application was significantly reduced by ~65% and cells ceased beating completely after 2 days. The decrease in activity was highly dependent on the concentration of the transfected siRNA and thus on knockdown efficiency (figure 67 A from Fang et al. 2016). Cardiomyocyte movement, as a surrogate parameter for contractile force, also significantly decreased after *Dnmt3a* knockdown in these experiments (figure 67 B). Moreover, Fang and colleagues reported a loss in beating synchronicity of their cardiomyocytes cultured in 2D and an increasing variability in beating rate over time. These observations were mirrored in the knockout EHT as reflected in the high RR scatter values and the increasingly irregular beating patterns. It is easily conceivable that the irregular beating pattern in EHTs was also caused by a loss of synchronicity of the individual cardiomyocytes in the EHT leading to less-organized beating activity.

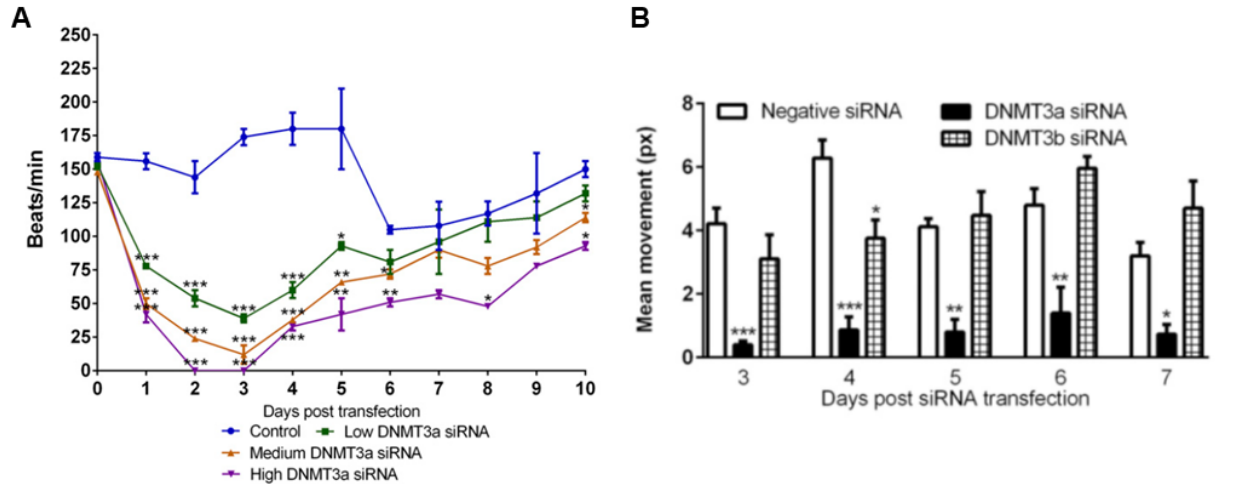


**Figure 67: Effect of siRNA-mediated Dnmt3a knockdown on primary mouse cardiomyocytes (Fang et al. 2016).** (A) Spontaneous cardiomyocyte beating frequency declined in an siRNA concentration-dependent manner after knockdown but slowly recovered over time. (B) Knockdown of Dnmt3a, but not Dnmt3b led to significantly lower cardiomyocyte movement.

The observed changes in contractility of DNMT3A knockout EHT were unlikely caused by fibrotic remodeling, since resting length of all EHT lines did not decrease over the culture period (supplementary figure S6) displaying no signs of fibrotic EHT shortening. Moreover, immunohistochemical staining for collagen 1 did not reveal any major collagen deposits in any of the EHTs (supplementary figure S4). Analysis of EHT by H&E staining, however, revealed an abnormal morphology of the cardiomyocytes in knockout EHTs with a less dense cell distribution and distinct vacuolic structures inside the cells. Staining for the myofilament protein MLC2v revealed a lower degree of longitudinal myofilament organization compared to ERC018 EHTs. The reduced cell density observed in the knockouts could not be attributed to an increase in cardiomyocyte apoptosis since immunohistochemical staining for the apoptosis marker caspase 3 yielded similar results in the control and knockout EHTs (supplementary figure S2). Moreover, cell-to-cell coupling of cardiomyocytes inside the EHTs did not seem to be influenced by the morphological changes in knockout EHTs, which displayed a similar staining intensity of the gap junction marker connexin 43 as control EHTs. Taken together, these results suggest that progressive accumulation of the observed vacuoles inside the cardiomyocytes over time negatively affected myofilament organization in the cells leading to impaired contractility of the single cells which in turn caused continuous loss of EHT contractility over time.

Before the contraction defects discussed above began to manifest, knockout EHTs regularly displayed significantly faster relaxation kinetics than the control cell lines. Although the same tendency was also observed in trisomy control cells, the difference between both controls and the homozygous and compound heterozygous knockout cell lines was still significant, when compared to trisomy control. A possible explanation for the differences could be the diverging expression of MYH6 and MYH7 in knockouts and controls. The  $\beta$ -MHC isoform encoded by MYH7 is associated with significantly slower contraction kinetics than the  $\alpha$ -MHC isoform encoded by MYH6 (Holubarsch et al. 1985; Sugiura et al. 1998). During human embryonic development  $\alpha$ -MHC is expressed both in the atria and ventricles. However, after birth a genetic switch occurs, resulting in dominant expression of the beta isoform in adult human ventricles (~90%  $\beta$ -MHC, 10%  $\alpha$ -MHC), which has been suggested to be mediated by increasing de novo methylation of the MYH6 promoter region (Gilsbach et al. 2014; Han et al. 2016). In knockout EHTs, expression of MYH6 was higher than in controls, while MYH7 expression was comparable to ERC018, possibly resulting from a lack of MYH6 repression due to the absence of de novo DNMTs in these cardiomyocytes. Consequently, this led to a lower ratio of  $\beta$ -MHC/ $\alpha$ -MHC in the cardiomyocytes which could explain the faster relaxation kinetics in the knockout cardiomyocytes. Moreover, the better pacing capture of knockout EHTs could also be accounted for by the higher  $\alpha$ -MHC content. Since pacing pulses at high frequencies can only be followed if the cells are able to return to their relaxed state fast enough to contract again at the next pulse, faster relaxation due to expression of the fast MHC isoform could lead to pacing capture up to higher frequencies. The trisomy control cells, which also exhibited a slightly lower  $\beta$ -MHC/ $\alpha$ -MHC ratio and moderately faster relaxation kinetics than ERC018, followed pacing up to higher frequencies than ERC018, but still lost capture significantly earlier than the homozygous DNMT3A knockout.

### 5.3.2 Calcium handling and action potentials

In the above-mentioned study published by Fang and colleagues (2016), siRNA-mediated knockdown of DNMT3A led to significant calcium handling disturbances in the cardiomyocytes with reduced calcium transients and deregulated expression of calcium signaling pathways. In contrast, knockout EHT did not differ significantly from ERC018 regarding calcium sensitivity and reaction to long-term calcium overload. However, minor differences were detected in the negative phase of the FFR-curves, with ERC018 EHTs exhibiting a progressively steeper decline in force with increasing frequencies, as compared to knockouts. Since frequency-induced force adaptations have been suggested to be dependent on the expression of calcium cycling proteins



such as SERCA2A (Hasenfuss et al. 1996), these observations could be an indicator of altered calcium handling in the absence of DNMT3A. Nevertheless, no differences in transcript levels of the analyzed sarcoplasmic reticulum calcium cycling proteins could be detected. The observed discrepancies between the experiments in mouse cardiomyocytes and human EHT could be attributed to the different calcium cycling mechanisms between the two species, as has been described before (Haghighi et al. 2003).

Another observation in the knockdown experiments in mouse cardiomyocytes was a scarcer spontaneous occurrence and lower maximal amplitude of field action potentials (Fang et al. 2016). In accordance with these findings, action potentials recorded from compound heterozygous knockout EHTs with sharp microelectrodes displayed a lower amplitude than ERC018 EHTs. Additionally, the overall shape of the action potential differed between the groups, with knockout EHTs displaying a distinct notch prior to plateau phase and a shorter repolarization phase. In line with this, analysis of ion channel transcript levels revealed a significantly altered ion channel expression after DNMT3A knockout. This was evidenced by higher expression of the genes encoding for the channels responsible for L-type and T-type calcium currents (CACNA1C and CACNA1G, respectively), as well as genes encoding for channels involved in the currents  $IK_1$  (KCNJ2),  $IK_r$  (KCNH2),  $I_{to}$  (KCND3, KCNA4, KCNIP2), and  $IK_{ATP}$  (KCNJ11). The higher  $I_{to}$  channel expression could be responsible for the observed notch prior to plateau phase, as the channel rapidly opens in response to membrane depolarization caused by sodium influx and results in quick repolarization due to potassium efflux. The channel is subsequently quickly deactivated, resulting in transition into the L-type and T-type calcium channel-mediated plateau phase of the action potential. Increased expression of the repolarizing currents  $IK_1$ ,  $IK_r$ , and  $IK_{ATP}$  on the other hand could facilitate faster efflux of potassium ions from the cell leading to significantly faster repolarization as observed in the knockouts (figure 68; Möller and Witchel 2011). The shorter APD in DNMT3A knockout hiPSC-EHTs suggest that the latter alteration outweighs the expected increase in AP plateau in consequence of higher calcium channel expression. Importantly, the observed dysregulation of ion channel expression patterns in the knockouts might directly be related to the absence of de novo methylation since expression of several ion channel genes including CACNA1C, CACNA1G, KCNH2, KCNA3, and KCNMA1 has been shown to be regulated by DNMT3A mediated methylation of the respective promoter regions (Toyota et al. 1999; Cicek et al. 2013; Chen et al. 2014; He et al. 2017; Kim et al. 2017b).

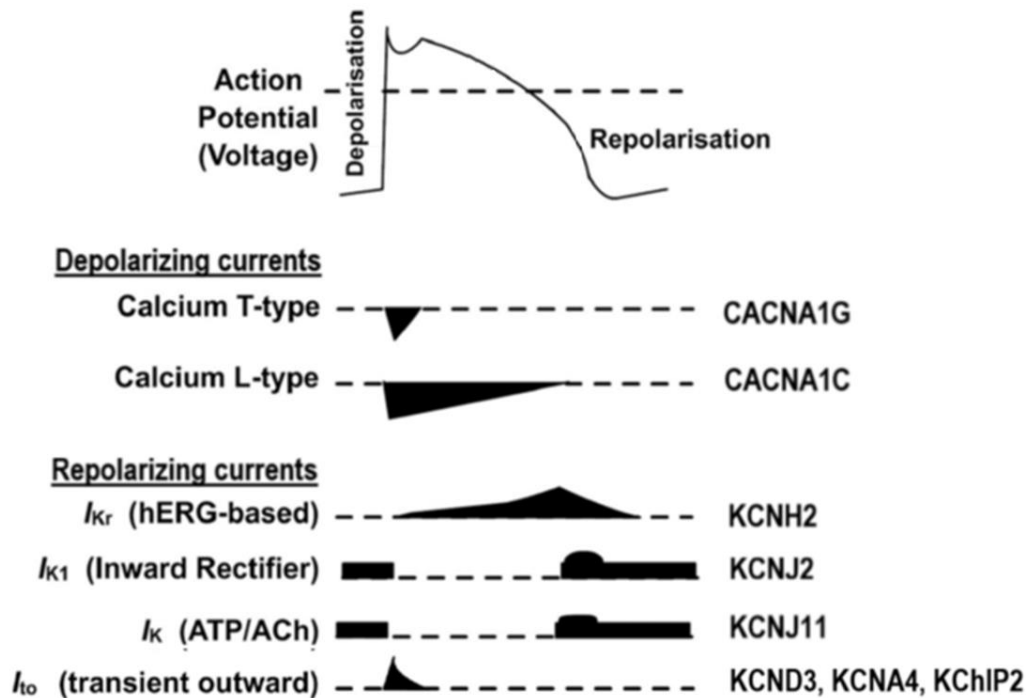


**Figure 68: Ion channel contribution to the altered cardiac action potential form in knockout EHTs.** Ion channel genes related to action potential form with increased expression in DNMT3A knockout EHTs. Depicted is the name of the current (left), the activation period (middle, black diagram), as well as the name of the gene encoding for the channel subunits (right). Adapted from Möller & Witchel 2011).

### 5.3.3 Vacuolic accumulations in knockout EHTs

The structure of the vacuoles observed inside the cardiomyocytes in knockout EHTs was reminiscent of adipose tissue, suggesting dysregulation of metabolic pathways leading to deposition of lipid accumulations in the knockout cells. Similar vacuolic deposits have been previously observed in histological analysis of human heart sections of patients suffering from metabolic syndrome (figure 69) and Oil red O staining revealed those vacuoles to be filled with lipids (Marfella et al. 2009). Interestingly, cardiac function of the patients negatively correlated with the degree of those lipid accumulations, suggesting at least a partial causality of the lipid deposition for cardiomyocyte dysfunction. In addition to the histological findings, Marfella and colleagues found significantly increased levels of the peroxisome proliferator-activated receptor gamma ( $PPAR\gamma$ ) in the patients, which, under physiological conditions, is only moderately expressed in the human heart.  $PPAR\gamma$  displays high expression levels in adipose tissue where it regulates the storage of fatty acids and glucose metabolism, as well as adipocyte differentiation

(Rosen et al. 1999). Moreover, PPAR $\gamma$  has been implicated in macrophage function, inflammation, and development of atherosclerosis (Zhang and Chawla 2004). Interestingly, cardiomyocyte-specific overexpression of PPAR $\gamma$  in mice also resulted in accumulation of vacuoles inside cardiomyocytes, suggesting a causal link of increased PPAR $\gamma$  expression and lipid deposition (Son et al. 2007). In this study, a significant increase in free fatty acids was observed in the cardiomyocytes, and Oil red O staining indicated accumulation of lipid droplets in the cytoplasm of the cardiomyocytes. In addition, the mice developed cardiac dysfunction and died at young age. Two other studies reported that retroviral overexpression of PPAR $\gamma$  in fibroblasts was sufficient to induce transdifferentiation of the cultured cells into adipocytes (Tontonoz et al. 1994) and that adenoviral expression of PPAR $\gamma$  in the liver of PPAR $\alpha$ -deficient mice induced expression of adipocyte-specific genes (Yu et al. 2003).

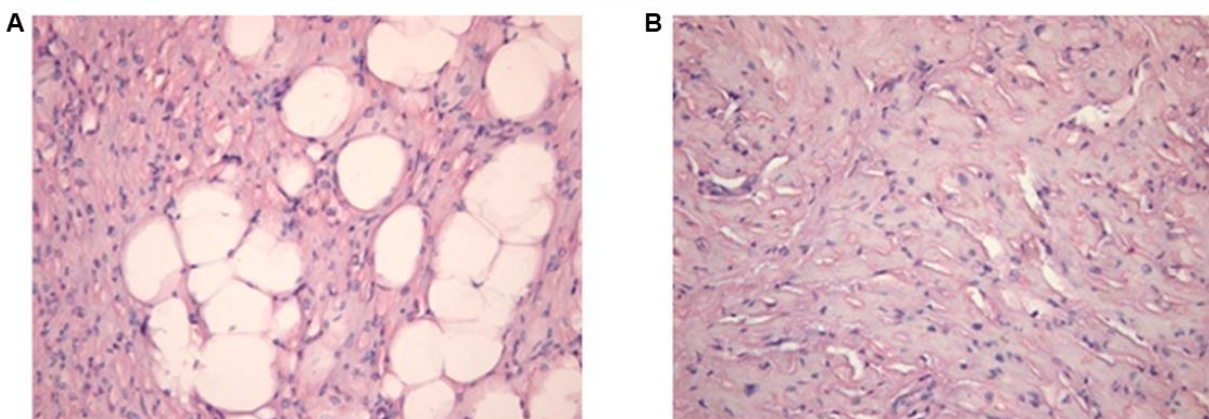


**Figure 69: Human heart sections stained with H&E (Marfella et al. 2009).** (A) Patient with metabolic syndrome. (B) Patient without metabolic syndrome. 600x magnification.

Interestingly, a study on epidermis-specific knockout of Dnmt3a in mice links dysregulation of PPAR $\gamma$  expression to the absence of Dnmt3a-mediated de novo methylation (Rinaldi et al. 2017). Knockout mice were prone to the development of squamous cell carcinomas which displayed dysregulated gene transcription with a clear upregulation of genes connected to lipid metabolism such as PPAR $\gamma$ , which was shown to be regulated by promoter methylation by Dnmt3a in mice. Expression analysis of PPAR $\gamma$  in the knockout EHTs indeed also revealed significantly higher transcript levels compared to the two controls, correlating with the degree of DNMT3A knockout. This was accompanied by upregulation of adiponectin in knockout EHTs, which has been shown to be involved in adipocyte differentiation and accumulation of lipids (Song et al. 2016). Additionally, the high transcript abundance of BCL2 in the knockout EHTs can be understood as an indicator for upregulated PPAR $\gamma$  activity, since it has been shown to be a major downstream target of activated

PPAR $\gamma$  signaling (Ren et al. 2009). Moreover, Oil red O staining of whole mount EHTs led to a clear staining pattern of the vacuoles, confirming the presence of lipid accumulations in the EHTs. Taken together, these results suggest that knockout of DNMT3A in cardiomyocytes led to derepression of PPAR $\gamma$ . Increasing levels of the receptor in turn promoted accumulation of lipids inside the cardiomyocytes, impairing their function which ultimately resulted in the observed functional degradation of knockout EHTs. Future studies will have to evaluate whether such adverse consequences only occur if DNMT3A is deleted or inhibited early in cardiomyocyte development or also later in life. The latter would raise concerns about the safety of DNMT inhibitors as therapy against hypertrophic heart diseases (Xiao et al. 2014; Watson et al. 2015; Stenzig et al. 2016; Stenzig et al. 2018).

#### 5.4 DNA methylation patterns and gene expression

Knockout of DNMT3A led to significant gene expression changes in the cardiomyocytes compared to ERC018. Interestingly, genes which were either not at all expressed or expressed at high levels in ERC018 EHTs were hardly affected by knockout of DNMT3A. This is in line with the concept of different modes of epigenetic gene regulation. Silenced genes are usually repressed by both DNA methylation and repressive histone marks, rendering the erasure of DNA methylation alone insufficient to induce gene transcription. Actively transcribed genes on the other hand, are often decorated by hypomethylated promoter regions and activating histone marks, resulting in no further effect of DNMT3A knockout on transcription activation. In contrast, almost all analyzed examples of genes expressed at low levels in ERC018 were highly upregulated in the absence of DNMT3A. This observation is in line with the observation that genes which are only repressed by DNA methylation in absence of additional repressive histone marks often show incomplete repression and are expressed at low levels (Ford et al. 2017). Knockout of DNMT3A in the present study could therefore have led to the observed higher expression of these genes, as the main gene repression mechanism of de novo methylation had been removed. The observed lower gene expression of some genes in the knockout compared to ERC018 could be explained by missing gene body methylation due to absence of DNMT3A, as gene body methylation has been associated with activation of gene transcription (Ball et al. 2009). In order to analyze the role of DNMT3A in cardiac disease, both control and knockout EHTs were treated with the pro-hypertrophic drugs PE and ET-1. Both compounds have been shown to induce a hypertrophic response in cardiomyocytes by activation of Akt, ERK1/2, calcineurin/NFAT and other signaling pathways, leading to expression of hypertrophic genes such as ANP and BNP, as well as to

downregulation of calcium handling proteins such as SERCA2A (Shubeita et al. 1990; Hasenfuss et al. 1994; Sugden 2003; Rolfe et al. 2005; Tham et al. 2015). In line with this, upregulation of ANP and BNP was observed both on transcript level and on immunohistochemically stained tissue sections, while downregulation of ATP2A2 encoding for SERCA2A was observed on transcript level.

Whole-genome DNA methylation analysis by RRBS revealed significantly lower global DNA methylation levels in the knockout EHTs compared to ERC018 underlining the importance of DNMT3A for DNA methylation homeostasis in cardiomyocytes. Knockout of DNMT3A had a significant impact on the DNA methylation status of defined regions resulting in almost 3,000 DMCs between the knockout and wildtype EHTs. More than two thirds of these DMCs displayed hypomethylation in the knockout compared to ERC018, which is in line with the absence of de novo methylation activity in the knockout. Analysis of the DMCs in knockout EHTs showed close clustering of the replicates with significant differences to the clustered ERC018 EHTs. This suggests that the methylation changes were not randomly established across the genome, but rather followed a specific pattern leading to similar DNA methylation profiles in all knockout EHTs. Pro-hypertrophic conditions (discussed in detail in 5.5) reduced the number of DMCs by almost two thirds with only 1,020 regions showing significant methylation differences between genotypes. However, also in this comparison most of the DMCs were hypomethylated compared to ERC018 (~80%) and the EHTs of each genotype clustered closely together with their respective replicates. One possible explanation for the lower number of DMCs between the genotypes under treatment could be related to the potential role of DNMT3A-mediated de novo methylation in late development and maturation (as discussed in 5.2). Several protein isoform switches of sarcomere proteins associated with maturation of cardiomyocytes have been shown to be regulated by promoter de novo methylation of the embryonic isoform (Gilsbach et al. 2014; Han et al. 2016). Absence of de novo methylation activity in the knockout cardiomyocytes could therefore lead to impaired cardiomyocyte maturation with retention of embryonic methylation and gene expression patterns, as was specifically observed for the  $\alpha/\beta$ -MHC isoforms. Pressure overload-induced cardiac hypertrophy partially resembles embryonic DNA methylation patterns (Gilsbach et al. 2014). Taking these observations together, it might be possible that treatment of ERC018 with PE and ET-1 induces a more immature DNA methylation profile in these cells, rendering methylation in hypertrophic controls more similar to the retained immature methylation patterns in the knockout cells, resulting in the observed lower number of DMCs between genotypes.

In contrast to the results of the genotype comparisons, treatment with the pro-hypertrophic substances had only moderate effects on DNA methylation in both genotypes (110 DMCs for

ERC018 and 250 DMCs for the knockout). This is in line with results published by Gilsbach and colleagues (Gilsbach et al. 2018), who found no major CpG methylation alterations in cardiomyocytes of heart failure patients compared to non-failing controls, but rather changes in histone marks correlating with gene expression changes. Nevertheless, the observed methylation changes in our study seemed to be specific for the treatment leading again to distinct clustering of the ERC018 EHTs according to their treatment condition. In the knockout, clustering was less distinct, suggesting that the establishment of the PE and ET-1-induced DNA methylation changes is – at least in part – dependent on the presence of DNMT3A. This hypothesis is supported by the division of DMCs in hyper and hypomethylated regions in each genotype. Out of the observed DMCs in ERC018, two thirds were higher methylated under hypertrophic treatment, which is in line with data from the in vivo study by Stenzig et al. (2018), where animals suffering from TAC-induced cardiac hypertrophy also displayed a trend towards higher DNA methylation. In contrast, more than 70% of DMCs observed under treatment of knockout EHTs with PE and ET-1 were hypomethylated compared to control conditions. This result is in accordance with the expected reduction or abolishing of de novo methylation in DNMT3A knockout cardiomyocytes. Moreover, while the absolute number of hypermethylated DMCs was similar in the two genotypes (74 versus 69 DMCs), there is almost no overlap in the affected regions (figure 70 A), with only two miRNAs and a pseudogene being hypermethylated under treatment in both genotypes. Similar results were obtained when comparing the hypomethylated regions between the two genotypes (figure 70 B), where only 2 DMCs, associated with a pseudogene and a phosphatase, were hypomethylated in both genotypes. These results indicate that the pro-hypertrophic treatment affects distinct DNA methylation modification pathways including different DNA methylation eraser pathways such as TET, depending on whether DNMT3A is present or absent in the tissue. This hypothesis, however, requires further investigation.

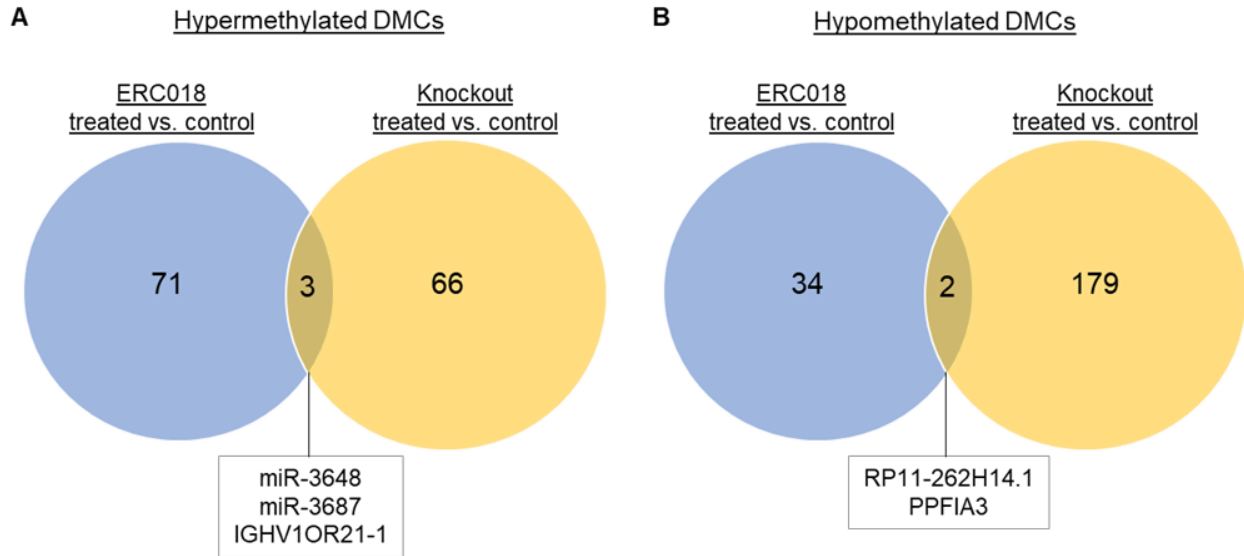


**Figure 70: DMCs under pro-hypertrophic treatment.** (A) Number of hypermethylated DMCs under treatment vs. control conditions for ERC018 (blue circle) and the knockout (yellow circle) and overlap between the two groups. (B) Number of hypomethylated DMCs under treatment vs. control conditions for ERC018 (blue circle) and the knockout (yellow circle) and overlap between the two groups. Gene names associated with the overlapping DMCs are indicated in the grey boxes.

When looking at the distribution of DMCs among functional regions of the genome, up to 50% of all DMCs were located within promoter regions, while less than 40% were found in intergenic regions. This distribution is inconsistent with the results from the above-mentioned study by Gilsbach and colleagues (2014), who observed only 2% of promoter-associated DMCs, while 71% were located in intergenic regions. This discrepancy can be explained by the different techniques used for DNA methylation analysis. The study by Gilsbach et al. used a whole-genome bisulfite sequencing approach covering all genomic regions to a similar degree. In contrast, the present study performed RRBS, which is biased towards CpG-rich genomic regions. Since functional regions such as promoters have a higher CpG content than intergenic regions (Smith and Meissner 2013) RRBS results are usually enriched for these functional regions.

The observed DMCs were tested for association with pathological pathways by IPA “tox list” analysis. The comparison of knockout and ERC018 EHTs yielded the most significant associations with “increases cardiac proliferation”, “RAR activation”, and “NRF2-mediated oxidative stress response”. The first two of these pathologies are associated with pathways of cell proliferation and cell dedifferentiation which supports the idea that knockout of DNMT3A in cardiomyocytes leads to more immature cells. Moreover, when looking at upstream regulators associated with the DMCs

in this group comparison, 15 out of the 34 regulators were related to the functional categories pluripotency, development and differentiation, a further hint to immaturity and incomplete differentiation of the knockout cardiomyocytes. The third pathology, associated with 25 DMCs in this comparison, “NRF2-mediated oxidative stress response”, has been consistently described as an upstream pathway regulating both PPAR $\gamma$  and lipogenic gene expression (Cho et al. 2010; Reddy and Standiford 2010; Huang et al. 2010; Polvani et al. 2012; Zhan et al. 2012), providing a plausible link to the observed increase in PPAR $\gamma$  expression and lipid accumulation.

Interestingly, the three pathways affected in DNMT3A-knockout EHT were less significantly associated with differential methylation under pro-hypertrophic conditions, leaving necrosis/cell death and TGF $\beta$ -signaling as the most significantly-associated pathologies. In concordance with this, the number of upstream regulators associated with immature cardiomyocyte functions like cell proliferation, pluripotency, development, and differentiation was much lower in this comparison. One possible explanation for this observation is that the pro-hypertrophic treatment promotes maturation of the knockout cardiomyocytes, as ET-1 has been described to lead to cardiomyocyte exit of the cell cycle, contributing to terminal cardiomyocyte differentiation during heart development (Paradis et al. 2014). In line with this idea, 6 out of 13 upstream regulators found under treatment conditions were related to cell cycle functions. Under treatment conditions, the NRF2 pathway lost association with more than half of the DMCs observed under control conditions, which could implicate a partial return of the pathway’s activity to control conditions in treated knockout EHTs. In line with this, the expression level of PPAR $\gamma$  in knockout EHTs under pro-hypertrophic treatment was no longer significantly higher than in treated and untreated ERC018 EHTs. PPAR $\gamma$  signaling has been shown to be associated with pathways involved in lipid metabolism, cell growth and proliferation, cell migration, and apoptosis (Kvandová et al. 2016). Interestingly, 21 out of the 34 upstream regulators associated with DMCs under control conditions were found to be linked to these functions, while under PE and ET-1 treatments association of regulators with fat metabolism, cell proliferation, and cell migration was almost lost, which could again point to a central role of PPAR $\gamma$  for the differences between knockout and ERC018 EHTs.



In a study published by Nührenberg and colleagues (2015), mice carrying a cardiomyocyte-specific Dnmt3a/3b double-knockout were analyzed under control and pressure overload-induced hypertrophic conditions. Although the authors reported no functional consequences of the knockout under control or hypertrophic conditions, they observed increased expression of several genes, which for the top three upregulated genes (Slc9a3, Krt8, Aldh1l1) correlated with a decrease in DNA methylation. Analysis of our own methylation data also revealed hypomethylation of those three loci (figure 71), suggesting conservation of these DNMT3A targets across species. However, since a comprehensive DNA methylation analysis for these animals was provided only as raw data (Nührenberg et al. 2015), further comparison of the effect of DNMT3A knockout on DNA methylation profiles was not possible due to lack of bioinformatics expertise.

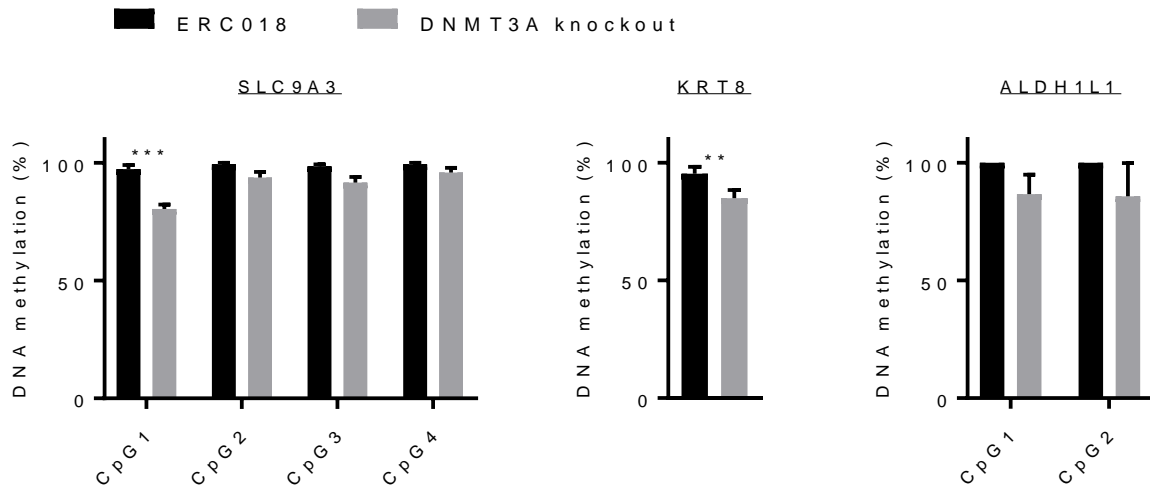


**Figure 71: DNA methylation differences of SLC9A3, KRT8, and ALDH1L1.** DNA methylation analysis by RRBS revealed significantly lower DNA methylation at the SLC9A3 and KRT8 gene loci in the knockout EHTs compared to ERC018. For ALDH1L1 the difference was not significant. n=3-4 EHTs, SLC9A3: 2way ANOVA plus Bonferroni's post-test, \*\*\*p<0.001; KRT8: Student's t-test, \*\*p<0.01.

## 5.5 DNMT3A and pro-hypertrophic treatment

Control and knockout EHTs were treated with the pro-hypertrophic drugs PE and ET-1 in order to analyze whether absence of de novo methylation has any influence on the pharmacological induction of cardiac hypertrophy. Treatment had a positive chronotropic effect on the EHTs, as expected for PE (Srivastava et al. 1977). Moreover, the treatment resulted in a reduction of contractile force in both control EHT lines, indicating hypertrophy-induced functional impairments as seen previously in rat EHTs (Hirt et al. 2014). Cardiac fibrosis, which is another important hallmark of cardiac hypertrophy, could not be observed in this model. This can be explained by

the too low abundance of matrix producing cells such as fibroblasts in the EHTs due to the high purity of the hiPSC-derived cardiomyocytes used for EHT generation, often reaching a cardiomyocyte purity of >90%. Nevertheless, typical gene expression and functional effects of pro-hypertrophic treatment could be observed, confirming the validity of the chosen treatment as a cardiac stress model.

Knockout of DNMT3A in EHTs did not influence the positive chronotropic response of the EHT to PE + ET-1 nor the hypertrophy-associated gene expression changes (discussed in 5.4). Gene expression of SERCA2A, ANP, and BNP in knockouts was altered in the same way as in the control lines under treatment, reaching transcript levels not significantly different from those observed in ERC018. These observations suggest that the “classical” gene expression changes induced by hypertrophic signaling in cardiomyocytes are largely independent of de novo DNA methylation by DNMT3A. Another indicator for dispensability of DNMT3A for hypertrophic signaling was the downregulation of DNMT3A transcript levels after PE and ET-1 treatment in all EHT lines, which we previously also observed in rats undergoing pressure overload by TAC surgery (own unpublished data, figure 72). Since global DNA methylation under hypertrophic conditions, as discussed in 5.4, showed a tendency towards higher global DNA methylation, it is possible that downregulation of DNMT3A in cardiomyocytes represents a compensatory mechanism.

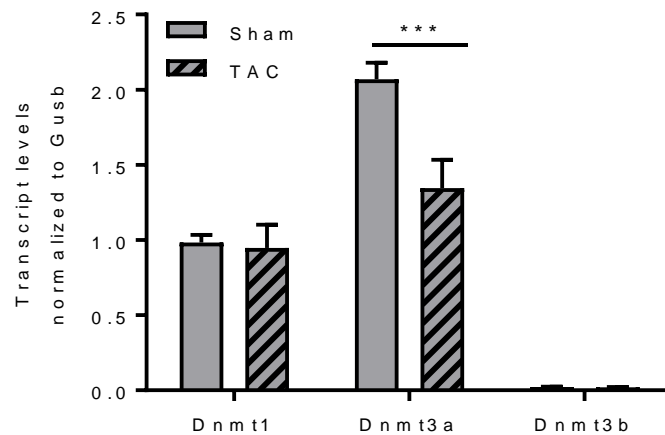


**Figure 72: Dnmt isoform expression in rats after TAC surgery (own unpublished data).**

While transcript levels of Dnmt1 and Dnmt3b were not significantly different between sham and TAC animals, TAC surgery led to significantly lower Dnmt3a transcript levels.  $n=3$  animals per group, 2way ANOVA plus Bonferroni's post-test for multiple comparisons, \*\*\* $p<0.001$ .

These results are also in line with data from Nührenberg and colleagues (2015) who found Dnmt3a and Dnmt3b to be expendable for pressure overload-induced hypertrophic signaling in mice. However, in contrast to the authors' finding that cardiomyocyte-specific double knockout of the de novo DNMTs also had no functional consequences of pressure overload-induced hypertrophy in mice, knockout of DNMT3A in our study abolished the loss of contractility in control EHT lines observed under PE and ET-1 treatment and in fact reversed the force-reducing in a force-increasing effect.

There are several possible explanations for these discrepant observations. First, in the study published by Nührenberg et al., pressure overload by TAC surgery was used to induce cardiac hypertrophy, while the present study relied on pharmacological treatment with pro-hypertrophic agents. This could lead to activation of different pro-hypertrophic pathways in the cardiomyocytes, as has been shown for hypertrophy induced by either pressure or volume overload (You et al. 2017). Additionally, species differences between mice and humans could contribute to differential responses to the same stimulus, as has been shown for many other aspects of cardiac physiology, including phospholamban mutations (Haghighi et al. 2003). Moreover, the in vivo study was carried out in a more complex setting which includes all different cell types of the heart, such as endothelial cells, macrophages, and fibroblasts. These also react to pressure overload by downstream signaling, inducing for example inflammation or fibrosis, which contribute to the hypertrophic response of the heart (Moore-Morris et al. 2014; Hashimoto and Kass 2015). Data from pharmacological DNMT inhibition in different models of cardiac hypertrophy further emphasizes this point. Watson and colleagues (2015) observed significantly less hypertension-induced hypertrophy in rats treated with the non-specific, nucleosidic DNMT inhibitor 5-azacytidine, which suggests contribution of DNA methylation in fibroblasts to the development of fibrosis during cardiac hypertrophy. Similar results were obtained from a rat EHT-based in vitro model of cardiac hypertrophy where treatment with the non-nucleosidic DNMT inhibitor RG108 significantly improved EHT contractility and prevented fibrosis under hypertrophic conditions (Stenzig et al. 2016). In contrast to the human EHT model, rat EHTs not only contain cardiomyocytes but comprise a mixture of all other cardiac cell types including fibroblasts. The above-mentioned knockout study by Nührenberg and colleagues was performed in a cardiomyocyte-specific manner. It is thus possible that hypertrophic signaling by fibroblasts and endothelial cells - with intact de novo methylation - on top of largely intact signaling in cardiomyocytes contributed to the hypertrophic remodeling and functional impairment observed in the knockout mice, together masking more subtle effects in cardiomyocytes.

The human DNMT3A knockout EHTs in this study bear the advantage of not being subject to these confounders, enabling analysis of the role of DNMT3A knockout specifically in cardiomyocytes. While hypertrophic signaling from the cell periphery to transcription appeared still intact in this setting (e.g. increased ANP/BNP), functional consequences of the hypertrophic agonists were directionally different in knockout EHTs, indicating dissociation of the two effects and involvement of DNMT3A-mediated DNA methylation in the signaling towards functional impairment. Interestingly, treatment with PE and ET-1 normalized the aberrant increase in gene expression of lowly expressed genes observed in untreated knockout EHTs, returning expression to levels to a state similar to expression in ERC018. One possible explanation for this is related to the general increase in mRNA and protein production induced by PE and ET-1 (Simpson et al. 1982; Long et al. 1989). Genes with high expression in cardiomyocytes not only display non-methylated promoters but carry additional activating chromatin marks and are accordingly strongly upregulated under PE and ET-1 treatment (Gilsbach et al. 2014). Lowly expressed genes, which are silenced in ERC018 only by DNA methylation, were higher expressed in the knockout due to the missing repression by promoter methylation (as discussed in detail in 5.4). However, since these regions do not carry the further activating chromatin marks present at highly expressed loci (such as histone H3K4 trimethylation), treatment with PE and ET-1 does not further induce gene transcription, leading to a relative normalization of the respective transcript concentrations.

Treatment with PE and ET-1 did not only fail to induce the expected functional impairments in knockout EHTs, but prevented the lipid accumulation and associated functional degradation observed in untreated knockout EHTs. Histological analysis revealed significantly less vacuoles and a partially rescued alignment of cardiomyocyte filaments along the EHT force lines, which was paralleled by rescued beating activity, beating regularity, and force generation, which under treatment all reached values similar to ERC018 control EHTs. The lipid storage master transcription factor PPAR $\gamma$ , possibly involved in the observed lipid accumulation (as discussed above), was also significantly downregulated, to a level only slightly above the one in treated ERC018 EHT. This could be a direct effect of PE and ET-1 treatment, as a negative effect on PPAR $\gamma$  gene expression has been described before for both compounds (Wolf et al. 2014; Gao et al. 2018). Figure 73 summarizes the proposed interplay of DNMT3A, PPAR $\gamma$ , and PE/ET-1 signaling in the EHTs.

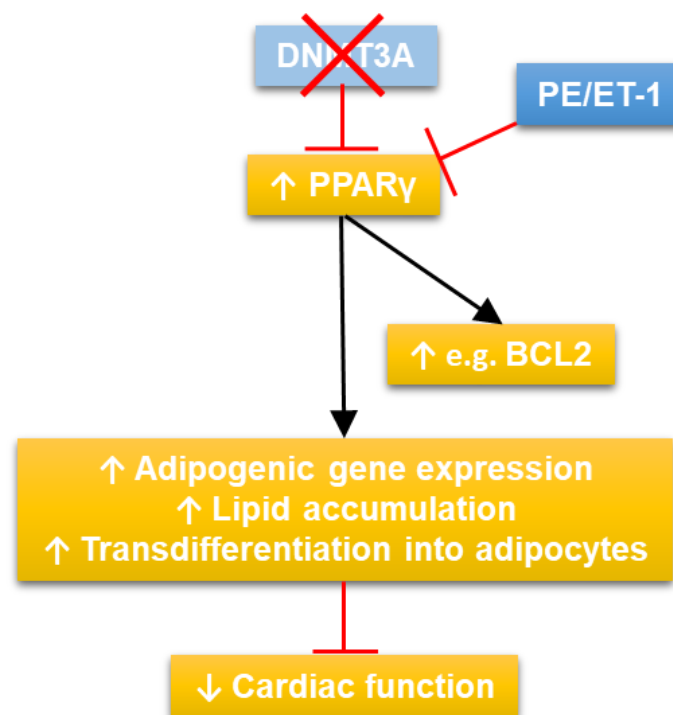


**Figure 73: Proposed interplay of signaling pathways.** In wildtype EHTs, DNMT3A represses expression of PPAR $\gamma$ . Knockout of DNMT3A leads to derepression of PPAR $\gamma$  which under non-treatment conditions increases expression of its downstream targets such as BCL2, as well as adipogenic gene expression, lipid accumulation, and transdifferentiation into adipocytes, leading to a decrease in cardiac function. Treatment with PE and ET-1 attenuates PPAR $\gamma$  expression and signaling, preventing the detrimental adipogenic changes.

## 5.6 Conclusion and future perspectives

Taken together, the data obtained from EHT generated from DNMT3A knockout hiPSC-derived cardiomyocytes provided important insights into the role of de novo DNA methylation in cardiomyocytes under control and stress conditions. It could be demonstrated that DNMT isoform 3A is dispensable for hiPSC culture and differentiation into the cardiac lineage but has important functions for cardiomyocyte physiology. Both, the shape of the action potential and the contraction and relaxation kinetics of cardiomyocytes were significantly altered in DNMT3A knockout EHTs, paralleled by transcript level changes of genes encoding for ion channels (IK<sub>1</sub>, IK<sub>r</sub>, IK<sub>ATP</sub>, I<sub>to</sub>) and contractile proteins ( $\alpha/\beta$ -MHC). These findings indicated that DNMT3A is involved in the regulation of those genes, leading to deregulated expression in absence of DNMT3A, which in turn influences the action potential shape and kinetics of contraction. Additionally, ablation of de novo methylation

activity resulted in higher transcript abundance of PPAR $\gamma$ , as well as an increase in adipogenic signaling and lipid accumulation in the EHTs. This suggested a role for DNMT3A in repression of PPAR $\gamma$  and thereby prevention of PPAR $\gamma$ -mediated activation of adipogenic signaling pathways in cardiomyocytes. Moreover, absence of DNMT3A did not interfere with PE and ET-1 induced hypertrophic signaling itself, but inhibited manifestation of functional impairments following this treatment.

For further characterization of the knockout EHTs, RNA sequencing and/or proteome analysis is indispensable to reach a more complete understanding of the gene clusters and pathways regulated by DNMT3A. Additionally, knockout EHTs should be treated with a PPAR $\gamma$ -antagonist in order to verify whether upregulation of PPAR $\gamma$  itself is causative for the observed morphological aberrations and lipid accumulation. As the importance of DNA methylation in other cell types has also been implicated before, the DNMT3A knockout hiPSC could perspective be differentiated into fibroblasts or endothelial cells, in order to also analyze the role of de novo methylation in these cells. Implementation of these cell types into the EHT model as previously established in our laboratory (Tessa Werner 2018) could also help improving the system for better representation of the physiological situation in the heart and thus allow for analysis of other aspects of cardiac hypertrophy such as cardiac fibrosis and the role of DNA methylation for it.

## 6 Summary

In recent years, DNA methylation has gained increasing attention as a regulator of gene transcription, but its role in heart disease is not well understood. To better characterize the function of DNA methylation in cardiomyocytes under physiological and stress conditions, the main cardiac DNA methyltransferase isoform, DNMT3A, was knocked out in human induced pluripotent stem cells (hiPSC) by CRISPR/Cas9 gene editing at the heterozygous, homozygous and compound heterozygous state, allowing the establishment of gene-dose relationships. The consequences of the knockout were analyzed in engineered heart tissues (EHT) generated from knockout hiPSC-derived cardiomyocytes in comparison to control EHTs from isogenic wildtype cells under baseline and pro-hypertrophic treatment conditions.

Knockout of DNMT3A had no effect on differentiation of hiPSC into the cardiac lineage, yielding beating cardiomyocytes at high purity. Functional analysis revealed significantly faster relaxation kinetics and shortened action potentials in knockout EHTs compared to controls and significant functional degradation as well as arrhythmias after three weeks of culture. Hypertrophic intervention by treatment of EHTs with phenylephrine and endothelin-1 for 7 days, as expected, reduced contractile force in auxotonically contracting control EHTs, while it increased contractile force in knockout EHTs, reaching values of control EHTs in the absence of hypertrophic agonists.

Molecular analysis revealed significant hypomethylation in knockout compared to controls. Several genes with low expression in control cardiomyocytes were upregulated in the absence of DNMT3A, suggesting direct regulation of those genes by DNA methylation. Among these genes were several potassium currents, possibly accounting for shorter action potentials and abbreviated relaxation, and the transcription factor peroxisome proliferator-activated receptor gamma (PPAR $\gamma$ ), normally regulating fat metabolism in adipocytes and hepatocytes. In accordance with the latter, histological analysis revealed accumulation of lipid droplets in the knockout cardiomyocytes. Hypertrophic treatment of knockout EHTs prevented both the upregulation of PPAR $\gamma$  and the accumulation of lipids, suggesting a causal link between upregulation of PPAR $\gamma$ , lipid accumulation, and functional degradation of the knockout EHTs.

## 7 Zusammenfassung

Die regulatorischen Funktionen der DNA-Methylierung haben in den letzten Jahren zunehmend Beachtung gefunden. Ihre genaue Rolle in Herzkrankheiten ist dennoch bisher weitgehend ungeklärt. Die DNA-Methyltransferase DNMT3A, die wichtigste Isoform in Kardiomyozyten, wurde mit Hilfe von CRISPR/Cas9-Geneditierung in humanen induzierten pluripotenten Stammzellen (hiPSC) abgeschaltet. Aus hiPSC-abgeleiteten Kardiomyozyten wurde dann künstliches Herzgewebe (engineered heart tissue, EHT) zur Untersuchung der Funktion der DNA-Methylierung unter Kontroll- und Stressbedingungen generiert.

DNMT3A-Defizienz hatte keinen Einfluss auf die Differenzierung der hiPSC, sodass schlagende Kardiomyozyten generiert werden konnten. Auf funktioneller Ebene führte die Abschaltung von DNMT3A zu schnellerer Relaxation der EHTs im Vergleich zu Kontrollen, zu verkürzten Aktionspotentialen, sowie einer funktionellen Degeneration der EHTs mit zunehmenden Arrhythmien nach drei Wochen in Kultur. Behandlung von Kontroll-EHTs mit den pro-hypertrophen Substanzen Phenylephrin und Endothelin-1 führte wie erwartet zu einer Abnahme der Kontraktilität, wogegen in den methylierungsdefizienten EHTs die funktionelle Degeneration durch die Behandlung verhindert wurde.

In der molekularen Analyse war eine signifikante Hypomethylierung in den DNMT3A-defizienten EHTs im Vergleich zu Kontroll-EHTs sowie eine hohe Expression mehrerer Gene, die in Kontroll-Kardiomyozyten nur gering exprimiert waren, zu beobachten. Dies legte eine direkte Regulation der entsprechenden Gene durch DNA Methylierung nahe. Neben Ionenkanälen, deren Hochregulation an der beschleunigten Relaxationskinetik der DNMT3A-defizienten EHTs beteiligt sein könnten, war eines der besagten Gene der Peroxisom-Proliferator-aktivierte Rezeptor Gamma ( $PPAR\gamma$ ). Dieser ist normalerweise an der Regulation des Fett-Metabolismus in Adipozyten und Hepatozyten beteiligt. Im Einklang mit dieser Beobachtung zeigte sich in einer histologischen Analyse eine Akkumulation von Fetteinlagerungen in Kardiomyozyten in DNMT3A-defizienten EHTs. Die pro-hypertrophe Behandlung der EHTs verhinderte sowohl die höhere Expression von  $PPAR\gamma$ , als auch die Einlagerung des Fettes, was auf einen kausalen Zusammenhang zwischen höherer  $PPAR\gamma$  Expression, Fetteinlagerungen und der funktionellen Degeneration der EHTs hinweisen könnte.



## 8 References

- Aasen T, Raya A, Barrero MJ, et al (2008) Efficient and rapid generation of induced pluripotent stem cells from human keratinocytes. *Nat Biotechnol* 26:1276–1284. doi: 10.1038/nbt.1503
- Aguirre-Arteta AM, Grunewald I, Cardoso MC, Leonhardt H (2000) Expression of an alternative Dnmt1 isoform during muscle differentiation. *Cell Growth Differ* 11:551–9
- Aoi T, Yae K, Nakagawa M, et al (2008) Generation of Pluripotent Stem Cells from Adult Mouse Liver and Stomach Cells. *Science* (80- ) 321:699–702. doi: 10.1126/science.1154884
- Arai M, Alpert NR, MacLennan DH, et al (1993) Alterations in Sarcoplasmic Reticulum Gene Expression in Human Heart Failure A Possible Mechanism for Alterations in Systolic and Diastolic Properties of the Failing Myocardium KEY WoRDs \* ryanodine receptor \* phospholamban \* calsequestrin \* sarcoplasmic . *Circ Res* 72:463–469
- Ball MP, Li JB, Gao Y, et al (2009) Targeted and genome-scale strategies reveal gene-body methylation signatures in human cells. *Nat Biotechnol* 27:361–368. doi: 10.1038/nbt.1533
- Bashtrykov P, Jankevicius G, Jurkowska RZ, et al (2014) The UHRF1 protein stimulates the activity and specificity of the maintenance DNA methyltransferase DNMT1 by an allosteric mechanism. *J Biol Chem* 289:4106–4115. doi: 10.1074/jbc.M113.528893
- Berenji K, Drazner MH, Rothermel BA, Hill JA (2005) Does load-induced ventricular hypertrophy progress to systolic heart failure? *Am J Physiol Circ Physiol* 289:H8–H16. doi: 10.1152/ajpheart.01303.2004
- Boch J, Scholze H, Schornack S, et al (2009) Breaking the Code of DNA Binding. *Science* (80- ) 1509:1509–12. doi: 10.1126/science.1178811
- Boland MJ, Nazor KL, Loring JF (2014) Epigenetic regulation of pluripotency and differentiation. *Circ Res* 115:311–324. doi: 10.1161/CIRCRESAHA.115.301517
- Breckwoldt K, Letuffe-Brenière D, Mannhardt I, et al (2017) Differentiation of cardiomyocytes and generation of human engineered heart tissue. *Nat Protoc* 12:1177–1197. doi: 10.1038/nprot.2017.033
- Brenière-Letuffe D, Domke-Shibamiya A, Hansen A, et al (2018) Clonal dynamics studied in cultured induced pluripotent stem cells reveal major growth imbalances within a few weeks. *Stem Cell Res Ther* 9:165. doi: 10.1186/s13287-018-0893-2
- Burridge PW, Anderson D, Priddle H, et al (2007) Improved Human Embryonic Stem Cell Embryoid Body Homogeneity and Cardiomyocyte Differentiation from a Novel V-96 Plate

- Aggregation System Highlights Interline Variability. *Stem Cells* 25:929–938. doi: 10.1634/stemcells.2006-0598
- Burridge PW, Keller G, Gold JD, Wu JC (2012) Production of de novo cardiomyocytes: Human pluripotent stem cell differentiation and direct reprogramming. *Cell Stem Cell* 10:16–28. doi: 10.1016/j.stem.2011.12.013
- Caramazza D, Hussein K, Siragusa S, et al (2010) Chromosome 1 abnormalities in myeloid malignancies: A literature survey and karyotype-phenotype associations. *Eur J Haematol* 84:191–200. doi: 10.1111/j.1600-0609.2009.01392.x
- Challen G a, Sun D, Jeong M, et al (2011) Dnmt3a is essential for hematopoietic stem cell differentiation. *Nat Genet* 44:23–31. doi: 10.1038/ng.1009
- Chen M, Dasgupta C, Xiong F, Zhang L (2014) Epigenetic Upregulation of Large-Conductance Ca<sup>2+</sup>-Activated K<sup>+</sup> Channel Expression in Uterine Vascular Adaptation to Pregnancy. *Hypertension* 64:610–618. doi: 10.1161/HYPERTENSIONAHA.114.03407
- Cho H-Y, Gladwell W, Wang X, et al (2010) Nrf2-regulated PPAR $\gamma$  Expression Is Critical to Protection against Acute Lung Injury in Mice. *Am J Respir Crit Care Med* 182:170–182. doi: 10.1164/rccm.200907-1047OC
- Cicek MS, Koestler DC, Fridley BL, et al (2013) Epigenome-wide ovarian cancer analysis identifies a methylation profile differentiating clear-cell histology with epigenetic silencing of the HERG K<sup>+</sup>channel. *Hum Mol Genet* 22:3038–3047. doi: 10.1093/hmg/ddt160
- Dunn TM, Grunfeld L, Kardon NB (2001) Trisomy 1 in a clinically recognized IVF pregnancy. *Am J Med Genet* 99:152–153. doi: 10.1002/1096-8628(2000)9999:999<00::AID-AJMG1130>3.0.CO;2-P
- Eder A, Hansen A, Uebeler J, et al (2014) Effects of proarrhythmic drugs on relaxation time and beating pattern in rat engineered heart tissue. *Basic Res Cardiol* 109:436. doi: 10.1007/s00395-014-0436-7
- Ehrlich M (2003) Expression of various genes is controlled by DNA methylation during mammalian development. *J Cell Biochem* 88:899–910. doi: 10.1002/jcb.10464
- Eschenhagen T, Fink C, Remmers U, et al (1997) Three-dimensional reconstitution of embryonic cardiomyocytes in a collagen matrix: a new heart muscle model system. *FASEB J* 11:683–694. doi: 10.1096/fasebj.11.8.9240969
- Esteban MA, Xu J, Yang J, et al (2009) Generation of induced pluripotent stem cell lines from

- Tibetan miniature pig. *J Biol Chem* 284:17634–17640. doi: 10.1074/jbc.M109.008938
- Fang X, Poulsen RR, Wang-Hu J, et al (2016) Knockdown of DNA methyltransferase 3a alters gene expression and inhibits function of embryonic cardiomyocytes. *FASEB J* 30:1–18. doi: 10.1096/fj.201600346R
- Fink C, Ergün S, Kralisch D, et al (2000) Chronic stretch of engineered heart tissue induces hypertrophy and functional improvement. *FASEB J* 14:669–79. doi: 10.1007/0-387-21547-6\_18
- Ford EE, Grimmer MR, Stolzenburg S, et al (2017) Frequent lack of repressive capacity of promoter DNA methylation identified through genome-wide epigenomic manipulation. *bioRxiv* 170506:. doi: 10.1101/170506
- Fraher D, Ellis MK, Morrison S, et al (2015) Lipid abundance in zebrafish embryos is regulated by complementary actions of the endocannabinoid system and retinoic acid pathway. *Endocrinology* 156:3596–3609. doi: 10.1210/EN.2015-1315
- Gao R-R, Wu X-D, Jiang H-M, et al (2018) Traditional Chinese medicine Qiliqiangxin attenuates phenylephrine-induced cardiac hypertrophy via upregulating PPAR $\gamma$  and PGC-1 $\alpha$ . *Ann Transl Med* 6:153–153. doi: 10.21037/atm.2018.04.14
- Gilsbach R, Preissl S, Grüning B a., et al (2014) Dynamic DNA methylation orchestrates cardiomyocyte development, maturation and disease. *Nat Commun* 5:5288. doi: 10.1038/ncomms6288
- Gilsbach R, Schwaderer M, Preissl S, et al (2018) Distinct epigenetic programs regulate cardiac myocyte development and disease in the human heart in vivo. *Nat Commun* 9:391. doi: 10.1038/s41467-017-02762-z
- Gore A, Li Z, Fung HL, et al (2011) Somatic coding mutations in human induced pluripotent stem cells. *Nature* 471:63–67. doi: 10.1038/nature09805
- Haas J, Frese KS, Park YJ, et al (2013) Alterations in cardiac DNA methylation in human dilated cardiomyopathy. *EMBO Mol Med* 5:413–429. doi: 10.1002/emmm.201201553
- Haghighi K, Kolokathis F, Pater L, et al (2003) Human phospholamban null results in lethal dilated cardiomyopathy revealing a critical difference between mouse and human. *J Clin Invest* 111:869–876. doi: 10.1172/JCI17892
- Han P, Li W, Yang J, et al (2016) Epigenetic response to environmental stress: Assembly of BRG1–G9a/GLP–DNMT3 repressive chromatin complex on Myh6 promoter in pathologically

- stressed hearts. *Biochim Biophys Acta - Mol Cell Res* 1–10. doi: 10.1016/j.bbamcr.2016.03.002
- Hang CT, Yang J, Han P, et al (2010) Chromatin regulation by Brg1 underlies heart muscle development and disease. *Nature* 466:62–67. doi: 10.1038/nature10222
- Hanna JS, Shires P, Matile G (1997) Trisomy 1 in a clinically recognized pregnancy. *Am J Med Genet* 68:98. doi: 10.1002/1096-8628(2000)9999:999<00::AID-AJMG1130>3.0.CO;2-P
- Hansen a., Eder a., Bonstrup M, et al (2010) Development of a Drug Screening Platform Based on Engineered Heart Tissue. *Circ Res* 107:35–44. doi: 10.1161/CIRCRESAHA.109.211458
- Hargreaves DC, Crabtree GR (2011) ATP-dependent chromatin remodeling: Genetics, genomics and mechanisms. *Cell Res* 21:396–420. doi: 10.1038/cr.2011.32
- Hasenfuss G, Reinecke H, Studer R, et al (1994) Relation Between Myocardial Function and Expression of Sarcoplasmic Reticulum Ca<sup>2+</sup>-ATPase in Failing and Nonfailing Human Myocardium. *Circ Res* 75:434–442
- Hasenfuss G, Reinecke H, Studer R, et al (1996) Calcium cycling proteins and force-frequency relationship in heart failure. *Basic Res Cardiol* 91 Suppl 2:17–22
- Hashimoto T, Kass DA (2015) Stressed hearts inflame the body (in a good way). *Proc Natl Acad Sci U S A* 112:7113–4. doi: 10.1073/pnas.1507821112
- He T, Wang C, Zhang M, et al (2017) Epigenetic regulation of voltage-gated potassium ion channel molecule Kv1.3 in mechanisms of colorectal cancer. *Discov Med* 23:155–162
- Heineke J, Molkentin JD (2006) Regulation of cardiac hypertrophy by intracellular signalling pathways. *Nat Rev Mol Cell Biol* 7:589–600. doi: 10.1038/nrm1983
- Hinson JT, Chopra A, Nafissi N, et al (2015) Titin mutations in iPS cells define sarcomere insufficiency as a cause of dilated cardiomyopathy. *Science* (80- ) 349:982–986. doi: 10.1126/science.aaa5458
- Hirt MN, Boeddinghaus J, Mitchell A, et al (2014) Functional improvement and maturation of rat and human engineered heart tissue by chronic electrical stimulation. *J Mol Cell Cardiol* 74:151–161. doi: 10.1016/j.yjmcc.2014.05.009
- Hirt MN, Sörensen N a., Bartholdt LM, et al (2012) Increased afterload induces pathological cardiac hypertrophy: a new in vitro model. *Basic Res Cardiol* 107:307. doi: 10.1007/s00395-012-0307-z
- Holubarsch C, Goulette RP, Litten RZ, et al (1985) The economy of isometric force development,

- myosin isoenzyme pattern and myofibrillar ATPase activity in normal and hypothyroid rat myocardium. *Circ Res* 56:78–86. doi: 10.1161/01.RES.56.1.78
- Huang J, Tabbi-Anneni I, Gunda V, Wang L (2010) Transcription factor Nrf2 regulates SHP and lipogenic gene expression in hepatic lipid metabolism. *Am J Physiol Liver Physiol* 299:G1211–G1221. doi: 10.1152/ajpgi.00322.2010
- Huang V, Li LC (2012) miRNA goes nuclear. *RNA Biol* 9:269–273. doi: 10.4161/rna.19354
- Jackson M, Krassowska A, Gilbert N, et al (2004) Severe Global DNA Hypomethylation Blocks Differentiation and Induces Histone Hyperacetylation in Embryonic Stem Cells. *Mol Cell Biol* 24:8862–8871. doi: 10.1128/MCB.24.20.8862-8871.2004
- Jenuwein T (2001) Translating the Histone Code. *Science* (80- ) 293:1074–1080. doi: 10.1126/science.1063127
- Jinek M, Chylinski K, Fonfara I, et al (2012) A Programmable Dual-RNA – Guided DNA Endonuclease in Adaptive Bacterial Immunity. *Science* (80- ) 337:816–822. doi: 10.1126/science.1225829
- Kaebisch C, Schipper D, Babczyk P, Tobiasch E (2015) The role of purinergic receptors in stem cell differentiation. *Comput Struct Biotechnol J* 13:75–84. doi: 10.1016/j.csbj.2014.11.003
- Karakikes I, Stillitano F, Nonnenmacher M, et al (2015) Correction of human phospholamban R14del mutation associated with cardiomyopathy using targeted nucleases and combination therapy. *Nat Commun* 6:1–10. doi: 10.1038/ncomms7955
- Kim EJ, Kang KH, Ju JH (2017a) CRISPR-Cas9: a promising tool for gene editing on induced pluripotent stem cells. *Korean J Intern Med* 32:42–61. doi: 10.3904/kjim.2016.198
- Kim YG, Cha J, Chandrasegaran S (1996) Hybrid restriction enzymes: zinc finger fusions to Fok I cleavage domain. *Proc Natl Acad Sci* 93:1156–1160. doi: 10.1073/pnas.93.3.1156
- Kim YJ, Park HJ, Jahng GH, et al (2017b) A pilot study of differential brain activation to suicidal means and DNA methylation of CACNA1C gene in suicidal attempt patients. *Psychiatry Res* 255:42–48. doi: 10.1016/j.psychres.2017.03.058
- Kleinstiver BP, Pattanayak V, Prew MS, et al (2016) High-fidelity CRISPR–Cas9 nucleases with no detectable genome-wide off-target effects. *Nature* 529:490–495. doi: 10.1038/nature16526
- Klose RJ, Bird AP (2006) Genomic DNA methylation: The mark and its mediators. *Trends Biochem Sci* 31:89–97. doi: 10.1016/j.tibs.2005.12.008

- Kong P, Christia P, Frangogiannis NG (2014) The pathogenesis of cardiac fibrosis. *Cell Mol Life Sci* 71:549–574. doi: 10.1007/s00018-013-1349-6
- Kosicki M, Tomberg K, Bradley A (2018) Repair of double-strand breaks induced by CRISPR–Cas9 leads to large deletions and complex rearrangements. *Nat Biotechnol*. doi: 10.1038/nbt.4192
- Kou CY-C, Lau SL-Y, Au K-W, et al (2010) Epigenetic regulation of neonatal cardiomyocytes differentiation. *Biochem Biophys Res Commun* 400:278–283. doi: 10.1016/j.bbrc.2010.08.064
- Kvandová M, Majzúnová M, Dovinová I (2016) The Role of PPAR $\gamma$  in Cardiovascular Diseases. *Physiol Res* 65:343–363. doi: 10.2174/157489006777442441
- Laflamme MA, Chen KY, Naumova A V., et al (2007) Cardiomyocytes derived from human embryonic stem cells in pro-survival factors enhance function of infarcted rat hearts. *Nat Biotechnol* 25:1015–1024. doi: 10.1038/nbt1327
- Latronico MVG, Condorelli G (2009) MicroRNAs and cardiac pathology. *Nat Rev Cardiol* 6:418–429. doi: 10.1038/nrcardio.2009.56
- Lecina M, Ting S, Choo A, et al (2010) Scalable Platform for Human Embryonic Stem Cell Differentiation to Cardiomyocytes in Suspended Microcarrier Cultures. *Tissue Eng Part C Methods* 16:1609–1619. doi: 10.1089/ten.tec.2010.0104
- Li E, Bestor TH, Jaenisch R (1992) Targeted mutation of the DNA methyltransferase gene results in embryonic lethality. *Cell* 69:915–926. doi: 10.1016/0092-8674(92)90611-F
- Liao J, Karnik R, Gu H, et al (2015) Targeted disruption of DNMT1, DNMT3A and DNMT3B in human embryonic stem cells. *Nat Genet* 47:469–478. doi: 10.1038/ng.3258
- Lips DJ, DeWindt LJ, Van Kraaij DJW, Doevendans PA (2003) Molecular determinants of myocardial hypertrophy and failure: Alternative pathways for beneficial and maladaptive hypertrophy. *Eur Heart J* 24:883–896. doi: 10.1016/S0195-668X(02)00829-1
- Liu H, Zhu F, Yong J, et al (2008) Generation of Induced Pluripotent Stem Cells from Adult Rhesus Monkey Fibroblasts. *Cell Stem Cell* 3:587–590. doi: 10.1016/j.stem.2008.10.014
- Locher MR, Razumova M V, Stelzer JE, et al (2011) Effects of low-level  $\alpha$ -myosin heavy chain expression on contractile kinetics in porcine myocardium. *Am J Physiol Circ Physiol* 300:H869-78. doi: 10.1152/ajpheart.00452.2010
- Loh Y, Agarwal S, Park I, et al (2009) Generation of induced pluripotent stem cells from human

- blood. *Hematop Stem Cells* 113:1–3. doi: 10.1182/blood-2009-02-204800. The
- Long CS, Ordahl CP, Simpson PC (1989)  $\alpha$ 1-Adrenergic receptor stimulation of sarcomeric actin isogene transcription in hypertrophy of cultured rat heart muscle cells. *J Clin Invest* 83:1078–1082
- Lorch Y, Kornberg RD (2015) Chromatin-remodeling and the initiation of transcription. *Q Rev Biophys* 48:465–470. doi: 10.1017/S0033583515000116
- Lü S, Wang H, Lu W, et al (2010) Both the Transplantation of Somatic Cell Nuclear Transfer- and Fertilization-Derived Mouse Embryonic Stem Cells with Temperature-Responsive Chitosan Hydrogel Improve Myocardial Performance in Infarcted Rat Hearts. *Tissue Eng Part A* 16:1303–1315. doi: 10.1089/ten.tea.2009.0434
- Lykke-Andersen S, Jensen TH (2015) Nonsense-mediated mRNA decay: An intricate machinery that shapes transcriptomes. *Nat Rev Mol Cell Biol* 16:665–677. doi: 10.1038/nrm4063
- Mali P, Esvelt KM, Church GM (2013) Cas9 as a versatile tool for engineering biology. *Nat Methods* 10:957–963. doi: 10.1038/nmeth.2649
- Mannhardt I, Breckwoldt K, Letuffe-Brenière D, et al (2016) Human Engineered Heart Tissue: Analysis of Contractile Force. *Stem Cell Reports* 7:29–42. doi: 10.1016/j.stemcr.2016.04.011
- Marfella R, Di Filippo C, Portoghese M, et al (2009) Myocardial lipid accumulation in patients with pressure-overloaded heart and metabolic syndrome. *J Lipid Res* 50:2314–2323. doi: 10.1194/jlr.P900032-JLR200
- Martin U (2017) Genome stability of programmed stem cell products. *Adv Drug Deliv Rev* 120:108–117. doi: 10.1016/j.addr.2017.09.004
- Martinez-Fernandez A, Nelson TJ, Reyes S, et al (2014) Ips cell-derived cardiogenicity is hindered by sustained integration of reprogramming transgenes. *Circ Cardiovasc Genet* 7:667–676. doi: 10.1161/CIRCGENETICS.113.000298
- Mayshar Y, Ben-David U, Lavon N, et al (2010) Identification and classification of chromosomal aberrations in human induced pluripotent stem cells. *Cell Stem Cell* 7:521–531. doi: 10.1016/j.stem.2010.07.017
- McClelland M, Ivarie R (1982) Asymmetrical distribution of CpG in an “average” mammalian gene. *Nucleic Acids Res* 10:7865–7877. doi: 10.1093/nar/10.23.7865
- Meissner A, Mikkelsen TS, Gu H, et al (2008) Genome-scale DNA methylation maps of pluripotent and differentiated cells. *Nature* 454:766–770. doi: 10.1038/nature07107

- Möller C, Witchel H (2011) Automated electrophysiology makes the pace for cardiac ion channel safety screening. *Front Pharmacol* 2 NOV:1–7. doi: 10.3389/fphar.2011.00073
- Moore-Morris T, Guimarães-Camboa N, Banerjee I, et al (2014) Resident fibroblast lineages mediate pressure overload-induced cardiac fibrosis. *J Clin Invest* 124:2921–2934. doi: 10.1172/JCI74783
- Moscou MJ, Bogdanove AJ (2009) A simple cipher governs DNA recognition by TAL effectors. *Science* (80- ) 326:1501. doi: 10.1126/science.1178817
- Mosterd A, Hoes AW, de Bruyne MC, et al (1999) Prevalence of heart failure and left ventricular dysfunction in the general population; The Rotterdam Study. *Eur Heart J* 20:447–55. doi: 10.1159/000360609
- Motta BM, Pramstaller PP, Hicks AA, Rossini A (2017) The impact of CRISPR/Cas9 technology on cardiac research: From disease modelling to therapeutic approaches. *Stem Cells Int* 2017:. doi: 10.1155/2017/8960236
- Movassagh M, Choy M-K, Knowles DA, et al (2011) Distinct Epigenomic Features in End-Stage Failing Human Hearts. *Circulation* 124:2411–2422. doi: 10.1161/CIRCULATIONAHA.111.040071
- Mummery C, Ward D, Van Den Brink CE, et al (2002) Cardiomyocyte differentiation of mouse and human embryonic stem cells. *J Anat* 200:233–242. doi: 10.1046/j.1469-7580.2002.00031.x
- Musunuru K, Sheikh F, Gupta RM, et al (2018) Induced Pluripotent Stem Cells for Cardiovascular Disease Modeling and Precision Medicine: A Scientific Statement From the American Heart Association
- Nakamura M, Sadoshima J (2018) Mechanisms of physiological and pathological cardiac hypertrophy. *Nat Rev Cardiol* 15:387–407. doi: 10.1038/s41569-018-0007-y
- Närvä E, Autio R, Rahkonen N, et al (2010) High-resolution DNA analysis of human embryonic stem cell lines reveals culture-induced copy number changes and loss of heterozygosity. *Nat Biotechnol* 28:371–377. doi: 10.1038/nbt.1615
- Nührenberg TG, Hammann N, Schnick T, et al (2015) Cardiac Myocyte De Novo DNA Methyltransferases 3a/3b Are Dispensable for Cardiac Function and Remodeling after Chronic Pressure Overload in Mice. *PLoS One* 10:e0131019. doi: 10.1371/journal.pone.0131019
- Okano M, Bell DW, Haber D a, Li E (1999) DNA methyltransferases Dnmt3a and Dnmt3b are



- essential for de novo methylation and mammalian development. *Cell* 99:247–57. doi: 10.1016/S0092-8674(00)81656-6
- Okano M, Xie S, Li E (1998) Cloning and characterization of a family of novel mammalian DNA (cytosine-5) methyltransferases. *Nat Genet* 19:219–220. doi: 10.1038/890
- Olah E, Balogh E, Kovacs I, Kiss A (1989) Abnormalities of chromosome 1 in relation to human malignant diseases. *Cancer Genet Cytogenet* 43:179–194
- Papait R, Greco C, Kunderfranco P, et al (2013) Epigenetics: a new mechanism of regulation of heart failure? *Basic Res Cardiol* 108:361. doi: 10.1007/s00395-013-0361-1
- Paradis A, Xiao D, Zhou J, Zhang L (2014) Endothelin-1 promotes cardiomyocyte terminal differentiation in the developing heart via heightened DNA methylation. *Int J Med Sci* 11:373–380. doi: 10.7150/ijms.7802
- Passier R, Oostwaard DW, Snapper J, et al (2005) Increased Cardiomyocyte Differentiation from Human Embryonic Stem Cells in Serum-Free Cultures. *Stem Cells* 23:772–780. doi: 10.1634/stemcells.2004-0184
- Pawlak M, Jaenisch R (2011) De novo DNA methylation by Dnmt3a and Dnmt3b is dispensable for nuclear reprogramming of somatic cells to a pluripotent state. *Genes Dev* 25:1035–1040. doi: 10.1101/gad.2039011
- Polvani S, Tarocchi M, Galli A (2012) PPAR and Oxidative Stress: Con() Catenating NRF2 and FOXO. *PPAR Res* 2012:1–15. doi: 10.1155/2012/641087
- Ponikowski P, Anker SD, Alhabib KF, et al (2014) Heart failure: Preventing disease and death worldwide. *Eur Soc Cardiol* 373:941–955. doi: 10.1016/S0140-6736(09)60236-1
- Ran FA, Hsu PD, Lin CY, et al (2013a) Double nicking by RNA-guided CRISPR cas9 for enhanced genome editing specificity. *Cell* 154:1380–1389. doi: 10.1016/j.cell.2013.08.021
- Ran FA, Hsu PD, Wright J, et al (2013b) Genome engineering using the CRISPR-Cas9 system. *Nat Protoc* 8:2281–2308. doi: 10.1038/nprot.2013.143
- Reddy RC, Standiford TJ (2010) Nrf2 and PPAR $\gamma$ . *Am J Respir Crit Care Med* 182:134–135. doi: 10.1164/rccm.201004-0457ED
- Ren Y, Sun C, Sun Y, et al (2009) PPAR gamma protects cardiomyocytes against oxidative stress and apoptosis via Bcl-2 upregulation. *Vascul Pharmacol* 51:169–174. doi: 10.1016/j.vph.2009.06.004
- Rinaldi L, Avgustinova A, Martín M, et al (2017) Loss of dnmt3a and dnmt3b does not affect

- epidermal homeostasis but promotes squamous transformation through PPAR-g. *Elife* 6:1–25. doi: 10.7554/eLife.21697
- Robinton DA, Daley GQ (2012) The promise of induced pluripotent stem cells in research and therapy. *Nature* 481:295–305. doi: 10.1038/nature10761
- Rolfe M, McLeod LE, Pratt PF, Proud CG (2005) Activation of protein synthesis in cardiomyocytes by the hypertrophic agent phenylephrine requires the activation of ERK and involves phosphorylation of tuberous sclerosis complex 2 (TSC2). *Biochem J* 388:973–84. doi: 10.1042/BJ20041888
- Rosen ED, Sarraf P, Troy AE, et al (1999) PPAR $\gamma$  is required for the differentiation of adipose tissue in vivo and in vitro. *Mol Cell* 4:611–617. doi: 10.1016/S1097-2765(00)80211-7
- Schaaf S, Shibamiya A, Mewe M, et al (2011) Human engineered heart tissue as a versatile tool in basic research and preclinical toxicology. *PLoS One* 6:. doi: 10.1371/journal.pone.0026397
- Scherer S, Davis RW (1979) Replacement of chromosome segments with altered DNA sequences constructed in vitro. *Proc Natl Acad Sci U S A* 76:4951–5. doi: 10.1073/pnas.76.10.4951
- Schlaeger TM, Daheron L, Brickler TR, et al (2015) A comparison of non-integrating reprogramming methods. *Nat Biotechnol* 33:58–63. doi: 10.1038/nbt.3070
- Schlegel A, Stainier DYR (2006) Microsomal triglyceride transfer protein is required for yolk lipid utilization and absorption of dietary lipids in zebrafish larvae. *Biochemistry* 45:15179–15187. doi: 10.1021/bi0619268
- Shimizu T (2002) Fabrication of Pulsatile Cardiac Tissue Grafts Using a Novel 3-Dimensional Cell Sheet Manipulation Technique and Temperature-Responsive Cell Culture Surfaces. *Circ Res* 90:40e–48. doi: 10.1161/hh0302.105722
- Shubeita HE, McDonough PM, Harris AN, et al (1990) Endothelin induction of inositol phospholipid hydrolysis, sarcomere assembly, and cardiac gene expression in ventricular myocytes. A paracrine mechanism for myocardial cell hypertrophy. *J Biol Chem* 265:20555–62
- Simpson P, McGrath A, Savion S (1982) Myocyte hypertrophy in neonatal rat heart cultures and its regulation by serum and by catecholamines. *Circ Res* 51:787–801. doi: 10.1161/01.RES.51.6.787
- Sirabella D, Cimetta E, Vunjak-Novakovic G (2015) “The state of the heart”: Recent advances in engineering human cardiac tissue from pluripotent stem cells. *Exp Biol Med* 240:1008–1018. doi: 10.1177/1535370215589910

- Smith C, Gore A, Yan W, et al (2014) Whole-genome sequencing analysis reveals high specificity of CRISPR/Cas9 and TALEN-based genome editing in human iPSCs. *Cell Stem Cell* 15:12–13. doi: 10.1016/j.stem.2014.06.011
- Smith ZD, Meissner A (2013) DNA methylation: Roles in mammalian development. *Nat Rev Genet* 14:204–220. doi: 10.1038/nrg3354
- Son N-H, Park T-S, Yamashita H, et al (2007) Cardiomyocyte expression of PPAR $\gamma$  leads to cardiac dysfunction in mice. *J Clin Invest* 117:2791–2801. doi: 10.1172/JCI30335
- Song NJ, Kim S, Jang BH, et al (2016) Small molecule-induced complement factor D (Adipsin) promotes lipid accumulation and adipocyte differentiation. *PLoS One* 11:1–15. doi: 10.1371/journal.pone.0162228
- Srivastava RD, Kalitha M, Varma P, Bhatnagar VM (1977) A mechanism of action of phenylephrine on heart. *Indian J Physiol Pharmacol* 21:167–74
- Stenzig J, Hirt MN, Löser A, et al (2016) DNA methylation in an engineered heart tissue model of cardiac hypertrophy: common signatures and effects of DNA methylation inhibitors. *Basic Res Cardiol* 111:9. doi: 10.1007/s00395-015-0528-z
- Stenzig J, Schneeberger Y, Löser A, et al (2018) Pharmacological inhibition of DNA methylation attenuates pressure overload-induced cardiac hypertrophy in rats. *J Mol Cell Cardiol* 120:53–63. doi: 10.1016/j.yjmcc.2018.05.012
- Stoehr A, Neuber C, Baldauf C, et al (2014) Automated analysis of contractile force and Ca<sup>2+</sup> transients in engineered heart tissue. *Am J Physiol Circ Physiol* 306:H1353–H1363. doi: 10.1152/ajpheart.00705.2013
- Stöhr A, Friedrich FW, Flenner F, et al (2013) Contractile abnormalities and altered drug response in engineered heart tissue from Mybpc3-targeted knock-in mice. *J Mol Cell Cardiol* 63:189–198. doi: 10.1016/j.yjmcc.2013.07.011
- Strøm CC, Aplin M, Ploug T, et al (2005) Expression profiling reveals differences in metabolic gene expression between exercise-induced cardiac effects and maladaptive cardiac hypertrophy. *FEBS J* 272:2684–2695. doi: 10.1111/j.1742-4658.2005.04684.x
- Sugden PH (2003) Ras, Akt, and Mechanotransduction in the Cardiac Myocyte. *Circ Res* 93:1179–1192. doi: 10.1161/01.RES.0000106132.04301.F5
- Sugiura S, Kobayakawa N, Fujita H, et al (1998) Comparison of unitary displacements and forces between 2 cardiac myosin isoforms by the optical trap technique: Molecular basis for cardiac

- adaptation. *Circ Res* 82:1029–1034. doi: 10.1161/01.RES.82.10.1029
- Taapken SM, Nisler BS, Newton M a, et al (2011) Karyotypic abnormalities in human induced pluripotent stem cells and embryonic stem cells. *Nat Biotechnol* 29:313–314. doi: 10.1038/nbt.1835
- Takahashi K, Tanabe K, Ohnuki M, et al (2007) Induction of Pluripotent Stem Cells from Adult Human Fibroblasts by Defined Factors. *Cell* 131:861–872. doi: 10.1016/j.cell.2007.11.019
- Takahashi K, Yamanaka S (2006) Induction of Pluripotent Stem Cells from Mouse Embryonic and Adult Fibroblast Cultures by Defined Factors. *Cell* 126:663–676. doi: 10.1016/j.cell.2006.07.024
- Takahashi T, Allen PD, Izumo S (1992) Expression of A- , B- , and C-Type Natriuretic Peptide Genes in Failing and Developing Human Ventricles Correlation With Expression of the Ca<sup>2+</sup> + -ATPase Gene. *Circ Res* 9–17
- Talkhabi M, Aghdami N, Baharvand H (2016) Human cardiomyocyte generation from pluripotent stem cells: A state-of-art. *Life Sci* 145:98–113. doi: 10.1016/j.lfs.2015.12.023
- Tan EP, Li Y, Del Castillo Velasco-Herrera M, et al (2015) Off-target assessment of CRISPR-Cas9 guiding RNAs in human iPS and mouse ES cells. *Genesis* 53:225–236. doi: 10.1002/dvg.22835
- Tham YK, Bernardo BC, Ooi JYY, et al (2015) Pathophysiology of cardiac hypertrophy and heart failure: signaling pathways and novel therapeutic targets. *Arch Toxicol* 89:1401–1438. doi: 10.1007/s00204-015-1477-x
- Thomas KR, Folger KR, Capecchi MR (1986) High frequency targetting of genes to specific sites in the mammalian genome. *Cell* 44:419–428
- Thomson JA, Itskovitz-eldor J, Shapiro SS, et al (2009) Embryonic Stem Cell Lines Derived from Human Blastocysts. *Science* (80- ) 1145:1145–1148. doi: 10.1126/science.282.5391.1145
- Tontonoz P, Hu E, Spiegelman BM (1994) Stimulation of adipogenesis in fibroblasts by PPAR $\gamma$ 2, a lipid-activated transcription factor. *Cell* 79:1147–1156. doi: 10.1016/0092-8674(94)90006-X
- Toyota M, Ho C, Ohe-Toyota M, et al (1999) Inactivation of CACNA1G, a T-type calcium channel gene, by aberrant methylation of its 5' CpG island in human tumors. *Cancer Res* 59:4535–41
- Trivedi CM, Luo Y, Yin Z, et al (2007) Hdac2 regulates the cardiac hypertrophic response by

- modulating Gsk3 $\beta$  activity. *Nat Med* 13:324–331. doi: 10.1038/nm1552
- Vandenburgh HH, Swasdison S, Karlisch P (1991) Computer-aided mechanogenesis of skeletal muscle organs from single cells in vitro. *FASEB J* 5:2860–7
- Veres A, Gosis BS, Ding Q, et al (2014) Low incidence of Off-target mutations in individual CRISPR-Cas9 and TALEN targeted human stem cell clones detected by whole-genome sequencing. *Cell Stem Cell* 15:27–30. doi: 10.1016/j.stem.2014.04.020
- Vujic a., Robinson EL, Ito M, et al (2015) Experimental heart failure modelled by the cardiomyocyte-specific loss of an epigenome modifier, DNMT3B. *J Mol Cell Cardiol* 82:174–83. doi: 10.1016/j.yjmcc.2015.03.007
- Wakatsuki T, Schlessinger J, Elson EL (2004) The biochemical response of the heart to hypertension and exercise. *Trends Biochem Sci* 29:609–617. doi: 10.1016/j.tibs.2004.09.002
- Wang XL, Yu L, Ding Y, et al (2015) Gene Manipulation of Human Embryonic Stem Cells by In Vitro-Synthesized mRNA for Gene Therapy. *Curr Gene Ther* 15:428–435. doi: 10.2174/1566523215666150515144533
- Watson CJ, Horgan S, Neary R, et al (2015) Epigenetic Therapy for the Treatment of Hypertension-Induced Cardiac Hypertrophy and Fibrosis. *J Cardiovasc Pharmacol Ther.* doi: 10.1177/1074248415591698
- Wei JQ, Shehadeh LA, Mitrani JM, et al (2008) Quantitative control of adaptive cardiac hypertrophy by acetyltransferase p300. *Circulation* 118:934–946. doi: 10.1161/CIRCULATIONAHA.107.760488
- Weinberger F, Breckwoldt K, Pecha S, et al (2016) Cardiac repair in guinea pigs with human engineered heart tissue from induced pluripotent stem cells. *Sci Transl Med* 8:363ra148–363ra148. doi: 10.1126/scitranslmed.aaf8781
- Werner T (2018) Humanes künstliches Herzgewebe aus mehreren Zelltypen zur Untersuchung kardialer Hypertrophie. Univ Hamburg, <http://ediss.sub.uni-hamburg.de/volltexte/2018/9072>
- Wettwer E, Christ T, Endig S, et al (2013) The new antiarrhythmic drug vernakalant: Ex vivo study of human atrial tissue from sinus rhythm and chronic atrial fibrillation. *Cardiovasc Res* 98:145–154. doi: 10.1093/cvr/cvt006
- Wienholz BL, Kareta MS, Moarefi AH, et al (2010) DNMT3L modulates significant and distinct flanking sequence preference for DNA methylation by DNMT3A and DNMT3B in vivo. *PLoS Genet* 6:. doi: 10.1371/journal.pgen.1001106

- Wijnker PJM, Friedrich FW, Dutsch A, et al (2016) Comparison of the effects of a truncating and a missense MYBPC3 mutation on contractile parameters of engineered heart tissue. *J Mol Cell Cardiol* 97:82–92. doi: 10.1016/j.yjmcc.2016.03.003
- Wolf D, Tseng N, Seedorf G, et al (2014) Endothelin-1 decreases endothelial PPAR $\gamma$  signaling and impairs angiogenesis after chronic intrauterine pulmonary hypertension. *Am J Physiol Cell Mol Physiol* 306:L361–L371. doi: 10.1152/ajplung.00277.2013
- Wu JI (2012) Diverse functions of ATP-dependent chromatin remodeling complexes in development and cancer Epigenetic Regulation of Transcription During Development Brg1 / Brm-Associated Factors ( BAF ), A Mammalian SWI / SNF-like ATP-dependent. *Breast* 54–69. doi: 10.1093/abbs/gmr099.Review
- Xi J, Khalil M, Shishechian N, et al (2010) Comparison of contractile behavior of native murine ventricular tissue and cardiomyocytes derived from embryonic or induced pluripotent stem cells. *FASEB J* 24:2739–2751. doi: 10.1096/fj.09-145177
- Xiao D, Dasgupta C, Chen M, et al (2014) Inhibition of DNA methylation reverses norepinephrine-induced cardiac hypertrophy in rats. *Cardiovasc Res* 101:373–382. doi: 10.1093/cvr/cvt264
- Xu GL, Bestor TH, Bourc'his D, et al (1999) Chromosome instability and immunodeficiency syndrome caused by mutations in a DNA methyltransferase gene. *Nature* 402:187–191. doi: 10.1038/46052
- Yang L, Rau R, Goodell MA (2015) DNMT3A in haematological malignancies. *Nat Rev Cancer* 15:152–165. doi: 10.1038/nrc3895
- You J, Wu J, Zhang Q, et al (2017) Differential cardiac hypertrophy and signaling pathways in pressure versus volume overload. *Am J Physiol Circ Physiol* ajpheart.00212. doi: 10.1152/ajpheart.00212.2017
- Yu S, Matsusue K, Kashireddy P, et al (2003) Adipocyte-specific gene expression and adipogenic steatosis in the mouse liver due to peroxisome proliferator-activated receptor  $\gamma$ 1 (PPAR $\gamma$ 1) overexpression. *J Biol Chem* 278:498–505. doi: 10.1074/jbc.M210062200
- Zaha V, Grohmann J, Göbel H, et al (2003) Experimental model for heart failure in rats--induction and diagnosis. *Thorac Cardiovasc Surg* 51:211–215. doi: 10.1055/s-2003-42264
- Zhan L, Zhang H, Zhang Q, et al (2012) Regulatory role of KEAP1 and NRF2 in PPAR $\gamma$  expression and chemoresistance in human non-small-cell lung carcinoma cells. *Free Radic Biol Med* 53:758–768. doi: 10.1016/j.freeradbiomed.2012.05.041

- Zhang CL, McKinsey TA, Chang S, et al (2002) Class II histone deacetylases act as signal-responsive repressors of cardiac hypertrophy. *Cell* 110:479–488. doi: 10.1016/S0092-8674(02)00861-9
- Zhang J, Klos M, Wilson GF, et al (2012) Extracellular matrix promotes highly efficient cardiac differentiation of human pluripotent stem cells: The matrix sandwich method. *Circ Res* 111:1125–1136. doi: 10.1161/CIRCRESAHA.112.273144
- Zhang L, Chawla A (2004) Role of PPAR $\gamma$  in macrophage biology and atherosclerosis. *Trends Endocrinol Metab* 15:500–505. doi: 10.1016/j.tem.2004.10.006
- Zhang QJ, Chen HZ, Wang L, et al (2011) The histone trimethyllysine demethylase JMJD2A promotes cardiac hypertrophy in response to hypertrophic stimuli in mice. *J Clin Invest* 121:2447–2456. doi: 10.1172/JCI46277
- Zhu R, Blazeski A, Poon E, et al (2014) Physical developmental cues for the maturation of human pluripotent stem cell-derived cardiomyocytes. *Stem Cell Res Ther* 5:117. doi: 10.1186/scrt507
- Zimmermann WH, Fink C, Kralisch D, et al (2000) Three-dimensional engineered heart tissue from neonatal rat cardiac myocytes. *Biotechnol Bioeng* 68:106–114. doi: 10.1002/(SICI)1097-0290(20000405)6
- Zimmermann WH, Schneiderbanger K, Schubert P, et al (2002) Tissue engineering of a differentiated cardiac muscle construct. *Circ Res* 90:223–230. doi: 10.1161/hh0202.103644

9 Supplement

9.1 Supplementary figures and tables

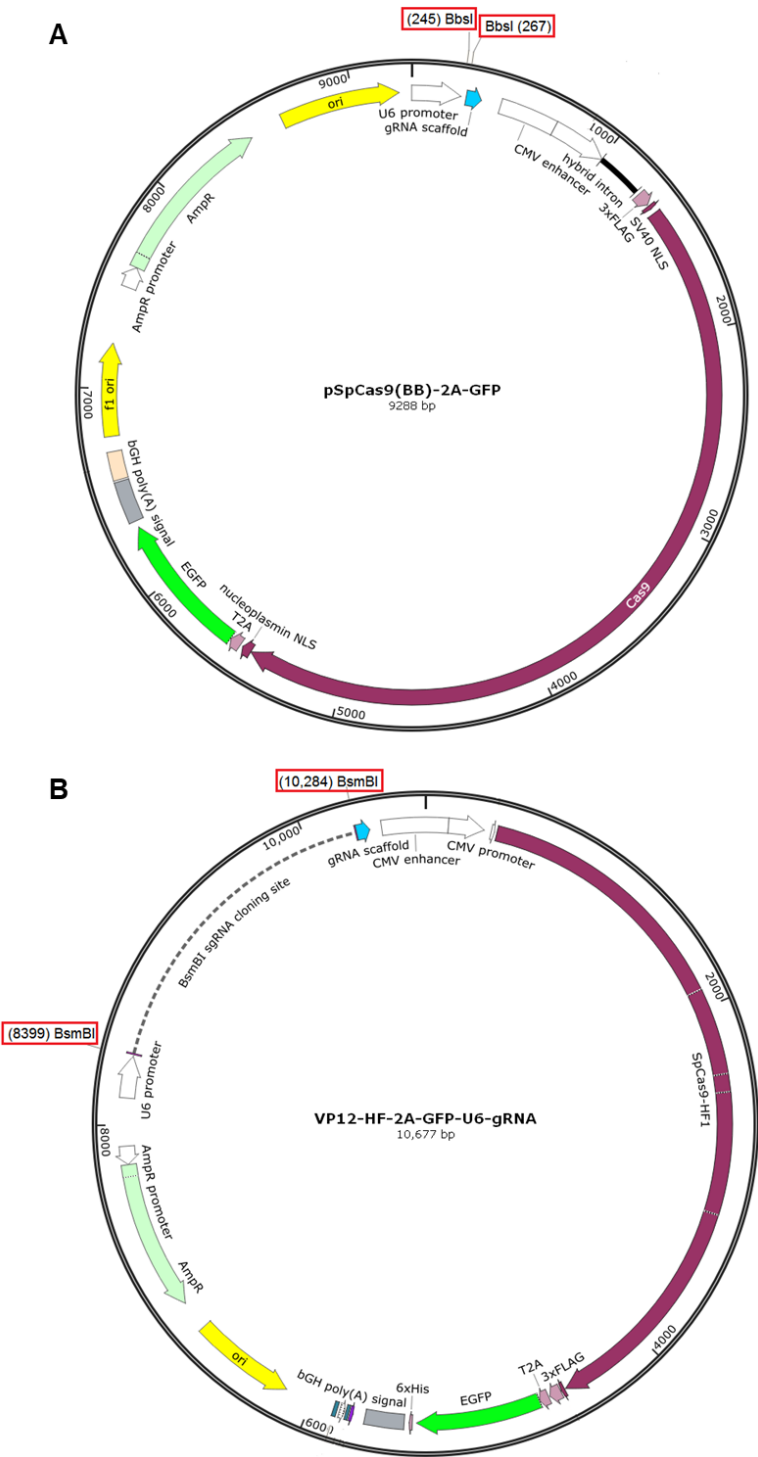


**Figure S1: Plasmid maps CRISPR vectors.** (A) pSpCas9(BB)-2A-GFP and (B) VP12-HF-2A-GFP-U6-gRNA. Restriction sites used for cloning are indicated in red boxes.



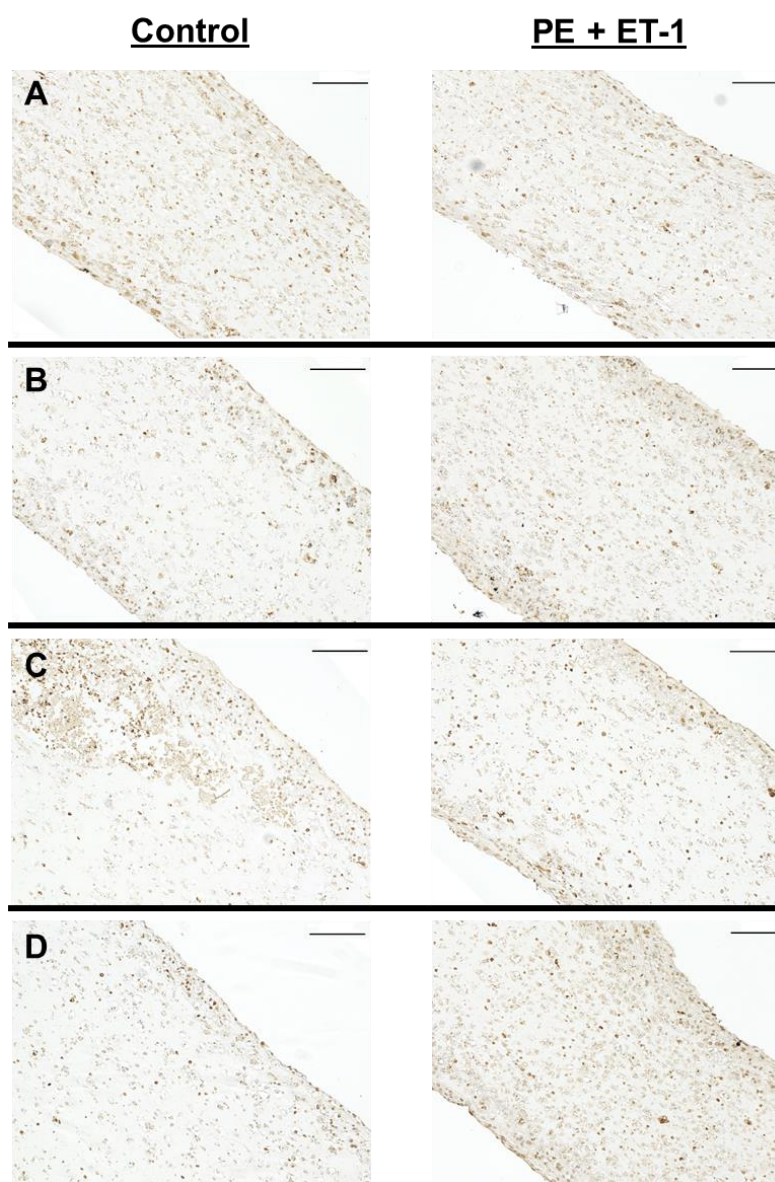


**Figure S2: Caspase 3 staining.** EHT paraffin sections of control EHTs (left columns) and PE + ET-1-treated EHTs (right columns) after caspase 3 staining. (A) ERC018, (B) heterozygous, (C) compound heterozygous, (D) homozygous. Scale bar = 100  $\mu$ m.

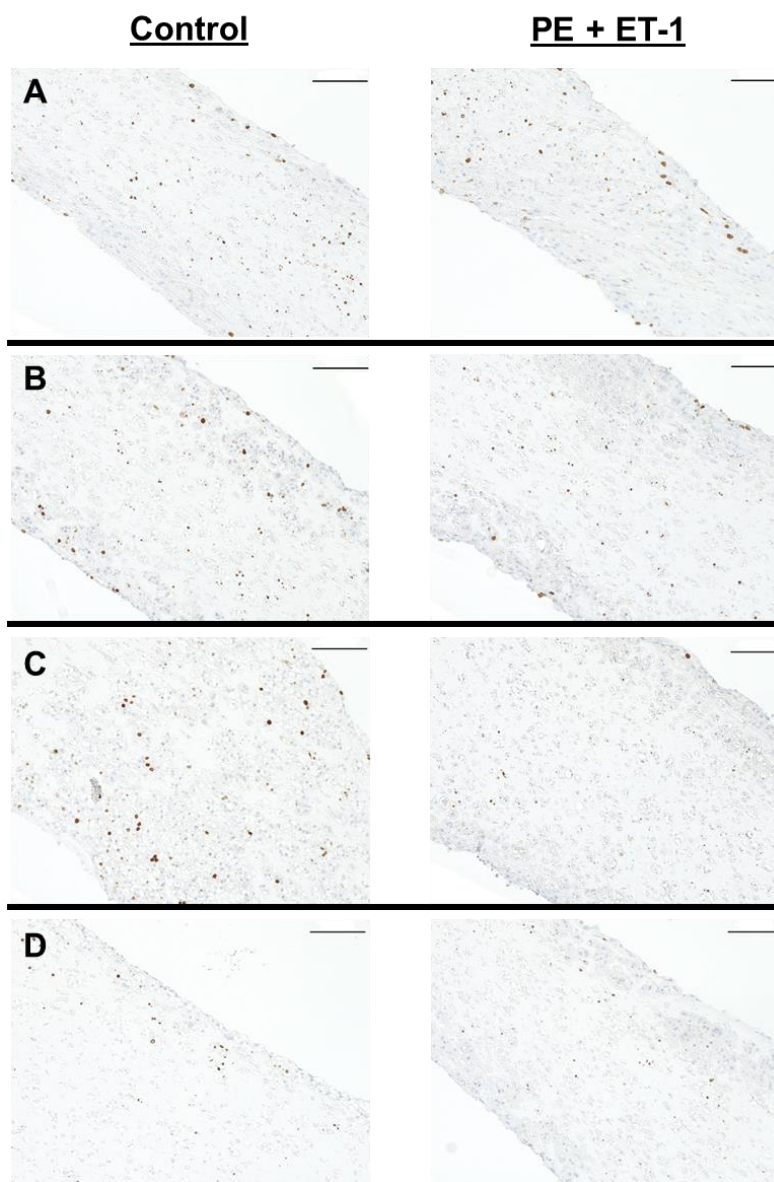


**Figure S3: Ki-67 staining.** EHT paraffin sections of control EHTs (left columns) and PE + ET-1-treated EHTs (right columns) after Ki-67 staining. (A) ERC018, (B) heterozygous, (C) compound heterozygous, (D) homozygous. Scale bar = 100  $\mu$ m.

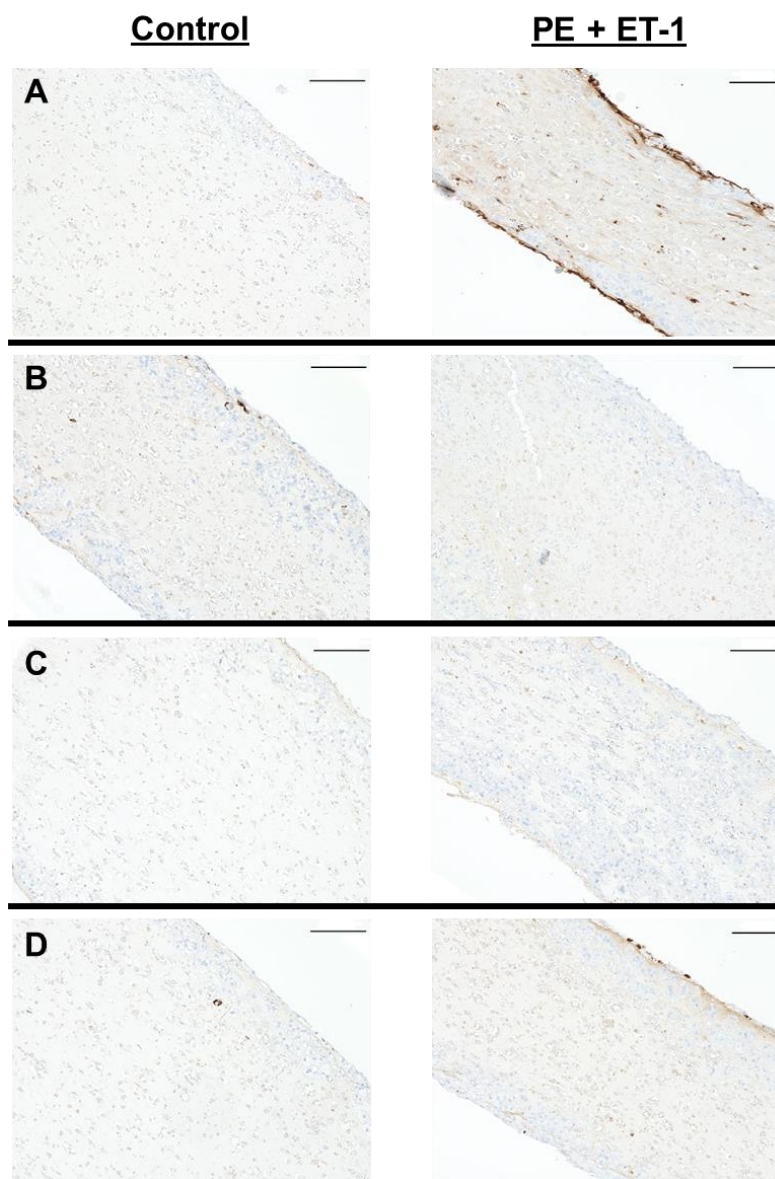


**Figure S4: Collagen staining.** EHT paraffin sections of control EHTs (left columns) and PE + ET-1-treated EHTs (right columns) after staining for collagen. (A) ERC018, (B) heterozygous, (C) compound heterozygous, (D) homozygous. Scale bar = 100  $\mu$ m.

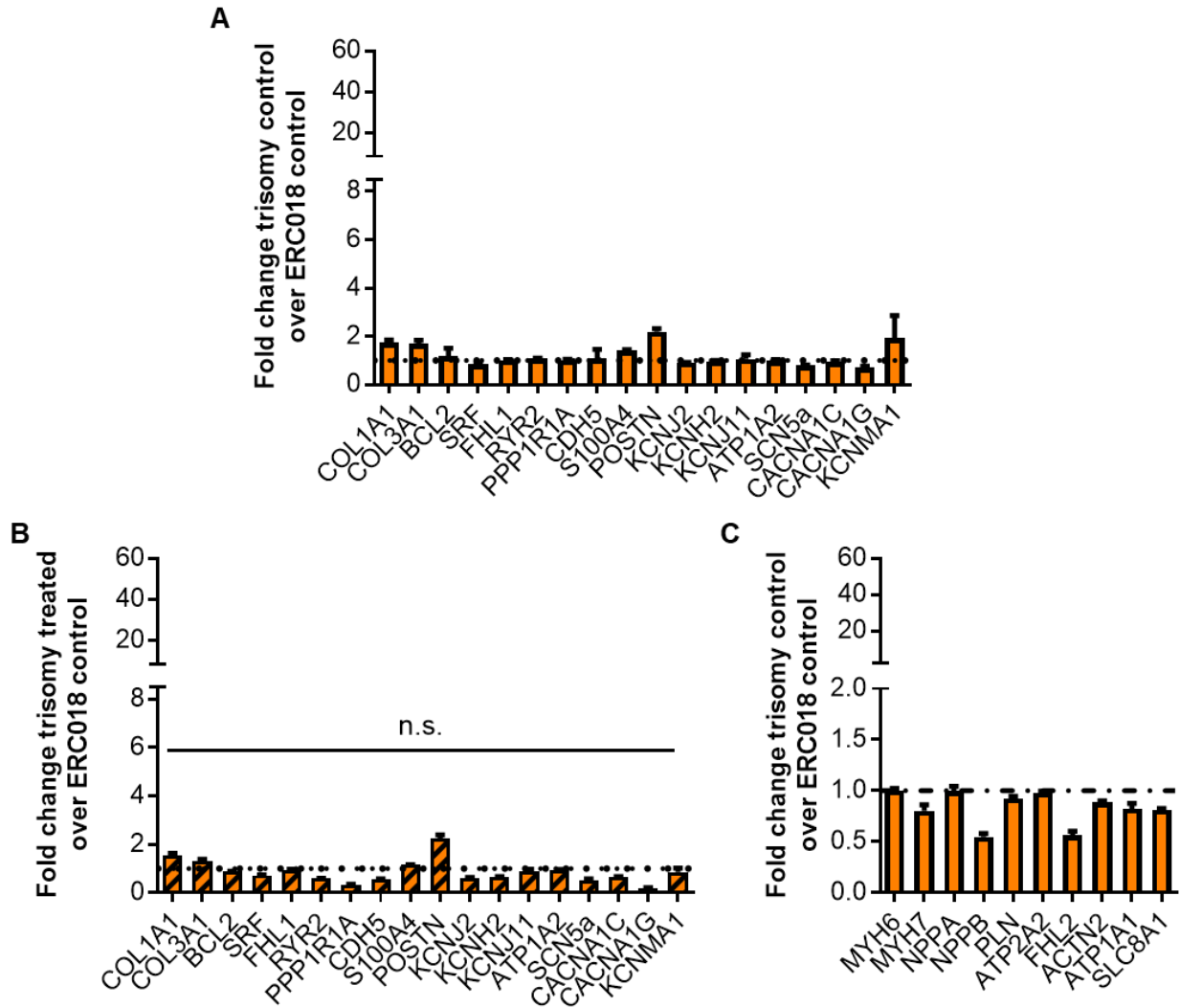


**Figure S5: Overview NanoString gene expression analysis.** (A) Fold change of low abundance genes in trisomy control EHTs compared to ERC018 control (dotted line). (B) Fold change of low abundance genes in PE and ET-1-treated trisomy EHTs compared to ERC018 control (dotted line). (C) Fold change of high abundance genes in trisomy control EHTs compared to ERC018 control (dotted line). n=3 EHT per group.

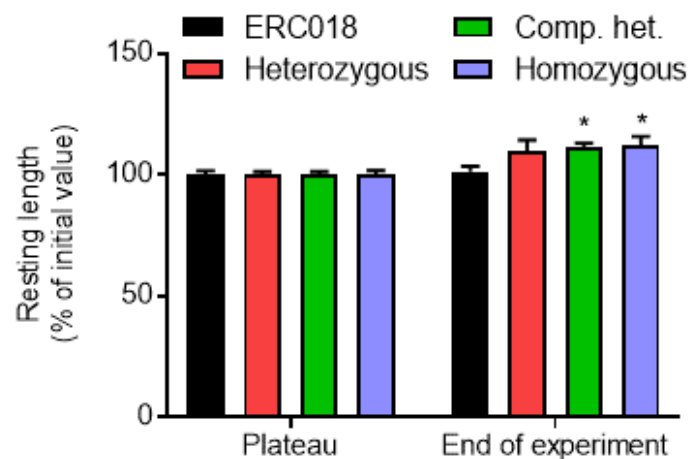


**Figure S6: EHT resting length over time.** Values for resting length calculated by the CTMV software during the plateau phase and at the end of the experiments expressed as percentage of initial resting length. n=16-21 EHTs per group, 2way ANOVA plus Bonferroni's post-test for multiple comparisons vs. ERC018, \*p<0.05.

Table S1: Upstream regulators associated with DMCs in the IPA analysis.

Knockout Ctrl vs. ERC018 Ctrl	Knockout PE+ET-1 vs. ERC018 PE+ET-1
BMP4	CEBPA
CRNDE	estrogen receptor
CTR9	EZH2
CYR61	HIC1
DCAF1	HSF1
DNA-methyltransferase	IgG
DNMT3B	MAPK9
estrogen receptor	MTOR
EZH2	MYC
GATA6	RARA
Growth hormone	SPDEF
HDAC6	TP53
HIC1	YAP1
IL4	
LEP	
MET	
mir-10	
miR-122-5p	
miR-145-5p	
MMP1	
NOTCH1	
PDLIM2	
POU5F1	
RARA	
SHC1	
SMAD4	
SNAI2	
SOX2	
SPDEF	
TAL1	
TERT	
TGFB1	
Wnt	
ZNF217	

## 9.2 List of abbreviations

### A

$\alpha$ -MHC	$\alpha$ -Myosin heavy chain
ACTA2	Alpha smooth muscle actin
ACTB	Beta-actin
ACTC1	Cardiac muscle alpha actin
ACTN2	Alpha-actinin 2
ADCR	ATP-dependent chromatin remodeling complex
ADD	ATRX, DNMT3, DNMT3L domain
AML	Acute myeloid leukemia
ANP	Atrial natriuretic peptide
APA	Action potential amplitude
APD	Action potential duration
APS	Ammonium persulfate
Aqua dest.	Aqua destillata (distilled water)
ATP	Adenosine triphosphate
ATP1A1	Sodium/potassium-transporting ATPase subunit alpha-1
ATP1A2	ATPase, Na <sup>+</sup> /K <sup>+</sup> transporting, alpha 2 (+) polypeptide
ATP2A2	Sarco/endoplasmic reticulum Ca <sup>2+</sup> -ATPase

### B

$\beta$ -MHC	$\beta$ -Myosin heavy chain
BAF	BRG1- or hbrm-associated factors
BAX	Bcl-2-associated X protein
BCL2	B-cell lymphoma 2
bFGF	Basic fibroblast growth factor
BMP-4	Bone-morphogenetic protein 4
BNP	Brain natriuretic peptide
bp	Base pair
bpm	Beats per minute
Brg1	ATP-dependent chromatin remodeler SMARCA4
Brm	ATP-dependent chromatin remodeler SMARCA2
BSA	Bovine serum albumin

### C

CACNA1C	Calcium channel, voltage-dependent, L type, alpha 1C subunit
CACNA1G	Calcium channel, voltage-dependent, T type, alpha 1G subunit
CaMKII	Ca <sup>2+</sup> /calmodulin-dependent protein kinase II
Cas9	CRISPR associated protein 9
CASP3	Caspase 3
CASQ2	Calsequestrin 2
CDH5	Cadherin 5
cDNA	Complementary DNA
CFD	Complement factor D
CLTC	Clathrin heavy chain 1

CM	Conditioned medium
c-Myc	Cellular myelocytomatosis
COL1A1	Alpha-1 type I collagen
COL3A1	Collagen alpha-1(III) chain
Comp. het.	Compound heterozygous
CRISPR	Clustered regularly interspaced short palindromic repeats
crRNA	CRISPR RNA
CTGF	Connective tissue growth factor
cTnT	Cardiac troponin T
Ctrl	Control
<b>D</b>	
d	Day
DMEM	Dulbecco's Modified Eagle Medium
DMSO	Dimethyl sulfoxide
DNA	Deoxyribonucleic acid
DNMT	DNA methyltransferase
dNTP	Deoxy-nucleoside triphosphate
DSB	Double strand break
DTT	Dithiothreitol
<b>E</b>	
EB	Embryoid body
EC <sub>50</sub>	Half maximal effective concentration
EDTA	Ethylenediaminetetraacetic acid
EHT	Engineered heart tissue
ESC	Embryonic stem cell
ET-1	Endothelin-1
<b>F</b>	
FACS	Fluorescence-activated cell sorting
FCS	Fetal calf serum
FFR	Force-frequency relationship
FHL1	Four and a half LIM domains protein 1
FHL2	Four and a half LIM domains protein 2
FITC	Fluorescein isothiocyanate
FN1	Fibronectin
FSC	Forward scatter
FTDA	bFGF, TGFβ1, dorsomorphin and activin A-based hiPSC culture medium
<b>G</b>	
g	Relative centrifugal force
GAPDH	Glyceraldehyde 3-phosphate dehydrogenase
GFP	Green fluorescent protein
GUSB	Beta-glucuronidase



**H**

H&E	Hematoxylin and eosin staining
HBSS	Hanks' Balanced Salt Solution
HCN4	Potassium/sodium hyperpolarization-activated cyclic nucleotide-gated channel 4
HDAC	Histone deacetylase
HDR	Homology-directed repair
HEPES	4-(2-hydroxyethyl)-1-piperazineethanesulfonic acid
hESC	Human embryonic stem cell
hiPSC	Human induced pluripotent stem cell
HMT	Histone methyltransferase
hPSC	Human pluripotent stem cell
Hz	Hertz

**I**

ICF	Immunodeficiency, centromere instability and facial anomalies syndrome
IEPT	Institute of Experimental Pharmacology and Toxicology
IHC	Immunohistochemistry
IK <sub>i</sub>	Inwardly rectifying potassium current
IK <sub>ATP</sub>	ATP-sensitive potassium current
Ik <sub>r</sub>	Rapid delayed rectifier potassium current
iPSC	Induced pluripotent stem cell
ISWI	Imitation SWI

**J**

JMJD2A	Lysine-specific demethylase 4A
--------	--------------------------------

**K**

kb	Kilobase
KCl	Potassium chloride
KCNA4	Potassium voltage-gated channel subfamily A member 4
KCNA5	Potassium voltage-gated channel, shaker-related subfamily, member 5
KCND3	Potassium voltage-gated channel subfamily D member 3
KCNE1	Potassium voltage-gated channel subfamily E member 1
KCNE2	Potassium voltage-gated channel subfamily E member 2
KCNH2	human Ether-à-go-go-Related Gene (hERG)
KCNIP2	Kv channel-interacting protein 2
KCNJ11	Potassium voltage-gated channel subfamily J member 11
KCNJ12	ATP-sensitive inward rectifier potassium channel 12
KCNJ2	Potassium voltage-gated channel subfamily J member 2
KCNJ3	Potassium inwardly-rectifying channel, subfamily J, member 3
KCNJ5	G protein-activated inward rectifier potassium channel 4
KCNMA1	Calcium-activated potassium channel subunit alpha-1
KCNN3	Small conductance calcium-activated potassium channel 3
KCNQ1	Potassium voltage-gated channel subfamily Q member 1
kDa	Kilodalton

Ki-67	Antigen KI-67
Klf4	Kruppel-like factor 4

**M**

MBP	Methyl-CpG-binding protein
MEOX1	Homeobox protein MOX-1
miRNA	Micro RNA
MLC2v	Myosin regulatory light chain 2, ventricular/cardiac muscle isoform
mM	Millimolar
mN	Millinewton
mRNA	Messenger RNA
MYH6	Myosin heavy chain, $\alpha$ isoform
MYH7	Myosin heavy chain, $\beta$ isoform

**N**

NFAT	Nuclear factor of activated T-cells
NFKB1	Nuclear factor NF-kappa-B
NHEJ	Non-homologous endjoining
NPPA	Atrial natriuretic peptide
NPPB	Brain natriuretic peptide

**O**

Oct4	Octamer-binding transcription factor 4
------	--

**P**

PAM	Protospacer adjacent motif
PBS	Phosphate-buffered saline
PCR	Polymerase chain reaction
PE	Phenylephrine
PGK1	Phosphoglycerate kinase 1
PLN	Phospholamban
POSTN	Periostin
PPAR $\gamma$	Peroxisome proliferator-activated receptor gamma
PPP1R1A	Protein phosphatase 1 regulatory subunit 1A
PTFE	Polytetrafluoroethylene
PVDF	Polyvinylidene fluoride
PWWP	Pro-Trp-Trp-Pro domain

**Q**

qPCR	Quantitative real-time PCR
------	----------------------------

**R**

RCAN1	Regulator of calcineurin 1
RNA	Ribonucleic acid
RNAa	RNA activation
RPMI	Roswell Park Memorial Institute

RT	Relaxation time
RYR2	Ryanodine receptor 2
<b>S</b>	
S100A4	S100 calcium-binding protein A4
SCN10A	Sodium voltage-gated channel alpha subunit 10
SCN5a	Sodium voltage-gated channel alpha subunit 5
SDS	Sodium dodecyl sulfate
SEM	Standard error of the mean
SERCA2a	Sarco/endoplasmic reticulum Ca <sup>2+</sup> -ATPase
sgRNA	single guide RNA
SLC8A1	Sodium-calcium exchanger
SLC9A1	Sodium-hydrogen antiporter 1
Sox2	Sex determining region Y-box 2
SRF	Serum response factor
SSC	Sideward scatter
SWI/SNF	SWItch/Sucrose Non-Fermentable
<b>T</b>	
T <sub>3</sub>	Triiodothyronine
TAC	Transverse aortic constriction
TALEN	Transcription activator-like effector nucleases
TBS	Tris-buffered saline
TEMED	Tetramethylethylenediamine
TF	Transcription factor
TGFβ	Transforming growth factor-β
TGS	Transcriptional gene silencing
T <sub>m</sub>	Melting temperature
tracrRNA	Trans-activating RNA
TTP	Time to peak
TUBB	Tubulin beta chain
<b>U</b>	
U	Unit
UKE	University Medical Center Hamburg Eppendorf
UTR	Untranslated region
<b>V</b>	
V <sub>max</sub>	Maximal upstroke velocity
VWF	Von Willebrand factor
<b>W</b>	
WB	Western Blot
<b>Z</b>	
ZFN	Zinc finger nuclease

### 9.3 Devices, materials and substances

#### 9.3.1 Devices

4D-Nucleofector™ Core Unit and X Unit (Lonza)  
 AbiPrism7900HT cycler (Applied Biosystems)  
 Analytic Scale Genius (Sartorius AG)  
 BD FACSAria™ IIIu (BD Biosciences)  
 BD FACSCanto™ II (BD Biosciences)  
 Benchmark XT (Ventana)  
 Bioanalyzer 2100 (Agilent)  
 C25 Incubator Shaker (New Brunswick Scientific)  
 Cell culture incubator CB 220 (Binder)  
 Cell culture incubators S2020 1.8, HERAcell 240 & 150i (Thermo Fischer Scientific)  
 Cell culture incubators MCO-19M & MCO-20AIC (Sanyo)  
 Centrifuges 5415 R & 5810 R (Eppendorf)  
 Centrifuge J-6B (Beckmann)  
 Centrifuges Rotanta/RP & Universal 30 RF (Hettich)  
 ChemiDoc™ Touch Imaging System (Bio-Rad Laboratories)  
 Cryopreservation system Asymptote EF600M (Grant Instruments)  
 Electrophoretic Transfer Cell Mini Trans-Blot cell (Bio-Rad Laboratories)  
 Gel electrophoresis cell Mini-PROTEAN 3 Cell (Bio-Rad Laboratories)  
 Gel electrophoresis tank Sub-cell® GT (Bio-Rad Laboratories)  
 Magnetic stirring and heating plate IKA Combimag RET (Janke & Kunkel GmbH & Co KG)  
 Magnetic stirring plate Variomag / Cimarec Biosystem Direct (Thermo Scientific)  
 Magnetic stirring plate Variomag / Cimarec Biosystem 4 Direct (Thermo Scientific)  
 Microscope Axioskop 2 with AxioCam Color (Zeiss)  
 Microscope Axiovert 25 (Zeiss) with ProgRes Speed XT core 5 camera (Jenoptik)  
 Microscope BZ-X710 (Keyence)  
 Microscope EVOS FL Cell Imaging System (Thermo Fischer Scientific)  
 NanoDrop ND-1000 Spectrophotometer (Thermo Fischer Scientific)  
 nCounter® SPRINT (NanoString)  
 Paraffin Dispenser EG 1120 (Leica)  
 Pipettes 10 / 100 / 1000 µL (Eppendorf)  
 Pipette controller Accu-jet® pro (Brand)  
 Power supply PowerPac Basic (Bio-Rad Laboratories)  
 Precision Advanced Scale (Ohaus)  
 S88X dual output square pulse stimulator (Grass)  
 Safety workbench HeraSafe (Heraeus)  
 Safety workbench Safe 2020 (Thermo Fischer Scientific)  
 Sequencer HiSeq 2500 (Illumina)  
 Thermal cycler Hybaid PCR Sprint (Thermo Fischer Scientific)  
 Thermal cycler vapo.protect (Eppendorf)  
 Thermomixer comfort (Eppendorf)  
 TissueLyser (QIAGEN)  
 Video-optical EHT analysis system (EHT Technologies GmbH)

Water bath 25900 (Medax)  
Warming cabinet Kelvitron® t (Heraeus)

### 9.3.2 Software

AxioVision Rel. 4.8.2 (Zeiss)  
Bismark (Babraham Institute)  
BZ-X Analyzer (Keyence)  
FACSDiva (BD Biosciences)  
FASTQC (Babraham Bioinformatics)  
Image Lab Version 5.2.1 (Bio-Rad Laboratories)  
ImageJ 1.47v (Wayne Rasband)  
Ingenuity Pathway Analysis software (IPA, QIAGEN)  
MethylKit for R software (R Development Core Team)  
ProgRes® Capture Pro 2.8.8 (Jenoptik)  
Prism 5 (GraphPad)  
SDS 2.4.1 (Applied Biosystems)  
SnapGene® 3.2.1 (GSL Biotech LLC)

### 9.3.3 Materials and equipment

250 mL Vacuum Filtration "rapid"-Filtermax (TPP, 99250)  
500 mL Vacuum Filtration "rapid"-Filtermax (TPP, 99500)  
Aspiration pipette 2 mL (Sarstedt, 86.1252.011)  
Cell culture flask T175 (Sarstedt, 83.3911.002)  
Cell culture flask T80 (Nunc, 178905)  
Cell culture flask T75 and T175 for suspension culture (Sarstedt, 83.3911.502 / 83.3912.502)  
Cell culture microplate 96 well µClear® black CELLSTAR® (Greiner Bio-One, 655090)  
Cell culture plate 6 / 12 / 24-well (Nunc)  
Cell scraper (Sarstedt, 83.1830)  
Cell strainer 30 µm (Sysmex, 04-004-2326)  
Cryovial CryoPure 1.6 mL (Sarstedt, 72.380)  
Flow cytometry tubes (Sarstedt, 55.1579)  
Neubauer counting chamber (Karl-Hecht KG)  
Pacing adapter/cables (EHT Technologies GmbH, P0002)  
Pacing electrode carbon (EHT Technologies GmbH, P0001)  
Pipette tips (Sarstedt)  
Pipette tips with Biosphere filter (Sarstedt)  
Reaction tube graduated 15 mL (Sarstedt, 62.554.502)  
Reaction tubes conical 15 / 50 mL (Sarstedt)  
Reaction tubes Safe Lock 0.2 – 2 mL (Eppendorf)  
Round bottom tube 12 mL (Greiner Bio-One, 163160)  
Serological pipettes 1 / 2 / 5 / 10 / 25 / 50 mL (Sarstedt)  
Silicone rack (EHT Technologies GmbH, C0001)  
Spinner flasks 500 / 1000 mL (Integra Biosciences, 182101 / 182051)

Syringe filtration unit Filtropur S 0.2 µm (Sarstedt, 83.1826.001)  
 Teflon Spacer (EHT Technologies GmbH, C0002)  
 TissueLyser Steel Beads (QIAGEN, 69989)

#### 9.3.4 Cell culture medium and serum

DMEM (Biochrom, F0415)  
 DMEM/F12 (Gibco, 21331-046)  
 Fetal calf serum (Biochrom, S0615)  
 Horse serum (Life Technologies, 26050088)  
 RPMI 1640 (Gibco, 21875)

#### 9.3.5 Reagents

1,4-Dithiothreitol (DTT, Roth, 6908.2)  
 10x DMEM (Gibco, 52100-021)  
 1-Thioglycerol (Sigma-Aldrich, M6145)  
 2-Mercaptoethanol (Sigma-Aldrich, M6250)  
 2-Propanol (Merck Millipore, 107022)  
 6x DNA loading dye (Thermo Fisher Scientific, R0611)  
 Accutase® Cell Dissociation Reagent (Sigma-Aldrich, A6964)  
 Acrylamide/Bis 40% (Bio-Rad Laboratories, 161-0146)  
 Activin A (R&D Systems, 338-AC)  
 Agarose (Invitrogen, 15510-027)  
 Ammoniumpersulfate (APS, Bio-Rad Laboratories, 161-0700)  
 Aprotinin (Sigma-Aldrich, A1153)  
 Aqua ad iniectabilia (Baxter S.A., 001428)  
 B27 Plus Insulin (Gibco, 17504-044)  
 Bacto™ Agar (BD, 214010)  
 Bacto™ Tryptone (BD, 211705)  
 Bacto™ Yeast Extract (BD, 212750)  
 bFGF (basic FGF, R&D Systems, 233-FB)  
 BMP4 (R&D Systems, 314-BP)  
 BTS (N-Benzyl-p-Toluenesulfonamide, TCI, B3082-25G)  
 Collagenase II (Worthington, LS004176)  
 D(+)-Glucose anhydrous (Roth, X997.2)  
 DMSO (Sigma-Aldrich, D4540)  
 DNase (Sigma-Aldrich, D8764)  
 Dorsomorphin (Abcam, ab120843 or Tocris, 3093)  
 EDTA (Roth, 8043.2)  
 Endothelin-1 (Sigma-Aldrich, E7764)  
 Ethanol, absolute (Chemsolute, 2246.1000)  
 Ethidium bromide (Sigma-Aldrich, E1510)  
 Fibrinogen (Sigma-Aldrich, F8630)  
 Fixable Viability Dye eFLUOR 450 (eBioscience, 65-0863-14)

Geltrex® (Gibco, A1413302)  
 GeneRuler 1 kb DNA Ladder (Thermo Fisher Scientific, SM0313)  
 GeneRuler 100 bp DNA Ladder (Thermo Fisher Scientific, SM0243)  
 HBSS (-) Ca<sup>2+</sup>/Mg<sup>2+</sup> (Gibco, 14175-053)  
 HEPES (Roth, 9105.4)  
 Human serum albumin (Biological Industries, 05-720-1B)  
 Hydrocortisone (Sigma-Aldrich, H4001)  
 Insulin (Sigma-Aldrich, I9278)  
 L-Glutamine (Gibco, 25030-081)  
 Lipidmix (Sigma-Aldrich, L5146)  
 Matrigel® Basement Membrane Matrix (Corning, 354234)  
 Matrigel® Growth Factor Reduced Basement Membrane Matrix (Corning, 354230)  
 Methanol (J. Baker, 8045)  
 Midori Green (Biozym, 617004)  
 Milk powder (Roth, T145.2)  
 N,N,N',N'-Tetramethylethylenediamine (TEMED, Bio-Rad Laboratories, 161-0801)  
 Na-Selenite (Sigma-Aldrich, T8158)  
 Nitrogen, liquid (TMG)  
 Non-essential amino acids (Gibco, 11140)  
 Oil red O (Sigma, O0625-25G)  
 Paraffin (Sigma-Aldrich, 327204)  
 Penicillin / Streptomycin (Gibco, 15140)  
 Phosphoascorbate (2-Phospho-L-ascorbic acid trisodium salt, Sigma-Aldrich, 49752)  
 Pluronic F-127 (Sigma-Aldrich, P2443)  
 Polyvinyl alcohol (Sigma-Aldrich, P8136)  
 PVA (Sigma-Aldrich, P8136)  
 (R)-(-)-Phenylephrine hydrochloride (Sigma-Aldrich, P6126)  
 Roti®-Histofix 4% (Roth, P087.3)  
 Saponin (Merck, 558255)  
 Sodium azide (Sigma-Aldrich, 71290)  
 Sodium chloride solution 0.9% (B. Braun, 3570210)  
 SuperSignal West Dura ECL (Thermo Fisher, 34075)  
 TBS (Sigma-Aldrich, T6664)  
 TGFβ1 (Peprotech, 100-21)  
 Thrombin (Sigma-Aldrich, T7513)  
 TOP10 chemically competent E. coli (Thermo Fischer Scientific, C404010)  
 Transferrin (Sigma-Aldrich, S5261)  
 Triiodothyronine (European Commission – Joint Research Center IRMM-469)  
 TRIS-hydrochloride (Roth, 9090.2)  
 Triton X®-100 (Roth, 3051.3)  
 Trizma® base (Sigma-Aldrich, T1503)  
 TRIzol (Life Technologies, 15596026)  
 Trypan Blue (Biochrom, L 6323)  
 Trypsin-EDTA 0.5% (Gibco, 15400054)  
 Tween 20 (Sigma-Aldrich, P1379)

XAV-939 (Tocris, 3748)  
Y-27632 (Biaffin, PKI-Y27632-010)

### 9.3.6 Kits and enzymes

5x HOT FIREPol® EvaGreen® qPCR Mix Plus ROX (Solis BioDyne, 08-24-00008)  
Agencourt AMPure XP - PCR Purification (Beckman Coulter, A63880)  
Amaxa™ P3 Primary Cell 4D-Nucleofector X Kit L (Lonza, V4XP-3024)  
Amaxa™ P4 Primary Cell 4D-Nucleofector X Kit L (Lonza, V4XP-4024)  
CloneJET PCR cloning kit (Thermo Fischer Scientific, K1232)  
DNeasy® Blood & Tissue Kit (QIAGEN, 69504)  
DreamTaq Green DNA Polymerase (Thermo Fischer Scientific, EP0711)  
EpiTect Bisulfite Kit (QIAGEN, 59104)  
FastDigest Esp3I/BsmBI (Thermo Fischer Scientific, FD0454)  
FastDigest BpiI/BbsI (Thermo Fischer Scientific, FD1014)  
HOT FIREPol® DNA Polymerase (Solis BioDyne, 01-02-00500)  
High-Capacity cDNA Reverse Transcription Kit (Applied Biosystems, 4368813)  
MinElute PCR Purification Kit (QIAGEN, 28004)  
MspI Restriction enzyme (Thermo Fischer Scientific, ER0541)  
NEBNext® Multiplex Oligos for Illumina® (NEB, E7335S)  
NEBNext® Ultra™ DNA Library Prep Kit for Illumina® (NEB, E7370S)  
NucleoBond® Xtra Maxi Kit (Macherey-Nagel, 740414.10)  
NucleoSpin® Plasmid Kit (Macherey-Nagel, 740588.250)  
PfuTurbo Cx Hotstart DNA Polymerase (Agilent, 600410)  
PrimeSTAR® HS DNA Polymerase (Takara, R010A)  
QIAquick® Gel Extraction Kit (QIAGEN, 28704)  
QIAquick® PCR Purification Kit (QIAGEN, 28104)  
Ribo-Zero rRNA Removal Kit (Illumina, MRZH116)  
RNA 6000 Pico Kit (Agilent, 5067-1513)  
RNeasy Plus® Mini Kit (QIAGEN, 74134)  
T4 DNA Ligase (NEB, M0202S)  
TRIzol Reagent (Life Technologies, 15596026)  
TruSeq Stranded Total RNA Library Prep Kit (Illumina, 20020596)  
Ultra View Universal DAB Detection Kit (Ventana, 05269806001)



9.3.7 Composition of reagents, buffers, and solutions**Table S2: Composition of used reagents, buffers, and solutions.**

Reagent / buffer / solutions	Composition
10x annealing buffer	100 mM Tris-HCl pH8 500 mM NaCl 10 mM EDTA Aqua dest.
Agar plates	15 g/L Bacto™ Agar Autoclave and cast into TC dish 100
Agarose for EHT casting	2% (w/v) Agarose 300 mL 1xPBS Sterilized by autoclaving before storage at 60 °C.
Aprotinin	33 mg/mL Aprotinin Aqua ad iniectabilia
Blotting buffer (1x)	20% (v/v) 5x Blotting buffer 20% (v/v) Methanol 60% (v/v) Aqua dest.
Blotting buffer (5x)	125 mM Trizma® base 950 mM Glycine Aqua dest.
BTS solution	30 mM BTS in DMSO
Dissociation buffer	HBSS (-) calcium/magnesium 200 U/mL Collagenase II 1 mM HEPES 10 µM Y-27632 30 µM BTS
DNase solution	100 mg DNase II, type V 50 mL PBS
EDTA	0.5 mM EDTA PBS
FACS buffer	PBS 5% (v/v) FCS 0.05% (v/v) Sodium azide 0.5% (w/v) Saponin (for intracellular staining)
Fibrinogen	200 mg/mL Fibrinogen 100 µg/mL Aprotinin 0.9%-NaCl solution
HEPES stock solution	1 M HEPES PBS Potassium hydroxide for adjustment of pH to 7.4

Laemmli buffer (1x)	0.2 g SDS 1 mg Bromphenol blue 1 g Glycerol 0.2 mL 0.5 M Tris (pH 6.8) 0.155 g DTT Aqua dest.
LB medium	10 g Bacto™ Tryptone 5 g Bacto™ Yeast Extract 10 g NaCl Ad 1 L aqua dest. pH 7.4
Phosphoascorbate, 250 mM	1 g Phosphoascorbate dissolved in 12.4 mL PBS
Pluronic F-127 solution	0.1% (v/v) Pluronic F-127 in PBS
Polyvinyl alcohol (50x)	20 g polyvinyl alcohol 100 mL Aqua dest.
SDS-PAGE electrophoresis buffer (10x)	250 mM Trizma® base 1.92 M Glycine 1% or 50% (w/v) SDS Aqua dest.
Separation gel SDS-Page (8%)	5.3 mL Aqua dest. 2 mL 40% Acrylamide 2.5 mL 1.5 M Tris pH 8.8 100 µL 10% SDS 100 µL 10% APS 10 µL TEMED
SOC medium	20 g Bacto™ Tryptone 5 g Bacto™ Yeast Extract 0.5 g NaCl 400 mL 1 M KCl pH 7.0; after autoclaving add 1 M MgCl <sub>2</sub> (sterile) 20 mL 1M Glucose (sterile)
Stacking gel SDS-Page (5%)	6 mL Aqua dest. 1.25 mL 40% Acrylamide 2.5 mL 0.5 M Tris pH 6.8 100 µL 10% (w/v) SDS 100 µL 10% (w/v) APS 10 µL TEMED
TAE buffer (50x) for agarose gel electrophoresis	242 g Trizma® base 37.2 g Titriplex III (EDTA) 57.1 mL concentrated acetic acid Ad 1 L aqua dest., pH 8.5 Use 1x diluted in aqua dest.

TBS (10x)	1 M Trizma® base or Tris-HCl 1.5 M NaCl Aqua dest.; pH 7.5 (adjust with 37% HCl)
Thrombin	100 U/mL Thrombin 60% (v/v) PBS 40% (v/v) Aqua ad iniectabilia
Transferrin–selenium	100 mg Transferrin 2 mL sodium selenite (382 µM)
Tris 0.5 M (pH 6.8)	60.6 g Trizma® base Ad 1 L Aqua dest.
Tris 1.5 M (pH 8.8)	181.7 g Trizma® base Ad 1 L Aqua dest.

### 9.3.8 Antibodies

**Table S3: Primary antibodies used for flow cytometry/FACS, western blot (WB), and immunohistochemistry (IHC) analysis.**

Antibody	Application & dilution	Company and #
Anti-ANP	IHC 1:6000	Millipore, MAB348
Anti-cardiac troponin T-FITC	FACS 1:10	Miltenyi Biotec, 130-106-687
Anti-Caspase3	IHC 1:300	R&D Systems, AF835
Anti-Collagen1	IHC 1:1500	abcam, Ab138492
Anti-Connexin43	IHC 1:100	BD Biosciences, 610061
Anti-DNMT3A	WB 1:500	CST, 2160
Anti-Ki-67	IHC 1:100	abcam, Ab15580
Anti-MLC2V	IHC 1:3000	Synaptic Systems, SY 310 111
REA Control (I)-FITC	FACS 1:10	Miltenyi Biotec 130-104-611

**Table S4: Secondary antibodies used for western blot analysis.**

Antibody	Dilution	Company and #
Anti-mouse IgG peroxidase-conjugated secondary antibody	1:10,000	Sigma, A3682
Anti-rabbit IgG peroxidase-conjugated secondary antibody	1:10,000	Sigma, A0545

### 9.3.9 Primer lists and NanoString Expression CodeSets

All primers were designed with the NCBI Primer-BLAST tool ([www.ncbi.nlm.nih.gov/tools/primer-blast/](http://www.ncbi.nlm.nih.gov/tools/primer-blast/)). For sequencing primers, the respective sequence from the NCBI genomic database was used as template and product size was chosen to be 250 – 650 bp. Primers for qPCR were designed complementary to the respective cDNA. To prevent amplification of genomic DNA contaminations, primers were designed to be located at exon-exon junctions and produce products of 150 – 300 bp which contain an intron on the DNA level (intron spanning). All primers were ordered as unmodified oligoes at MWG/Eurofins. The NanoString Expression CodeSets were ordered from NanoString in a customized manner. The basic tag set includes the 6 housekeeping genes (HKG), as well as 30 target genes. All extension tag sets include 24 additional genes.

**Table S5: Primer pairs for PCR and sequencing.**

Target	Sequence [5'→3']	Tm [°C]	Product [bp]
DNMT3A Seq	Fw: AATGACCTCTCCATCGTCAACC Rv: AGGCCCTTGCAAAGCAGAA	60.09 62.66	503
hU6-fw	Fw: GAGGGCCTATTTCCCATGATTCC	60.82	-
OT#1	Fw: CCATCATTGTGGGCATGCTG Rv: AATGGTCCTCGCTTTGCTGA	59.9 59.96	469
OT#2	Fw: GTGACTGCATGGCCTACACG Rv: GAGCTACGGCTCCGACAAG	61.36 60.23	450
OT#3	Fw: CGCCAGGTATAGGTGCTCAG Rv: AAGAGGTGATGAAGCACGCA	59.97 59.96	614
OT#4	Fw: TCCCTGCAGAACTCAGTCAC Rv: TGTCTGTGAGTCTTTGGGGC	59.32 59.89	490
OT#5	Fw: AAGCCTGGAAAAAGGGAGGC Rv: CACCTAAGGCTGGCTATCCC	60.54 59.6	573
OT#6	Fw: CAAGGCATTTGTCAGGAGTGC Rv: CAAAGGGGAACAAGGACCCA	60.07 59.81	464
OT#7	Fw: CACTGACGTCTGCGATGGG Rv: AGCTTCAGGTTGGGCCG	60.81 59.59	461
OT#8	Fw: CTGGACTTACCTCTCTTCTCCTG Rv: GCCCTTCAGTCCAGCACAAATT	59.3 61.66	580
OT#9	Fw: CTCATATTCAACTGTCCACTGCTC Rv: TACATTTCAAGGCTGATCCAGGCA	59.43 61.97	453
OT#10	Fw: CTTCCCCCAGAAAGCCTAAATGT Rv: TCTGGACACTTTCGTATGTCCC	60.56 59.77	487

Table S6: Primer pairs for qRT-PCR.

Target	Accession	Sequence [5'→3']	Product [bp]
DNMT1	NM_001130823.2	Fw: GGCAGACCATCAGGCATTCT Rv: TATTGGGACACCTCCGCTCT	279
DNMT3A	NM_153759	Fw: TCGCGATTTCTCGAGTCCAA Rv: TTGGCTATCCTGCCATGCTC	170
DNMT3B	NM_006892.3	Fw: GCAAGTTCTCCGAGGTCTCT Rv: ACGACGCACCTTCGACTTAT	293
GUSB	NM_000181.3	Fw: ACGATTGCAGGGTTTCACCA Rv: CACTCTCGTCGGTGACTGTT	171
Adipsin	NM_001317335.1	Fw: TGCTACAGCTGTCGGAGAAGG Rv: TCAAGCGCTCGGTGATGG	231
PPAR $\gamma$	NM_015869.4	Fw: CTTCCAACCTCCCTCATGGCA Rv: CGCCCAAACCTGATGGCATT	247

Table S7: NanoString Expression CodeSets

HKG	Basic tag set		Arrhythmia extension tag set	
<b>ABCF1</b>	ACTA1	FN1	ATP1A1	KCNJ11
<b>ACTB</b>	ACTA2	MEOX1	ATP1A2	KCNJ12
<b>CLTC</b>	ACTC1	MYH6	CACNA1C	KCNJ2
<b>GAPDH</b>	ACTN2	MYH7	CACNA1G	KCNJ3
<b>PGK1</b>	ATP2A2	NFKB1	HCN4	KCNJ5
<b>TUBB</b>	BAX	NPPA	KCNA4	KCNMA1
	BCL2	NPPB	KCNA5	KCNN3
	CASP3	PLN	KCND3	KCNQ1
	CASQ2	POSTN	KCNE1	SCN10A
	CDH5	PPP1R1A	KCNE2	SCN5a
	COL1A1	RCAN1	KCNH2	SLC8A1
	COL3A1	RYR2	KCNIP2	SLC9A1
	CTGF	S100A4		
	FHL1	SRF		
	FHL2	VWF		

## 9.4 Security information

The experiments were all performed in certified security standard S1 and S2 laboratories. All chemicals, buffers, and solutions were handled and disposed of according to their security data sheets in appropriate containers. Cell-containing or contaminated material was autoclaved before disposal. All surfaces that have been possibly contaminated with genetically modified organisms were cleaned with 70% ethanol.

**Table S8: Security information (H- and P-statements) of all used substances.**

Substance	CAS #	H-statement	P-statement
1,4-Dithiothreitol (DTT)	3483-12-3	H: 302, 315, 319, 412	P: 264, 270, 273, 280, 337+313, 501
1-Thioglycerol	96-27-5	H: 302-311-315-319-335	P: 261-280-305+351+338+312
2-Mercaptoethanol	60-24-2	H: 301+331, 310, 315, 317, 318, 373, 410	P: 270, 280, 302+352, 330, 304+340, 305+351+338, 310
2-Propanol	67-63-0	H: 225, 319, 336	P: 210, 261, 305+351+338
Acetic acid	64-19-7	H: 226-290-314	P: 210-280-301+330+331-305+351+338-308+310
Acrylamide/Bis solution, 29:1, 40%	79-06-1 110-26-9	H: 302, 312, 315, 319, 317, 340, 350, 361, 372	P: 260, 280, 281, 305+351+338, 405, 501
Ammonium persulfate (APS)	7727-54-0	H: 272, 302, 315, 317, 319, 334, 335	P: 221, 210, 285, 405 305+P351+P338, 501
Ampicillin trihydrate	7177-48-2	H: 317-334	P: 280-285, 302+352-304+341-333+313-342+311
Calcium chloride dihydrate (CaCl <sub>2</sub> x 2 H <sub>2</sub> O)	10035-04-8	H: 319	P: 305+351+388
Carbachol	51-83-2	H: 300	P 308+310
Dorsomorphin	866405-64-3	H: 302, 312, 332	P: 301+312, 304+340, 302+352, 261, 280, 264, 270, 271, 330, 501, 363
Ethanol, absolute	64-17-5	H: 225, 319	P: 210, 240, 305+351+338, 403+233
Ethidium bromide	1239-45-8	H: 331, 341	P: 261-281-311
EDTA	60-00-4	H: 319	P: 305+351+338
Formaldehyde	50-00-0	H: 351-331-311-301-314-317	P: 301+310-303+361+353-305+351+338, 320-361-405-501

Lipidmix	64-17-5	H: 225, 319	P210, 280, 305+351+338, 337+313, 403+235
Methanol	67-56-1	H: 225-331-311-301-370	P: 210-233-280-302+352
N,N,N',N'-Tetramethyl ethylenediamine (TEMED)	110-18-9	H: 225, 332, 302, 314	P: 210, 233, 280, 301+330+331, 305+351+338, 308, 310
Nitrogen, liquid (N <sub>2</sub> )	7727-37-9	H: 281	P: 282, 336+315, 403
Penicillin	61-33-6	H: 317	P: 280
Ponceau S	6226-79-5	H: 315-319-335	P: 261–305+351+338
Potassium di-hydrogen phosphate (KH <sub>2</sub> PO <sub>4</sub> )	7778-77-0	--	P: 260
Proteinase K	39450-01-6	H: 334	P: 304+340, 261, 342+311, 284
Roti®-Histofix 4%	50-00-0 67-56-1	H: 302, 317, 341, 350	P: 261, 280, 302+352, 308+313
Saponin	8047-15-2	H: 319, 335	P 261, 305+351+338
Sodium azide	26628-22-8	H: 300-400-410	P: 273–309-310
Sodium dodecyl sulfate (SDS)	151-21-3	H: 228, 302+332, 315, 318, 335, 412	P: 210, 261, 280, 302+352, 305+351+338, 312
Sodium hydroxide (NaOH)	1310-73-2	H: 314	P: 280–301+330+331–309–310-305+351+338
Sodium selenite	10102-18-8	H: 300+330, 315, 317, 319, 411	P: 260, 280, 301+330+331+310, 304+340+310, 403+233
Streptomycin	57-92-1	H: 302	--
Thrombin	9002-04-4	H: 315, 319, 334, 335	P: 261, 305+351+338, 342+311
Titriplex® III	6381-92-6	H: 332-373	P: 314
TRIS-Hydrochlorid (Tris-HCl)	1185-53-1	H: 315, 319, 335	P: 280, 302+352, 305+351+338
Triton X-100	9002-93-1	H: 302-318-411	P: 273-280-305+351+338
TRIzol reagent	108-95-2 593-84-0 1762-95-4	H: 301+311+331, 314, 335, 341, 373, 412	P: 201, 261, 261, 280, 273, 301+310, 302+352
Trypan blue	72-57-1	H: 350	P: 201-308+313
Y-27632	331752-47-7	H: 302-312-332	P: 280

9.4.1 EU-GHS Hazard (H) statements**H200** Unstable explosives.**H201** Explosive; mass explosion hazard.**H202** Explosive, severe projection hazard.**H203** Explosive; fire, blast or projection hazard.**H204** Fire or projection hazard.**H205** May mass explode in fire.**H220** Extremely flammable gas.**H221** Flammable gas.**H222** Extremely flammable aerosol.**H223** Flammable aerosol.**H224** Extremely flammable liquid and vapour.**H225** Highly flammable liquid and vapour.**H226** Flammable liquid and vapour.**H228** Flammable solid.**H229** Pressurised container: May burst if heated.**H230** May react explosively even in the absence of air.**H231** May react explosively even in the absence of air at elevated pressure and/or temperature.**H240** Heating may cause an explosion.**H241** Heating may cause a fire or explosion.**H242** Heating may cause a fire.**H250** Catches fire spontaneously if exposed to air.**H251** Self-heating: may catch fire.**H252** Self-heating in large quantities; may catch fire.**H260** In contact with water releases flammable gases which may ignite spontaneously**H261** In contact with water releases flammable gases.**H270** May cause or intensify fire; oxidizer.**H271** May cause fire or explosion; strong oxidizer.**H272** May intensify fire; oxidizer.**H280** Contains gas under pressure; may explode if heated.**H281** Contains refrigerated gas; may cause cryogenic burns or injury.**H290** May be corrosive to metals.**H300** Fatal if swallowed.**H301** Toxic if swallowed.**H302** Harmful if swallowed.**H304** May be fatal if swallowed and enters airways.**H310** Fatal in contact with skin.**H311** Toxic in contact with skin.**H312** Harmful in contact with skin.**H314** Causes severe skin burns and eye damage.**H315** Causes skin irritation.**H317** May cause an allergic skin reaction.**H318** Causes serious eye damage.**H319** Causes serious eye irritation.**H330** Fatal if inhaled.**H331** Toxic if inhaled.**H332** Harmful if inhaled.**H334** May cause allergy or asthma symptoms or breathing difficulties if inhaled.**H335** May cause respiratory irritation.**H336** May cause drowsiness or dizziness.**H340** May cause genetic defects.**H341** Suspected of causing genetic defects.**H350** May cause cancer.**H351** Suspected of causing cancer.**H360** May damage fertility or the unborn child.**H361** Suspected of damaging fertility or the unborn child.**H362** May cause harm to breast-fed children.**H370** Causes damage to organs.**H371** May cause damage to organs.**H372** Causes damage to organs through prolonged or repeated exposure.**H373** May cause damage to organs through prolonged or repeated exposure.**H400** Very toxic to aquatic life.**H410** Very toxic to aquatic life with long lasting effects.**H411** Toxic to aquatic life with long lasting effects.



**H412** Harmful to aquatic life with long lasting effects.

**H413** May cause long lasting harmful effects to aquatic life.

**H420** Harms public health and the environment by destroying ozone in the upper atmosphere.

#### 9.4.2 EU-GHS Precaution (P) statements

**P101** If medical advice is needed, have product container or label at hand.

**P102** Keep out of reach of children.

**P103** Read label before use.

**P201** Obtain special instructions before use.

**P202** Do not handle until all safety precautions have been read and understood.

**P210** Keep away from heat, hot surfaces, sparks, open flames and other ignition sources. No smoking.

**P211** Do not spray on an open flame or other ignition source.

**P220** Keep away from clothing and other combustible materials.

**P222** Do not allow contact with air.

**P223** Do not allow contact with water.

**P230** Keep wetted with...

**P231** Handle and store contents under inert gas/...

**P232** Protect from moisture.

**P233** Keep container tightly closed.

**P234** Keep only in original packaging.

**P235** Keep cool.

**P240** Ground and bond container and receiving equipment.

**P241** Use explosion-proof [electrical/ventilating/lighting/...] equipment.

**P242** Use non-sparking tools.

**P243** Take action to prevent static discharges.

**P244** Keep valves and fittings free from oil and grease.

**P250** Do not subject to grinding/shock/friction/...

**P251** Do not pierce or burn, even after use.

**P260** Do not breathe dust/fume/gas/mist/vapors/spray.

**P261** Avoid breathing dust/fume/gas/mist/vapors/spray.

**P262** Do not get in eyes, on skin, or on clothing.

**P263** Avoid contact during pregnancy and while nursing.

**P264** Wash ... thoroughly after handling.

**P270** Do not eat, drink or smoke when using this product.

**P271** Use only outdoors or in a well-ventilated area.

**P272** Contaminated work clothing should not be allowed out of the workplace.

**P273** Avoid release to the environment.

**P280** Wear protective gloves/protective clothing/eye protection/face protection.

**P282** Wear cold insulating gloves and either face shield or eye protection.

**P283** Wear fire resistant or flame retardant clothing.

**P284** [In case of inadequate ventilation] wear respiratory protection.

**P301** IF SWALLOWED:

**P302** IF ON SKIN:

**P303** IF ON SKIN (or hair)

**P304** IF INHALED:

**P305** IF IN EYES:

**P306** IF ON CLOTHING:

**P308** IF exposed or concerned:

**P310** Immediately call a POISON CENTRE/doctor/...

**P311** Call a POISON CENTRE/doctor/....

**P312** Call a POISON CENTRE/doctor/... if you feel unwell.

**P313** Get medical advice/attention.

**P314** Get medical advice/attention if you feel unwell.

**P315** Get immediate medical advice/attention.

**P320** Specific treatment is urgent (see ... on this label).

**P321** Specific treatment (see ... on this label).

**P330** Rinse mouth.

**P331** Do NOT induce vomiting

**P332** If skin irritation occurs:

**P333** If skin irritation or rash

**P334** Immerse in cool water [or wrap in wet bandages].

**P335** Brush off loose particles from skin.

**P336** Thaw frosted parts with lukewarm water. Do not rub affected area.

**P337** If eye irritation persists:

**P338** Remove contact lenses, if present and easy to do. Continue rinsing.

**P340** Remove person to fresh air and keep comfortable for breathing.

**P342** If experiencing respiratory symptoms:

**P351** Rinse cautiously with water for several minutes.

**P352** Wash with plenty of water/...

**P353** Rinse skin with water [or shower].

**P360** Rinse immediately contaminated clothing and skin with plenty of water before removing clothes.

**P361** Take off immediately all contaminated clothing.

**P362** Take off contaminated clothing.

**P363** Wash contaminated clothing before reuse.

**P364** And wash it before reuse.

**P370** In case of fire:

**P371** In case of major fire and large quantities:

**P372** Explosion risk.

**P373** DO NOT fight fire when fire reaches explosives.

**P375** Fight fire remotely due to the risk of explosion.

**P376** Stop leak if safe to do so.

**P377** Leaking gas fire: Do not extinguish, unless leak can be stopped safely.

**P378** Use ... to extinguish.

**P380** Evacuate area.

**P381** In case of leakage

**P390** Absorb spillage to prevent material damage.

**P391** Collect spillage.

**P401** Store in accordance with...

**P402** Store in a dry place.

**P403** Store in a well-ventilated place.

**P404** Store in a closed container.

**P405** Store locked up.

**P406** Store in a corrosion resistant/... container with a resistant inner liner.

**P407** Maintain air gap between stacks or pallets.

**P410** Protect from sunlight.

**P411** Store at temperatures not exceeding ...°C/...°F.

**P412** Do not expose to temperatures exceeding 50°C/ 122°F.

**P413** Store bulk masses greater than ... kg/... lbs at temperatures not exceeding ...°C/...°F.

**P420** Store separately.

**P501** Dispose of contents/container to ...

**P502** Refer to manufacturer or supplier for information on recovery or recycling.

## 9.5 Publications and congress participations

### 9.5.1 Publications

Stenzig J\*, Hirt MN\*, Löser A, Bartholdt LM, Hensel JT, Werner TR, Riemenschneider M, Indenbirken D, Guenther T, Müller C, Hübner N, Stoll M, Eschenhagen T. (2016) DNA methylation in an engineered heart tissue model of cardiac hypertrophy: common signatures and effects of DNA methylation inhibitors. *Basic Res Cardiol* 111:9.

Horváth A, Lemoine MD, Löser A, Mannhardt I, Flenner F, Uzun AU, Neuber C, Breckwoldt K, Hansen A, Girdauskas E, Reichenspurner H, Willems S, Jost N, Wettwer E, Eschenhagen T, Christ T. (2018) Low Resting Membrane Potential and Low Inward Rectifier Potassium Currents Are Not Inherent Features of hiPSC-Derived Cardiomyocytes. *Stem Cell Reports* 10:822–833.

Stenzig J\*, Schneeberger Y\*, Löser A, Peters BS, Schaefer A, Zhao R, Ng SL, Höppner G, Geertz B, Hirt MN, Tan W, Wong E, Reichenspurner H, Foo RS, Eschenhagen T. (2018) DNA methylation inhibition attenuates pressure overload-induced cardiac hypertrophy in rats. *J Mol Cell Cardiol* 07.2018.

Krause J\*, Löser A\*, Lemoine MD, Christ T, Scherschel K, Meyer C, Blankenberg S, Zeller T, Eschenhagen T, Stenzig J (2018) Rat atrial engineered heart tissue: a new in vitro model to study atrial biology. *Basic Res Cardiol*. 2018 Sep 3;113(5):41.

### 9.5.2 Participation at congresses and meetings

DZHK annual meeting, 16<sup>th</sup> – 19<sup>th</sup> September 2015, Potsdam, Germany; poster presentation “DNA methylation in engineered heart tissue subjected to increased afterload”

NCCR retreat, 29<sup>th</sup> – 30<sup>th</sup> January 2016; poster presentation “DNA methylation in an engineered heart tissue model of cardiac hypertrophy: effects of DNA methylation inhibitors”, awarded with a poster prize

DZHK annual meeting, 15<sup>th</sup> – 17<sup>th</sup> September 2016, Bad Aibling, Germany; second chair of the “CRISPR/Cas9 Genome Editing” session

34th Annual Meeting of the European Section of the ISHR, 24<sup>th</sup> - 27<sup>th</sup> July 2017, Hamburg, Germany; selected oral abstract and poster presentation “DNA Methylation in an Engineered Heart Tissue Model of Cardiac Hypertrophy: Effects of DNA Methylation Inhibitors”

DZHK annual meeting, 13<sup>th</sup> – 16<sup>th</sup> September 2017, Warnemünde, Germany; oral presentation “A new in vitro model for atrial physiology and disease”

AHA Scientific Sessions 2017, 11<sup>th</sup> – 15<sup>th</sup> November 2017, Anaheim, California, USA; poster presentation “Studying atrial physiology and drug response in a new engineered heart tissue model”

Symposium on Medical Epigenetics 2018, 12<sup>th</sup> – 14<sup>th</sup> March 2018, Freiburg, Germany

## 10 Acknowledgements

I would first of all like to thank my parents for their unconditional support in everything I have ever wanted to achieve in my life. They did everything in their power to provide me with the best possible opportunities for my future and supported me in every possible way during my time at university and during my PhD work and for this I am very thankful. I also owe deepest gratitude to my fiancé for his love and support in everything I do and for always being by my side through all the ups and downs of my life. Also, I am very grateful to my sister, for always being just one phone call away when I need her and for always having my back.

I want to thank Prof. Thomas Eschenhagen for giving me the opportunity to work in his institute in the scope of my PhD project. His scientific input and guidance greatly contributed to both the success of the project and my personal development as a scientist.

In this context, I also would like to thank Prof. Elke Oetjen for her interest in my work, for the supervision of my thesis on behalf of the Department of Chemistry, as well as for the evaluation of my dissertation and for presiding the disputation committee of my thesis.

Special thanks go to Justus Stenzig for supervising my work with the perfect combination of allowing me to work independently and nevertheless always being there whenever I had a problem or needed input. Working with him was a great pleasure. Many thanks are moreover due to Grit Höppner, Julia Krause, and Anika Knaust for always having a helping hand, for providing emotional support, and for being the best colleagues anyone could wish for. I also would like to thank everyone else at the Institute of Experimental Pharmacology and Toxicology who contributed to a pleasant working environment during these last 4 years.

I would additionally like to highlight the contribution of the people involved in the different parts of this thesis: the CRISPR/differentiation team around Sandra Laufer, Antonia Zech, Anika Knaust, Thomas Schulze, Birgit Klampe and Maksymilian Prondzynski; Kristin Hartmann from the UKE Mouse Pathology Core Facility for histological stainings; Bärbel Ulmer and Aya Shibamiya for providing the ERC018 trisomy cell line; Julia Krause and Tobias Krause for sharp electrode action potential measurements; Elisabeth Krämer for support with NanoString measurements; the Genome Institute of Singapore for RRBS analysis. I am very grateful to every one of these people for their help and support of my work, which would not have been the same without them.


## 11 Declaration of academic honesty - Eidesstattliche Erklärung

I hereby declare that my thesis entitled

“Epigenetic mechanisms of transcriptional regulation in cardiac hypertrophy using engineered heart tissue“

carried out at the Institute of Experimental Pharmacology and Toxicology, UKE Hamburg in the laboratory of Prof. Dr. Thomas Eschenhagen, with the support of Dr. Dr. Justus Stenzig and the supervision of Prof. Dr. Elke Oetjen for the Department of Chemistry, was written independently by myself. No other sources or aids than those indicated were used. The submitted written form of the thesis complies with the electronic version. This thesis was not handed in in any other form for another examination procedure.

Hamburg, 11.10.2018

  
Alexandra Löser


---

Hiermit versichere ich an Eides statt, die vorliegende Dissertation mit dem Titel

“Epigenetic mechanisms of transcriptional regulation in cardiac hypertrophy using engineered heart tissue“

durchgeführt am Institut für Experimentelle Pharmakologie und Toxikologie des Universitätsklinikums Hamburg-Eppendorf unter der Leitung von Herrn Prof. Dr. Thomas Eschenhagen, der Unterstützung von Herrn Dr. Dr. Justus Stenzig und der Betreuung durch Frau Prof. Dr. Elke Oetjen für den Fachbereich Chemie, selbst verfasst und keine anderen als die angegebenen Hilfsmittel benutzt zu haben. Die eingereichte schriftliche Fassung entspricht der elektronischen Version. Ich versichere, dass diese Dissertation nicht in einem früheren Promotionsverfahren eingereicht wurde.

Hamburg, den 11.10.2018

  
Alexandra Löser